Hybrid refrigeration system with a novel membrane exchanger

Rasha Mustapha

PSL UNIVERSITÉ PARIS

THÈSE DE DOCTORAT
DE L'UNIVERSITÉ PSL

Préparée à MINES ParisTech

Hybrid Refrigeration System with a Novel Membrane Exchanger

Système de Réfrigération Hybride Comportant un Echangeur Membranaire Innovant

Soutenue par

Rasha MUSTAPHA

Le 15 Novembre 2019

Ecole doctorale n° 621

Ingénierie des Systèmes, Matériaux, Mécanique, Énergetique

Spécialité

Énergétique et Procédés

Composition du jury :

Laurence, FOURNAISON Directrice de Recherche, Irstea	*Président*
Predrag, HRNJAK Professeur, Université d'Illinois	*Rapporteur*
Vincent, LEMORT Professeur, Université de Liège	*Rapporteur*
Khalil, EL KHOURY Professeur, Université Libanaise	*Examinateur*
Kamel, GHALI Professeur, Université Américaine de Beyrouth	*Examinateur*
Assaad, ZOUGHAIB Professeur, PSL-Mines ParisTech	*Directeur de thèse*

MINES ParisTech | PSL

To the Memory of my Dad

ACKNOWLEDGMENT

This thesis would never have been realized without some great people who contributed with their expertise and precious help.

I am absolutely thankful to my thesis advisor Dr. Assaad ZOUGHAIB for his continuous support and insightful comments. His encouragement, friendly attitude and one-of-a-kind sense of humor were the main sources of motivation during these three years.

Besides my adviser, I wish to thank the members of my dissertation committee: Dr. Predrag HRNJAK, Dr. Vincent LEMORT, Dr. Laurence FOURNAISON, Dr. Kamel GHALI and Dr. Khalil EL KHOURY for generously offering their time, support, guidance and good will throughout the preparation and review of this thesis. I feel proud and honored that you have accepted to be on my committee.

I would like to gratefully acknowledge the financial support of ERANETMED project Sol-Cool-Dry, ID number: ERANETMED_ENERG-11-138 under ERA-MET Initiative "EURO-MEDITERRANEAN Cooperation through ERANET joint activities of FP7 INITIATIVE ERANETMED.

Throughout the ERANETMED project, I had the chance to participate in international academic discussions. I am indebted to those who contributed to the rich exchange of ideas and information especially Dr. Nesreen GHADDAR and Dr. Kamel GHALI. This research process was greatly supported by their valuable insights. I would like to thank them as well for supplying us with some membrane materials manufactured in the laboratories of the American University of Beirut.

I wish to record my gratitude to Dr. Khalil EL KHOURY for his help and constructive advices throughout these years and who has always generously made his broad international relationships available for his students.

My debts go to my colleagues for providing a stimulating environment for learning and growing and even far beyond to those who read the manuscript and those who have accompanied me from one moment to another during this period of research life.

Finally, nobody has been more important for me in the completion of this work than my family members, Daad, Samer, Nathalie, Reem, Roni, Rayn and last but least Rami. I would like to thank them all for their endless love and support providing me the necessary faith and strength to pursue my goals. Without them life would have been much harder.

Table of Contents

List of Figures

List of Tables

Nomenclature

Latin letters

A	Area	[m^2]
C	Concentration	[kg/kg] unless indicated otherwise
C_p	Specific heat at constant pressure	[J/kg.K]
D	Mass diffusion coefficient	[m^2/s]
D	Hydraulic diameter	[m]
g	Gravitational acceleration,	[m/s^2]
h	Specific enthalpy	[J/kg]
H	Enthalpy	[J]
H	Height	[m]
H_f	Fan static pressure	[m]
h_{fg}	Latent heat of vaporization of water	[J/kg]
H_p	Pump head	[m]
h_M	Mass transfer coefficient	[kg/m^2.s]
h_T	Heat transfer coefficient	[W/m^2.K]
h_{Tc}	Heat transfer coefficient in the confined space	[W/m^2.K]
K_T	Thermal conductivity	[W/m.K]
k_m	Mass conductivity of the membrane	[kg/m.s]
L	Length	[m]
L_c	Characteristic length for convection correlations	[m]
m	Mass	[kg]
$\dot{m}$	Mass flow rate	[kg/s] unless indicated otherwise
Ni	Number of discretization in the direction of x-axis	[-]
Nj	Number of discretization in the direction of z-axis	[-]
P	Pressure	[Pa]
Q	Load or heat transfer	[W]
R	Resistance to heat and mass transfer	[m^2s/kg] unless indicated otherwise
R’	Ratio of latent to sensible load	[%]
RH	Relative humidity	[%]
t	Time	[s]
T	Temperature	[K] unless indicated otherwise
u	Uncertainty	[%]
U_M	Overall mass exchange coefficient	[kg/m^2.s]
W	Width	[m]
X	Mass of water per mass of dry desiccant	[kg_w/kg_d]
Y	Mass of water vapor per mass of dry air	[kg_v/kg_{da}]

Z	Height of the dehumidifier	[m]

Dimensionless Numbers

Gr	Grashof number	[-]
Le	Lewis number	[-]
Nu	Nusselt number	[-]
Pr	Prandtl number	[-]
Ra	Rayleigh number	[-]
Re	Raynold number	[-]

Greek symbols

α	Correction factor at low air speed	[-]
β	Coefficient of volume expansion	[1/K]
γ	Correction factor at low air speed	[-]
δ	Thickness	[m]
η	Efficiency	[%]
θ	Reduced temperature	[-]
ϑ	Kinematic viscosity of the fluid	[m^2/s]
μ	Dynamic viscosity	[$N.s/m^2$]
ξ	Concentration of desiccant in the solution	[kg/kg]
ρ	Density	[Kg/m^3]

Subscripts

a	Humid air
avg	Average
b	Boundary layer
c	Cavity
C	Celsius
cf	Cold fluid
comp	Compressor
cond	Condenser
d	Dry desiccant
da	Dry air
dp	Dew point
evap	Evaporator
f	Fan
f	Falling film
hf	Hot fluid
i	Inlet
is	Isentropic

L	Latent
m	Membrane
ma	Membrane-air
ms	Membrane-solution
mw	Membrane-water
o	Outlet
or	Outlet return
p	Pump
r	Return
ref	Refrigerant
reg	Regenerator
s	Desiccant solution
S	Sensible
T	Total
v	Vapor
w	Liquid water

Abbreviations and Acronyms

AC	Air Conditioner
ACH	Air Changes per Hour
ASTM	American Society for Testing and Materials
$CaCl_2$	Calcium Chloride
CO	Carbon Monoxide
CO_2	Carbon Dioxide
COP	Coefficient of Performance
ESA	European Space Agency
GHG	Green House Gases
HVAC	Heating, Ventilation and Air Conditioning
hx	Heat Exchanger
IEA	International Energy Agency
IPCC	Intergovernmental Panel on Climate Change
ISO	International Organization for Standardization
LAMEE	Liquid to Air Membrane Energy Exchanger
LiBr	Lithium Bromide
LiCl	Lithium Chloride
MAE	Mean Absolute Error
NOAA	National Oceanic and Atmospheric Administration
NO_x	Nitrogen Oxides
NTU	Number of Transfer Units
NWF	Non Woven Fabric

PCM	Phase Change Material
PDF	Probability Density Function
PE	Poly-Ethylene
PP	Poly-Propylene
PTFE	Poly-Tetra-Fluoro-Ethylene
RMSE	Root Mean Square Error
SHGC	Solar Heat Gain Coefficient
SO_x	Sulfur Oxides
std	Standard Deviation
VCC	Vapor Compression Cycle

General Introduction

The drastic impact of high energy consumption on the environment and on human's health is raising a critical alert which requires global strategic plans to overcome its destructive consequences. Energy consumption has been remarkably increasing during the last few decades and is likely to rise further in light of the developing global economy. In particular, higher electricity demands are forecasted mainly for heating and cooling in some cities of the world. Amidst the universal growth in the energy demand and its significant environmental impacts, it is of great importance to find techniques that provide the energy needs of the economies and simultaneously reduce the GHG emissions. Fundamental changes in the energy sector is evolving worldwide primarily driven by the integration of renewable energy sources and more energy efficient technologies.

Our work starts by describing the energy and environmental context related to the world electricity final consumption and percentage of CO_2 emissions by sector. It is shown that buildings play a dominant role accounting to 36% of global final energy consumption and having the largest share of the energy-related CO_2 emissions. Electricity use in buildings has had the largest growth of 15% between 2010 and 2017 with the space cooling leading this growth by more than 20% (International Energy Agency and the United Nations Environment Program, 2018). Space cooling is usually performed through vapor compression cycles that have low Coefficients of Performance (COP) and show deficiencies in handling latent loads. They consume excessive energy to remove humidity through cooling the air below its dew point temperature and then they reheat it to the desired indoor temperature. Therefore, realizing the potential of the buildings sector in contributing to the electricity consumption triggers the initiation of energy efficient building measures aiming to improve applications related mainly to space cooling.

Hybrid liquid desiccant vapor compression systems showed to be reliable alternatives for the conventional cooling systems by which the control of latent and sensible load is done separately. In these systems, a liquid desiccant cycle dehumidifies the air prior to its cooling by the vapor compression cycle. In some cases, the desiccant cycle could contribute simultaneously to both dehumidifying and partially cooling the air. This is accomplished through passing the desiccant solution by the evaporator of the vapor compression cycle to decrease its temperature. After absorbing water vapor from the air, the concentration of the desiccant solution decreases. Thus, it needs to be reactivated through a regeneration cycle that exchanges the solution with high temperature air heated by the free energy provided by the condenser of the vapor compression cycle. The movement of water vapor to or from the solution depends on the difference of vapor pressure between the solution and the surrounding air. A literature review of such hybrid systems is investigated in the first chapter focusing on the dehumidifier and the regenerator which are membrane based heat and mass exchangers. Their existing designs are then subjected to deep analysis and their drawbacks are inspected. In a way to solve their drawbacks, an innovative membrane based heat and mass exchanger is described and analyzed. It addresses a new

technique based on vertically spraying the liquid desiccant to increase the indirect contact surface area between the air and the liquid. Moreover, it questions the possibility of using certain low cost materials with convenient enduring characteristics as membranes for these exchangers. Yet, the challenge remains to find the physical properties of these materials that were originally fabricated for uses other than heat and mass exchange.

One major property of these materials, the mass conductivity, is determined in the second chapter. It is the ability to transmit water vapor and it greatly affects the transfer of heat and mass within the material. Aiming to infer the water vapor permeability of these materials, a collection of different fabrics is tested by a modified upright cup method, based on the ASTM E96 standard, but using a new methodology. The results of this test are subjected to an uncertainty analysis to assess the accuracy of our measurements. From the tested materials, the fabric with the best cost/quality compromise is then adopted and employed as a membrane to cover the channels of a prototype of a cross flow heat and mass exchanger.

The prototype is tested on a dedicated test bench allowing evaluating its performance. Validation experiments are performed at different operating conditions and data is collected from the different sensors inserted in the system. Next, in order to numerically predict the behavior of such an exchanger, a detailed mathematical model is developed using conjugate heat and mass transfer based on fitted algebraic equations and specific correlations. Simulations are performed and the validity of the suggested model is analyzed by comparing the simulation results to the experimental data mainly related to the power of the exchanger at the water side.

Finally, in the last chapter a complete evaluation of a hybrid liquid desiccant system is conducted to assess the seasonal air conditioning operation of an office located in a Mediterranean climate in the south of France. Several flexible configurations of such a hybrid system are suggested by adding heat exchangers and changing their location for different applications. Our developed model is used to estimate the performance of the dehumidifier and regenerator of the hybrid system. This study sheds the light on the importance of the system's flexibility and on the effect of the indoor latent to sensible load ratio (R') on the system's performance. As a final point, the simulation results of the three configurations are then compared to that of a conventional air conditioning system to evaluate their potential savings.

Chapitre 1 Contexte, Etat de l'art et la Problématique (résume)

1.1 Contexte

1.1.1 Le contexte énergétique et environnemental

L'énergie et l'environnement sont les problèmes globaux qui semblent préoccuper sérieusement les sociétés. Le réchauffement climatique représente le principal problème environnemental auquel le monde est confronté de nos jours. La principale cause du réchauffement de la planète est l'émission de CO2 dans l'atmosphère qui est causée principalement par la combustion de combustibles fossiles. Si le réchauffement de la planète continue d'augmenter, des changements climatiques importants se produiront et des effets graves auront lieu à long terme. Ces impacts incluent la fonte des masses glacières polaires menant à la montée de la mer et menaçant les villes côtières et les zones de faible altitude. Selon l'Agence Spatiale Européenne (ESA), le niveau de la mer a augmenté de 20 % entre 1992 et 2012. D'autres impacts consistent en l'assèchement des climats tropicaux, principalement en Afrique et en Inde, les phénomènes météorologiques extrêmes comme les inondations et les tempêtes, l'acidité accrue des océans et l'air plus pollué. Ces changements affectent la santé humaine par la dégradation de la qualité de l'eau et des aliments. En outre, le changement climatique provoque des maladies contagieuses et des élévations de température, ce qui entraîne la perturbation de notre écosystème et réduisant ainsi les ressources nécessaires à un mode de vie sain.

La croissance de la population et les progrès technologiques des dernières décennies ont fait grimper la demande d'énergie et donc d'électricité. La consommation mondiale d'électricité était de 5271 TWh en 1974 et en 2016 cette valeur a atteint 20864 TWh, 3,2% de plus que celle de 2015 (fig.1). Les sources utilisées pour produire de l'électricité font évoluer le monde vers un changement climatique significatif grâce aux émissions de GES et, plus particulièrement, de CO2, et des études montrent qu'environ la moitié des émissions mondiales de CO2 sont dues à la production d'électricité et de chaleur.

La croissance de la consommation d'électricité s'est principalement produite dans le secteur du bâtiment qui constitue les bâtiments résidentiels et commerciaux et les bâtiments de service public. Cela fait du secteur du bâtiment le plus grand consommateur d'électricité dépassant la part industrielle. L'utilisation de l'électricité dans les bâtiments a connu la plus forte croissance de 15 % entre 2010 et 2017, le rafraichissement des espaces ayant conduit cette croissance de plus de 20 % (Agence internationale de l'énergie et Programme des Nations Unies pour l'environnement, 2018). En outre, le secteur du bâtiment a la plus grande part des émissions de CO2 liées à l'énergie. Ainsi, prendre des mesures responsables et durables concernant nos ressources naturelles et notre écosystème contribue au bien-être de la population.

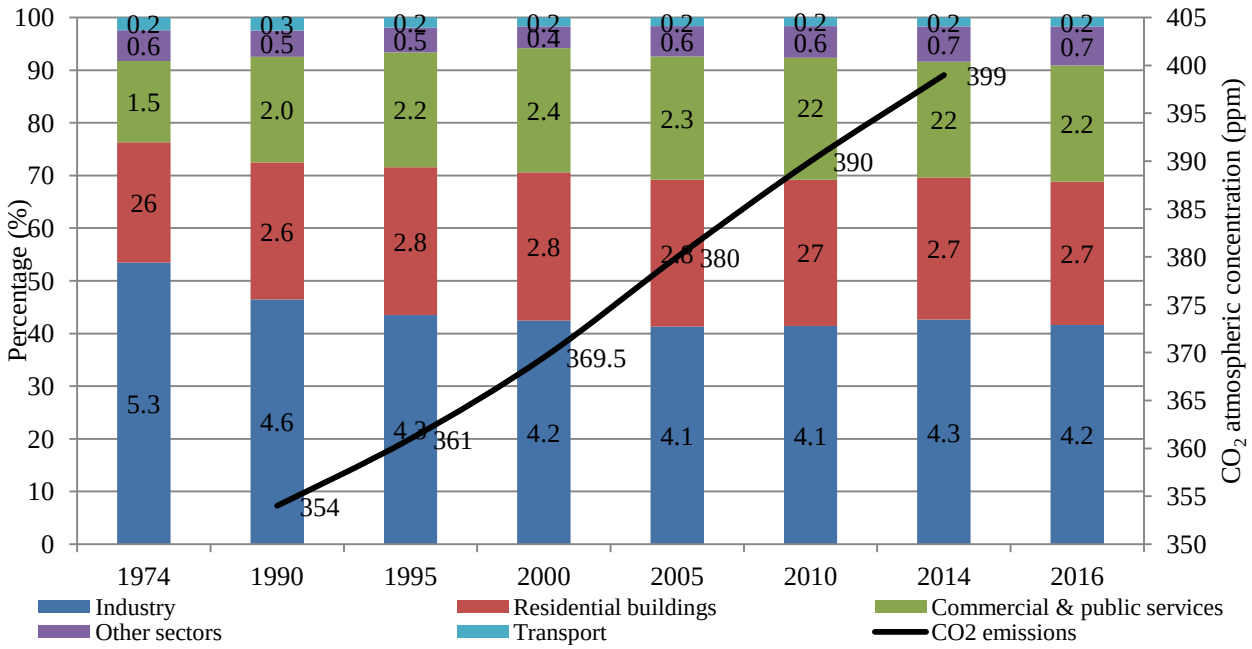

Figure 11: Consommation finale mondiale d'électricité par secteur et concentration atmosphérique de CO_2

1.1.2 Le contexte de climatisation

Le graphique de la figure 2 montre l'expansion de l'électricité utilisée pour la climatisation au fil des ans ainsi que sa part dans la consommation totale d'électricité dans les bâtiments (Birol, 2018). La climatisation consomme assez d'électricité, cependant nous sommes certains que le besoin de climatisation va augmenter globalement dans les décennies à venir. Cette augmentation est le résultat du changement climatique, de l'élévation de la température, de la croissance de la population et d'un plus grand désir de confort thermique. L'électricité consommée par la climatisation pourrait croître de 1997 TWh en 2016 à 6200 TWh en 2050 selon le scénario de base ou à 3400 TWh selon un scénario de climatisation efficace. L'utilisation de nouvelles technologies de climatisation à basse énergie permet alors de maîtriser la consommation d'énergie au niveau global en réduisant celle de l'électricité.

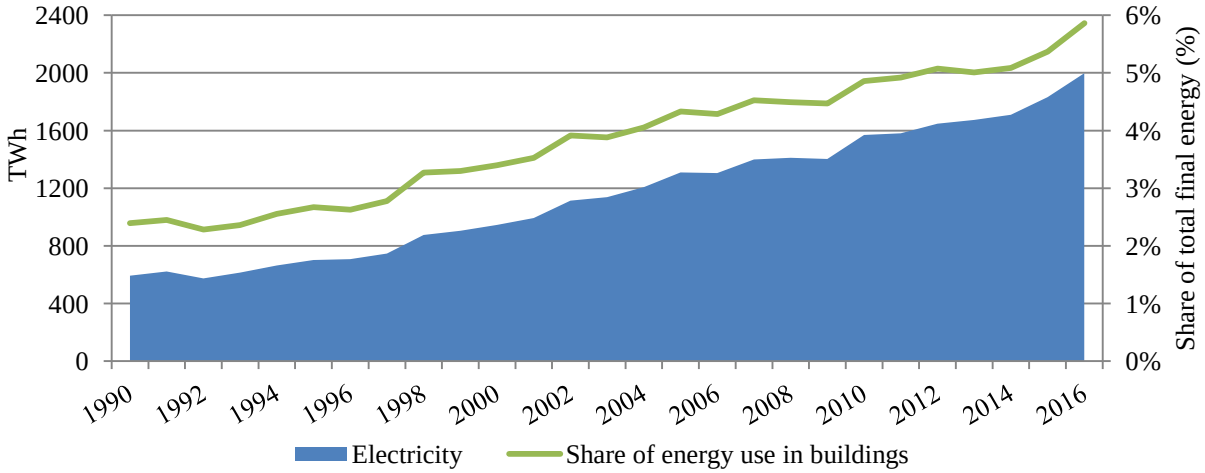

Figure 2: Consommation mondiale d'énergie pour la climatisation de l'espace dans les bâtiments

Les climatiseurs (AC) souvent utilisés sont généralement basés sur une technologie à cycle de compression de vapeur. Il n'est pas surprenant que le nombre d'unités de l'AC augmente rapidement en raison de l'augmentation de la température mondiale et des capacités d'achat dans les pays en développement, ce qui peut justifier le stock mondial de ces unités : En 2000, le nombre d'unités stockées était de 815 millions et a doublé en 2016 pour atteindre 1622 millions. La croissance prévue du marché de l'AC d'ici à 2050 montre que la majorité des unités AC mondiales sera concentrée dans les pays du sud les plus touchés par l'augmentation de la température, d'où le besoin le plus crucial pour la climatisation.
Les systèmes de climatisation à compression de vapeur AC peuvent gérer efficacement la température, mais ils présentent certaines lacunes lorsqu'il s'agit de contrôler l'humidité intérieure.

1.1.3 Problème de contrôle de l'humidité

Afin d'extraire l'humidité, les cycles à compression de vapeur abaissent la température de l'air en dessous de celle du point de rosée afin d'éliminer l'humidité par le processus de condensation, et de réchauffer l'air ensuite pour atteindre la température de confort intérieure désirée. Ce processus consomme environ 20 à 40 % de l'énergie totale et augmente la demande d'électricité (Zhang et al., 2010). Un autre inconvénient est la faible qualité de l'air généré qui cause des problèmes de santé et qui affecte le bien-être humain.

1.1.4 Conclusion

Vue la relation directe entre la climatisation et la consommation d'électricité, et tenant compte de tous les problèmes environnementaux liés à l'exploitation des ressources fossiles pour produire de l'électricité, il est désormais prioritaire de développer de nouveaux systèmes de réfrigération économes en énergie. Ces systèmes innovants devraient réduire la consommation d'énergie et répondre à l'augmentation de la demande pour le confort en termes de bien-être thermo hygrométrique et de la qualité de l'air.
L'une de ces solutions alternatives est l'utilisation de la technique de desiccation pour réaliser la déshumidification avant le refroidissement de l'air d'alimentation. Cela sépare le contrôle de l'humidité de celui de la température dans les systèmes traditionnels de climatisation, ce qui améliore leur efficacité énergétique globale et réduit les coûts énergétiques qui en résultent.

1.2 Système de dessiccation

1.2.1 Types de dessiccants

Un dessiccant a la propriété d'absorber une grande quantité de vapeur d'eau et de la désorber facilement en étant réactivé à une température de régénération relativement basse. Il peut être de type solide sous forme de roue tournante (fig.3) (Jani et al., 2016, p. 20; Rambhad et al., 2016) ou liquide comme solution d'eau et de sel (fig.4) (Abdel-Salam et Simonson, 2016). L'objectif principal du dessiccant est d'absorber l'humidité de l'air à travers la différence de pression de vapeur entre la surface du desiccant et l'air qui agit comme force motrice pour le transfert de masse ou d'humidité (Mohammad et al., 2016). Lorsque la pression de vapeur à la surface du desiccant est inférieure à celle de l'air, la déshumidification se produit et vice versa. Le processus

de déshumidification se poursuit jusqu'à ce que les pressions de vapeur soient égales. Après ce point, la vapeur d'eau commencera à se déplacer dans le sens opposé qui va du dessiccant à l'air. Afin de réactiver le desiccant, sa pression de vapeur de surface doit être augmentée par préchauffage après avoir quitté l'unité de déshumidification. La régénération se fait généralement à basse température, de 30 à 80 °C environ.

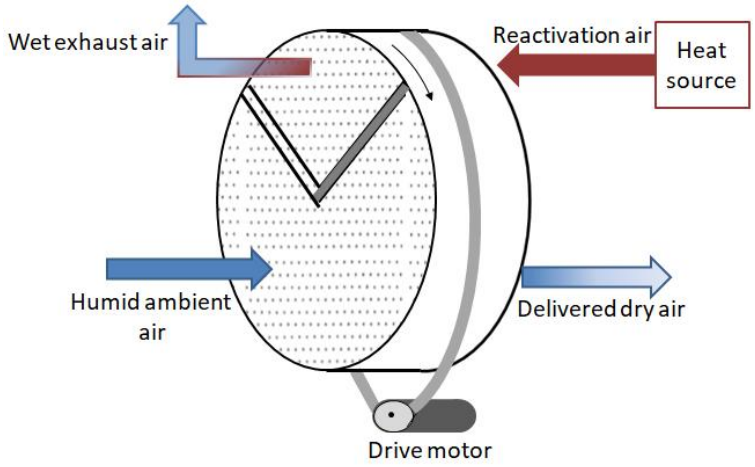

Figure 3: Schéma d'une roue de dessiccation solide

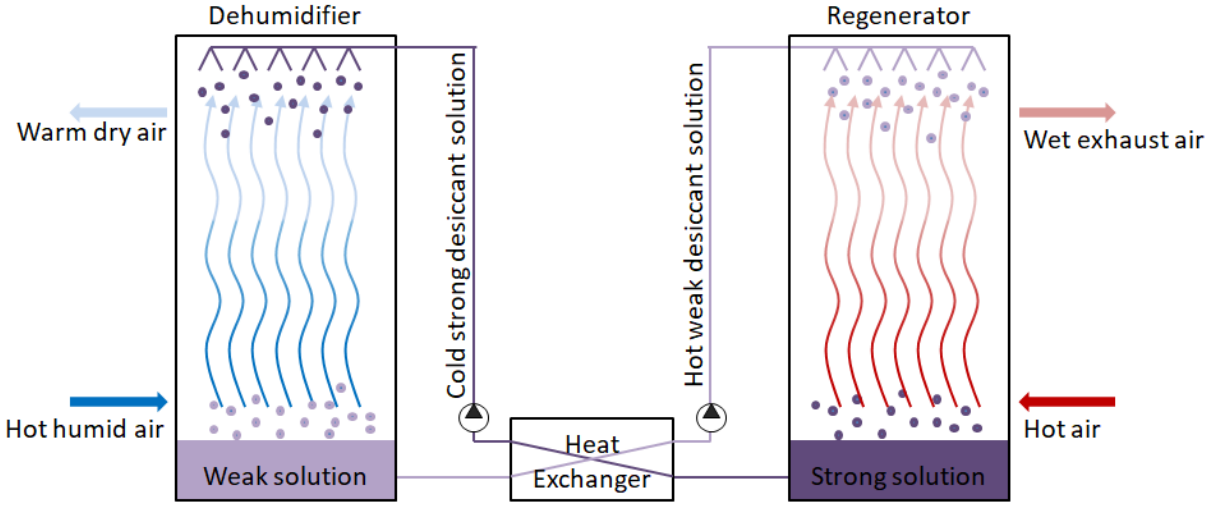

Figure 4: Système de déshumidification par dessiccation liquide avec échangeur de chaleur liquide-liquide

1.2.2 Systèmes hybrides de compression des déformations/vapeurs

Les systèmes hybrides basés sur des desiccants liquides sont donc de bons candidats pour permettre le contrôle séparé de la charge latente et sensible. La figure ci-dessous (fig. 5) montre le principe de cette technologie. Dans ces systèmes, un cycle de dessiccation liquide déshumidifie l'air et le refroidissement et réalisé par le cycle de compression de vapeur. Dans certains cas, le cycle desiccant pourrait contribuer simultanément à la déshumidification et au refroidissement partiel de l'air. Pour ce faire, la solution desiccante est traverse par l'évaporateur du cycle de compression de vapeur pour réduire sa température. Après avoir absorbé la vapeur d'eau de l'air, la concentration de la solution dessiccante diminue. Ainsi, il doit être réactivé par

un cycle de régénération qui échange la solution avec de l'air à haute température (chauffé par l'énergie libre fournie par le condenseur du cycle de compression de vapeur).

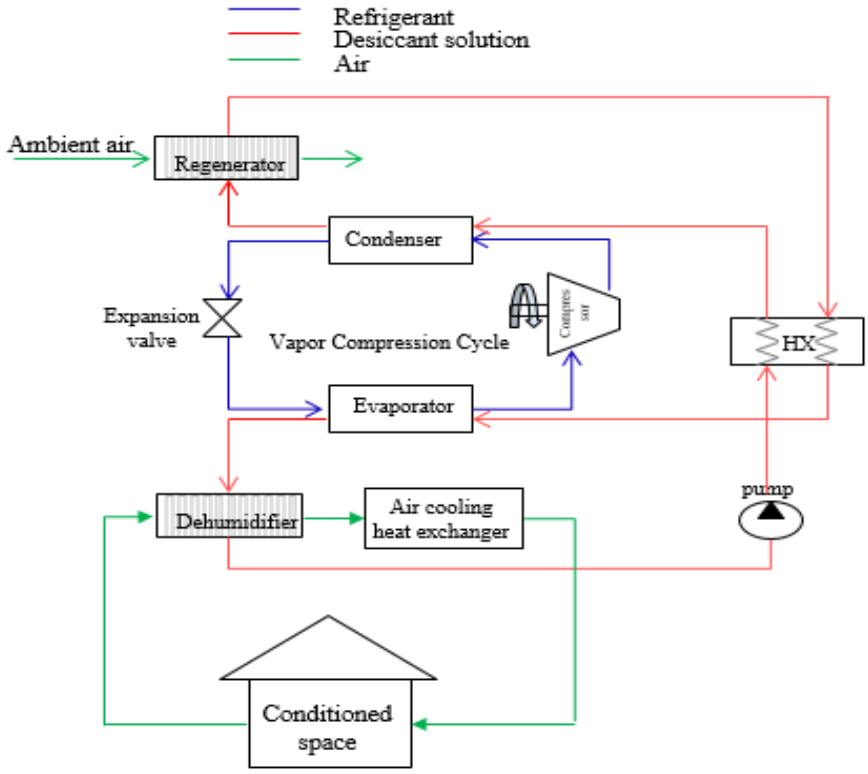

Figure 5: Système hybride de refroidissement par compression de vapeur de liquide dessiccant

Le déshumidificateur et le régénérateur d'un tel système hybride sont considérés comme les composants principaux sachant que leur conception affecte énormément le contrôle de la température et de l'humidité. Un autre défi lié à ces échangeurs de chaleur et de masse est l'entrainement possible de gouttelettes de solution desiccante générant des problèmes de corrosion. Pour ces raisons, plusieurs études ont été réalisées et de nouvelles technologies ont été mises au point sur ces deux composants et sur les échanges de chaleur et de masse accompagnés.

1.2.1 Les échangeurs de chaleur et de masse

Ils peuvent être de type direct ou indirect. Dans le type direct, le transfert simultané de chaleur et de masse se fait entre deux fluides à grande surface de contact alors que dans les échangeurs à contact indirect, les flux de fluide sont toujours séparés par une paroi de séparation.

1.2.1.1 Type Direct

Dans les échangeurs de type direct, il est possible d'atteindre des rendements de transfert de chaleur et de masse très élevés parce que les deux fluides sont en contact et donc des approches de température plus faibles sont atteintes. On peut les trouver dans différentes applications, y compris les processus de dessalement de l'eau, la production d'énergie géothermique et le stockage de la chaleur (Hyun et al., 2005; Mahood, 2008). Leur coût d'exploitation est également faible en raison de l'efficacité du transfert de chaleur et de masse élevée. Les tours de refroidissement sont des exemples où le fluide qui doit être refroidi (habituellement de l'eau) est

dispersé sur un courant d'air et le contact direct permet à l'air de refroidir l'eau par évaporation et convection (Evans, 2016). Le processus d'entrainement de gouttes dû au transfert du fluide refroidi par l'air représente un inconvénient majeur de ces dispositifs. Dans le cas où une solution de dessiccation doit être refroidie, l'entrainement de fines gouttelettes transportées par l'air contiendra du sel qui se dépose dans les zones avoisinantes et dans le processus. Le dépôt de sel est nocif pour le procédé et l'équipement en raison de son caractère corrosif.

1.2.1.2 Type indirect

Les échangeurs de type indirect sont utilisés lorsque le contact direct entre les deux fluides est indésirable, comme dans le cas de l'air et de la solution dessiccante. Ici, le contact direct entre les deux fluides qui s'écoulent est complètement évité par une paroi de séparation, mais le transfert de la chaleur et de la masse se font à travers la paroi. Le transfert se produit lorsqu'une force motrice est appliquée et qui est généralement une différence de pression ou de concentration entre les fluides des deux côtés de la paroi. Les parois (aussi appelées membranes) ont la capacité d'empêcher la solution liquide de se diriger vers l'air humide, mais ils permettent le transport de vapeur d'eau et de chaleur de la solution dessiccante vers l'air et vice versa. Ils peuvent être constitués de polypropylène (PP), de polyéthylène (PE) ou de polytétra-fluoro-éthylène (PTFE) recouvertes d'une couche dense de silicium ou de téflon amorphe (Huang et Zhang, 2013).
De nombreuses études ont porté sur la performance des échangeurs de chaleur et de masse, soulignant par exemple l'importance des propriétés de la membrane dans les types indirects ou l'avantage de certains arrangements utilisant des techniques de pulvérisation dans les types directs. Toutefois, après avoir décrit les dessins ou modèles existants de ces échangeurs, on peut remarquer qu'ils présentent encore certains inconvénients.

1.2.1.3 Inconvénients des échangeurs existants et des solutions possibles

La technologie de pulvérisation d'eau dans les tours de refroidissement a prouvé son importance e t sa bonne performance mais le problème d'entrainement conduit à de graves complications en pa rticulier lorsque les gouttelettes de solution de sel sont transportées par l'air. (Ruiz et al., 2016). En outre, en ce qui concerne les échangeurs membranaires de chaleur et de masse, il y a des défis à relever. Premièrement, ces systèmes sont généralement sophistiqués en raison de l'installation et de la distribution de canaux avec différentes configurations. Deuxièmement, elles sont coûteuses en raison du prix élevé des membranes qui sont faites de structures complexes et sont difficiles à traiter. Concernant les membranes, l'un des inconvénients est qu'elles devraient pouvoir résister à une pression liquide sans être endommagées ou mouillées, de sorte qu'elles doivent être assez rigides pour résister à la différence de pression (X Zhao et al., 2008). L'imperméabilité à l'eau liquide constitue également un autre défi important pour les membranes par lesquelles l'eau liquide ne devrait jamais pénétrer de l'autre côté de la membrane chaque fois qu'une pression d'eau est appliquée. Cependant, la vapeur d'eau devrait toujours pouvoir se déplacer d'un côté de la membrane à l'autre. Toutes ces caractéristiques exigent des propriétés spécifiques qui devraient être présentes dans la membrane, telles que des conductivités thermiques et massiques acceptables, la tension de surface et la résistance à l'usure (Onsekizoglu, 2012). Ainsi, la résistance au transfert de chaleur et de masse de la membrane devrait être aussi basse que

possible et la conductivité thermique devrait être suffisamment petite pour réduire la perte de chaleur entre les côtés de la membrane. La conductivité thermique de la membrane est liée à ses caractéristiques physiques et à sa géométrie, ainsi qu'à sa capacité de conduire la chaleur. Une autre limite des membranes proposées dans la littérature est leur coût et leur faible performance, car les membranes doivent être renforcées mécaniquement, ce qui conduit à une faible conductivité de masse.

Afin d'obtenir un système performant, des propriétés membranaires pratiques devraient être disponibles et les défis susmentionnés devraient être surmontés. Dans tous les systèmes existants, ces propriétés sont en contradiction les unes avec les autres. Chaque fois que la membrane est capable de résister à une pression liquide, sa perméabilité à la vapeur d'eau diminue en réduisant sa conductivité de masse. Ces contradictions dans le système, ainsi que le coût élevé de fabrication et la complexité du système dans son ensemble, favorisent le développement d'un nouveau système innovant capable de répondre à tous les besoins et défis susmentionnés.

1.3 Conception nouvelle de l'échangeur de chaleur et de masse à membrane

Une nouvelle technologie brevetée par "Armines" est proposée. Cette technologie fait un usage positif de la présence de la membrane pour résoudre le problème de l'entrainement et les inconvénients des technologies membranaires réelles. La figure 6 représente notre système proposé consistant en un échangeur à flux croisé où la solution dessiccante est projetée verticalement vers le bas entre les membranes, représentées par les couches vertes, et où l'air s'écoule dans un flux perpendiculaire. La solution dessiccante avec une faible concentration est ensuite collectée au bas de l'échangeur et renvoyée à un régénérateur pour être réactivée.

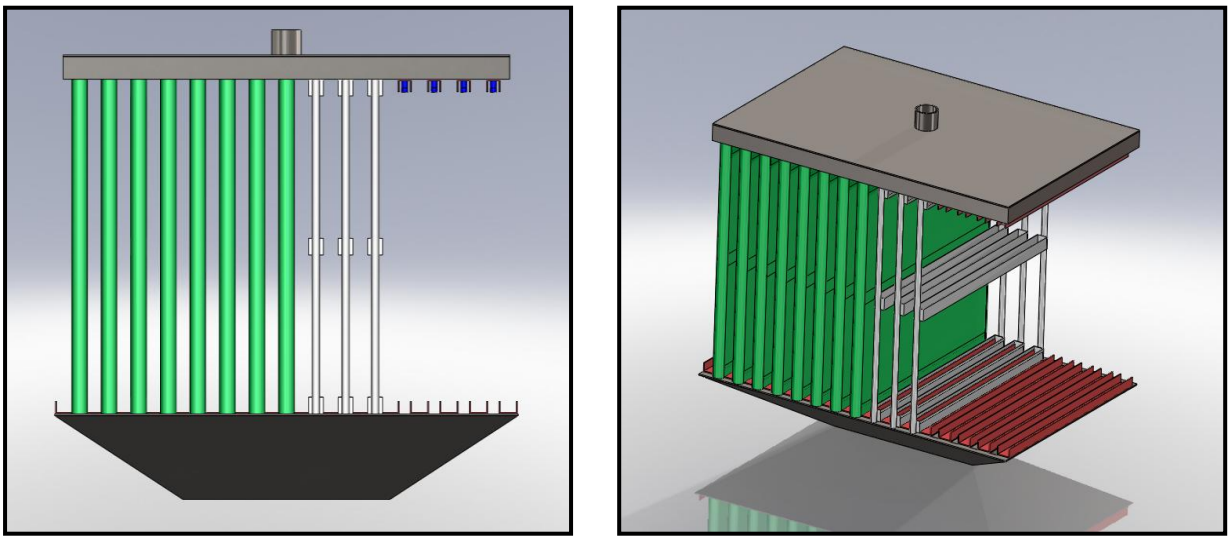

Figure 6: Modèle de conception du système proposé

Afin de réduire l'importance de la résistance à une pression liquide, il est souhaitable de pulvériser le liquide dessiccant uniformément au travers des buses situées en haut du système. La pulvérisation verticale du liquide facilite la configuration de la conception puisqu'il descend par gravité (fig. 7).

Figure 7: Le système proposé avec le dessiccant pulvérisateur

La pulvérisation du liquide non seulement diminue la pression de l'eau sur la membrane, mais elle disperse aussi l'eau en petites gouttelettes augmentant la surface de contact indirect entre l'air et le liquide (Gluesenkamp et Radermacher, 2011). Cela conduit à une plus grande turbulence du côté de l'air près de la membrane, ce qui augmente à son tour le transfert de chaleur et de masse dans cette zone et minimise sa résistance interne. La pulvérisation du liquide induit une pression identique des petites gouttelettes liquides pulvérisées et de l'air par lequel les propriétés mécaniques de la membrane ainsi que son imperméabilité ne seront plus de fortes contraintes. Par conséquent, les contradictions qui ont été présentées dans la section précédente sont maintenant évitées en adoptant cette conception.

En ce qui concerne le coût relativement élevé associé au processus de fabrication des membranes, notre objectif est d'utiliser des matériaux à faible coût qui sont fabriqués à l'origine pour des utilisations autres que l'échange de la chaleur et de masse. Certains de ces matériaux qui semblent être une excellente alternative aux membranes traditionnelles à coût élevé peuvent être des tissus non tissés (NWF) qui sont des toiles ou des structures de toile de fibres liées ensemble de différentes façons. D'autres candidats se trouvent également dans différentes industries comme des membranes de sous toiture. Les propriétés intrinsèques des tissus non tissés sont déterminées par les propriétés individuelles des fibres qui les composent; leur diamètre, leur porosité et leur orientation (Chen et al., 2019). Certains de ces tissus non tissés ont une excellente résistance à l'humidité ou ou une excellente répulsion, ils n'absorbent pas l'eau, mais ils sont perméables à l'air. De plus, ces tissus sont souples, légers, poreux, lavables, jetables, bon marché et faciles à fabriquer. Ainsi, la nouvelle conception d'échangeur proposée peut être réalisée en choisissant des tissus non tissés pour servir de membranes en raison de leurs avantages importants, principalement en ce qui concerne leur perméabilité à la vapeur, leur résistance au liquide et leur faible coût de fabrication. Le choix principal de ces matériaux dépend principalement de la capacité de la membrane à transmettre de la vapeur d'eau de manière à maximiser la chaleur et le transfert de masse.

La figure 8 montre certaine des membranes en tissus non tissés et autres matériaux.

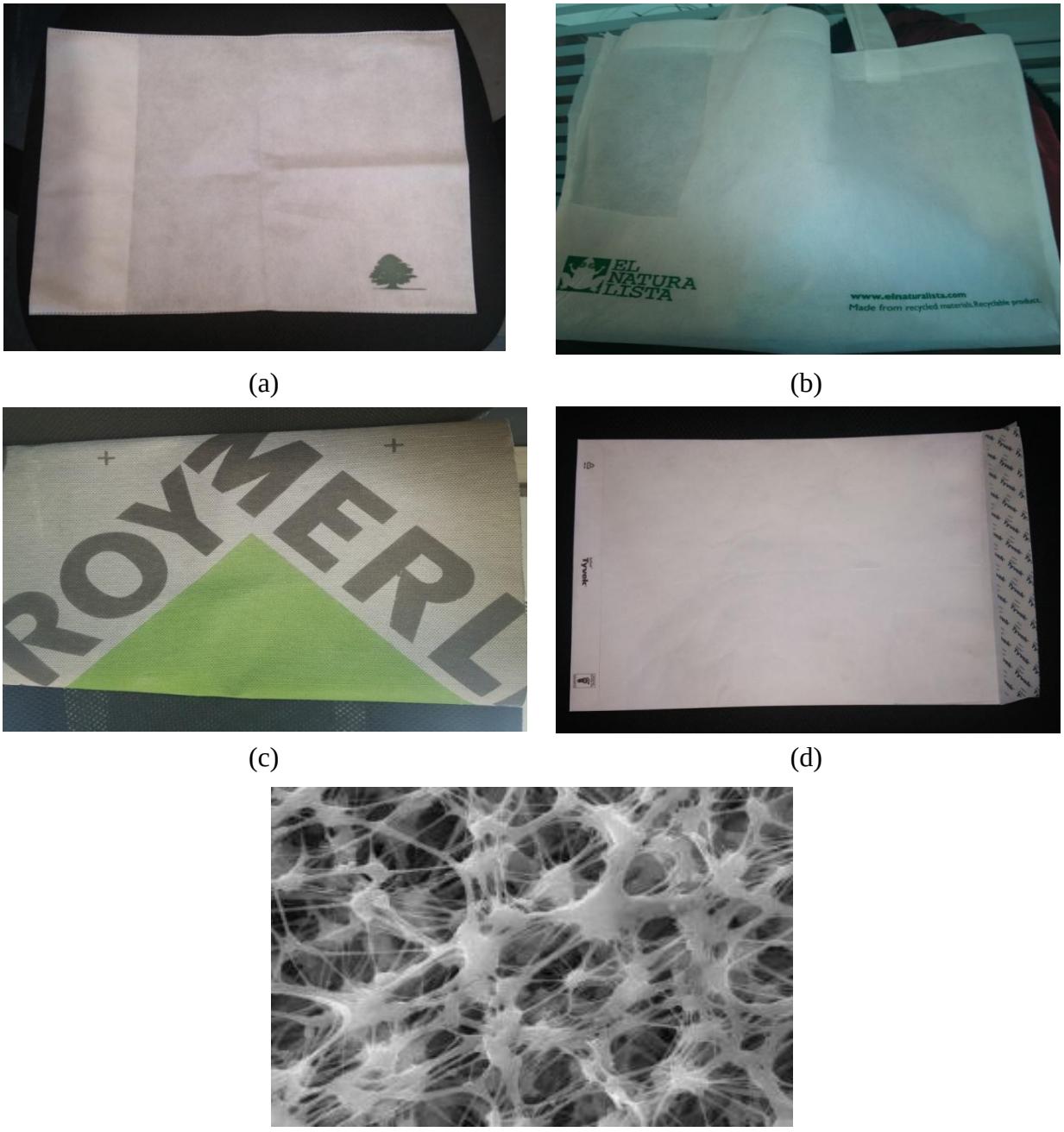

(a) (b)

(c) (d)

(e)

Figure 8: Une collection de différentes membranes a) caisses d'oreillers, b) sac, c) sous-toiture, d) enveloppe de courrier Tyvek, e) nano-fibres électrofilées

Toutefois, l'utilisation de tissus non tissés qui sont initialement fabriqués pour des raisons autres que l'utilisation à des fins de transfert de chaleur et de masse élargit la portée à de nouvelles perspectives ainsi qu'à de nouveaux défis scientifiques et technologiques. Les défis concernant ces matériaux sont le manque de caractéristiques scientifiques et d'informations sur leurs propriétés. Afin de déterminer leur perméabilité à la vapeur d'eau, ces matériaux ont été testés expérimentalement à l'aide d'un essai à la coupe modifiée et la méthodologie utilisée sera discutée dans le prochain chapitre.

1.4 La problématique de la thèse

Les systèmes hybrides de compression de vapeur à base de desiccant liquide semblent des candidats fiables qui permettent un contrôle adéquat de l'humidité dans les applications de climatisation et un fonctionnement sans givre dans le cas de la réfrigération, avec un COP potentiellement accrue. Comme le dessiccant solide présente l'inconvénient des températures de régénération élevées et de la complexité de leur intégration dans les systèmes, les dessiccants liquides sont plus attrayants en montrant des températures de régénération basses et des capacités de déshumidification remarquables. D'après les recherches il a été déterminé que la configuration du système hybride et son architecture offrent une grande efficacité dans toute une gamme de conditions d'exploitation avec différents rapports de charge latent à sensible. Cette gamme de conditions d'exploitation varie d'une architecture à l'autre; il est clair que le maintien d'un système hybride à haute performance ne pourrait être réalisé que par une conception flexible fonctionnant tout au long d'une saison de manière efficace sur le plan énergétique. Ceci définit l'objectif final de cette thèse de concevoir des systèmes hybrides de climatisation à haute performance, abordables et flexibles, ainsi qu'une méthodologie de conception et des outils de modélisation.

Le déshumidificateur et le régénérateur d'un tel système hybride sont considérés comme les principaux éléments et leur conception propre a une incidence considérable sur le contrôle de la température et de l'humidité. Comme nous l'avons vu, l'un des défis liés à ces échangeurs est leur capacité d'empêcher l’entrainement des gouttelettes de solution dessiccante vers l'air en évitant les problèmes de corrosion tout en les gardant simples à construire et à faible coût. Les échangeurs membranaires à constituent une réponse technologique à ces problèmes, mais les technologies existantes présentent de nombreux inconvénients, comme nous l'avons expliqué. Dans cette thèse, la nouvelle technologie présentée dans la section précédente sera soigneusement étudiée. Elle utilise de nouveaux matériaux membranaires et une nouvelle conception liée à la distribution de liquide. Les défis concernant ces matériaux sont le manque de caractéristiques scientifiques et d'informations concernant leurs propriétés, principalement leur perméabilité de la vapeur d'eau. Pour découvrir cette propriété, ces matériaux sont testés expérimentalement à l'aide d'une méthode modifiée de coupe verticale et la méthodologie utilisée sera discutée dans le prochain chapitre.

Le troisième chapitre de cette thèse vise à comprendre profondément le comportement et la performance de ce nouvel échangeur. La bonne compréhension et la modélisation des transferts couplés de chaleur et de masse au sein de cet échangeur innovante sont des facteurs clés pour les intégrer efficacement dans les processus et pour bénéficier de leurs avantages par rapport aux technologies conventionnelles existantes. Une approche de modélisation des phénomènes de transfert de chaleur et de masse est développée en modélisant les échangeurs conçus et est soutenue par une caractérisation expérimentale.

Ce modèle est utilisé dans le dernier chapitre pour étudier l'intérêt énergétique de l'intégration de ces échangeurs dans les applications de climatisation et pour concevoir une architecture flexible capable de faire face à la variation saisonnière du rapport de charge thermique.

Chapter 1 Context, State of the Art and Problem Statement

1.1 Context

1.1.1 The energy and environmental context

Energy and environment are the most trending worldwide issues that seem to be of a serious concern for societies. Global warming represents the major environmental problem that the world is facing nowadays. The principal cause of global warming is the emission of CO_2 in the atmosphere which is caused mainly by the burning of fossil fuels. Burning fossil fuels such as oil, coal and natural gas does not only generate CO_2 (the main greenhouse gas) but also generates other pollutant gases like SO_x, NO_x, CO and fine particles (Bose, 2010). These greenhouse gases (GHG) trap the solar heat in the atmosphere and raise the earth's temperature causing harmful impacts on the environment. Across the globe, the past five years have been recorded as the hottest years (e.g. year 2018 was considered to have very high unusual temperatures and ranked as the fourth hottest year on record). Further increase in temperature is estimated by the United Nations IPCC (*Climate Change 2014 Summary for Policymakers*, 2014). As mentioned in their report an increase in the global mean surface temperature is expected by the end of this century under three possible scenarios. The most optimistic one would be through applying stringent mitigation measures whereas the worst one would be through maintaining the same rate of GHG emissions. In the first scenario the increase would be from 0.3°C to 1.7°C, while in the baseline scenario the increase can reach higher values from 2.6°C to 4.8°C.

This increase triggers the usage of more electricity for cooling purposes. Likewise, the climate change in some cold countries such as North America and due to colder-than-average temperature in winters, an additional increment in heating requirements is expected. In 2018, a rise by 4% was recognized in the global energy demand presenting the fastest pace since 2010 after the recovery of the global economy from the financial crisis. Studies indicate that about one fifth of the increase in energy demands was directly related to the change in weather conditions (IEA, 2018, p. 2). In addition to the increase in the heating and cooling demands, some other factors affect the electricity consumption. It is interesting to mention that the United States and China together account for around 70% of the global demand growth reflecting by that the high standards of living in the first country and the rapid growth in the industrial sector in the second. The graph in figure 1.1 shows the continuous growth in the electricity consumption over the past few decades.

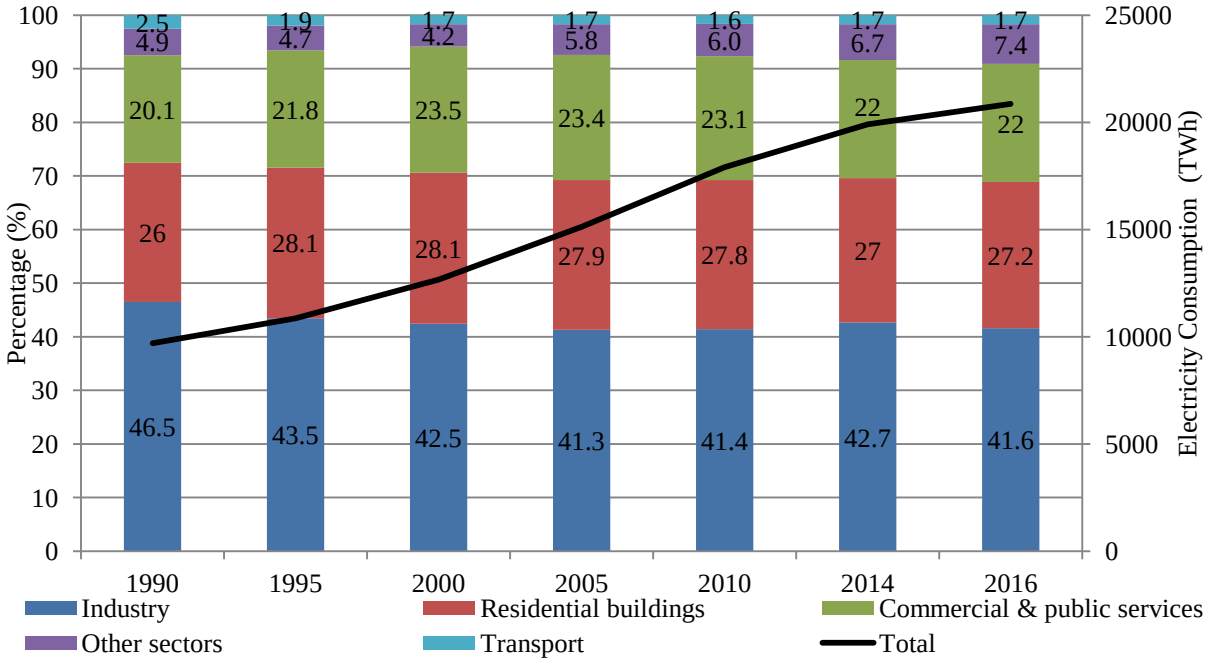

Figure 1.1: World electricity final consumption by sector

In year 1990 the world electricity consumption was 9699 TWh and in 2016 this value has reached 20864 TWh, 3.2% above that of 2015. The growth in the electricity consumption mainly took place in the building sector that constitutes the residential as well as the commercial and public service buildings as observed in the graph of fig. 1.1. The share of residential combined with the commercial and public service sectors increased from 46% in 1990 to 49.3% in 2016. This makes the building sector the highest electricity consumer surpassing the industrial share. Although the electricity consumed by the industries has incremented throughout the years yet its share has fallen from 46.5% in year 1990 to 41.6% in year 2016, yielding the share mostly towards the commercial and service sector. Thus, It can be clearly noticed that the building sector contributes to around half of the global electricity consumption. This is due to the excessive use of electronic and telecommunication equipment and to the employment of heating and cooling systems that consume lots of electricity.

As the need for electricity grows, fulfilling this demand has been challenging concerning the sources used to generate electricity. As per the report of the International Energy Agency (IEA) in 2018, around 64% of our electricity is produced by fossil fuels of which 38% comes from coal, 23% comes from gas and 3% from oil. 10% of the global electricity demands are generated by nuclear sources and the remaining 26% comes from renewable resources. The following figure (fig. 1.2) summarizes the worldwide change in the shares of the sources used to generate electricity in the past 14 years (“World Energy Outlook,” 2018)

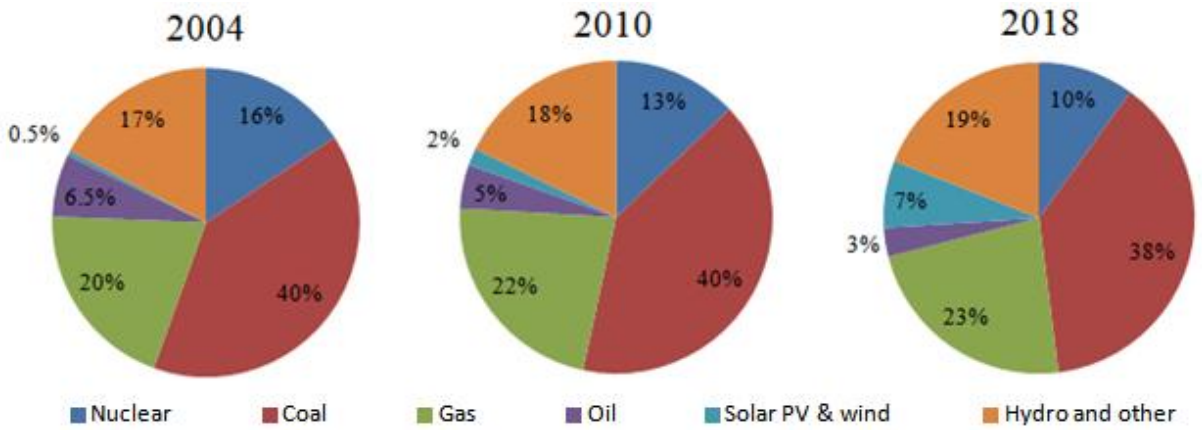

Figure 1.2: Global electricity generation by source and its evolution throughout the years

Different policies are already established by governments all over the world including the Nationally Determined Contributions achieved in Paris agreement in 2016 to reduce emissions and energy consumption. If these policies are adopted the share of coal will decrease from 38% to 25% in year 2040 according to the IEA. This is in favor for a significant development in the renewable energy shares including solar, wind, hydro and marine sources that could reach 40%. Whilst if more strict approaches are followed under a sustainable development scenario, the coal's share would decrease to 5% in 2040 and that of renewable energy would reach 66% ("Sustainable Development Scenario," 2018).

The sources used to generate electricity are moving the world into a significant climate change through the emission of GHG and most critically the CO_2. It has been estimated that man-made fossil fuel burning including cement production is responsible for around 91% of atmospheric CO_2 generation in 2015 (Griffin, 2017).The combustion of solid fuels (e.g. coal) contributes to the highest percentage (42%) among them, followed by the liquid fuels (e.g. oil) with 33% and then gases (e.g. natural gas) with 18%. These primary sources are mainly used by people in the form of electrical devices, transportation, heating and cooling, industrial production, communication and services, etc. Studies show that around half of the global CO_2 emissions is due to electricity and heat production. Other sectors such as oil-based transport and manufacturing industries contribute to about 20% (Ritchie and Roser, 2017). The distribution of CO_2 emissions from fuel combustion by sector is shown in the following chart of figure 1.3 along with the evolution of the CO_2 atmospheric concentration over 24 years.

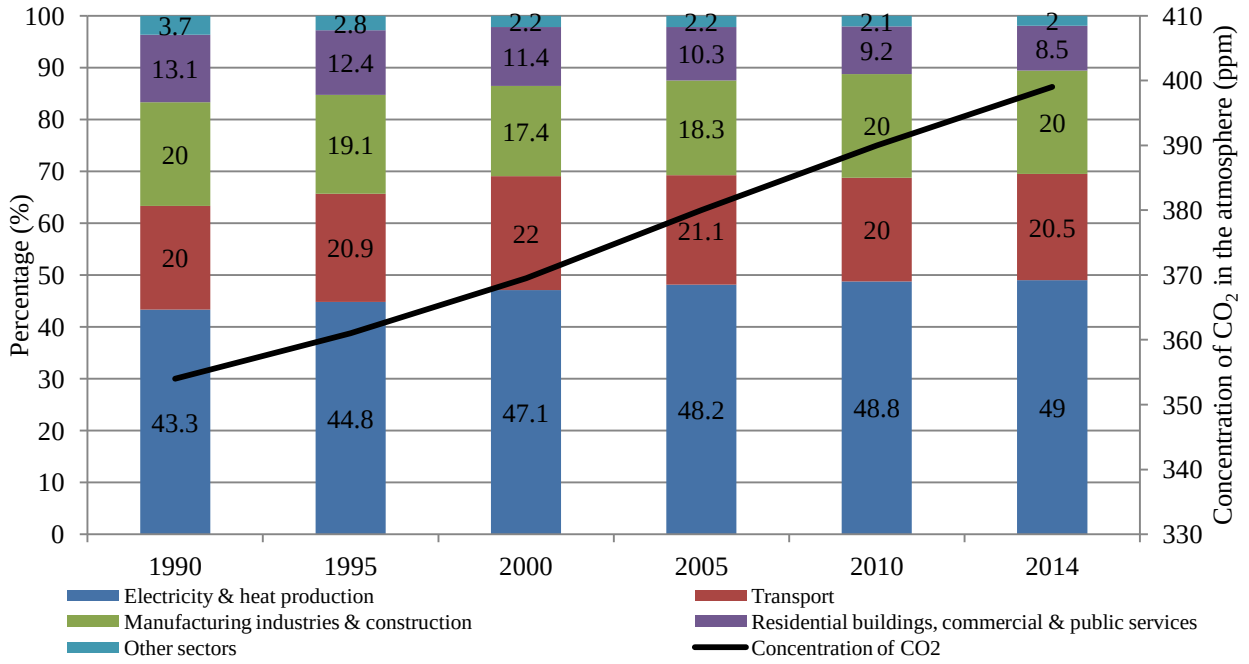

Figure 1.3: World percentage CO2 emissions by sector with its atmospheric concentration in ppm

Over the course of few decades, the global concentration of CO_2 in the atmosphere in particles per million (ppm) was observed and studied by scientists. According to NOAA the particles of CO_2 per million molecules of dry air increased significantly (NOAA, 2019). The CO_2 atmospheric concentration shown in figure 1.3 is based on data records through the direct measurements of CO_2 in the atmosphere at Muana Loa Observatory in Hawaii. The data reveals that the global atmospheric carbon dioxide concentration was 354 ppm in year 1990 and reached around 399 ppm in year 2014.

The curve of the CO_2 data is widely recognized to have a possible exponential nature and thus its future behavior could be predictable. By introducing the measured values in a model and applying several corrections related to oil shocks, population increase and other factors that might affect CO_2 production, extrapolation would give a future evolution of CO_2 concentration in the atmosphere ("Concentrations de CO2 dans l'Atmosphere. Elements de Prospective," 2015). According to the model prediction of the CO_2 levels if the worldwide emissions continue with a similar pace following the same trend the numbers might reach 510 ppm in the year 2050.

The trend of other GHG is similar to that of CO_2 and the consequences of the continuous growth in the emissions are undesirable and potentially harmful. If global warming keeps increasing, significant climate change will occur and severe long term effects will take place. These impacts involve higher sea levels due to the melting of the ice mass at the poles threatening coastal cities and low-lying areas. According to the European space agency (ESA) there had been a rise in 20% of the sea levels between 1992 and 2012 (ESA, 2018). Other impacts include severe dryness in tropical climates mainly in Africa and India, extreme weather events like floods and storms, increased acidity of oceans and more polluted air (Wilkinson et al., 2007). These changes are most likely to affect humans' health through the deterioration in water and food security.

Moreover, climate change induces the spread of infectious diseases and higher-than-normal temperatures result in the disruption of our ecosystem reducing the resources needed for a healthy lifestyle (Kovats and Butler, 2012).
Furthermore, climate change induces damaging effects on the global economic development. According to the International Labor Organization ("World Employment and Social Outlook 2018 – Greening with jobs," 2018), the agricultural crops are expected to decline affected by the global increase in temperature and dryness threatening about 1.2 billion jobs directly dependent on ecosystem services. These might include employments in agriculture, fisheries and forestry especially in developing countries like India and Brazil that are directly affected by global warming. In addition to the unemployment, agricultural deterioration raises the food prices enhancing malnutrition and poverty.

1.1.2 The refrigeration and cooling context

The growth in population and in technological advancements in the past few decades has surged the demand for more energy and thus higher electricity consumption. Cooling has an important share in electricity consumption and one of the things we are certain about is the global increase in the need for space cooling for decades to come. Both the building sector and the industrial sector confront an increase in the electricity consumption mainly related to the space and process heating/cooling purposes. This rise is a result of the economic and population growth leading to a greater thermal comfort desire. The climate change with the global temperature increment tends to additionally increase this rise. The graph of figure 1.4 shows the expansion of electricity used for space cooling throughout the years as well as the share of space cooling in the total electricity use in buildings (Birol, 2018);

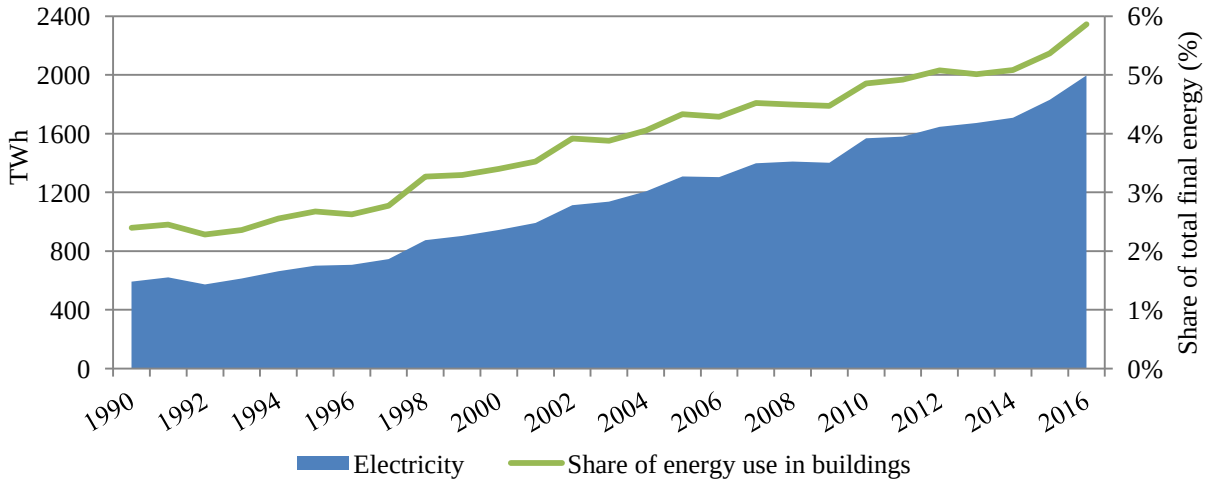

Figure 1.4: World energy consumption for space cooling in buildings

This demand will keep developing indeed but there might be an uncertainty on how much exactly the rate of growth would be. According to (IEA) two scenarios are suggested to assess the long-term trend of the electricity demand for space cooling. The first baseline scenario focuses on the causes mentioned above related to the increase in population and in the purchasing power associated to higher standards of living. It doesn't take into consideration any additional policies

beyond the ones that have already been announced around the world. The second scenario favors a more optimistic trend considering the adoption of further rigorous policies with more efficient cooling measures in the aim of reducing the amount of energy needed. According to the baseline scenario the electricity consumed by space cooling is expected to increase from 1997 TWh in 2016 to 6200 TWh in 2050 while this value would be 3400 TWh if an efficient cooling scenario is followed (45% lower than the baseline projection) as shown in figure 1.5 (Birol, 2018). Hence employing new energy efficient technologies in space cooling contributes to the global energy savings through reducing electricity consumption.

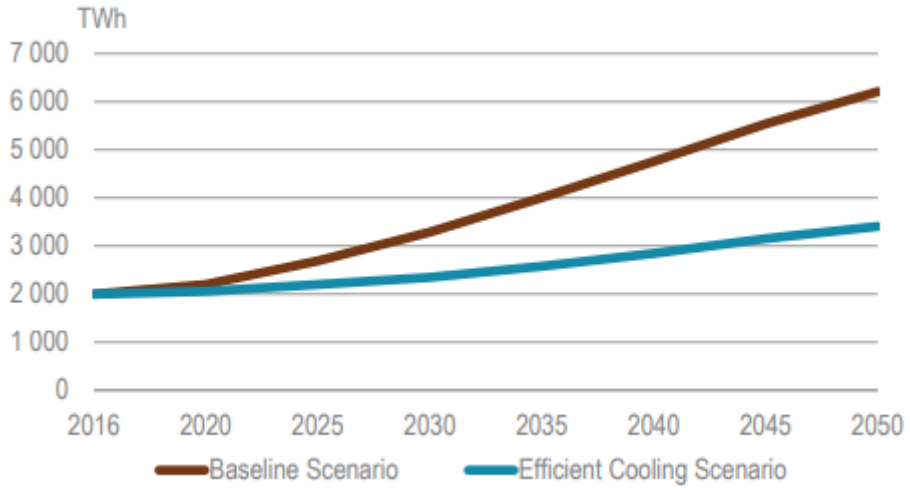

Figure 1.5: World electricity consumption for space cooling in the baseline and efficient cooling scenarios (Birol, 2018)

In order to perform space cooling, air conditioners (ACs) are the most common used appliances worldwide. Very few of them are powered by natural gas and the rest by electricity. The AC systems include split units that are usually used in houses and residential entities and water chillers that are mainly used in commercial buildings. Relying mostly on electricity for the power generation, space cooling contributes to the growth of the overall energy demand. Unsurprisingly, the number of AC units is also expanding as a result of the global increase in temperature and this can be significant from the global stock of these units. As shown in figure 1.6, in year 2000, the number of stocked units of ACs was 815 million and it doubled in 2016 to reach 1622 million. The projected growth in the AC market shows that the lion's share of the global AC units will be concentrated in the southern countries which are confronting the highest economic development leading to an increased standard of living. These countries are also being the most affected by the increase in the global earth temperature and thus the need for cooling becomes more crucial. The graph indicates that the expectations are at their highest in India, Indonesia and China with just the three of them contributing to half of the total growth in the number of AC units (Birol, 2018)

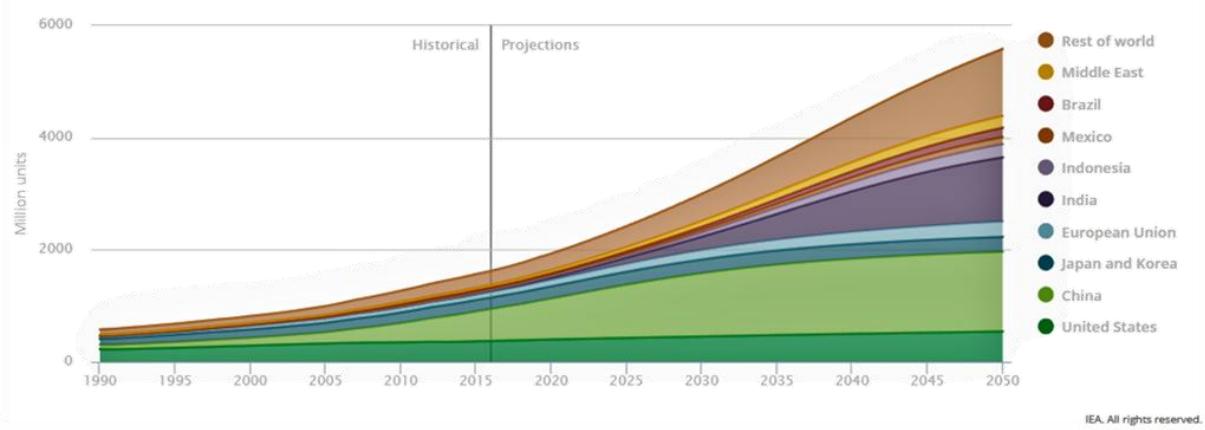

Figure 1.6: Stock of AC in the baseline scenario by country/region (Birol, 2018)

The majority of ACs is based on a vapor compression cycle technology. Conventional vapor compression air conditioning systems use the basic air source heat pump cycle in order to control the climate of our houses or any place where cooling or heating is required. The heat pump extracts heat from one place and transfers it to another. Most of these equipment operate in two modes that allows year-round climate control by heating in winter, and cooling and dehumidifying in summer (Boles and Cengel, 1998). In winter the air-source heat pumps absorb heat from the outdoor air towards the inside of the room while in summer they reject heat from the inside towards outdoor air. They transfer heat by circulating a refrigerant through a cycle of expansion, evaporation, compression and condensation. Its main components are the expansion valve, the evaporator, the compressor and the condenser.

During the cooling cycle, a high pressure liquid refrigerant passes through the expansion valve where its temperature and pressure are reduced at two phases mixture (liquid/vapor). Then it passes by the indoor coil, which in the cooling case is the evaporator, to be fully evaporated after absorbing heat from the indoor space. The vapor then enters the compressor and leaves it at high pressure and high temperature after being compressed. Finally, the high temperature and pressure vapor passes through the condenser which is the outdoor coil where it releases heat to the outdoor space causing the refrigerant to condense into a liquid state before entering the expansion valve to begin the cycle again (Canada and Office of Energy Efficiency, 2004).

1.1.3 The humidity control issue

During hot and humid seasons conventional vapor compression cycles show some limitations since they are supposed to control both sensible and latent loads. Most of these cooling devices can efficiently control the sensible load but they become inefficient when it comes to the control of humidity. In humid climates, the humidity issue is a major contributor to the energy inefficiency of the conventional vapor compression systems. In order to extract humidity, vapor compression cycles lower the air temperature below its dew point temperature to remove its moisture by the condensation process and then reheat it to reach the desired indoor comfort temperature. This process consumes around 20 to 40% of the total energy and increases peak electricity demands (Zhang et al., 2010). Moisture in the air passing over the indoor coil condenses on the coil's surface and is collected in a pan at the bottom of the coil. In addition to

wasting energy, the condensation of air leads to the growth of molds and different fungi viruses on the air ducts and on the tubes of the exchanger. These impurities would be carried by the air to the indoor space causing poor indoor air quality and serious problems for human health.
In other cases where refrigeration applications are needed in industrial storage rooms for example, indoor air temperatures close to zero (positive temperature) or inferior to zero (freezers) with very low levels of absolute humidity are required. To be able to cool the air to the required temperature, the evaporating temperature of the cooling coil should be significantly low and this requires adequate choice of the refrigerant circulating in the cycle. These spaces are usually constructed with extreme tightness and proper sealing to maximize the efficiency of the cooling system. However, due to infiltration through doorways from nearby warmer areas and due to the absence of ventilation systems, undesired warm humid air may enter the storage room and in other cases internal sources of humidity may be present (respiration, cleaning processes, etc.). The moisture present in the air condenses on the walls and ceilings of the room causing the formation of molds and bacteria nests that may damage the stored items; moreover, in case of freezers, this condensation leads to frost that makes some areas slippery and dangerous to workers. In these spaces, usually the vapor compression cycle that is used to control the temperature is also designed to control the humidity level. In this case when air passes through the cooling coil, it condenses on the fins causing ice buildup and frost formation and the amount of frost depends on the moisture in the air. Frost normally accumulates when the space temperature is below 5°C with a relative humidity over 60% (Byrne et al., 2011). When a large amount of frost is present over the cooling coil, the air flow rate would be reduced due to the blocked air passages which in turn lowers the heat transfer (Byrne et al., 2011; Staffell et al., 2012). In order to avoid the blockage of the heat exchangers by frost buildup three different methods are available and widely adopted these days. One of these methods is reversing the cycle (Ding et al., 2004; Shen et al., 2019). In this way the inside unit will act as the condenser and the passing hot refrigerant will melt the frost. But the disadvantage of this approach is that by reversing the cycle, the evaporator inside the room will be heated up and will consume a great part of the cooling capacity to be re-cooled after the defrost cycle. Another method is by the addition of an electric resistance heater to melt the ice that is formed on the cooling coil (Yin et al., 2012). This approach is also unfavorable because it increases the equipment cost due to the addition of auxiliary heating elements and this will lead to supplementary electrical consumption. Bansal et al. (Bansal et al., 2010) analyzed a defrost cycle using an electric heater in a domestic freezer. They concluded that this defrost method increased the power consumption of the freezer by 17.7% and that the efficiency of the heater that is used for defrosting is only 30.3% while the rest of the heat is dissipated to the surrounding. The third method is by using hot gas refrigerant by-pass where the superheated refrigerant from the compressor directly flows to the evaporator bypassing the condenser and the expansion device (Byun et al., 2008; Hoffenbecker et al., 2005; Wenju et al., 2011). This is also considered a costly process with some limitations since the amount of heat in the hot gases might not last enough to do all the needed defrost if a large amount of ice was compiled on the coil. In addition to the direct energy penalty of defrost, defrosting the evaporator may increase the room temperature

creating a constraint in the case where the temperature of the products should not fluctuate much.

1.1.4 Conclusion

In the absence of determined preventive means, excessive energy consumption threatens economic structures and causes serious environmental, social and health disorders. Therefore, efforts should be doubled for the aim of protecting future human health and preserving our natural ecosystem. This can be done by promoting environmental policy programs encouraging renewable energy alternatives such as solar, biomass, etc. and by supporting energy efficient measures to ameliorate both health and environmental conditions.

Due to the direct relation between refrigeration along with space heating/cooling and electricity consumption and in the light of all the mentioned environmental concerns associated with burning fossil fuels for electricity generation, it is now a priority to develop new energy-efficient refrigeration systems. Indeed, consuming lots of electricity for performing dehumidification of air in hot and humid conditions and wasting energy to carry out defrosting cycle in near zero and sub zero refrigeration conditions are of the major causes why conventional vapor compression cycles are not an energy efficient technology. This is to be added to the fact that the low quality air delivered by the vapor compression cycles causes health problems and affects human well-being.

Innovative refrigeration and space air conditioning systems should involve novel solutions that can reduce energy consumption and respond to the increase in the occupant comfort demand in terms of both thermo-hygrometric well-being and air quality. One of these alternatives is the use of desiccant techniques for the dehumidification process prior to the cooling of supply air. This separates humidity control from temperature control in the traditional air conditioning systems thus improving their overall energy efficiency and reducing their resultant energy costs. The next section is a review of the desiccant systems aiming to introduce the concept that is developed in this thesis.

1.2 Desiccant Systems Review

Desiccants are not only environmentally friendly because of the absence of refrigerants that contribute to global warming, but at the same time they take use of recovered or renewable heating sources like solar energy or waste heat gases or biomass (Yu et al., 2009). A desiccant material has the property to absorb a large amount of water vapor and desorb easily by being reactivated at relatively low regeneration temperature. It can be of a solid type in the form of a rotating wheel (Jani et al., 2016, p. 20; Rambhad et al., 2016) or a liquid type as a solution of water and a salt (Abdel-Salam and Simonson, 2016). The main purpose of the desiccant is to absorb moisture from air through the difference in vapor pressure between the surface of the desiccant material and the air which acts as the driving force for mass or moisture transfer (Mohammad et al., 2016). When the vapor pressure at the surface of the desiccant solution is lower than that of the process air, dehumidification occurs and vice versa. Dehumidification process continues until the vapor pressures are equal. After that point, the moist or water vapor

will start moving in the opposite sense that is from the desiccant to the air. In order to reactivate the desiccant, its surface vapor pressure must be increased by preheating it after leaving the dehumidification unit. Regeneration is usually done at low temperatures from approximately 30°C to 80°C using available wasted heated or solar energy. Misha et al. (Misha et al., 2012) found out that with the same regeneration temperature, a liquid desiccant has higher moisture removal capacity than a solid desiccant. The main advantage of the desiccant system is that it consumes low level energy. They seem to be feasible and economical alternatives that help reach the required level of humidity more effectively and without compromising indoor air quality and comfort conditions especially in hot and humid weather. The absorption performance of a 40% LiCl solution was studied on selected indoor pollutants such as formaldehyde (Fu and Liu, 2017). It was concluded that the formaldehyde purification efficiency can reach up to 53% in summer conditions.

1.2.1 Types of Desiccant

There are two types of desiccants, the solid desiccants and the liquid desiccants.

1.2.1.1 Solid desiccants

Solid desiccants consist of a slowly rotating wheel of absorbent bed made of a thin layer of desiccant material (Daou et al., 2006). The cross section of the wheel is divided into a humid air side and a reactivation air side as shown in figure 1.7. As the wheel rotates, the humid air is dehumidified by the desiccant material due to its absorption capacity. The moist which is lost from the process air is captured by the desiccant that becomes wet and should be regenerated to maintain efficient dehumidification. This is done simultaneously on the other side of the wheel by bringing in hot dry air over the solid desiccant. Hot air has a vapor pressure lower than that of the weak desiccant and thus it absorbs its moisture and leaves the wheel with a greater water content.

In some applications where continuous refrigeration processes are required, such as freezing tunnels, solid desiccants may be used to control the humidity in a way to avoid interrupting the process for defrosting reasons. This also reduces the penalty caused by sub-cooling the air below dew point temperatures to remove some of its water content. Several types of solid materials can retain water vapor such as silica’s, polymers, zeolites, aluminas, etc. They are inexpensive, non-flammable, non-corrosive and environmentally friendly (Jani et al., 2016). Their drying capability is higher than other types of desiccants, they can be cleaned easily and they do not react chemically with the moisture of the process air. However, the main drawbacks of solid desiccants are that they can’t be easily conveyed (in tubes or pipes) and they require relatively high regeneration temperatures in the range of 80°C (Wu et al., 2018).

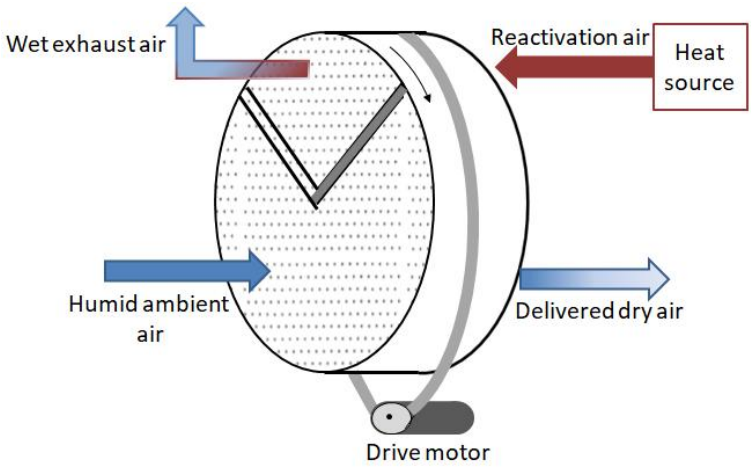

Figure 1.7: Schematic of a solid desiccant wheel

1.2.1.2 Liquid desiccants

The main components of the liquid desiccant system are the dehumidifier and the regenerator as shown in fig. 1.8. In this system the latent load is controlled in the dehumidifier by the transfer of mass (moisture) from the humid air to the liquid desiccant surface. When the weak desiccant leaves the dehumidifier soaked with water, it moves to the regenerator to be reactivated. Inside the regenerator, hot air is made in contact with the weak solution, it carries away with it the water vapor and the solution regains its strength (Rafique et al., 2016). After leaving the regenerator, the warm solution should be cooled again, therefore it is preferable to use a heat exchanger in between the two streams of the desiccant solution to effectively pre-cool the strong solution entering the dehumidifier and pre-heat the weak solution leaving it. However, the direct contact of the desiccant solutions with the process air should be avoided to prevent droplets carryover.

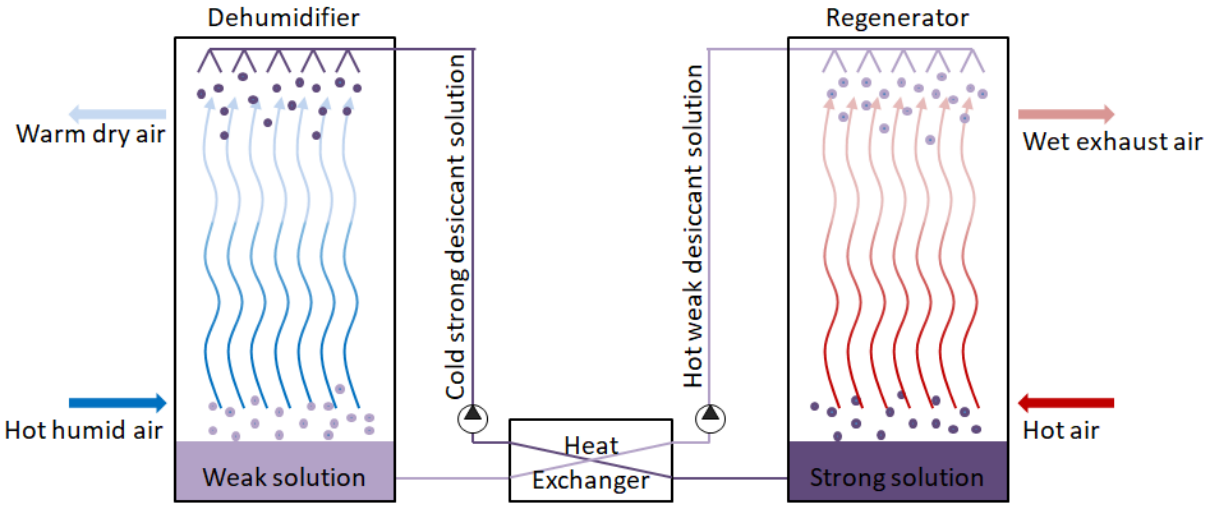

Figure 1.8: A liquid desiccant dehumidification system with a liquid–liquid heat exchanger

Liquid desiccants should have some general properties in order to be classified as good desiccants (Mohammad et al., 2013). One important characteristic is their low regeneration temperature ranging from approximately 30°C to 70°C (Cho et al., 2019). Other properties are

also essential even if it is hard to find them all together in a single desiccant. These properties include being non-volatile, non-corrosive, non-toxic, non-flammable, inexpensive. They should also have low viscosity, high rates of heat and mass transfer, low vapor pressure, large saturation absorption capacity, low crystallization point and high density. Liquid desiccants should as well possess certain characteristics to be considered of high performance. These characteristics may include a limited liquid side resistance to moisture diffusion, a large surface contact area per unit volume, a good capacity of energy storage and a large availability in nature.

Some commonly used liquid desiccants are glycols and solutions of halide salts including calcium chloride ($CaCl_2$), lithium chloride (LiCl), lithium bromide (LiBr), tri-ethylene glycol, or a mixture of any of these salts. It is essential to adequately select the desiccant because of its direct effect on the system design and dehumidification capacity. Glycols are of limited use because of their high viscosity. They are also highly volatile that they might evaporate with air into the indoor space and may be considered as undesirable impurities. $CaCl_2$ is the cheapest desiccant and it is readily available in nature, however, its stability is dependent on its concentration in the solution and on the inlet air conditions which contributes to its reduced use. LiCl is considered to be a highly performing desiccant because of its significant stability and its extremely low vapor pressure. In addition, at ambient conditions it doesn't vaporize and it requires a reduced pumping power due to its low viscosity. Yet, this desiccant is considered corrosive and is expensive compared to others such as $CaCl_2$ (Bouzenada et al., 2016).

1.2.2 Hybrid desiccant/vapor compression systems

The use of desiccant technique prior to cooling process of the supply air can improve humidity control independent of temperature control in air conditioning systems enhancing the overall energy efficiency and reducing energy costs. In this way, the dew point temperature of air entering the cooling coil decreases which is, in the case of near/subzero applications, the key for frost free operations. Therefore, the combination of desiccants with conventional refrigeration systems avoids evaporating below the dew point temperature to handle dehumidification. As a consequence, this avoids frost formation in refrigeration applications by separating the treatment of latent and sensible loads. The figure below (fig. 1.9) shows the principle of this technology where first the hot and humid ambient air passes by the dehumidifier which is a heat and mass exchanger operating either with a solid or a liquid desiccant (Daou et al., 2006). If the temperature of the desiccant is less than that of the temperature of air, the desiccant would as well engage slightly in the cooling of the air. For further cooling, the dry air is then transferred to the cooling system which can be a chiller or a heat pump. Thus the air leaving dry and cool is now ready to be delivered to the indoor space.

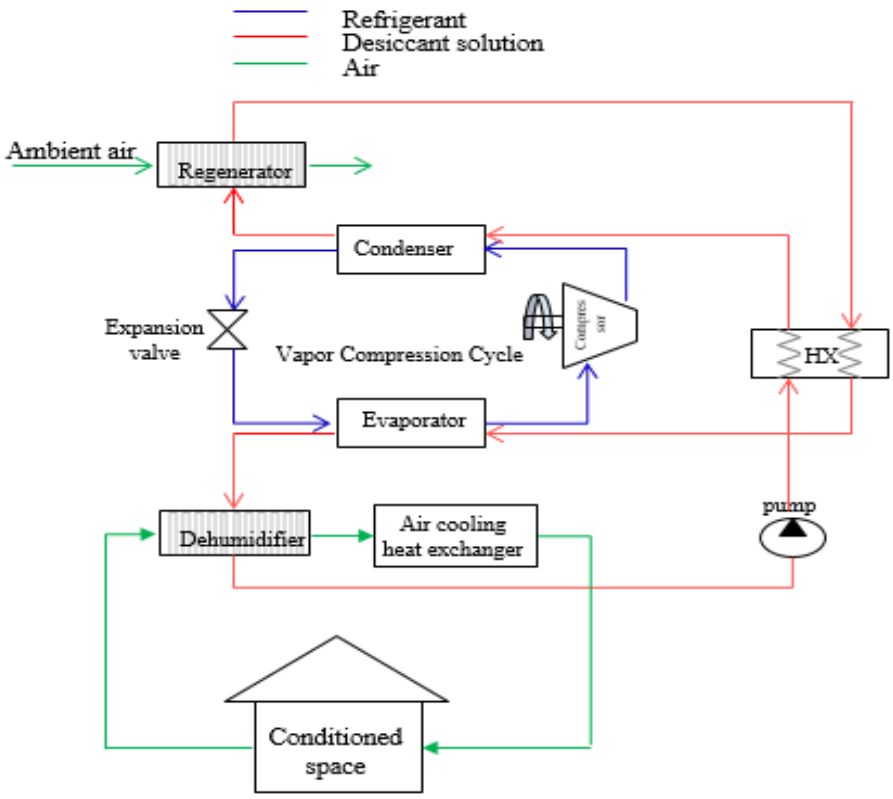

Figure 1.9: A hybrid liquid desiccant vapor compression cooling system

Several studies have been done on hybrid systems to study their behavior and performance. Nei et al. (Nie et al., 2017) modeled and tested a heat pump assisted with a solid desiccant wheel in hot and humid conditions. In their system, the desiccant rotor was regenerated by the waste heat produced by the condenser of the cooling system. Their system showed efficient energy performance with high air purification potential and it was concluded that its performance was sensitive to the outdoor humidity. Another study was conducted by Qin et al. (Qin and Schmitz, 2006) on an energy driven hybrid solid desiccant air conditioning system. Their experimental results suggested that by regenerating the desiccant using recovered waste heat, more than 30% savings in operational cost could be attained. The solid desiccant rotor was used as well with a heat pump operating in heating and cooling mode (Ge et al., 2011). It was found that the energy requirement can be reduced by around 8% in the cooling mode and 14% in the heating mode. For the cooling operations in industrial fields one of the applications was mentioned by Capozzoli et al. (Capozzoli et al., 2006) which was the insertion of a solid desiccant wheel and a sensible heat exchanger to an air conditioning system of a supermarket. In this study the desiccant wheel was regenerated by air heated with gas fired heater and the results showed operating cost savings by about 5-13% compared to traditional systems. In a way to improve the performance of solid desiccant hybrid systems in commercial buildings a study was conducted by Fong et al. (Fong et al., 2011). They proposed the use of a silica gel desiccant wheel with its regeneration heat coming mainly from solar collectors by transforming solar radiation into heat energy. It was shown that

their system could lower the annual primary energy consumption by more than 49% in a hot and humid climate in a Chinese restaurant.

However, using solid desiccants requires high regeneration temperatures which is considered as a penalty because heat at temperatures higher than 80°C is not always available and it becomes costly when investing in solar collectors. In many cases, electrical resistances or gas combustion were used for this reason increasing the overall energy consumption of the system. Thus further energy reduction can be done by regenerating the desiccant through waste heat produced by nearby sources or heat generated by the condenser of the conventional cycle but this is usually incompatible with solid desiccants.

Liquid desiccants present a real advantage compared to solid desiccants thanks to their lower regeneration temperature and to the flexibility of their integration into other systems, being in liquid state. Liquid desiccants hence allow higher efficiency due to flexible architecture and may valorize renewable heating sources like solar energy or low temperature waste heat. Considering their availability and inexpensiveness, their relative low regeneration temperature, their strong ability to control humidity and to provide high indoor air quality, liquid desiccant cooling technology is being extensively spread and research on this field is arising. Specifically, this technology has been widely implanted in the air conditioning industry and embedded within the vapor compression cycles in different applications. Zhang et al. (T. Zhang et al., 2012) carried out a performance optimization on a heat pump driven liquid desiccant system with condenser's dissipated heat enough to regenerate the desiccant. They compared different types of condensers to find out which configuration is the most efficient. This integration generates a hybrid liquid desiccant based vapor compression system which has received much attention as a viable alternative for the conventional air conditioning systems. Likewise, the research of Rafique et al. (Rafique et al., 2016) presented the different configurations available for liquid desiccant cooling technologies. They compared desiccant cooling to conventional cooling in terms of the system's efficiency, energy savings, CO_2 emissions and indoor air quality. Seenivasan et al. (Seenivasan et al., 2014) tested experimentally the effects of some parameters on the efficiency of dehumidification using $CaCl_2$ as a desiccant material. These parameters included the desiccant temperature, concentration and flow rate as well as the air temperature, relative humidity and flow rate. Their investigations came out with the conclusion that the mass flow rate of the solution was the most influencing parameter. In his work Khalil (Khalil, 2012) used a hybrid liquid desiccant integrated with a small capacity vapor compression air conditioning system. It was shown that the COP of such a system was 3.8 meaning 68% higher than that of a conventional VCC. In their work, Cheng et al. (Cheng and Zhang, 2013) identified that the regeneration process is the most energy consuming in hybrid liquid desiccant air conditioning systems. Thus they compared different regeneration methods using solar energy. Qi et al. (Qi and Lu, 2014) carried out a research on LiCl desiccant solution heated by a solar collector and cooled by a cooling tower. The modeling of such a system revealed energy savings of about 11-35% however these savings reached 22-47% when a cooling coil was added aiming to adjust the inlet temperature of the desiccant solution. Zhang et al. (L. Zhang et al., 2012) outlined the use of liquid desiccant technique for frost free applications to increase the efficiency of such systems.

They designed and tested a hybrid frost free air source heat pump under low temperatures and high relative humidity conditions. The COP of the proposed system varied between 2.6 and 2.9 and these values seemed to be 30-40% higher than that of a heat pump integrated with an electric heater for defrosting purpose. In some studies (Lin et al., 2018), the desiccant solution in the dehumidifier was used to do the humidity control contributing at the same time to the temperature reduction of the process air. In other studies (Niu et al., 2010), the liquid desiccant was used only to remove the latent load and in order to treat the sensible load, the air was passed by the cooling coil of the vapor compression cycle. Bergero and Chiari (Bergero and Chiari, 2011) suggested the addition of a storage tank between the regenerator and the dehumidifier of the liquid desiccant cycle so that the change in concentration and temperature inside the tank was always compensated from both cycles. Also, in a way to improve the flexibility of the system Dai et al. (Dai et al., 2001) added an evaporative cooler after the dehumidifier. Its role was to cool the dehumidified air in the form of direct or indirect evaporative cooling according to the desired comfort level. In their work the outlet air temperature and absolute humidity were assumed constant in the simulations of a traditional hybrid system since it was difficult to change the dehumidification capacity through changing the design of the dehumidifier and the regenerator. Another investigation was performed by Wang et al. (Wang et al., 2017) on the coupled heat and mass transfer process in a counter flow adiabatic packed tower. It was realized that in extremely high humidity conditions the dehumidification was highly influenced by liquid to air mass flow rate ratio and slightly influenced by the desiccant temperature and concentration compared to a low humidity condition. Fumo and Goswami experimentally studied an aqueous lithium chloride liquid desiccant dehumidification hybrid system. Their findings indicated that the effectiveness as well as the rates of the dehumidification and regeneration processes were not much affected by the desiccant flow rate. Instead the desiccant's temperature and concentration in addition to the inlet air conditions had significant effects on dehumidification and regeneration abilities. By limiting the number of parameters that could affect the dehumidification and regeneration abilities the degrees of freedom decrease leading to less flexible systems.

From the literature review above, it was shown that liquid desiccant based hybrid systems are an interesting technology for reducing the energy consumption while providing a good control of both sensible and latent load. Many authors discussed different architectures of such systems aiming to study the impact of the hybridization on the flexibility of these systems and their ability to keep a high performance level while facing variable operating conditions. However, whatever the considered architecture is, the dehumidifier and the regenerator of such a hybrid system are considered the main challenging components and their proper designs greatly affect the temperature and humidity control. Another challenge related to these heat and mass exchangers is their ability to prevent the escarpment of the desiccant solution droplets towards the air avoiding corrosion problems. For these reasons, several studies have been made and new technologies appeared focusing on these two components and on the accompanied heat and mass exchanges. In the next section, a state of the art of these components is discussed in details showing the existing technologies, their properties, advantages and drawbacks.

1.2.3 Heat and mass exchangers

Heat and mass exchangers are present in many applications such as cooling towers, humidifiers and dehumidifiers. Heat and mass exchanger technology is used to transfer energy in the form of both heat and moisture between two fluid streams flowing in different configurations (cross-flow, counter flow, etc.), at different temperatures, concentrations, and flow rates. Therefore it can be used as both sensible and latent load exchanger where the heat and mass transfers are coupled. The heat transfer is driven by thermal non-equilibrium and occurs as a function of the temperature gradient between the fluids. The thermal performance is mainly affected by the exchanger's geometry and by the flow configuration of the streams. As for the moisture transfer, it takes place due to the difference in the vapor pressure or in the concentration of these two fluids. It also depends on the exchanger's geometry as well as on the kind of fluids passing, on their densities, viscosities and concentrations. The heat and mass exchangers can be of direct type or of indirect type. In the direct type, simultaneous heat and mass transfer takes place between two fluids with a large surface of contact whereas in indirect contact exchangers the fluid streams are always separated by a dividing wall.

1.2.3.1 Direct type

In the direct type heat and mass exchangers it is possible to reach very high heat and mass transfer efficiencies because the two fluids are in contact and thus closer temperature approaches are attained. For example in such devices the temperature difference between the circulating fluids can reach as low as 1°C. They can be found in different applications including water desalination processes, geothermal power generation, heat storage, and in solar and low grade energy production (Hyun et al., 2005; Mahood, 2008). Common applications usually engage both heat and mass transfer (such as in evaporative cooling) and those involving only heat transfer are very rare. The enthalpy that is due to the phase change -which constitutes the mass transfer- represents a significant amount of the total energy transferred and this enthalpy enhances heat transfer. Adiabatic type dehumidifiers are examples of direct contact exchangers that are widely used for residential and commercial cooling applications. Direct contact exchangers have simple configurations, they are easily constructed from cheap materials and reduced amount of metals thus they have low capital cost (Baqir et al., 2016). Their operational cost is also low due to the high heat and mass transfer efficiency and to the large surface of contact between the flowing fluids compared to indirect types. Another advantage of direct contact exchangers is the absence of fouling problems due to the absence of a heat transfer surface or a wall between the fluids (Zohuri, 2017). Several research was performed on hybrid liquid desiccant systems using direct contact dehumidifiers and regenerators. An internally cooled direct contact dehumidifier was studied by Khan et al. (Khan and Sulsona, 1998) where a solution of lithium chloride was sprayed uniformly over the air. The dehumidifier had a cross flow configuration where the desiccant solution was sprayed vertically at the top of the exchanger and then recollected in a sump. Profiles of the temperature and humidity ratio of the process air, of the temperature and concentration of the desiccant and of the quality of the refrigerant in the cooling coil were analyzed and presented in their work. Dai et al. (Dai et al., 2001) investigated the use of direct

contact air to liquid desiccant exchanger to improve the efficiency of vapor compression cycles. The dehumidifier and regenerator of the desiccant system were direct contact exchangers. The system showed lower electricity consumption, higher COP and reduced size compared to a conventional compression cycle. Mahood et al (Mahood et al., 2015) experimentally investigated the heat transfer efficiencies and the capital costs of different direct contact exchangers. They also assessed how these values were affected by changing the mass flow rates and temperatures of the fluids used. Nomura et al. (Nomura et al., 2013) focused on the performance of a direct contact heat exchanger using a phase change material (PCM) and examined the effects of different PCM operating conditions on the latent and sensible heat storage. Cooling towers are other examples where the fluid that needs to be cooled, which is usually water, is dispersed over an upcoming stream of air and the direct contact enables air to cool water through evaporation and convection (Evans, 2016). The drift process due to the carryover of the fluid that needs to be cooled by the air represents a main drawback of such devices. In various industries desiccant dehumidification towers are installed where the fluid that needs to be cooled is a desiccant solution instead of water. In this case, the drift of fine droplets carried by the air emitted from these towers will contain desiccant salt which deposits on the nearby areas and in the process. Salt deposition is harmful for the process and the equipment because of its corrosive character. In many cases and for sanitary reasons it may be unacceptable to bare the risk of the presence of salts in products. Another limitation of this type is the large pressure drop created on the process air side while flowing through the packing materials that are used to provide contact surface for fluids interaction.

1.2.3.2 Indirect type

Indirect type exchangers are employed when the direct contact between the two fluids is undesirable as in the case of air and desiccant solution. Here, the direct contact between the two flowing fluids is completely prevented by a dividing wall yet heat and mass transfer takes place into or out of the separating wall. The transfer occurs when a driving force is applied and which is generally a pressure or a concentration difference between the fluids across the wall. To prevent the contact between air and liquid desiccant non-porous or hydrophobic micro porous membranes are used as separators. They have the ability to prevent the liquid solution from crossing towards the moist air yet they allow the transport of water vapor and heat from the desiccant solution towards the process air and vice versa. Membranes can be made of polypropylene (PP), polyethylene (PE) or poly-tetra-fluoro-ethylene (PTFE) coated with a dense silicon or gel layer or dense layer of amorphous Teflon (Huang and Zhang, 2013). They may also vary in material such as being organic or inorganic and their performance depend on their pore radius and on the exerted desiccant solution surface tension. The elastic and moisture transfer properties of polypropylene and polyethylene in such systems were evaluated by Larson et al. (Larson et al., 2007). Much work has been conducted to fabricate novel membranes with improved characteristics to achieve better system performance as in (Zhang et al., 2008). The effect of the membrane properties on the efficiency of a membrane exchanger integrated with a heat pump was analyzed by (Woods et al., 2009). They estimated the temperature lift of the heat

pump by varying the membrane's porosity, conductivity and thickness and the results showed that increasing the porosity, reducing the thermal conductivity or the thickness of the membrane improve the performance of the system. (Das and Jain, 2017) experimentally investigated a solar assisted liquid desiccant cooling system with an indirect contact dehumidifier using a polypropylene membrane with pore size 2 μm. The performance of the system and the dehumidifier's effectiveness were analyzed at different operating conditions. Another study of the energy performance of membrane based liquid desiccant systems integrated with air conditioning was examined by (Bergero and Chiari, 2010). They proposed a hybrid system with no droplets carryover and the results revealed significant energy savings that could exceed 50%. Some internally cooled dehumidifiers are examples of indirect type heat and mass exchangers. Indirect exchangers have relatively high cost compared to the first type, yet lower desiccant temperatures can be reached even without the necessity of a high desiccant flow rate. This is due to the possibility of adding cooling coils prior to the dehumidification process to remove the heat added to the desiccant solution.

As a comparison between these two exchangers (internally cooled indirect type and a direct one), (Huang et al., 2016) Huang et al. examined two configurations for each: cross-flow and quasi-counter flows. The lower membrane surface temperature provided by the internal cooling was the main reason why the effectiveness of the indirect exchanger could be improved compared to the adiabatic direct type exchanger. When comparing an indirect to a direct contact heat exchanger, it can be noticed that the latter achieves very high heat transfer rates, the exchanger construction is relatively inexpensive, and the fouling problem (which is the accumulation of unwanted material on solid surfaces) is generally nonexistent due to the absence of a heat transfer surface or wall between the two fluids. However, the applications of direct type heat and mass exchangers are limited to those situations where a direct contact of two fluid streams is permissible. In the case where liquid desiccants are used, the direct contact between the solution and the air should always be avoided because of the problem of carryover of salts by the air. If the salt is carried by the air, the indoor air quality is affected and corrosion problems in the indoor space will occur thus increasing the cost of maintenance. Therefore, the use of membranes in combination with the liquid desiccant air dehumidification systems is greatly important to separate the air from the desiccant solution. In this case indirect type liquid-air membrane energy exchangers (LAMEE) are used where a porous membrane is integrated into the liquid desiccant system. The membranes based heat and mass exchangers can be of several kinds, the two most known types are parallel plate and hollow fiber.

- Parallel Plate membrane exchangers

Parallel plate exchangers are the most commonly used to recover both sensible and latent loads due to their simple structure and large packing densities. In parallel plate membranes (fig. 1.10), the membranes are stacked together, keeping equal spaces between each two neighboring membranes to form flow channels allowing the fluids to pass in between (Huang et al., 2012). On one side of the membrane the air stream flows and on the other side another fluid flows that can be air, water, or a desiccant solution depending on the application involved.

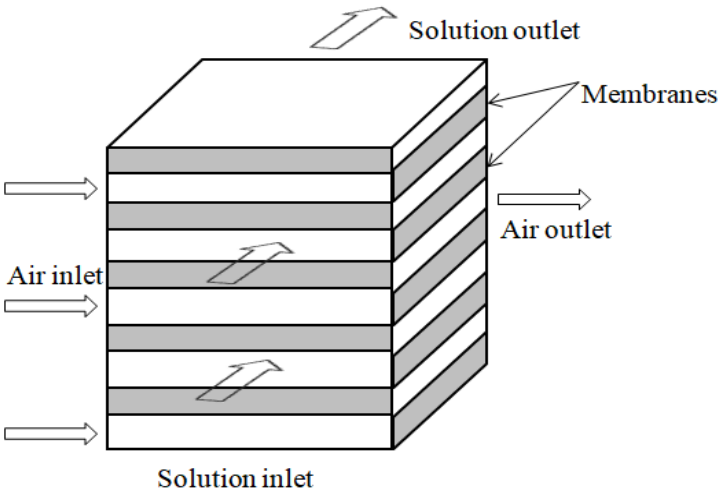

Figure 1.10: A schematic of a parallel plate cross flow membrane exchanger

The configurations could be either a cross flow or a parallel or a counter flow design. Although a counter flow arrangement has a better performance, a cross flow arrangement is found more often in air-to-air applications because the alternate flow passages can be sealed off at the outer edge of the exchanger. There is also a quasi-counter flow arrangement where the solution stream travels along an S-shaped path through the solution channel and the flowing arrangement between the air and the solution streams is similar to a combination of counter and cross-flow. There might be other possible more complicated arrangements but the first two are the simplest to be constructed and the easiest for duct sealing. Not to forget that a simple structure is necessary for lowering the cost, a pre-requisite condition for commercialization. A study was carried out by Zhao et al. (X. Zhao et al., 2008) on a novel counter flow exchanger used for indirect evaporative cooling. Numerical simulations were performed to improve the cooling efficiency and the effectiveness of the exchanger by optimizing the geometrical sizes and the operating conditions of the exchanger. A thorough comparison of the condensation behavior between cross flow and counter flow exchangers used as pre-cooling units was done by Min et al. (Min et al., 2019). Their research found out that the condensation ratio of cross flow exchangers was 2-15% lower than that of counter flow under same operating conditions. However for NTU values larger than 3.1, the plate area of cross flow exchangers should be 1.2 to 1.3 times larger than that of counter flow to achieve the same energy savings. Zhang and Niu (Zhang and Niu, 2002) evaluated the performance of parallel plate exchangers and provided a correlation for effectiveness calculation. According to the methodology, mean heat and mass transfer coefficients were estimated between the air and the surface of the membrane as well as the resistance through the membrane. Uncertainties might have been high because the resistance of the membrane also has an influence on boundary conditions. In most applications, the Reynolds numbers were below 2000, therefore a laminar flow could be assumed in such exchangers. In some practical applications, control of pressure drop and noise within an acceptable level is necessary and therefore the parallel plate ducts are usually short in length. Due to their simplicity and compactness, assumptions of a uniform temperature and a uniform heat flux along the ducts were made. They were first used as air to air exchangers and then they were extended to different applications such as humidifiers

and dehumidifiers used as LAMEE as it is the case here (Huang et al., 2014; Vali et al., 2009). The performance of a cross flow flat plate membrane based heat and mass exchanger for regeneration (Bai et al., 2018) and dehumidification processes was evaluated in several studies. They experimentally and numerically assessed the effects of the main operating parameters on the regeneration and dehumidification by varying the inlet properties of the solution and the air. (Abdel-Salam et al., 2013) studied a system where two LAMEEs were used, one in the dehumidifier for drying the process air and the other in the regenerator for the reactivation of the desiccant. An analysis of a LAMEE using LiCl desiccant solution for both dehumidification and regeneration was conducted by Ge et al. (Ge et al., 2014). They experimentally tested the effect of changing the inlet conditions of the solution and the air (including concentration, flow rates and temperatures) on the performances of the exchanger in both devices and they compared them to those of direct contact liquid desiccant devices. Another application for the LAMEE was in the energy recovery ventilators where they could be placed in the supply and exhaust air streams (Al-Waked et al., 2018). Effectiveness and moisture removal rate were the most common indices that determine their performance. The configuration of the liquid-air flow within the exchanger was one of the essential design parameters that can affect the performance of a LAMEE. A quasi counter flow parallel plate membrane heat pump was proposed by (Huang, 2015; Huang et al., 2014). A numerical calculation was done to show the effects of the channels structure on the solution temperature lift and efficiency. (Liang, 2014) Liang tested experimentally the sensible, latent and total energy transfer in a parallel plate enthalpy exchanger under various operating conditions. The results showed that the sensible, latent and total heat effectiveness decrease with the increase in the air mass flow rate and increase with the increase of the air temperature. Another study done by Nielsen et al. (Nielsen et al., 2013) focused on the influence of the fluid flow maldistribution on the performance of non-homogenous parallel plate exchangers. Their model showed that the flow maldistribution reduced greatly the performance of non-homogenous stacks of parallel plates compared to uniform plate stacks.

- Hollow Fiber

Similar to parallel plate membrane exchangers, in the hollow fiber types the air stream and the liquid stream do not mix together; each will be flowing on one side of the membrane (fig. 1.11). It is like a shell and tube heat exchanger where the tube side is formed by a bundle of hollow fiber membranes placed inside a shell. The shell side flow is formed in the cavities between the shell and the fibers. The best performance can be expected by transverse flow configurations with well-defined fiber spacing leading to a low pressure drop and a sufficient mass transfer (Yang et al., 2013). Two possible configurations can be done; the first one is to allow the desiccant solution to flow outside the tubes while the airstream inside the tubes. However, in most engineering applications, the solution flows in the tube side while the air moves in the shell side in a counter flow arrangement. The benefit of this flowing configuration is that the pressure drop for the air flow in the shell side is less and the performance is better (Bruining, 1989).

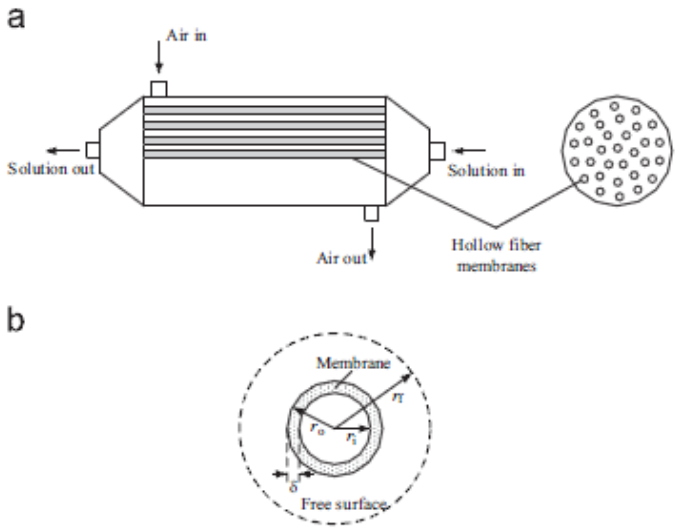

Figure 1.11: Schematic of the hollow fiber membrane module and the cell with a free surface model (L.-Z. Zhang et al., 2012). (a) The shell and the tube structure; (b) The cell with a free surface

The hollow fiber membranes are gaining more attraction from researchers because they have a higher packing density and a larger heat and mass transfer capability. A general review of hollow fiber contactors was given by (Gabelman and Hwang, 1999) including their field of applications, their design considerations and their operating principles. Pabby et al. (Pabby and Sastre, 2013) examined the most recent developments concerning the hollow fiber membrane contractors estimating their potential success and proposing possible future applications in which they might have promising role in industrial production cycles. Hollow fiber contractors were also investigated in air dehumidification processes as presented by Zhang and Huang (Zhang and Huang, 2011). They investigated, experimentally and analytically, the heat and mass transfer in a counter flow hollow fiber membrane module that showed very high performance and it was found that the membrane properties greatly affected the mass transfer of the exchanger. Further studies were done by Zhao et al. (Zhao et al., 2015) who evaluated experimentally a hollow fiber membrane exchanger performance during vacuum dehumidification. After running the test bench for 150 hours they found that the potential reduction in energy consumption of such a system could reach up to 26% compared to a conventional vapor compression cycle. Similar to dehumidifiers, regenerators were also made of hollow fiber membrane contractors. Zhang (Zhang and Zhang, 2014) integrated these contractors with a heat pump system to perform dehumidification prior to air cooling and regeneration of the liquid desiccant. The system was experimentally assessed under different operating conditions and the numerical results showed that the system performed properly even under very hot and humid weather. Research on the role of hollow fiber exchangers in gas separation applications was widely published throughout the years. Feron and Jason (Feron and Jansen, 2002) employed a hollow fiber membrane contractor for CO_2 separation with a porous polypropylene membrane. The aqueous solution used as absorbent was “Coral”, a novel absorption liquid based on mixtures of salts and amino acids.

Due to the numerous amounts of fibers in the shell, a direct modeling of the whole module is difficult. The mathematical models of the heat and mass transfer in the gas-liquid hollow fiber membrane contactors were established in several references and there have been many researches on this kind of exchangers. Zhang et al. (L.-Z. Zhang et al., 2012) investigated a laminar fluid flow heat and mass transfer in a hollow fiber membrane contactor for liquid desiccant air dehumidification. A cross flow arrangement was used where the solution flowed inside the fiber tubes while the air in the shell side. Their study resulted in obtaining the total drag coefficient, and the Nusselt and Sherwood numbers for a certain range of Reynolds number. Kistler and Cussler (Kistler and Cussler, 2002) also investigated the feasibility of using hollow fiber polymer membranes to recover heat and mass from ventilation air. Johnson et al. (Johnson et al., 2003) experimentally studied the influence of the membrane and the operating parameters on achievable mass and heat flux in order to be able to assess the efficiency of hollow fiber exchangers in evaporative cooling. They showed that reasonable numbers of fibers and membrane surface area could provide more cooling effectiveness comparable to conventional evaporative cooling equipment.

1.2.3.3 Drawbacks of the existing heat and mass exchangers and possible solutions

In the previous paragraphs, many of the mentioned studies focused on the performance of heat and mass exchangers highlighting for instance the importance of the properties of the membrane in indirect types or the advantage of some arrangements using spraying techniques in direct contact ones. However, after describing the existing designs where these exchangers are applied, it could be noticed that they still have certain drawbacks.

Regarding the direct contact water spraying in cooling towers, this technology proved its importance and good performance yet the problem of drift lead to serious complications especially when salt solution droplets were carried by the air and could ruin nearby spaces (Ruiz et al., 2016). Moreover, concerning the actual membrane based heat and mass exchangers, there exist some challenges that need to be enhanced and much research is being conducted concerning the amelioration of their effectiveness. First, these systems are usually sophisticated due to the installation and distribution of channels with different configurations. Second, they are costly due to the high price of the membranes that are of made of complex structures and are difficult to process. Concerning the membranes, one of the drawbacks is that they should be able to withstand a liquid pressure without being damaged or wetted thus they must be stiff enough to withstand the pressure difference and limit the surface warping under both dry and wet conditions (X Zhao et al., 2008). The impermeability to liquid water is also another important challenge for the membranes by which liquid water should never penetrate or permeate to the other side of the membrane whenever a water pressure is applied. However, water vapor should always be able to move from one side of the membrane to the other. All these characteristics require specific properties that should be present within the membrane such as acceptable thermal and mass conductivities, surface tension and elasticity, wear-resistant and high strength in order to promote the heat and moisture transfer (Onsekizoglu, 2012). Thus the heat and mass transfer resistance of the membrane should be as low as possible and the thermal conductivity should be small enough

to reduce the heat loss between the sides of the membrane. The thermal conductivity of the membrane is related to its physical characteristics and geometry and to its ability to conduct heat. Another limitation of the proposed membranes in the literature is their expensiveness and low performance since the membranes need to be mechanically reinforced which leads to a low mass conductivity.

In order to get a high performing system, convenient membrane properties should be available and the above mentioned challenges should be overcome. In all the existing systems these properties are found to be in contradiction with each other. Whenever the membrane is capable to withstand a liquid pressure its permeability to water vapor decreases reducing its mass conductivity. These contradictions in the system along with the challenging leak tightness feature, the high manufacturing cost and the complexity of the system as a whole, promote the development of a new competent system capable of responding to all the above mentioned needs and challenges.

1.2.3.4 Novel design of membrane based heat and mass exchanger

A novel technology patented by "Armines" is proposed. This technology makes a positive use of the presence of the membrane to solve the drift problem and the drawbacks of the actual membrane based technologies.

Figure 1.12 represents our proposed system consisting of a cross flow heat and mass exchanger where the desiccant solution is sprayed vertically downwards in between the membranes, represented by the green layers, and the air flows in a perpendicular stream. The weakened desiccant solution is then collected in the sump at the bottom of the exchanger and sent back to a regenerator in order to be reactivated.

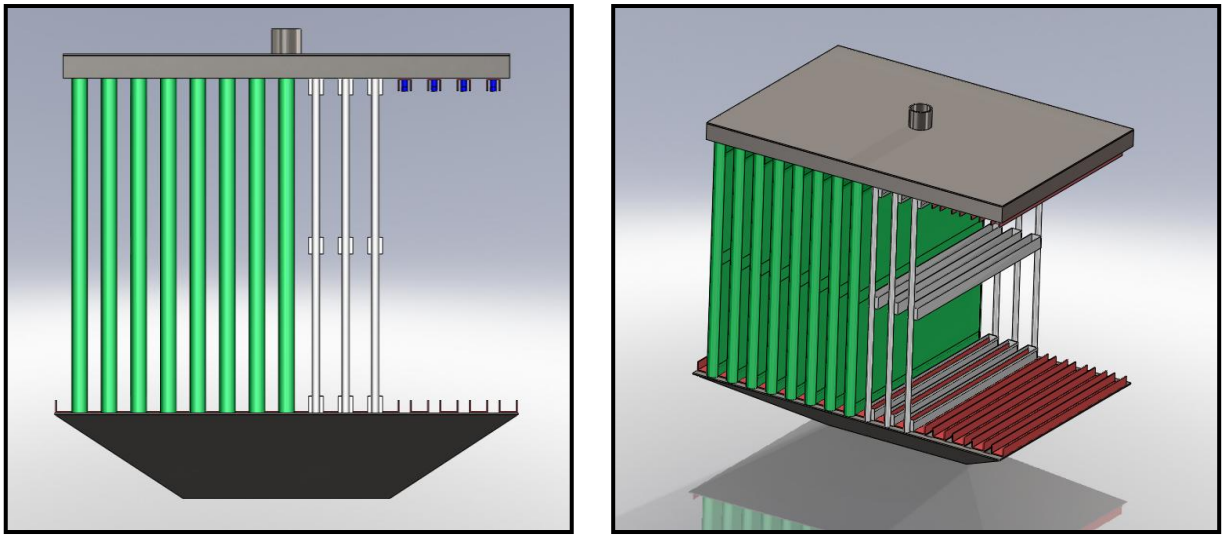

Figure 1.12: Design model of the proposed system

In a way to decrease the importance of withstanding a liquid pressure, spraying the liquid desiccant evenly through nozzles at the top of the system represents a desirable alternative. The vertical spraying of the liquid facilitates the design configuration as it flows downward by gravity (fig. 1.13).

Figure 1.13: A picture of the proposed system with the spraying desiccant

The spraying of the liquid not only decreases the water pressure over the membrane, but also scatters the water into tiny droplets increasing the indirect contact surface area between the air and the liquid (Gluesenkamp and Radermacher, 2011). This leads to greater turbulence at the air side close to the membrane which in turn increases the heat and mass transfer in this zone and minimizes the internal resistance at the air side. Spraying the liquid induces identical pressure of the small sprayed liquid droplets and the process air by which the enduring properties of the membrane along with its liquid impermeability and leakage tightness will no longer be of high constraints. Therefore, the contradictions that were presented in the section before are now avoided by adopting this design.

As for the relative high cost accompanied with the membranes manufacturing process, our aim is to use low cost materials that are originally fabricated for uses other than heat and mass exchange. Some of these materials that seem to be a great alternative to the conventional high cost membranes can be non-woven fabrics (NWF) that are sheets or web structures of fibers bonded together in different ways. They are usually used in clothing as waddings in jackets, diapers and shoes liners, or in home furnishing as pillow cases, sleeping bags, sacks and bags, coffee filters, envelopes, or in medical textiles as masks, bandages and caps. Other material candidates can also be found in different industries: in buildings as underlays for roofs and claddings for tubes, and in agricultural industries serving as covers for greenhouses and for capillary irrigations. Substantially the properties of these fabrics are determined by the individual properties of the constituting fibers; their diameter, porosity, and orientation (Chen et al., 2019). Some of these non-woven fabrics have excellent moisture resistance or repellency, they do not absorb water yet they are vapor permeable. In addition, those fabrics are flexible, light, porous, washable, disposable, cheap and easy to manufacture. New designs can be applicable by choosing non-woven fabrics to act as membranes in heat and mass exchangers due to their significant advantages mainly regarding their vapor permeability, their impermeability to liquids and their low manufacturing cost. The main choice of these materials depends primarily on the ability of the membrane to transmit water vapor in a way to maximize the heat and mass transfer.

Fig. 1.14 shows some of the membranes made of non-woven fabrics and other materials used in various fields.

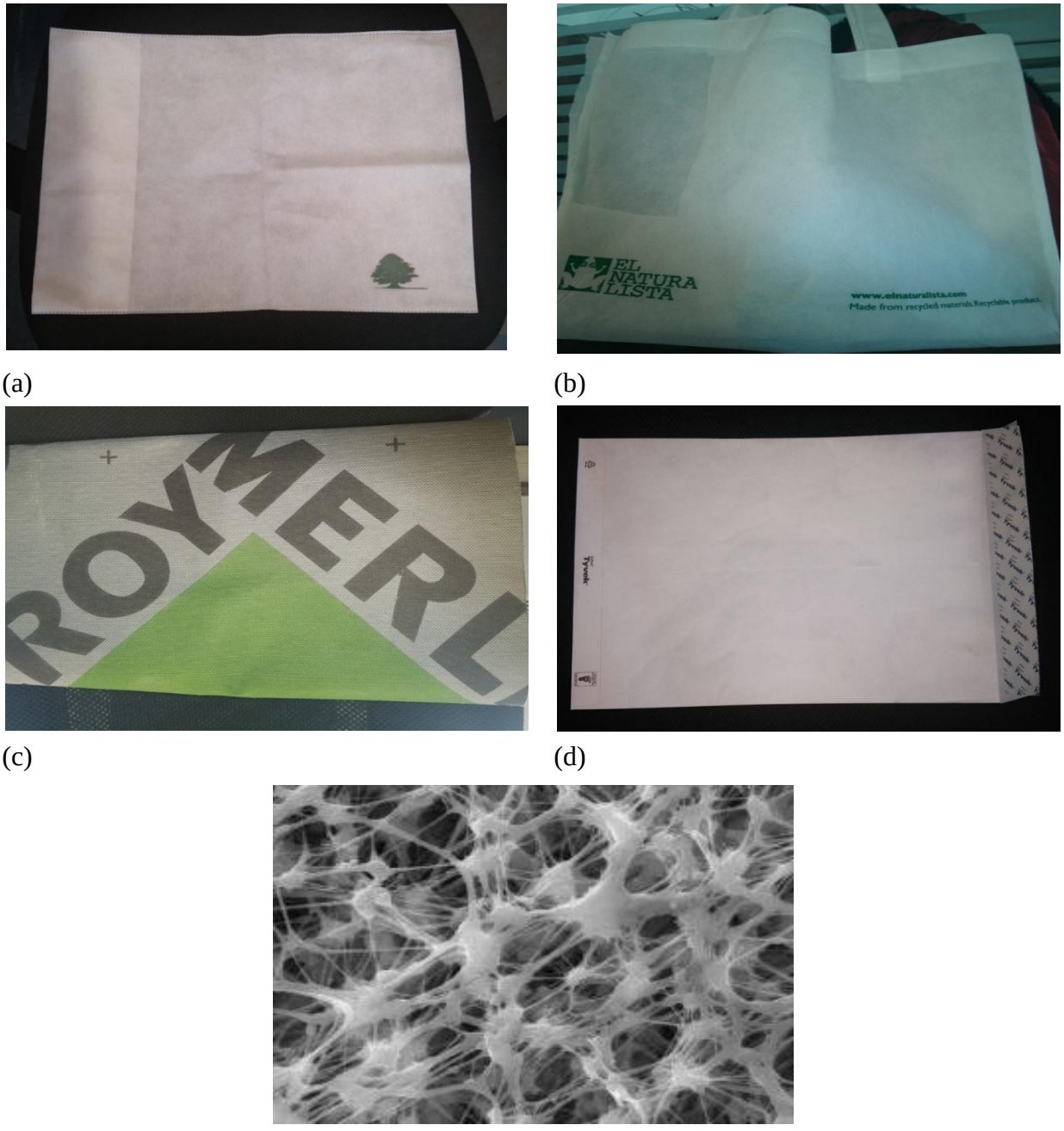

(a) (b)

(c) (d)

(e)

Figure 1.14: A collection of different membranes (a) pillow cases, (b) sack, (c) roof underlay, d) Tyvek mail envelope, (e) electrospun nanofiber

Spraying the desiccant as well as using low cost materials offer a solution to the inconveniences mentioned in the previous paragraph. However, using materials that are initially manufactured for considerations other than operating as heat and mass transfer purposes extends the scope towards

new perspectives as well as new scientific and technological burdens that will be explained and solved in the next chapter.

1.3 Thesis Problem Statement

Hybrid systems based on coupling desiccant cycle and vapor compression cycle seem reliable candidates that allow proper humidity control in air conditioning applications and a frost free operation in the case of refrigeration, with a potentially increased COP. Since solid desiccant present the drawback of high regeneration temperatures and complexity in their integration in systems, liquid desiccants are more attractive showing low regeneration temperatures and remarkable dehumidification capacities. From the previous cited research, it was determined that the configuration of the hybrid system and its architecture offer high efficiency over a range of operating conditions with different latent to sensible load ratio. This range of operating conditions varies from one architecture to another; it is clear that maintaining a high performing hybrid system could only be accomplished by a flexible design operating through a whole season in an energy efficient way. This defines the final objective of this thesis to design high performance, affordable and flexible hybrid refrigeration and air conditioning systems along with a design methodology and modeling tools.

The dehumidifier and the regenerator of such a hybrid system are considered the main challenging components and their proper designs greatly affect the temperature and humidity control. As discussed, one challenge related to these heat and mass exchangers is their ability to prevent the escarpment of the desiccant solution droplets towards the air avoiding corrosion problems while keeping them simple to build and low in cost. The membrane heat and mass exchangers constitute a technological response for such issues but the state of the art technologies present many drawbacks as explained earlier. In this thesis, the novel technology presented in the preceding section will be thoroughly studied. It uses original membrane materials and new design related to liquid distribution. The challenges concerning these materials are the lack of scientific characteristics and information concerning their properties mainly their water vapor permeability. To find out this property, these materials are tested experimentally using a modified cup test and the used methodology will be discussed in the coming chapter.

The third chapter of this thesis aims to deeply understand the behavior and the performance of this novel indirect contact heat and mass exchanger. The proper understanding and modeling of coupled heat and mass transfers within this novel exchanger are key factors to efficiently integrate them into processes and to benefit from their advantages over the existing conventional technologies. A modeling approach of the heat and mass transfer phenomena is developed by modeling the designed membrane exchangers and is supported by experimental characterization.

This model is used in the last chapter to study the energy interest of the integration of these exchangers in air conditioning applications and to design a flexible architecture able to cope with the seasonal variation of the load ratio.

Chapitre 2 Méthode Modifiée de la coupe pour Tester la Perméabilité de la Vapeur D'eau dans les Membranes Poreuses (résumé)

2.1 Introduction

Comme indiqué dans le chapitre précédent, les systèmes hybrides de climatisation (dessiccant liquide avec cycle de compression de vapeur) utilisant des échangeurs membranaires de chaleur et de masse peuvent être des alternatives prometteuses aux systèmes traditionnels de climatisation (Abdel-Salam et al., 2013); Huang et al., 2013; Zhang et Zhang, 2014). Certaines propriétés d'une membrane, comme son épaisseur, sa porosité, sa conductivité thermique et celle de masse, affectent l'efficacité des échangeurs. La conductivité de masse, aussi appelée perméabilité à la vapeur d'eau, a un impact majeur sur le transfert de la vapeur d'eau à l'intérieur de la membrane et donc sur la performance globale des échangeurs (Zhang, 2006). Il s'agit de la mesure de la quantité de vapeur d'eau qui passe d'un milieu à un autre à travers un matériau d'une épaisseur et d'une surface données et à une unité de temps définie. La transmission de la vapeur d'eau est induite par la différence de pression de vapeur entre les deux milieux causée par la différence de température et de concentration (Gurubalan et al., 2017). Si la perméabilité de la membrane est très faible la vapeur d'eau serait piégée dans le matériau qui provoque la condensation (si sa température atteint la saturation). Par conséquent, l'humidité interne augmente, ce qui bloque le transfert massique de l'échangeur. Le taux de transmission de la vapeur d'eau des matériaux poreux dépend fortement des propriétés physiques de la membrane, comme les dimensions de ses pores (Mukhopadhyaya et al., 2005). Afin de pouvoir comparer cette grandeur dans différentes membranes, il est important de s'assurer que ces membranes sont analysées et testées selon la même méthode et procédure d'essai (Li et Yao, 2018). Diverses techniques existent pour mesurer la perméabilité à la vapeur d'eau dans les membranes de différents types et caractéristiques. La méthode la plus couramment utilisée est le test de la coupe basé sur les normes publiées par la ASTM E96. La méthode de la coupe décrite dans la norme ASTM E96 est principalement utilisée pour prédire le taux de transmission de la vapeur d'eau dans des matériaux poreux ayant une perméabilité faible à modérée. L'une des hypothèses principales des normes ASTM est que la valeur de la résistance de l'air n'est pas indépendamment calculée. Par contre, on l'estime en supposant en même temps que la résistance de la membrane étant considérablement plus élevée. Pourtant, cette supposition n'est plus valide lorsque les matériaux testés ont une grande perméabilité à la vapeur d'eau. La perméabilité élevée implique une faible résistance au transfert de masse et donc la résistance à l'air ne serait plus négligeable par rapport à celle du matériau. Dans notre étude, nous sommes intéressés par les matériaux qui permettent une transmission de vapeur d'eau élevée et donc la résistance à l'air devrait être calculée séparément. Le test ASTM E96 ne fournit pas de données sur la façon de calculer cette résistance ; par conséquent, ce chapitre décrit brièvement l'essai de coupe et introduit une technique modifiée pour estimer la

transmission de la vapeur d'eau même dans des matériaux à hautes perméabilités considérant séparément la résistance à l'air. Plusieurs expériences ont été menées sur différentes membranes poreuses et la perméabilité de chacune d'elles a été dérivée à l'aide d'une méthode d'identification. Les résultats des expériences ont ensuite été soumis à une analyse de l'incertitude afin d'évaluer l'exactitude de la technique de mesure de cet essai modifié.

2.2 ASTM E96: L'essai de la coupe verticale

Lors de l'essai de la coupe verticale, deux approches sont considérées pour mesurer la transmission de la vapeur d'eau, méthode de la coupe sèche et de la coupe humide (fig.1). Ces deux tests ont des configurations expérimentales similaires mais avec des conditions différentes. Dans le premier, la coupe contient un matériau desiccant solide tandis que dans le second, le desiccant est remplacé par de l'eau. La norme ASTM explique que la méthode de la coupe humide devrait être utilisée lorsqu'on s'attend à une humidité relative élevée du matériau testé, tandis que chaque fois que les niveaux d'humidité relative sont plus faibles, on devrait utiliser un essai de coupe sèche.

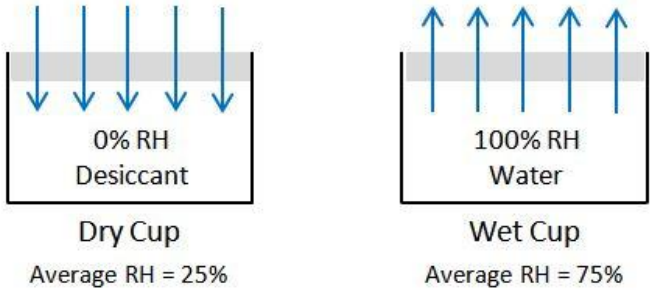

Figure 15: ASTM E96 essai de coupe pour mesurer la transmission de vapeur d'eau

2.3 Méthode modifiée

La méthode modifiée consiste à insérer trois coupes contenant de l'eau chaude dans un bain d'eau (30°C-35°C) où l'une des coupes reste non couverte et les deux autres coupes sont recouvertes de deux échantillons différents de membranes dont les bords sont bien scellées (fig.2). Sept matériaux différents ont été testés parmi lesquels : une membrane fabriquée en nanofibres électro-filées, une feuille de polypropylène, un écran de sous troiture, Tyvek, et quatre tissus non tissés (NWF) utilisés pour les sacs et les housses d'oreillers. La coupe non couverte est une coupe de contrôle dont les résultats sont utilisés plus tard pour déduire le coefficient de transfert de masse de l'air. Une petite lame d'air est maintenue entre l'eau et la membrane, ce qui provoque une résistance au transfert de masse de la vapeur d'eau. Pourtant, cette lame ne peut être supprimée afin de réduire le risque de contact entre la membrane et l'eau. Un ventilateur est déclenché pour forcer le mouvement de l'air au-dessus des coupes afin de réduire sa résistance. Il existe une différence de gradient de température et de concentration de vapeur d'eau entre l'eau à l'intérieur des tasses et l'air qui passe au-dessus, ce qui crée une différence de pression de vapeur. Ainsi, un flux de vapeur se produit du côté de l'eau à travers les membranes vers l'air. La température d'entrée et l'humidité relative de l'air sont mesurées en continu à l'aide d'un thermocouple et d'un hygromètre et les données sont enregistrées. De plus, la température de l'eau

à l'intérieur des coupes ainsi que son poids sont mesurées périodiquement pour déterminer le taux de transmission de la vapeur d'eau.

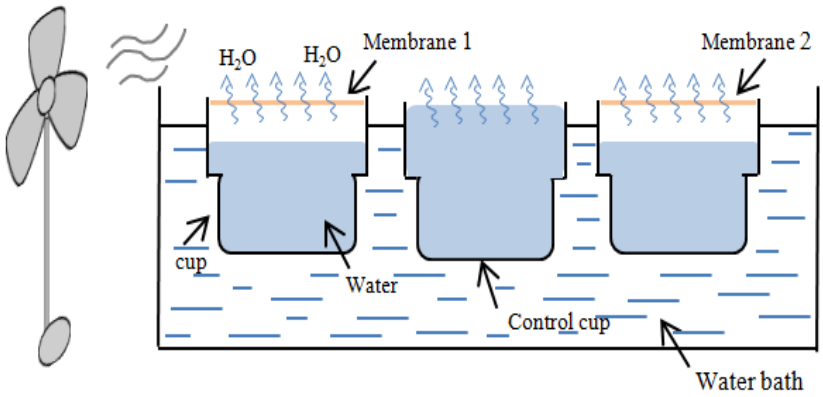

Figure 16: Dessin schématique de la méthode de la coupe modifiée

La température élevée de l'eau contribue à sa forte pression de vapeur, ce qui est très différent de celui de l'air ambiant. En raison de cette différence, la vapeur d'eau va être transférée à travers les membranes du côté de l'eau vers le côté de l'air. La vapeur s'évapore de l'eau à haute température et entre en contact avec la partie supérieure de la membrane. La masse de l'eau à l'intérieur des coupes est mesurée environ toutes les 10 à 15 minutes pendant environ 6 heures et d'après les mesures expérimentales périodiques, on peut montrer qu'avec le temps cette masse diminue.

2.3.1 Coupe de contrôle

La variation de masse de l'eau à l'intérieur des coupes en fonction du temps est ensuite tracée sur une courbe (i).

En raison de l'absence de membrane, la seule résistance est la résistance de l'air. Ainsi, elle est utilisée dans notre expérience pour déduire la valeur réelle du coefficient de transfert de masse de l'air qui dépend des conditions d'entrée (température, humidité relative et vitesse). L'équation de transfert de masse entre l'air et l'eau dans la coupe de contrôle est dérivée et résolue numériquement en utilisant le langage Modelica dans le logiciel Dymola en utilisant l'équation suivante:

$$h_{ma}A(Y - Y_w) = \frac{dm}{dt} \quad (1)$$

Ensuite, la courbe de la variation de la masse d'eau en fonction du temps a été tracée par la courbe (ii). L'optimisation de la valeur du coefficient de transfert de masse de l'air h_{ma} minimise l'erreur entre la courbe (i) et la courbe (ii); donc lorsque cette erreur est minimale h_{ma} est déduite.

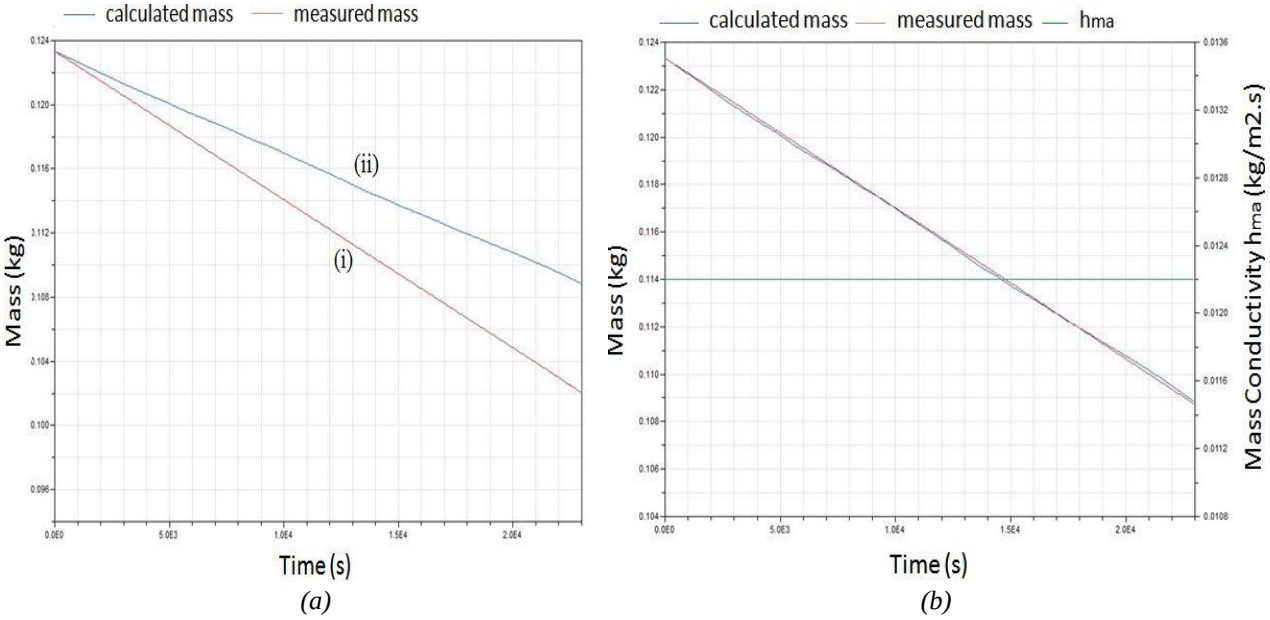

Figure 117: a) Variation de la masse mesurée (i) et de la masse calculée (ii) de l'eau par rapport au temps dans la coupe de contrôle, b) conductivité de masse de l'air déterminée par optimisation

2.3.2 Coupes recouvertes des membranes

Pour les autres coupes, la résistance totale du système est égale à la somme des résistances individuelles (fig.4).

$$R_{total} = R_a + R_m + R_c = \frac{1}{h_{Ma}} + \frac{\delta}{k_m} + \frac{1}{h_{Mc}} \quad (2)$$

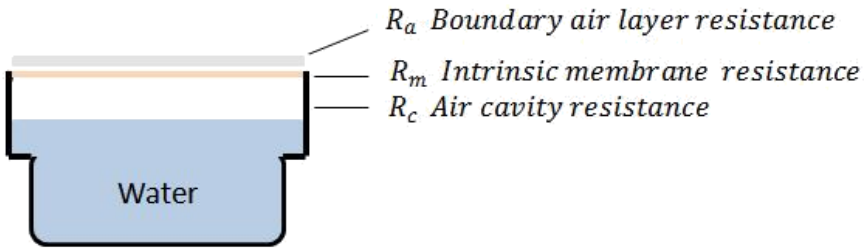

Figure 18: Trois résistances au transfert de vapeur d'eau

- Le coefficient de transfert de masse h_{mc} dans l'espace confiné

Dans l'espace confiné, le transfert de chaleur et de masse qui se produit dépend de la géométrie et de l'orientation des surfaces ainsi que des propriétés thermiques des fluides concernés. Dans notre cas, nous avons deux surfaces horizontales où la plus basse est une surface chaude (eau chaude) alors que la plus haute est une surface froide (membrane en contact avec l'air ambiant). L'air adjacent à la surface plus chaude (qui est plus léger) s'élève et l'air adjacent à la surface plus froide (qui est plus lourd) s'enfonce d'un mouvement de rotation qui augmente le transfert de chaleur par convection naturelle entre les deux surfaces. Par conséquent, le coefficient de transfert de chaleur de l'air qui circule naturellement dans l'espace confiné doit être calculé à partir de corrélations pour la convection naturelle entre deux surfaces isothermes. Avec le temps, la quantité d'eau à l'intérieur des coupes diminue aussi, mais avec une vitesse plus lente que la

coupe de contrôle. Ainsi, l'espace confiné entre l'eau et la membrane augmente, ce qui entraîne une diminution de sa conductivité de masse et donc une augmentation de sa résistance. Le nombre de Nusselt est exprimé dans le cas d'une cavité horizontale chauffée par le bas, par :

$$Nu = 1 + 1.44\left[1 - \frac{1708}{Ra}\right] + \left[\frac{Ra^{\frac{1}{3}}}{18} - 1\right] \quad (3)$$

Et donc le coefficient de transfert de masse h_{mc} est déduit en utilisant l'analogie de Lewis

$$h_{mc} = \frac{h_{Tc}}{C\ Le^{\frac{2}{3}}} \quad (4)$$

Avec

$$Nu = \frac{h_{Tc} L_c}{k} \quad (5)$$

➢ Déduction de k_m

Les équations de transfert de masse d'une coupe recouverte d'une membrane peuvent être écrites comme suit:

$$\frac{dm}{dt} = h_{mc} A(Y_{mw} - Y_w) \quad (6)$$

$$h_{ma} A(Y - Y_{ma}) = \frac{k_m}{\delta} A(Y_{ma} - Y_{mw}) \quad (7)$$

$$h_{mc} A(Y_{mw} - Y_w) = \frac{k_m}{\delta} A(Y_{ma} - Y_{mw}) \quad (8)$$

Ce système est utilisé pour déterminer les inconnues Y_{ma}, Y_{mw} et k_m en substituant la valeur de la conductivité de masse déduite précédemment de l'air h_{ma} et de la cavité h_{mc}. La solution du système d'équation de transfert de masse dans les coupes couvertes permet de tracer la courbe de la variation de masse calculée en fonction du temps (ii). Minimiser l'erreur entre ces deux courbes nous permet de trouver la conductivité de la masse de la membrane k_m (fig.5).

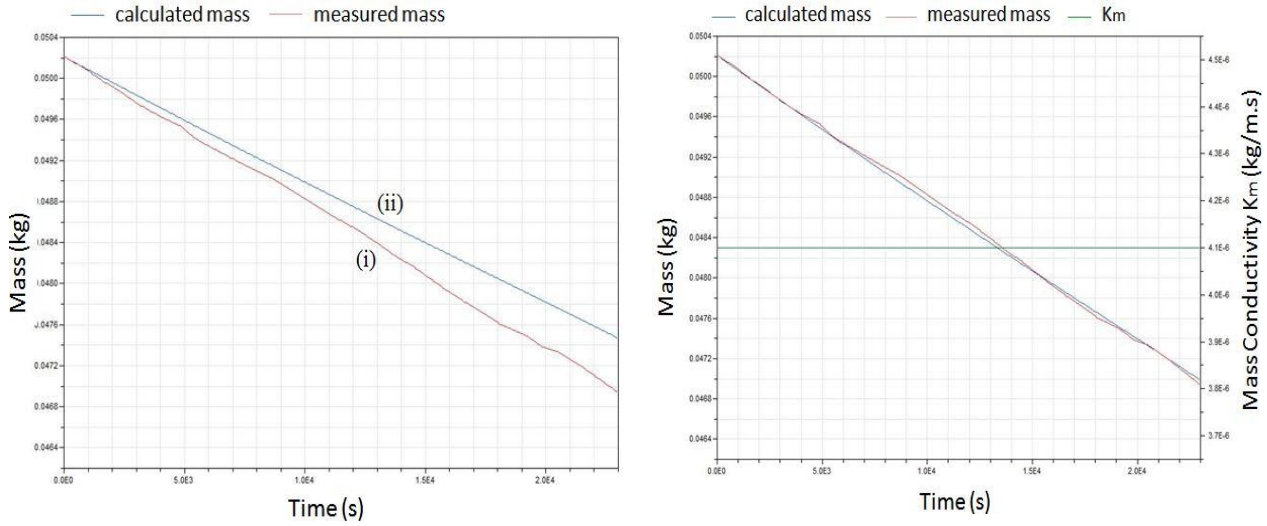

(a) (b)

Figure 19: a) Variation de la masse mesurée (i) et de la masse calculée (ii) de l'eau par rapport au temps dans la coupe recouverte d'une membrane, b) conductivité de masse de la membrane déterminée par optimisation

2.4 Résultats

En répétant les expériences plusieurs fois, chaque fois en comparant deux membranes différentes, nous permet de classer les membranes en fonction de leur capacité à laisser passer la vapeur d'eau. Chaque membrane est testée entre 2 et 3 fois et pour chaque test k_m est déduite par la même méthode. Les valeurs de la conductivité de masse de chaque membrane sont tracées dans le graphique de la figure 6 de la conductivité de masse la plus élevée à celle la plus faible.

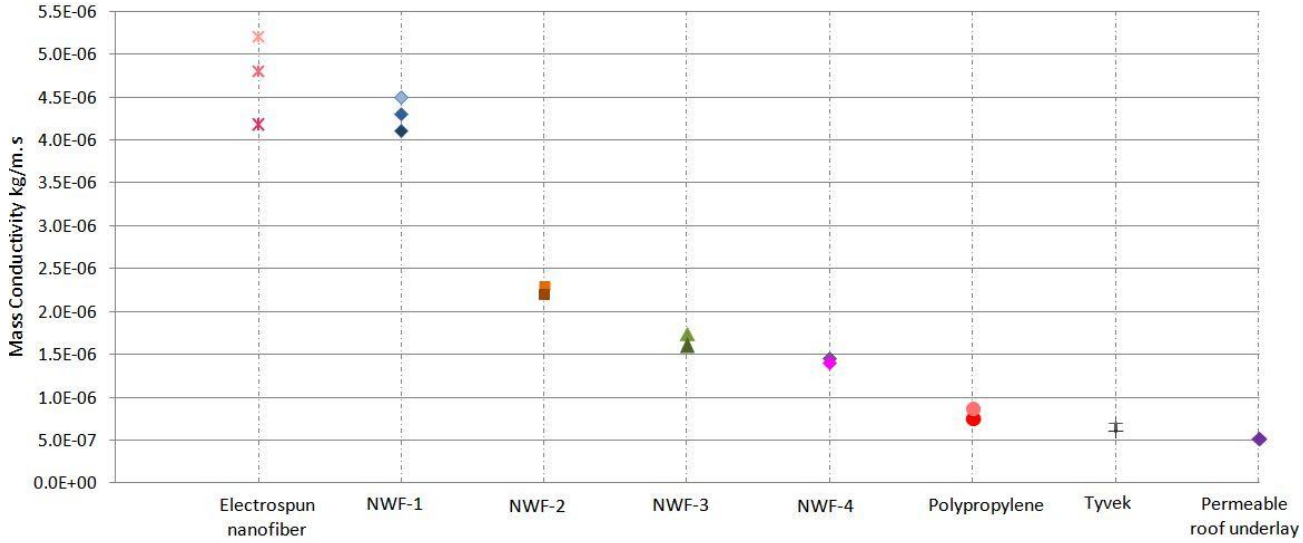

Figure 20: Résultats de conductivité de masse pour toutes les membranes de toutes les expériences

2.5 Analyse de l'incertitude

La conductivité de masse de chaque matériau a été déterminée pour chaque expérience, et la moyenne est determinée. Les résultats des expériences ont ensuite été soumis à une analyse d'incertitude afin d'évaluer la précision de la technique de mesure de cet essai et la méthode Monte Carlo a été utilisée pour évaluer la propagation de l'incertitude. Les résultats indiquent que les valeurs d'incertitude varient d'environ 8% à 26% (tableau 1). Ainsi, les matériaux à haute conductivité de masse (faible résistance au transfert de chaleur et de masse) qui sont perméables à la vapeur mais non pas au liquide et qui sont capable de résister à la pression de l'eau peuvent être utilisés comme membranes dans les échangeurs de chaleur et de masse.

Tableau 1: Épaisseur, conductivité moyenne et résistance au transfert de masse de toutes les membranes

Type de membrane	std (kg/m.s)	$k_{m,moy}$ (kg/m.s)	Incertitude (%)
NWF-1	7.84E-07	4.30E-06	17.43
Electrospun nano fibre	8.17E-07	4.49E-06	15.41
NWF-4	3.93E-07	1.43E-06	26.23
NWF-2	2.78E-07	2.25E-06	12.64
NWF-3	3.29E-07	1.68E-06	21.98
Polypropylène	1.43E-07	8.10E-07	16.86
Tyvek	8.43E-08	6.40E-07	14.05
Sous-toiture perméable	4.14E-08	5.30E-07	7.96

2.6 Conclusion

La perméabilité à la vapeur d'eau est la propriété principale des membranes qui influence sa capacité de transfert de masse. Dans ce chapitre, on a identifié différents matériaux à faible coût qui sont initialement fabriqués pour des usages autres que l'utilisation comme membranes. Ces matériaux ont été testés expérimentalement à l'aide d'un essai de coupe modifié et d'une méthode d'identification afin de déterminer leur perméabilité à la vapeur d'eau. Dans cette méthodologie, nous avons réussi à déduire explicitement la valeur des résistances de l'air au-dessus des coupes et de l'air coincé entre l'eau et la membrane. En substituant ces valeurs dans le système d'équations de conservation de masse, on a déterminé la conductivité de masse des membranes. Ces valeurs allaient de 5,3 x 10-7 à 4,49 x 10-6 kg/m.s. Ainsi, la mesure, l'analyse et l'interprétation des résultats pour les différents matériaux nous permettent de classer et de comparer la capacité de transfert de masse de chacun. Une analyse de l'incertitude a ensuite été effectuée pour évaluer l'exactitude de cette approche et la méthode Monte Carlo a été utilisée pour évaluer la propagation de l'incertitude. L'utilisation pratique des simulations de Monte-Carlo pour l'estimation des incertitudes est un outil fondamental dans ce domaine, capable de résoudre des problèmes de mesure complexes. Les résultats ont montré que les valeurs d'incertitude variaient d'environ 8 % à 26 %. Ces chiffres, bien qu'ils n'aient pas été jugés suffisamment bas, n'ont pas permis de modifier la classification des tissus testés par ordre de perméabilité de la vapeur d'eau. Par la suite, une analyse de l'impact de l'incertitude de la conductivité de masse sur la puissance totale de l'échangeur de chaleur et de masse sera effectuée. Cela donnerait une idée si ces grandes valeurs d'incertitude sur k_m ont un grand effet sur les résultats numériques de la performance de l'échangeur ou non. Dans ce chapitre, nous avons pu classer les matériaux à haute conductivité de masse (faible résistance à la chaleur et transfert de masse) et possédant les caractéristiques d'être perméable à la vapeur, imperméable au liquide et capable de résister à la pression d'eau peuvent être utilisés comme membranes dans les échangeurs de chaleur et de masse. Selon nos résultats, la membrane composée de nanofibres électrospun semblait avoir la conductivité de masse la plus élevée parmi les membranes testées; c'est un bon candidat potentiel pour notre échangeur. Cependant, elle est produite par une nouvelle technique de fabrication alors que les tissus non tissés sont largement disponibles. Ainsi, dans le chapitre à venir, la NWF-1, qui présente la plus faible résistance au transfert de masse et qui possède les propriétés durables requises, est utilisée comme membrane dans notre prototype d'un échangeur de chaleur et de masse.

Chapter 2 Modified Upright Cup Method for Testing Water Vapor Permeability in Porous Membranes

2.1 Introduction

As discussed in the previous chapter, hybrid air conditioning systems (liquid desiccant with vapor compression cycle) using porous membrane based heat and mass exchangers may be ideal alternatives to traditional air conditioning systems (Abdel-Salam et al., 2013; Huang et al., 2013; Zhang and Zhang, 2014). Some of the properties of a membrane such as its thickness, porosity, thermal conductivity, and mass conductivity affect the efficiency of the heat and mass exchangers (Sabek et al., 2016). Mass conductivity, also known as water vapor permeability, has a main impact on the transport of water vapor within the membrane and thus on the overall performance of the membrane based exchangers (Zhang, 2006). It is the measure of the amount of water vapor that passes from one medium to another through a material of a given thickness and surface area and at a defined unit of time. The water vapor transmission is induced by the difference in vapor pressure between the two different media caused by the difference in temperature and concentration (Gurubalan et al., 2017). If the membrane is not permeable or has a very low permeability, water vapor would be trapped within the material causing condensation to occur if its temperature reaches the saturation one. Consequently, internal moisture increases which blocks the mass transfer of the membrane exchanger. The water vapor transmission rate of porous materials highly depends on the physical properties of the membrane such as its material and the dimensions of its pores (Mukhopadhyaya et al., 2005). In order to be able to compare this magnitude in different membranes, it is important to be sure that these membranes are analyzed and tested to the same test method and procedure (Li and Yao, 2018). This property has often been determined by standard methods such as the ISO 2528 (*ISO 2528 Sheet materials – Determination of water vapour transmission rate – Gravimetric (dish) method.*, 1995) and ASTM E96 (*ASTM E 96 Standard Test Methods for Water Vapor Transmission of Materials.*, 2013). The most commonly used method is the cup test based on the standards published by The American Society for Testing and Materials (ASTM). The upright cup test described in the ASTM E96 standard is mainly used to predict the values of low to moderate permeable materials where the air resistance above the cup is assumed to be relatively small. This chapter briefly describes the basic cup test and introduces a modified technique that infers the water vapor transmission even in highly permeable materials by considering explicitly the resistance of the air. Several experiments were conducted on different porous membranes and the permeability of each was derived using an inverse method. The results of the experiments were then subjected to an uncertainty analysis in order to assess the accuracy of the measuring technique of this modified cup test.

2.2 ASTM E96 Upright Cup Method

In the upright cup test, two approaches can be done to measure the water vapor transmission, a dry cup and a wet cup method. These two tests have similar experimental setups but with different conditions. In the former the cup contains a solid desiccant material while in the latter the desiccant is replaced with liquid water (Seng et al., 2018). The ASTM standard explains that the wet cup method should be used whenever a high relative humidity is expected in the vicinity of the tested material while whenever relative humidity levels are lower a dry cup test should be used (Murphy, 2010). In the dry test the desiccant absorbs the water vapor which migrates from the air in the environmental chamber through the porous material and then into the cup. While in the wet cup method water molecules move from the water side to the air side crossing the membrane (Joseph W. Lstiburek, 2017) as shown in figure 2.1.

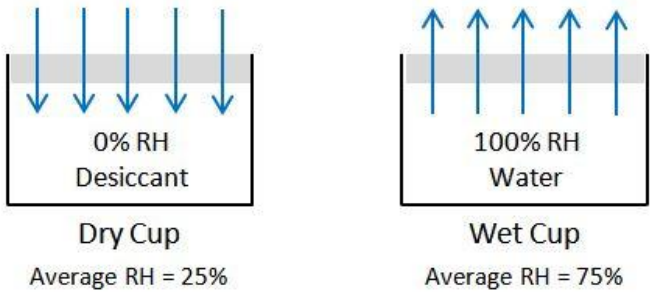

Figure 2.1 ASTM E96 upright cup test for measuring water vapor transmission

Procedure

The procedure for both tests is similar. A cup is filled either with a solid desiccant material or with distilled water leaving a small air space between them and the membrane. The sample of the porous material that needs to be tested is properly sealed to the edge of the cup to prevent side diffusion (Richter and Staněk, 2016). The initial weight of the cup is taken and then the cup is placed in an environmental chamber where the air temperature and relative humidity are continuously measured. The test cup is then weighed periodically to provide enough number of data points throughout the test. For the dry test weight is gained inside the cup due to the transfer of the water vapor from the chamber (high humidity) to the desiccant (low humidity). As for the wet test, it marks weight loss where the water vapor is transmitted from the cup (high humidity) to the atmosphere inside the chamber (low humidity).

Assumptions

The permeation values obtained from the tests of this standard depend on a set of conditions under which these tests are conducted. The following assumptions as mentioned in (Sloane Taliaferro, 2015) and (A. P. S. Sawhney et al., 1993) are considered:

- An ideal sealing material should be used such that there is no weight gain or loss from or to the test chamber (evaporation, oxidation, hygroscopicity).
- A dish made of glass or any rigid, impermeable, corrosion-resistant material is preferred over lightweight metals like aluminum since oxidation might take place resulting in an increase of the cup weight.
- Three resistances are considered in the system, one caused by the air boundary layer R_a the other by the membrane R_m and the third by the air gap between the water surface and the membrane R_c as shown in figure 2.2.
- The tested fabrics have low to moderate permeability which gives high resistance values.
- Air moving above the cups has a relatively high speed lowering its resistance. Thus the air side resistance R_a would not be calculated individually, it would be included with the resistance of the membrane R_m.
- The air cavity between the water surface and the membrane has a high resistance to vapor transfer that could be sometimes greater than that of the membrane itself.
- Mass transfer through this air gap is assumed to occur due to pure diffusion.
- The total resistance of the system is equal to the sum of the individual resistances $R_{total} = R_a + R_m + R_c$. It can be calculated through Fick's law by equation (2.1).

$$R_{total} = \left(\frac{1}{\dot{m}}\right) D(\Delta C) A \tag{2.1}$$

where R is the resistance (exceptionally here it is expressed in m), $\dot{m}$ is the mass flux of water vapor in $\frac{g}{s}$, D is the diffusion coefficient of water vapor in air $\frac{m^2}{s}$, ΔC is the concentration difference also exceptionally expressed in $\frac{g}{m^3}$ and A is the area in m.

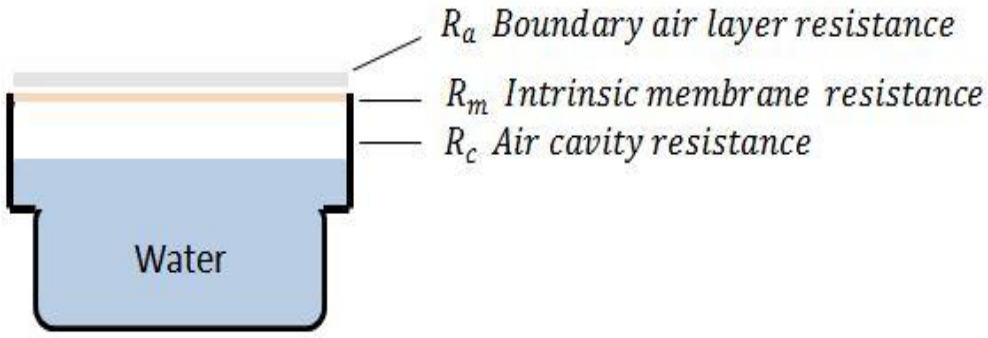

Figure 2.2: Three resistances to water vapor transfer in ASTM E96 standard

Discussion

As mentioned in the assumptions of the ASTM test, the value of the air side resistance is not calculated explicitly. Instead, it is estimated together with the resistance of the membrane being considerably smaller. However, this assumption is questionable when the tested fabrics have high

permeability to water vapor. High permeability implies small resistance to heat and mass transfer and thus the resistance at the air side would not be negligible with respect to that of the fabric. In our experiments, we are interested in fabrics that allow a high water vapor transmission and thus the air resistance should be calculated separately. The ASTM E96 test doesn't provide data on how to calculate this resistance, hence this chapter introduces a modified method to deduce the membrane mass conductivity by predicting the air resistance separately. This approach uses an inverse methodology and will be explained in the coming steps.

2.3 Modified Upright Cup Method

In order to find the mass transfer properties of the membranes, tests were conducted on three cups simultaneously containing hot water. One of the cups is remained uncovered and it stands as a control cup whose results are used later to deduce the mass transfer coefficient of air. The other two cups are covered by two different samples of membranes with their edged properly sealed. A tiny air gap is kept between the water and the membrane which causes a water vapor mass transfer resistance. Yet, this gap cannot be neglected because it is necessary to reduce the risk of water touching the membrane. Figure 2.3 represents the schematic drawing of the modified method used in our experiment.

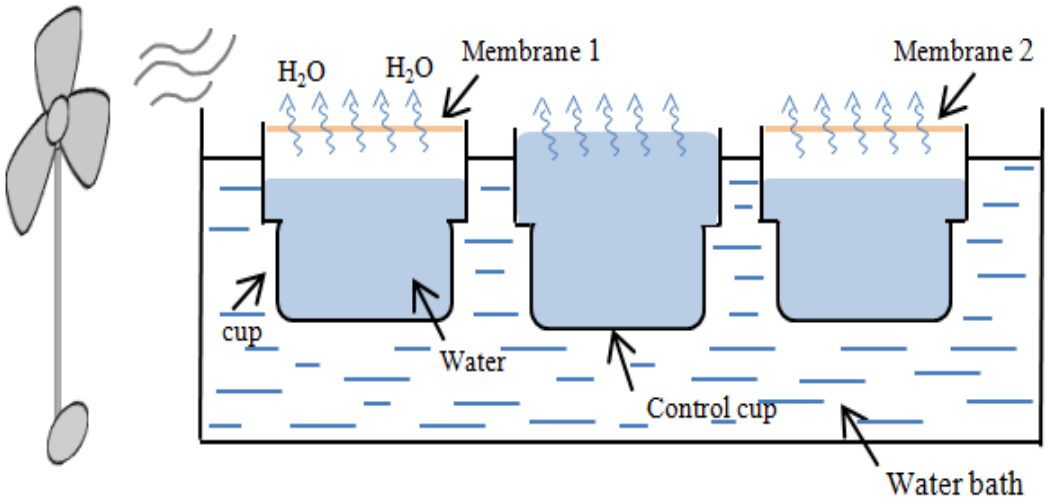

Figure 2.3: Schematic drawing of the modified cup method

The pans are maintained in a water bath of regulated temperature inside a room of ambient air at 25°C and 40% relative humidity. As described by the ASTM standard, a dry cup test is used when low relative humidity is expected in the vicinity of the tested material. Yet in our case water is used even though the ambient air relative humidity is not high enough. This is justified by the fact that in our application of the heat and mass membrane exchanger, the liquid (desiccant solution) is at a relatively high temperature which provokes a higher vapor pressure difference between it and the air outside and thus a higher heat and mass transfer. Therefore, for a true resemblance of our application, the water inside the cup is maintained at relatively high temperature.

A fan is turned on to force the air movement above the pans in order to decrease the air side mass transfer resistance. A temperature and water vapor concentration gradient difference exists between the water inside the pans and the air passing above them which creates a difference in the vapor pressure. Thus a vapor flow occurs from the water side through the permeable membranes towards the air side. The inlet temperature and the relative humidity of the air are continuously measured using a digital thermocouple and a hygrometer and the data is recorded. In addition, the temperature of the water inside the cups is repeatedly measured and periodic weighing of the test pans is made to determine the rate of water vapor transmission.

2.3.1 Experimental Conditions Assessment

The high temperature of water contributes to its high vapor pressure with a significant difference from that of the ambient air. Due to this difference the water vapor is going to be transferred through the membranes from the water side to the air side. The vapor is evaporated from the water at high temperature and comes in contact with the cool upper side of the membrane which has a temperature T_m. However, if the temperature of the water inside the cups is greatly higher than that of air, a condensation process takes place by which the condensed water deposits on the membrane. When these droplets pile up on the lower surface of the membrane they fall back in the pan. In this case, the model representing the heat and mass transfer in the air gap between the liquid level and the membrane fails to be accurate and the results in term of membrane vapor permeability are not reliable. So in a way to be able to avoid the condensation problem, the temperature of the water should be kept just slightly greater than that of the air. Water vapor continues to be transmitted from the water to the air as long as the vapor pressure of the water is higher than that of air. The experiments are done with a water temperature between 30°C and 35˚C and the mass of the water inside the pans is measured approximately every 10 to 15 minutes for around 6 hours.

2.3.2 Tested Membranes

Seven different materials were tested including a membrane fabricated from electro-spun nanofiber, a sheet of polypropylene, a permeable roof underlay material, Tyvek, and four non-woven fabrics used for pillow cases and sacs. The main choice of these materials depends firstly on their prevention to liquid water permeation and secondly on their allowance to water vapor transfer. This makes them good candidates for being used as membranes in a heat and mass exchanger.

2.3.3 Experimental Data and Measurements

A total of 11 experiments were done, such that for every material the test is repeated 2 or 3 times. The conditions upon which the 11 experiments were performed are summarized in table 2.1 along with the results of the decrease in the water content in each cup.

Table 2.1: Input conditions of the different experiments along with the mass of water variation with time

Exp	Duration (h)	Membrane Type	Air average Temp (°C)	Air average RH (%)	Solution Temp (°C)	Decrease in water content (g)
1	6.23	Control	24.6	44	30	14.11
		NWF-1				3.18
		NWF-2				2.86
2	7.4	Control	27.8	41.3	30	15.9
		Tyvek				2.34
		Electrospun nanofiber				2.85
3	6.6	Control	26.1	37.6	30	14.47
		Polypropylene				2.97
		Permeable roof underlay				1.18
4	6.55	Control	27.4	46.7	30	12.01
		Polypropylene				2.4
		NWF-1				2.84
5	6.34	Control	26.8	34.4	30	16.12
		NWF-3				2.78
		NWF-4				3.13
6	6.39	Control	26.3	35.7	30	17.01
		NWF-3				2.95
		Tyvek				2.24
7	7.35	Control	26.8	41.2	30	16.2
		NWF-2				3.22
		Permeable roof underlay				1.19
8	7.1	Control	27.9	36.1	34	19.81
		NWF-1				4.54
		NWF-4				4.08
9	7.18	Control	27	38.5	34	22.72
		Electrospun nanofiber				5.39
		Tyvek				3.43
10	7.06	Control	26.2	42.5	34	21.02
		NWF-1				4.89
		Electrospun nanofiber				4.68
11	6.19	Control	26.6	47.9	34	17.54
		Electrospun nanofiber				4.1
		Polypropylene				3.625

2.3.4 Deduction of Water Vapor Permeability

In the following section the methodology used to infer the water vapor permeability of the tested materials is discussed. The control cup is used to deduce the air side resistance as it is explained in the next paragraph.

2.3.4.1 Control Cup

➢ Measurements

From the periodic experimental measurements, it can be shown that with time there is a decrease in the mass of water inside the cup. The mass variation of water inside the cups as a function of time can be plotted as curve (i) in figure 2.4a. This curve illustrates an example for the evolution of the water content in the control cup of experiment 1.

➢ Numerical model

In the case of the control cup, due to the absence of a membrane, the only resistance is the air resistance. Thus it is used in our experiment to deduce the real value of the mass transfer coefficient of the air which is dependent on the inlet air conditions (temperature, relative humidity and velocity). The mass transfer equation between the air and the water in the control cup is derived and expressed in equation (2.2).

$$h_{Ma}A(Y - Y_w) = \frac{dm}{dt} \tag{2.2}$$

Where h_{ma} is the mass transfer coefficient of air in $\frac{kg}{m^2 s}$, A is the exchange area between the air and the water in m^2, Y is the absolute humidity in $\frac{kg}{kg\ (d.a)}$ and $\frac{dm}{dt}$ is the variation of the mass of water as a function of time in $\frac{kg}{s}$.

By solving equation (2.2) numerically using Modelica language in Dymola software, the curve of the variation of the mass of water as a function of time in experiment 1 is shown by curve (ii) in figure 2.4a.

➢ Deduction of the mass transfer coefficient h_{Ma}

The optimization of the value of h_{Ma} minimizes the error between curve (i) and curve (ii). Then when this error is minimal, this would give the value of the mass transfer coefficient of air h_{Ma} as shown in figure 2.4b.

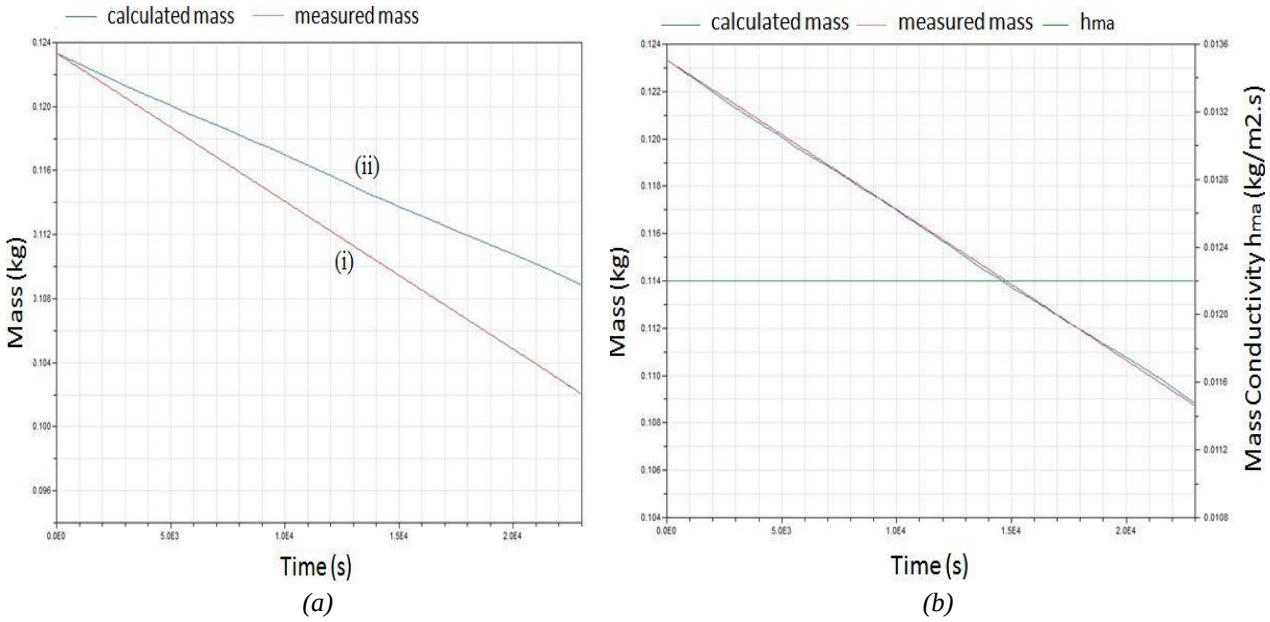

Figure 2.4: a) Variation of the measured mass (i) and calculated mass (ii) of water with respect to time in the control cup, b) mass conductivity of air determined by optimization

2.3.4.2 Cups Covered with Membranes

➢ Measurements

From the periodic experimental measurements, the curve of the mass variation of water as a function of time inside the cup covered with a membrane was plotted. This curve shows a decrease in the water mass inside the cups which is less than the decrease in the control cup. The curve (i) of the change in the water content of the cup covered with NWF-1 in experiment 1 is plotted in figure 2.5.

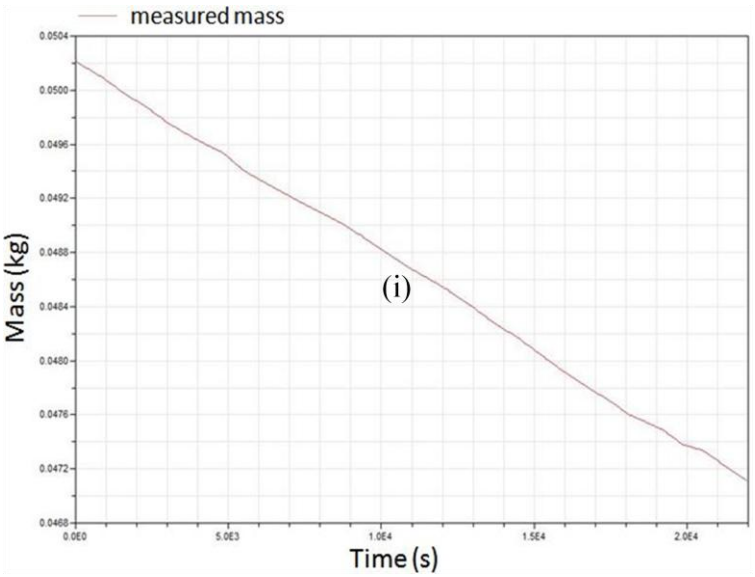

Figure 2.5: Variation of the measured mass (i) of water with respect to time in the cup covered with NWF-1in experiment 1

➢ Numerical model

The cups that are covered with membranes have a small air gap between the membranes and the water and this cavity has a resistance R_c. Figure 2.6 demonstrates the global resistance of the cup with membranes where the surface of the membrane can be considered at the interface of the two fluids.

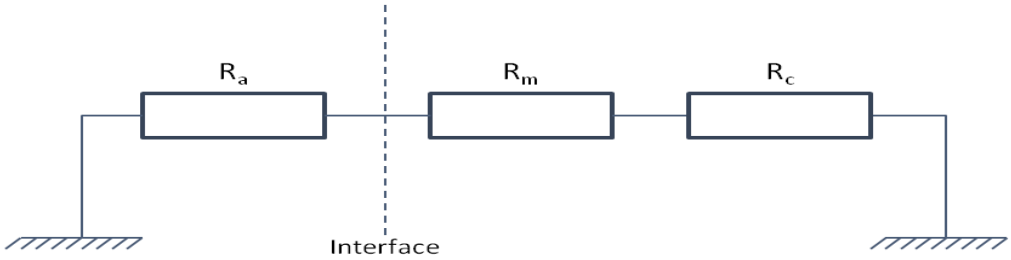

Figure 2.6: Mass conductivity results for all membranes from the 11 experiments

With time the quantity of water inside the pans decreases thus this confined air space increases causing a decrease in its mass conductivity and hence an increase in its resistance. The overall resistance of the system can be represented by equation (2.3).

$$R_{total} = R_a + R_m + R_c = \frac{1}{h_{Ma}} + \frac{\delta}{k_m} + \frac{1}{h_{Mc}} \quad (2.3)$$

Where R is the resistance in $\frac{m^2 s}{kg}$, δ is the thickness of the membrane in m, k_m is the mass conductivity of the membrane in $\frac{kg}{m.s}$ and $h_{Ma}$and h_{Mc} are respectively the mass transfer coefficient of air and of the confined space in $\frac{kg}{m^2 s}$.

➢ Heat and mass transfer in the confined space

In the confined space, the heat and mass transfer that takes place depends on the geometry and the orientation of the surfaces as well as on the thermo physical properties of the fluids involved. The characteristics of the heat transfer depend on whether the upper surface is the cold or the hot surface. If the cold surface is at the bottom and the hot surface is above, then no natural convection takes place since the lighter fluid will always be on top of the heavier fluid (Incropera, 2007); in that case, the mass transfer is purely diffusive. In our case, we have two horizontal surfaces where the lower is a hot surface (hot water) while the upper is a cold surface (membrane in contact with ambient air). The air adjacent to the hotter surface (which is lighter) rises and the air adjacent to the cooler surface (which is heavier) falls setting off a rotational motion that enhances the heat transfer by natural convection between the two surfaces. Therefore, the heat transfer coefficient of the air flowing naturally in the confined space should be calculated from correlations for natural convection between two isothermal surfaces.

➢ Data evaluation of the mass transfer coefficient h_{Mc} inside the confined space

The heat transfer coefficient is related to Nusselt number by the formula

$$Nu = \frac{h_{Tc} L_c}{K_T} \quad (2.4)$$

where h_{Tc} is the heat transfer coefficient of the cavity, K_T is its thermal conductivity and L_c is its characteristic length considered between the membrane and the water given by eq. (2.5)

$$L_c = L_t - L_t(\frac{m}{m_t}) \tag{2.5}$$

With L_t being the total length of the cup (4.3 cm), m the mass of water inside cup at every measurement and m_t the total mass of water in the cup.

The mass transfer coefficient is deduced by using the Lewis analogy

$$h_{Mc} = \frac{h_{Tc}}{C_p\, Le^{\frac{2}{3}}} \tag{2.6}$$

with C_p being the specific heat capacity and Le the Lewis number.

The Nusselt number is expressed as a function of Rayleigh number which in turn is expressed as a function of Grashof and Prandtl numbers. For a horizontal plate that represents an upper surface of a hot plate or a lower surface of a cold plate, the correlation for the Nusselt number is the following (Incropera, 2007):

$$Nu = 1 + 1.44\left[1 - \frac{1708}{Ra}\right] + \left[\frac{Ra^{\frac{1}{3}}}{18} - 1\right] \qquad \text{Ra}<10^8 \tag{2.7}$$

$$Nu = 1 + 1.44\left[1 - \frac{1708}{Ra}\right] \qquad \text{Ra}<5832 \tag{2.8}$$

$$Nu = 1 \qquad \text{Ra}<1708 \tag{2.9}$$

Where $Ra = Gr.\,\mathrm{Pr} = \frac{g\beta(T_{hf}-T_{cf})L_c^3}{\vartheta^2}Pr$ and $\beta = \frac{2}{T_{hf}+T_{cf}}$ is the coefficient of volume expansion in $\frac{1}{K}$, g is the gravitational acceleration in $\frac{m}{s^2}$, T_{hf} and T_{cf} are the temperatures of the surface of the hot and cold fluids in K (in our case they are the temperature of water and air respectively) and ϑ is the kinematic viscosity of the fluid inside the cavity in $\frac{m^2}{s}$.

In our case, the temperature of the hot surface is considered to be equal to the temperature of the water T_w. While the temperature of the cold surface, for more precision, it is considered to be equal to the temperature of the upper side of the membrane T_m which is in contact with the air (and not the temperature of air itself). In order to find T_m the energy or heat conservation equation of the system must be derived and it is expressed in eq. (2.10) with h_{Ta} being the heat transfer coefficient of air.

$$h_{Tc}A(T_w - T_m) = h_{Ta}A(T_m - T_a) \tag{2.10}$$

Therefore, by calculating Rayleigh and Nusselt numbers, the convective heat and mass transfer coefficients in the confined space between the hot water and the membrane can be deduced.

➢ Deduction of k_m

The mass transfer equations of a cup covered with a membrane can be written as:

$$\frac{dm}{dt} = h_{Mc}A(Y_{mw} - Y_w) \tag{2.11}$$

$$h_{Ma}A(Y - Y_{ma}) = \frac{k_m}{\delta}A(Y_{ma} - Y_{mw}) \tag{2.12}$$

$$h_{Mc}A(Y_{mw} - Y_w) = \frac{k_m}{\delta}A(Y_{ma} - Y_{mw}) \tag{2.13}$$

This system is used to solve for the unknowns of this equation that are Y_{ma}, Y_{mw} (the moist air humidity ratio on membrane-air and membrane-water sides) and $k_m$by substituting the value of the previously deduced mass conductivity of air h_{Ma} and cavity h_{Mc} in equations (2.11), (2.12), (2.13). Knowing the thickness of the membrane allows deducing the value of the mass conductivity of each membrane k_m.

Similar to the methodology used for the uncovered cup, we plot the curve (ii) of the calculated mass variation which is deduced from the system of equation as shown in figure 2.7a. Minimizing the error between these two curves allows us to find the mass conductivity of the membrane k_m as illustrated in figure 2.7b.

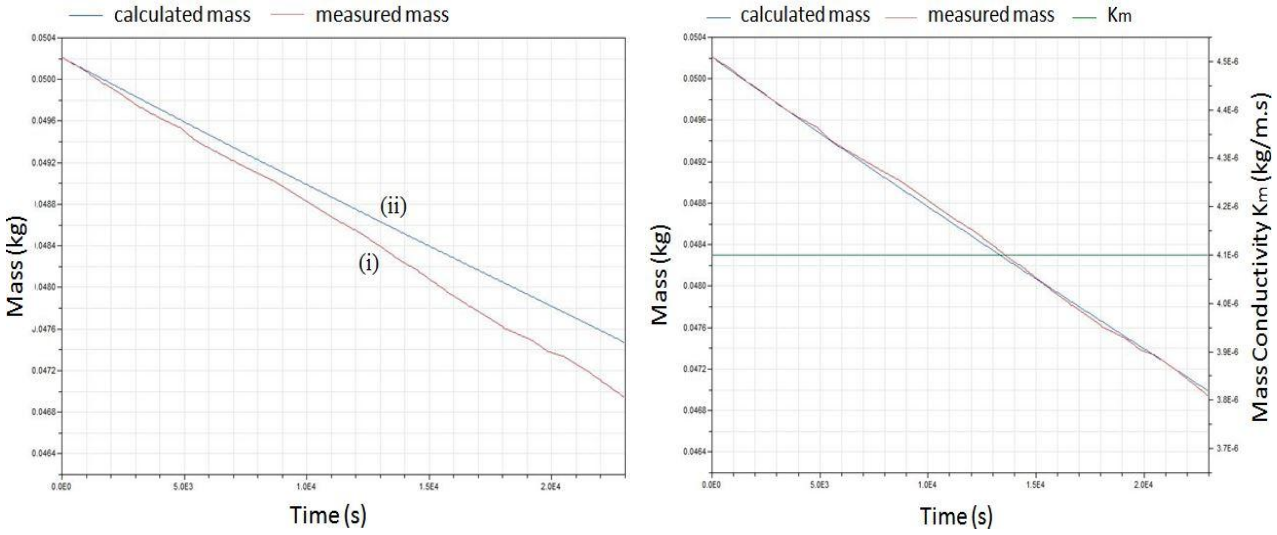

(a) (b)

Figure 2.7: a) Variation of the measured mass (i) and calculated mass (ii) of water with respect to time in a covered up, b) mass conductivity of membrane determined by optimization

2.3.5 Results

Repeating the experiments several times, each time comparing two different membranes, enables us to classify the membranes according to their ability to transport water vapor. Each membrane is tested for between 2 and 3 times and for each test k_m is deduced by the same inverse method. It is necessary to mention that in some of the performed tests, the result value of the conductivity was largely far from the other deduced values for the same membranes. This is probably due to some measurement mistakes caused by accidental water spill. For this reason such results were discarded. The acceptable repeatable values (of all the performed tests) of the mass conductivity

of each membrane are plotted in the graph of figure 2.8 from the highest to the lowest mass conductivity.

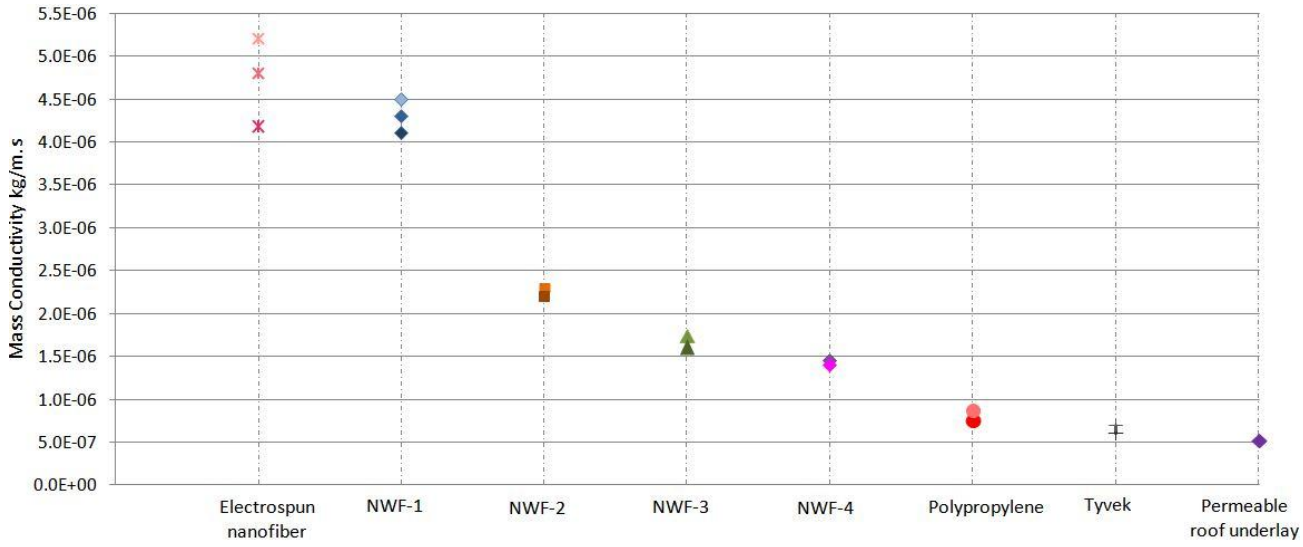

Figure 2.8: Mass conductivity results for all membranes from the 11 experiments

The average value of the mass conductivity of each membrane is then summarized in table 2.2. In this table also we can see the values of the resistance to heat and mass transfer which can be calculated by eq. (2.14). The membranes are classified from the least to the most resistant to heat and mass transfer.

$$R_m = \frac{\delta}{k_m} \tag{2.14}$$

Table 2.2: The thickness, average mass conductivity and mass transfer resistance of all membranes

Membrane Type	**Thickness (m)**	**Mass Conductivity k_m (kg/m.s)**	**Resistance R_m (m^2.s/kg)**
Non-woven fabric-1	1.57E-04	4.30E-06	44
Electrospun nanofiber	2.56E-04	4.49E-06	68
Non-woven fabric-4	9.60E-05	1.43E-06	81
Non-woven fabric-2	1.67E-04	2.25E-06	89
Non-woven fabric-3	1.58E-04	1.68E-06	113
Polypropylene	8.00E-05	8.10E-07	119
Tyvek	1.50E-04	6.40E-07	281
Permeable roof underlay	4.05E-04	5.30E-07	917

2.3.6 Uncertainty Analysis

In order to assess the method's accuracy for determining the membrane mass conductivity, an uncertainty analysis is performed because measurements are never made under perfect conditions, they are always subjected to certain errors and uncertainties (Bell, 1999). Measurement uncertainty is a quantitative indication of the quality of the measurement results and of the confidence range concerning these results. The quality of measuring represents the

accuracy of the results where it defines an interval by which the measured value lies around the true value. These measurements include the air temperature and relative humidity, the water temperature and mass as well as the thickness of the membrane and the diameter of the pan. Many conditions can affect the results of the readings of the measurements. Sometimes the measuring process itself is hard to make like in the case of the mass measurement of the water where the variation is very slow with respect to time. In other cases the measurement instruments can suffer from errors including bias or built in calibration uncertainty that influence the uncertainties of the measurements we take. These different uncertainties produced by each of these sources and other sources would be considered as inputs contributing to the overall uncertainty of the measurements done through the experiment. When different measuring instruments are used as in our experiment, in order to be able to evaluate the overall uncertainty of a certain value some main steps must be taken into consideration (Guimaraes Couto et al., 2013).

2.3.6.1 Methodology

- Definition of the measured and input sources

All the variables that directly or indirectly influence the determination of the measured quantities should be separately identified and they are known as the input sources.

- Modeling

Using the mass transfer equations (2.11), (2.12) and (2.13), the measured values are expressed as a function of the input sources. This phase helps visualize a cause-effect relation by knowing how the input sources affect the measured values.

- Estimation of the uncertainties of the input sources

There are two approaches to estimate uncertainties called ‘type A’ and ‘type B’ evaluation. ‘Type A’ evaluations are done using statistics when a set of several repeated readings is taken. In this case the average value as well as the standard deviation is deduced from these readings. While in ‘type B’ evaluations, the uncertainty is estimated from other information such as from calibration certificates of instruments, from manuals and manufacturer’s specifications or from estimates based on long-term experience.

- Estimation of PDF for the input sources

Estimate and select the most appropriate probability density function (PDF) that presents each of the input quantities. The spread of the set of values can take different forms such as a Gaussian distribution or a rectangular or uniform distribution. In our cases, we consider a typical normal Gaussian distribution where the values are more likely to fall near the mean rather than further away, i.e. 68% of the data falls within one standard deviation of the mean, 95% of the data falls within two standard deviations of the mean and 99.7% of the data falls within three standard deviations of the mean.

- Selection of the best approach for simulation

After all the input PDFs have been defined, one has to choose the best tool or approach to be able to successfully handle the different measurement uncertainties and to provide a reliable result of

the output. One of the most reliable approaches used to estimate the measurement uncertainties is the Monte Carlo method which is adopted in our study for the following reasons (Farrance, 2014):

- It involves the propagation of the distribution of the input sources of uncertainties by using a model to provide the distribution of the output result.
- This method is easy to run, is faster and less tedious than other methods also the results are less subject to distortion.
- It can be successfully applied to cases where complex equations are used or whenever three or more measured variables are required for the uncertainty calculations.
- It effectively handles the probability distribution for each measured value; it allows us to choose any distribution as well as different distributions for different variables.

The Monte Carlo method uses the model to provide output distribution from the propagation of the distributions of input sources of uncertainty as illustrated in figure 2.9. The input quantities are represented by x_1, x_2 and x_3 where $g(x_1)$, $g(x_2)$ and $g(x_3)$ are their distribution functions. The measurand is displayed as y and g(y) is its distribution function (Guimaraes Couto et al., 2013). When propagating distributions, the whole information contained in the input distributions are transmitted to the output. In our case, the model is non linear leading to a non direct relation between the inputs and the output. In such situation, it is possible to run simulations using on the model Monte Carlo method to find the combined standard uncertainty from the different individual ones.

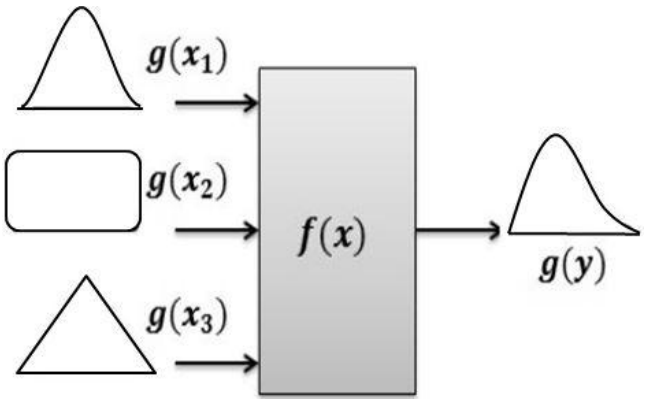

Figure 2.9: Illustrations of the methodologies of propagation of distributions (Guimaraes Couto et al., 2013).

2.3.6.2 Detailed Application of the Input Sources

A detailed application is presented for NWF-1 in experiment 8 where 17 measurements are taken with an average interval of 10 to 15 minutes between each. The Gaussian PDFs of the different inputs are derived and every input source is represented as an array of 17 elements. Then a Monte Carlo approach is adopted where the total number of trials N is taken as 4000 corresponding to the number of simulations done. Several input sources of uncertainty can be considered and they are expressed in the following:

➢ Air Temperature (°C)

The data logger used to measure the input air temperature has a certified value for its temperature ranges, and its calibration certificate states an uncertainty of ±0.3°C at temperature 25°C. For every value of the temperature, a PDF is used where the mean is taken as the value of the measured temperature and the standard deviation is 0.3.

➢ Relative Humidity (%)

The data logger used to measure the air relative humidity has a certificate stating an uncertainty of 2% for a relative humidity measured at 25°C. Every value of the measured relative humidity stands as the mean of the PDF with a standard deviation equal to 2.

➢ Water Temperature (°C)

To measure the temperature of water inside the pans, a thermocouple is used with a certificate stating an uncertainty of ±0.3°C. So similar to the case of the air temperature, the mean of the PDF is the value of the measured temperature and the standard deviation is 0.3.

➢ Mass (kg)

The mass of the water inside the pans is obtained from weighing it periodically by a certified balance so several measured values are taken. The uncertainty associated with the mass using the data from the calibration certificate and the manufacturer's recommendations on uncertainty estimation is ±0.01 g. So the uncertainty of each measured mass is represented by a separate PDF. The mean value of each PDF is taken as the measured mass value with a standard deviation of 10^{-5} kg.

➢ Thickness (m)

The thickness of the membrane is measured repeatedly for 16 times in a digital caliper with a capacity of 150 mm. This source of uncertainty is purely statistical and is classified as being of type A. The PDF that best represents this input source has a mean of 0.157 mm and a standard deviation of $5\ x\ 10^{-6}$ m due to repeatability.

In addition, the caliper used for taking the measurements has a certificate stating an uncertainty of ±0.03 mm. The uncertainty of the thickness due to the calibration of the caliper constitutes another source of uncertainty considered to be as type B involving the same input quantity (thickness). In this case the PDF used to represent this input uncertainty has a mean of zero and standard deviation of $3x10^{-5}$ m. The use of zero as the mean value is a mathematical artifice to take into account the variability due to this source of uncertainty without changing the value of the quantity used in the model. Then the combined PDF of the thickness of the membrane has a mean value of $1.57x10^{-4}$m with a standard deviation of $\sqrt{(5\ x\ 10^{-6})^2 + (3x10^{-5}\ )^2} = 3.04x10^{-5}$m. Figure 2.10a represents the random change by N times of the thickness of the membrane around its mean.

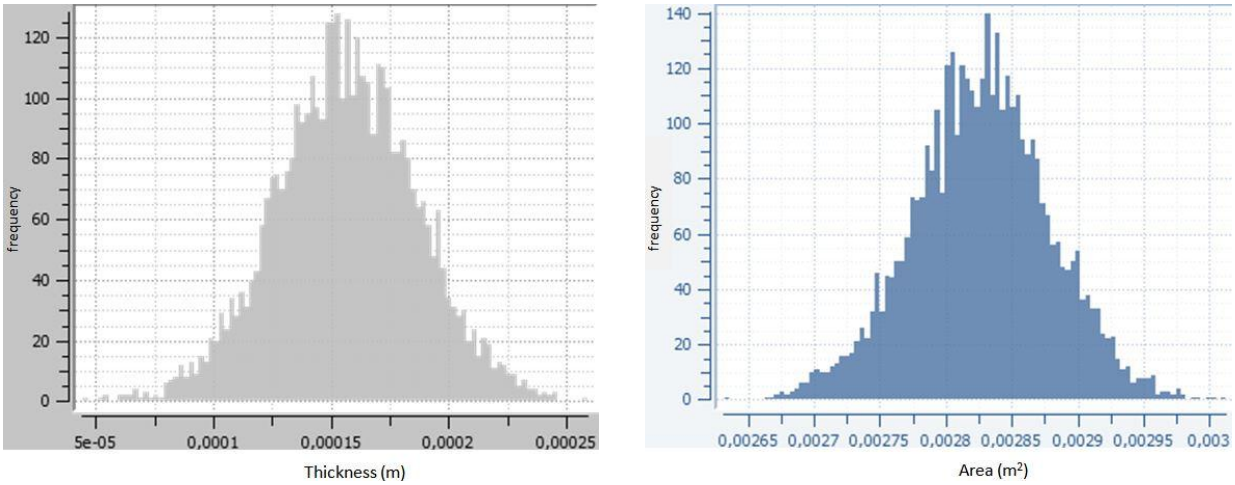

(a) (b)

Figure 2.10: Histogram of a) thickness of the membrane b) exchange surface area

➢ Diameter (m)

The diameter of the pans was measured 16 times as well with the same digital caliper. The mean value is 6 cm with a standard deviation of $5.5x10^{-2}$cm. Then, the PDF of type A has a mean of 0.06 m and a standard deviation of $5.5x10^{-4}$ m. The type B uncertainty of the diameter of the pans is expressed with a mean value of zero and a standard deviation of $3x10^{-5}$ m. Thus the combined PDF of the diameter of the pan has a mean of 0.06 m and a standard deviation of $5.508x10^{-4}$ m.

➢ Area (m^2)

The measurement of the diameter affects the value of the surface area of exchange between the water inside the pan and the air outside. The mean value of the diameter is 0.06 m so the mean value of the area is 0.0028274 m^2. The standard deviation of the diameter is $5.508x10^{-4}$m so that of the area is $5.19x10^{-5}m^2$. Figure 2.10b represents the change by N times of the exchange surface area of the membrane around its mean.

Table 2.3 summarizes the input sources of NWF-1 membrane with the type and PDF distribution of each parameter.

Table 2.3: A summary of the Gaussian PDF for all input uncertainties of NWF-1

Input source	**Type**	**PDF**	**PDF parameters**
Air Temperature (°C)	B	Gaussian	Mean: T[i], std: 0.3°C
Relative Humidity (%)	B	Gaussian	Mean: RH[i], std: 2%
Water Temperature (°C)	B	Gaussian	Mean: T[i], std: 0.3°C
Water mass (kg)	B	Gaussian	Mean: m[i], std: 10^{-5} kg
Thickness (m)			
Due to repeatability	A	Gaussian	Mean: $1.57x10^{-4}$ m, std: $5\ x10^{-6}$ m
Due to certificate	B	Gaussian	Mean: 0 m, std: $3x10^{-5}$ m
Combined	A&B	Gaussian	Mean: $1.57x10^{-4}$ m, std: $3.04\ x10^{-5}$ m
Diameter (m)			
Due to repeatability	A	Gaussian	Mean 0.06 m, std: $5.5\ x10^{-4}$ m
Due to certificate	B	Gaussian	Mean: 0 m, std: :$3x10^{-5}$ m
Combined	A&B	Gaussian	Mean: 0.06 m, std: $5.508\ x10^{-4}$ m
Area (m^2)			
Combined	A&B	Gaussian	Mean: $2.8274x10^{-3}$ m^2, std: $5.19x10^{-5}$ m^2

2.3.6.3 Results

By following the same procedure, the uncertainty study was done for every material considering only one experiment for each. The input uncertainty sources were deduced in each experiment and then the mass conductivity of each membrane was calculated by performing simulations. Dymola was controlled through Python and the simulation were run 4000 times while substituting the actual values of the air temperature and relative humidity, the water temperature, the measured mass, the thickness of each membrane and the exchange area by their previously determined Gaussian PDFs. The simulation for one experiment gave 4000 values of the mass conductivity of the membrane k_m. $k_{m,mean}$ the mean for these values with its standard deviation std was determined then the percentage uncertainty was calculated by the eq. (2.15). Table 2.4 gives the values of the output uncertainties of the different membranes.

$$u = \frac{std}{k_{m,mean}} * 100 \qquad (2.15)$$

Table 2.4: Percentage uncertainty for the tested membranes

Membrane Type	std **(kg/m.s)**	$k_{m,mean}$ **(kg/m.s)**	**Uncertainty (%)**
Non-woven fabric-1	7.84E-07	4.30E-06	18.23
Electrospun nanofiber	8.17E-07	4.49E-06	15.41
Non-woven fabric-4	3.93E-07	1.43E-06	26.23
Non-woven fabric-2	2.78E-07	2.25E-06	12.64
Non-woven fabric-3	3.29E-07	1.68E-06	21.98
Polypropylene	1.43E-07	8.10E-07	16.86
Tyvek	8.43E-08	6.40E-07	14.05
Permeable roof underlay	4.14E-08	5.30E-07	7.96

The values of the mass conductivities of the membranes with their standard deviations are shown on the graph of figure 2.11. They are plotted in decreasing order of mass conductivity. From this

graph we can observe that even if the uncertainty on the mass conductivity is relatively high, yet the classification of the membranes by decreasing order of permeability would not change remarkably.

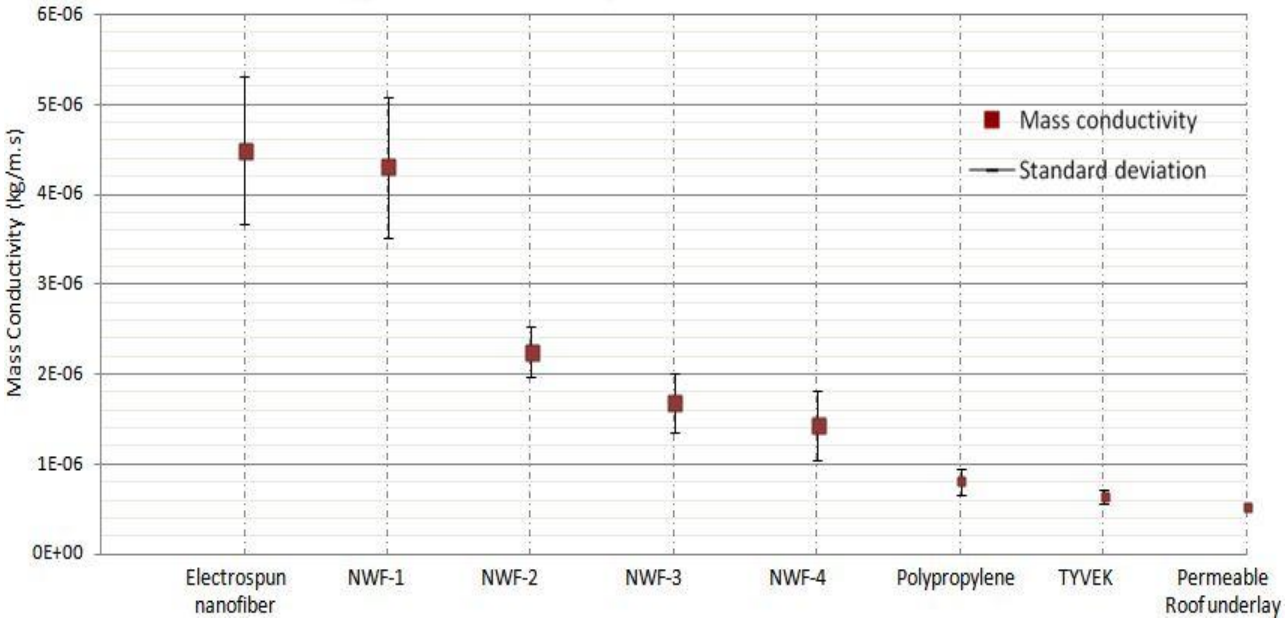

Figure 2.11: Mass conductivities of the different membranes with their error distribution

2.4 Conclusion

Water vapor permeability is the main property of membranes that influences its capacity of mass transfer. In this chapter different possible low cost materials that are initially manufactured for considerations other than operating as membranes were identified. These materials were tested experimentally using a modified cup test and an inverse methodology in order to find out their water vapor permeability. In this methodology we succeeded to deduce explicitly the value of the resistances at the air above the cups and of the air trapped between the water and the fabric. By substituting these values in the system of mass equations, the mass conductivities of the materials were determined. These values ranged from $5.3\text{x}10^{-7}$ to $4.49\text{x}10^{-6}$ kg/m.s. Thus measuring, analyzing and then interpreting the results for the different materials allow us to classify and compare the mass transfer capacity of each. Then an uncertainty analysis was performed to assess the accuracy of this approach and Monte Carlo method was used to evaluate the uncertainty propagation. The practical use of Monte Carlo simulations on the estimation of uncertainties has proved to be a fundamental tool in this area, being able to address complex measurement problems. The results showed that the uncertainty values varied from around 8% to 26%. These figures, although not considered low enough, yet, didn't bring a change to the classification of the tested fabrics by order of the water vapor permeability. In later steps, an analysis of the impact of the uncertainty of the mass conductivity on the total power of the heat and mass exchanger is going to be performed. This would give an idea whether these large uncertainty values on k_m have a great effect on the numerical results of the performance of the exchanger or not. In this chapter we were able to classify highly permeable materials and the ones

with a high mass conductivity (low resistance to heat and mass transfer) and possessing the characteristics of being permeable to vapor, impermeable to liquid and capable to withstand water pressure can be employed as membranes in heat and mass exchangers. As per our results, the membrane made of electrospun nanofiber seemed to have the highest mass conductivity among the tested membranes; it is a potential good candidate for our exchanger. However, it is produced by a novel fabrication technique whereas the non-woven fabrics are widely available. Thus in the coming chapter, NWF-1, having the lowest resistance to mass transfer and possessing the required enduring properties, is employed as a membrane in our prototype of a liquid to air cross flow heat and mass exchanger.

Chapitre 3 Modélisation de l'échangeur de chaleur et de masse et validation expérimentale (résumé)

3.1 Introduction

Les échangeurs membranaires de chaleur et de masse ont été étudiés en profondeur et ont prouvés leurs efficacités dans les applications de déshumidification de l'air par une solution desicante liquide. Des études numériques et expérimentales réalisées antérieurement ont révélé que le taux d'absorption de l'humidité et divers niveaux de performances des échangeurs membranaires de chaleur et de masse dépendent essentiellement des conditions opératoires et de la perméabilité de la membrane. Comme démontré dans le chapitre précédent, l'emploi de la NWF-1 serait favorable parce qu'elle a des propriétés structurelles convenable, possède l'une des conductivités massiques les plus élevées et a le coût de fabrication le plus faible. Ainsi, dans ce chapitre, NWF-1 est utilisé dans un prototype avec un nouveau concept d'échangeurs membranaires de chaleur et de masse. Ce prototype proposé et soumis à une caractérisation expérimentale.
Lorsque le liquide qui passe à l'intérieur des canaux est une solution de dessiccant, il est essentiel qu'aucun contact direct avec l'air ne soit autorisé pour éviter les entrainements qui causent des problèmes de corrosion. Dans notre banc d'essai, pour des applications plus simples et sans risque, au lieu d'une solution dessiccante, le liquide pulvérisé à l'intérieur des canaux est de l'eau. Plusieurs expériences sont menées pour évaluer la performance de cet échangeur en tenant compte des différentes conditions d'entrée. Afin de prédire son comportement, un modèle mathématique détaillé en 2-D est développé et écrit en langage Modelica en utilisant le logiciel Dymola. Les équations de transfert d'énergie et de masse sont dérivées, puis discrétisées et résolues à l'aide d'une approche en volume fini en régime permanent. Les simulations sont effectuées et la validité du modèle est vérifiée par confrontation avec les données expérimentales. Par la suite, une analyse de l'incertitude est effectuée sur les valeurs expérimentales et numériques à l'aide de la méthode Monte Carlo. Une compatibilité acceptable des résultats expérimentaux et numériques démontrerait alors que le modèle peut être utilisé pour prédire la performance d'un tel échangeur.

3.2 Description du banc d'essai

Le prototype est un échangeur membranaire de chaleur et de masse à flux croisés (air-liquide), de forme rectangulaire, en acier inoxydable et composé de 15 canaux contenant du liquide. Au fond, un réservoir initialement rempli d'un liquide et dont le volume est d'environ 0,1 m3 est placé. Chaque canal a une largeur de 2 cm, une profondeur et une hauteur de 40 cm chacune et il est recouvert des deux côtés de la membrane choisie. La distance entre deux canaux consécutifs correspondant à la largeur du canal de circulation de l'air est également de 2 cm. Ainsi, la largeur totale de l'échangeur avec un cadre en acier de 5 cm (2,5 cm de chaque côté) est de 67 cm. La hauteur et la profondeur de l'échangeur (y compris l'épaisseur du cadre en acier) sont de 45 cm chacune (fig.1).

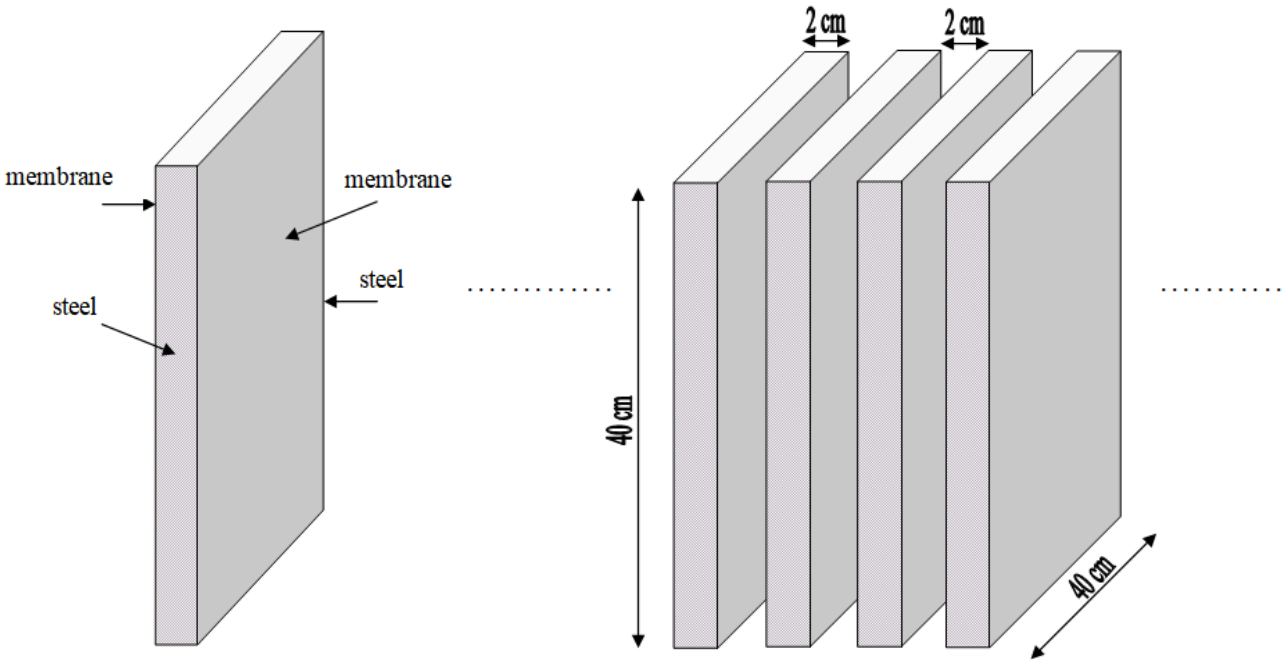

(a) (b)

Figure 12: a) Un canal recouvert d'une membrane, b) Quatre canaux consécutifs de l'échangeur et leurs dimensions

Les buses, de type compact, sont en laiton pour éviter la corrosion lorsque la solution dessiccante les traverse. Elles sont choisies avec un angle de pulvérisation le plus élevé, 120°, pour assurer une couverture maximale du canal grâce à une répartition du liquide uniforme et parabolique ("buses à jet plat", n.d.). Le débit volumique de liquide admissible varie de 0,71 à 2,24 l/min quand la pression de la buse passe de 1 à 10 bars.

3.2.1 Circuits de liquide et d'air

Le liquide, qui coule verticalement entre les canaux, sort de l'échangeur à travers un conduit en forme d'entonnoir et est ensuite recueilli dans le réservoir. L'air quitte l'échangeur directement dans la pièce, sans un conduit, en raison des contraintes d'espace.

Lorsque la solution chaude est pompée vers l'échangeur, elle passe par un distributeur qui alimente les buses avant d'être pulvérisée. Dans ce distributeur, un purgeur d'air et un capteur de pression sont placés. Le premier sert à assurer une bonne évacuation de l'air et le second à mesurer la pression du liquide dans le système. Ensuite, la solution est pulvérisée verticalement par les buses à l'intérieur de chaque canal et, après une certaine distance, un mince film de solution commence à se former sur les membranes des deux côtés du canal. Un filtre fin est placé dans le circuit liquide avant la voie d'évacuation pour éliminer les impuretés présentes qui pourraient bloquer les buses. La solution est collectée dans le réservoir sous l'échangeur. Un échange de chaleur et de masse a lieu entre ces deux flux. Un débitmètre est situé après la pompe afin de mesurer le débit de la solution circulant dans le système. L'air ambiant est soufflé entre les canaux, grâce à un ventilateur, perpendiculairement au flux liquide. Un anémomètre est utilisé pour mesurer la vitesse de l'air; le débit d'air est calculé en multipliant cette vitesse par la surface considérée.

Les figures 2 et 3 montrent une vue de profil et une vue de face du schéma représentant le banc d'essai respectivement.

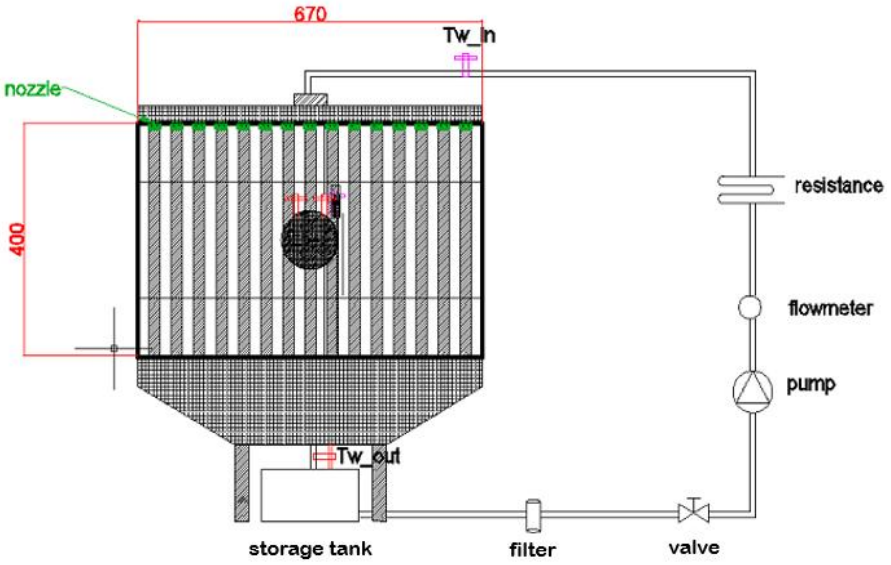

Figure 13: Dessin du banc d'essai du point de vue avant

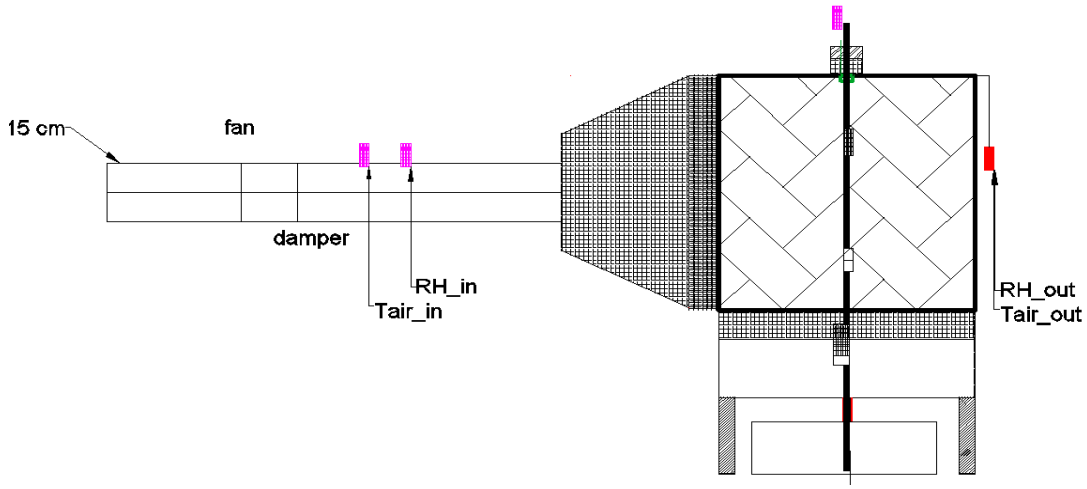

Figure 14: Dessin du banc d'essai du côté gauche

3.3 Expériences

Afin de déterminer la performance de cet échangeur en terme de transfert de chaleur, on mesure les températures d'entrée et de sortie de l'air ainsi que de la solution. En plus, pour déterminer la masse de vapeur transférée, la variation de la quantité d'eau dans l'air a été calculée en mesurant l'humidité de l'air entrant et sortant. C'est pourquoi des thermocouples et des hygromètres sont nécessaires pour mesurer la température et l'humidité relative de l'air entrant et sortant. Lorsque la différence entre la température de la solution et celle de l'air augmente, le transfert de chaleur et de masse augmente à cause de l'augmentation de la différence de pressions de vapeur entre les deux fluides. Dans le cas où la température de la solution est supérieure à celle de l'air, comme c'est le cas pour nos expériences, la direction suivie par le flux de vapeur d'eau est de la solution

vers l'air. L'air devrait ainsi quitter l'échangeur chargé de vapeur d'eau avec une humidité absolue plus élevée. Les hygromètres et les thermocouples sont reliés à un système d'acquisition de données.

Le banc d'essai est démarré et après environ 30 minutes du début de l'expérience, la température de l'air de sortie et son humidité relative deviennent stables, ce qui indique que l'état d'équilibre est atteint. Ensuite, des mesures sont prises pendant un intervalle de 20 minutes. Au total, 18 expériences ont été réalisées sur l'échangeur. L'eau a été injectée dans les buses au lieu de la solution dessiccante pour plus de facilité et sans risque. Deux séries d'expériences sont réalisées; l'une à basse vitesse avec le volet du ventilateur partiellement ouvert et l'autre à pleine vitesse. Le ventilateur entrainait un débit d'air d'environ 330 m^3/h à basse vitesse et de 690 m^3/h à grande vitesse. Pour chaque série, 9 expériences ont été effectuées à chaque fois en modifiant le débit massique de l'eau (le débit le plus faible était de 4,5 l/min et le plus élevé de 9,1 l/min). Pour les valeurs supérieures à 9,1 l/min, la différence de température entre l'eau d'entrée et l'eau de sortie ne serait pas très significative et l'incertitude de mesure influencerait donc fortement nos résultats. L'air d'entrée est l'air ambiant; sa température et son humidité relative sont mesurées en continu. La température de l'eau d'entrée est fixée, mais elle est affectée par les fluctuations de la résistance. Pour cela elle est mesurée également de façon continue et les valeurs sont enregistrées par le système d'acquisition de données. Les paramètres qui sont modifiés d'une expérience à une autre sont principalement les débits d'entrée d'air et d'eau. Le tableau 1 récapitule les expériences sur leurs conditions:

Tableau 2: Conditions initiales d'entrée de chaque expérience

Experiment	$\dot{m}_a$ (m^3/h)	$\dot{m}_w$ (L/min)	T_a $(°C)$	RH_a (%)	T_w $(°C)$	Pressure at nozzle (bars)
Exp 1	20.7	4.5	24.3	85.6	38.7	0.79
Exp 2	20.7	5.3	26.8	71.7	44.0	0.86
Exp 3	20.7	6	25.5	78.9	39.3	0.95
Exp 4	20.7	6.6	27.0	76.2	42.3	1
Exp 5	20.7	7.3	26.0	78.1	38.7	1.11
Exp 6	20.7	7.7	26.6	77.3	40.1	1.18
Exp 7	20.7	8.2	27.1	78.7	38.9	1.25
Exp 8	20.7	8.7	26.4	77.3	39.0	1.33
Exp 9	20.7	9.1	26.4	81.7	36.9	1.4
Exp 10	43.2	4.5	29.2	70.6	45.1	0.79
Exp 11	43.2	5.3	29.2	72.0	43.0	0.86
Exp 12	43.2	6	29.2	72.0	41.4	0.95
Exp 13	43.2	6.6	29.2	72.3	40.0	1
Exp 14	43.2	7.3	28.9	77.9	40.2	1.11
Exp 15	43.2	7.7	28.0	82.1	38.3	1.18
Exp 16	43.2	8.2	29.0	76.6	38.5	1.25
Exp 17	43.2	8.7	28.9	74.9	37.9	1.33
Exp 18	43.2	9.1	28.8	72.8	37.3	1.4

Dans les expériences 1 à 4 et 10 à 13, la pression à une buse est inférieure à 1 bar et, par conséquent, comme nous l'avons vu plus haut, le jet n'est pas uniformément réparti sur le canal et les canaux ne sont pas entièrement couverts par l'eau. Ainsi, ces expériences sont retirées de notre analyse.

3.4 Modèle

Afin de prédire le comportement de l'échangeur utilisé dans notre banc d'essai, un modèle mathématique détaillé en 2-D est développé et codé en langage Modelica en utilisant le logiciel Dymola pour un échangeur de chaleur et de masse à membrane à flux de liquide et d'air croisés. Des équations de bilans d'énergie et de masse ont été dérivées, puis discrétisées et résolues en utilisant une approche en volumes finis en régime permanent.

Le modèle est composé de 16 sous-modèles associés au nombre de canaux d'air. La figure représente l'échangeur avec 15 canaux liquides entourés de 16 canaux d'air. Sur la figure, nous pouvons remarquer que, depuis le canal d'air numéro 2 au canal d'air numéro 15, il y a un échange entre deux demi-canaux de liquide et deux demi-canaux d'air (fig.4). En ce qui concerne les premier et dernier canaux d'air (canaux d'air 1 et 16), l'échange a lieu entre chacun de ces canaux d'air et la moitié adjacente du canal liquide. Nos 16 sous-modèles sont divisés en conséquence ; le premier et le dernier modèle représentent un échange entre un canal d'air et la moitié d'un canal liquide tandis que tous les autres représentent un échange entre un canal d'air et un canal liquide.

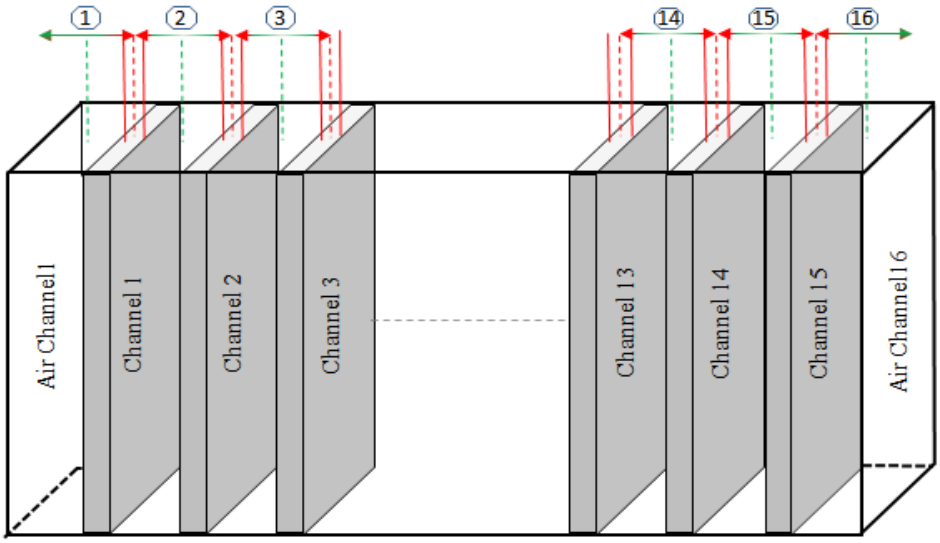

Figure 15: Section de l'échangeur avec 15 canaux liquides

Le modèle discrétise les équations; chacun des axes x et z a été discrétisé en segments de tailles égales. Au début, le modèle a été écrit pour prédire l'échange entre un dessiccant liquide et l'air. Cependant, comme dans notre banc d'essai, le liquide pulvérisé est de l'eau, et afin de refléter le cas réel, le modèle proposé a été réécrit en tenant compte des propriétés de l'eau avec des équations de transfert de masse et d'énergie modifiées du côté liquide.

La surface de la membrane était représentée par une série de points du maillage et son domaine est discrétisé en cellules de mailles égales. Nos volumes de contrôle sont choisis pour être identiques aux cellules du maillage et des points nodaux sont utilisés à l'intérieur de ces volumes de contrôle pour interpoler les variables de la zone. Trois méthodes de calcul sont proposées pour approximer les valeurs de ces quantités nodales.

➢ 1ere méthode

Dans la première méthode, les valeurs des quantités nodales liées aux paramètres de l'air sont calculées compte tenu de l'interface de surface ouest d'un volume de contrôle général (i,j) et celles liées à la solution sont calculées compte tenu de l'interface de surface nord (fig.5).

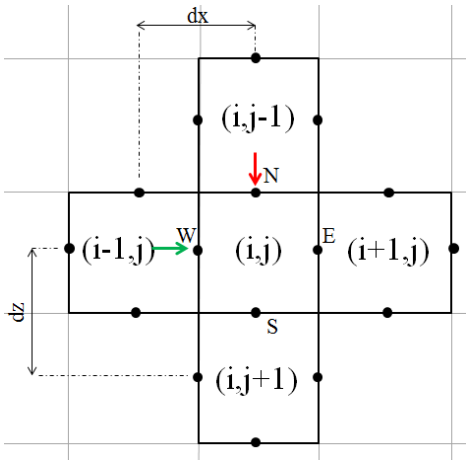

Figure 16: Représentation des quantités nodales de la grille de la première méthode

➢ 2ème méthode

Dans le deuxième méthode, les valeurs des quantités nodales liées aux paramètres de l'air sont calculées en tenant compte de l'interface de surface est d'un volume de contrôle général (i,j) et celles liées à la solution sont calculées en tenant compte de l'interface de surface sud (fig.6).

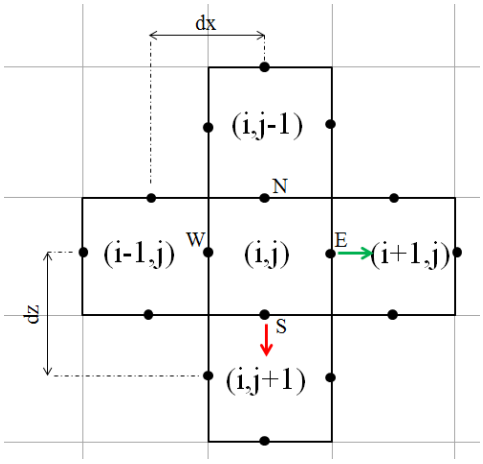

Figure 17: Représentation des quantités nodales de la grille de la deuxième méthode

➢ 3ème méthode

Quant à la troisième méthode, pour une modélisation plus précise, les valeurs des quantités nodales sont considérées comme des valeurs moyennes des deux premières configurations. Les

quantités nodales liées aux paramètres de l'air sont calculées en tenant compte de la moyenne à l'interface des surfaces ouest et est d'un volume de contrôle général (i,j) et celles liées à la solution sont calculées en tenant compte de la moyenne à l'interface des surfaces nord et sud (fig.7).

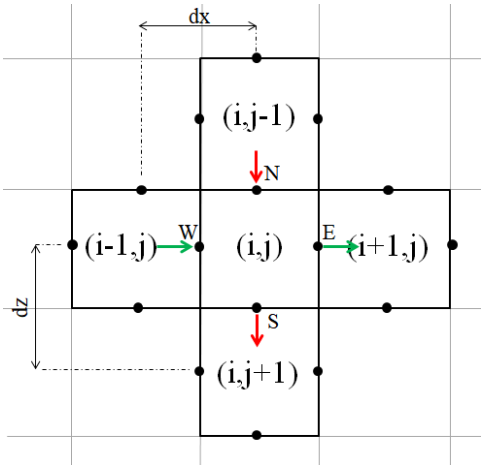

Figure 18: Représentation des quantités nodales de la grille de la troisième méthode

Les équations de l'énergie et de la masse ont été calculées pour chaque méthode et on les montre pour la troisième comme suit :

a) Air

➢ Équation de conservation de masse pour la vapeur d'eau

$$\dot{m}_{da}\frac{dz}{Z}(Y[i+1,j]-Y[i,j]) + 2A_a\left(\frac{U_M[i,j]+U_M[i+1,j]}{2}\right)\left(\frac{Y[i,j]+Y[i+1,j]}{2} - \frac{Y_s[i,j]+Y_s[i,j+1]}{2}\right)=0 \quad (1)$$

➢ Équation de conservation de l'énergie pour l'air humide

$$\dot{m}_{da}\frac{dz}{Z}\left(\frac{C_{p,da}[i,j]+C_{p,da}[i+1,j]}{2} + \left(\frac{C_{p,v}[i,j]+C_{p,v}[i+1,j]}{2}\right)\left(\frac{Y[i,j]+Y[i+1,j]}{2}\right)\right)(T_a[i+1,j]\text{ - } + 2A_a\left(\frac{h_{Ta}[i,j]+\ h_{Ta}[i+1,j]}{2}\right)\left(\frac{T_a[i,j]+T_a[i+1,j]}{2} - \frac{T_{ma}[i,j]+T_{ma}[i+1,j]}{2}\right)=0 \quad (2)$$

b) Solution

➢ Équation de conservation de masse pour l'eau liquide

$$\dot{m}_d \frac{dx}{L}(X[i,j+1]-X[i,j]) - 2A_a\left(\frac{U_M[i,j]+U_M[i+1,j]}{2}\right)\left(\frac{Y[i,j]+Y[i+1,j]}{2} - \frac{Y_s[i,j]+Y_s[i,j+1]}{2}\right)=0 \quad (3)$$

➢ Équation de conservation de l'énergie pour l'air humide

$$\dot{m}_d \frac{dx}{L}(1+X[i,j+1])\left(\frac{C_{p,s}[i,j]+C_{p,s}[i,j+1]}{2}\right)(T_s[i,j+1]-T_s[i,j]) - 2A_a\left(\frac{U_M[i,j]+U_M[i+1,j]}{2}\right)\left(\frac{h_{fg}[i,j]+h_{fg}[i,j+1]}{2}\right)\left(\frac{Y[i,j]+Y[i+1,j]}{2} - \frac{Y_s[i,j]+Y_s[i,j+1]}{2}\right) + 2A_s\left(\frac{h_{Ts}[i,j]+h_{Ts}[i,j+1]}{2}\right)\left(\frac{T_s[i,j]+T_s[i,j+1]}{2} - \frac{T_{ms}[i,j]+T_{ms}[i,j+1]}{2}\right) = 0 \quad (4)$$

c) Membrane

➢ Équation de conservation de l'énergie

$$A_a\left(\frac{h_{Ta}[i,j]+h_{Ta}[i+1,j]}{2}\right)\left(\frac{T_a[i,j]+T_a[i+1,j]}{2} - \frac{T_{ma}[i,j]+T_{ma}[i+1,j]}{2}\right) - \frac{K_{T,m}}{\delta}A_m\left(\frac{T_{ma}[i,j]+T_{ma}[i+1,j]}{2} - \frac{T_{ms}[i,j]+T_{ms}[i,j+1]}{2}\right) = 0 \quad (5)$$

$$A_s\left(\frac{h_{Ts}[i,j]+h_{Ts}[i,j+1]}{2}\right)\left(\frac{T_s[i,j]+T_s[i,j+1]}{2} - \frac{T_{ms}[i,j]+T_{ms}[i,j+1]}{2}\right) + \frac{K_{T,m}}{\delta}A_m\left(\frac{T_{ma}[i,j]+T_{ma}[i+1,j]}{2} - \frac{T_{ms}[i,j]+T_{ms}[i,j+1]}{2}\right) = 0 \quad (6)$$

Où $dx = \frac{L}{Ni}$ et $dz = \frac{Z}{Nj}$ et le coefficient global d'échange de masse est défini entre le flux d'air humide et l'interface membrane-solution par les éléments suivants:

$$U_M = (\frac{1}{h_{Ma}} + \frac{\delta}{k_m} + \frac{1}{h_{Ms}})^{-1} \quad (7)$$

avec h_{Ma} et h_{Ms} les coefficients de transfert de masse de l'air et de la solution respectivement, calculés à l'aide de corrélations mathématiques entre le nombre Nusselt et les coefficients de transfert de chaleur.

Les trois méthodes d'approximation peuvent être utilisées pour calculer les équations de masse et d'énergie qui accompagnent le transfert de masse et de chaleur dans les échangeurs de contact indirects. Par la suite, une analyse de sensibilité est effectuée sur le modèle représentant l'échangeur de banc d'essai pour comparer ces trois approches et vérifier leur précision.

3.4.1 Coefficients de transfert de chaleur

Pour les coefficients de transfert de chaleur et de masse de l'eau et de l'air utilisés dans le modèle, une analyse de sensibilité a été réalisée pour déterminer la corrélation la plus fiable.

- Côté air

Pour le côté air, afin de déterminer les caractéristiques du flux dans les deux cas : écoulement développé et se trouvant encore dans la région d'entrée de la phase de développement, une évaluation des conditions aux limites a été effectuée. Il a ensuite été démontré que, pour les expériences effectuées à basse vitesse, le débit d'air se trouvait toujours dans la région d'entrée hydrodynamique où le profil de vitesse changeait constamment. Par suite, la corrélation suggérée par (Sieder et Tate, 1936) est utilisée pour calculer le coefficient de transfert de chaleur de l'air.

$$Nu_l = 1.86\, \tau^{-\frac{1}{3}} \left(\frac{\mu}{\mu_p}\right)^{0.14} \quad (8)$$

où $\tau = \frac{l}{D.Re_D.Pr}$ et $\frac{\mu}{\mu_p}$ est le rapport de la viscosité globale par rapport à la viscosité près de la paroi. Cette corrélation est valide pour $0.48 < Pr < 16.7$.

Pour les expériences effectuées à haute vitesse, l'écoulement devient turbulent entièrement développé à une distance de 20 cm Pour les flux turbulents, pour tenir compte des coefficients dans un régime transitoire non entièrement développé Hausen a proposé l'ajout d'un facteur de correction à la corrélation donnée par Gnielinski. Il suggère de multiplier l'équation par $(1 + \left(\frac{D}{L}\right)^{\frac{2}{3}})$ en tenant compte de la région d'entrée. D'après les travaux précédents effectués par (Dirker et al., 2017), ce facteur a ensuite été modifié pour mieux prédire leurs résultats expérimentaux et devenir $(1 + \left(\gamma \frac{D}{L}\right)^{\frac{2}{3}})$où $\gamma = \frac{34{,}500}{Re}$. Ensuite, le nombre de Nusselt modifié est donné par l'équation suivante :

$$Nu = \frac{\left(\frac{ff}{8}\right)(Re - 1000)\, Pr}{1 + 12.7\left(\frac{ff}{8}\right)^{\frac{1}{2}}(Pr^{\frac{2}{3}} - 1)} (1 + \left(\gamma \frac{D}{L}\right)^{\frac{2}{3}}) \quad (9)$$

- Côté liquide

Différentes corrélations ont aussi été discutées pour le coefficient de transfert de chaleur coté eau. Toutefois, aucune d'entre elles n'a pu vraiment refléter le cas présenté dans notre banc d'essai. Les corrélations disponibles relatives aux jets considèrent que le jet est perpendiculaire à une surface horizontale alors que, dans notre cas, le jet est plat et parallèle à la surface des membranes. Ainsi, notre recherche a été étendue pour examiner les corrélations des films tombants. Cependant, en réalité, même un film tombant ne représente pas totalement l'écoulement dans notre échangeur. En effet, chaque fois qu'une buse fonctionne dans une plage de pression inférieure à la plage optimale, l'eau ne serait pas entièrement distribuée avec un angle de 120°, ce qui résulte en une configuration de pulvérisation indésirable. Dans ce cas, le flux ne doit pas être considéré comme un film puisqu'il est encore divergent et que le canal n'est pas complètement couvert par la pulvérisation. Par conséquent, une comparaison de l'ordre de grandeur entre les corrélations liées aux jets et celles liées aux films tombants a été effectuée afin de vérifier les différences entre elles et de décider laquelle choisir et utiliser dans notre modèle. L'étude de l'effet des valeurs du coefficient de transfert de chaleur du coté eau sur la puissance totale de l'échangeur a montré que les corrélations sont du même ordre de grandeur. La corrélation donnée par (Zhu, 2013) a été choisie vu qu'elle a fourni une valeur moyenne parmi les corrélations examinées.

$$Nu = 0.36\, Re^{0.55}\, Pr^{\frac{1}{3}} \tag{10}$$

où $Re = \frac{\rho v D_e}{\mu}$ et D_e étant le diamètre latéral équivalent en m.

3.4.2 Comparaison des trois méthodes d'estimation des propriétés

Après avoir trouvé les paramètres nécessaires pour résoudre les équations d'énergie et de masse, les trois méthodes sont comparées par leur précision, le temps nécessaire pour une simulation et la façon dont ils sont affectés par certains paramètres de modélisation. Pour cette comparaison, la puissance de sortie est calculée pour chaque méthode en modifiant la discrétisation du modèle.

La création et la sélection de la taille de la discrétisation dans le modèle est une étape importante, car pendant les simulations, le maillage est considéré comme le facteur le plus consommateur de mémoire. Ainsi, le choix d'un nombre commode de maillage peut contribuer à réduire les besoins en mémoire et à réduire le temps de calcul nécessaire à une simulation. D'autre part, l'abaissement du nombre de maillages peut affecter la précision des résultats numériques de notre modèle. Un maillage pratique garantit un résultat numérique plus précis, tandis qu'un maillage insuffisant affecte la convergence de la solution. Afin de trouver un nombre acceptable de maillages par lesquels il existe un compromis entre la précision du modèle et les restrictions de mémoire et de temps, une analyse de sensibilité est effectuée. Cela se fait en simulant plusieurs fois les modèles des trois méthodes, en ne modifiant que le nombre de maillages Ni et Nj dans chacun des modèles. L'étude se concentre sur la puissance totale de l'échangeur et examine sa variation avec l'augmentation de Ni et Nj de 5 à 40 par pas de 5 à chaque fois. Cette étude donne une idée de l'effet de la modification de la taille du maillage sur les résultats numériques

concernant la puissance totale de l'échangeur côté eau, comme le montre la figure 3.12. Le graphique montre que les 3 courbes représentant la puissance de l'échangeur commencent à devenir plus plat à l'approche d'une asymptote quand le nombre de mailles augmente,. Quant aux très petites valeurs de Ni et de Nj, ces valeurs sont loin de leur valeur asymptotique. On peut aussi remarquer que la différence de puissance totale calculée par les trois méthodes diminue à mesure que le nombre de mailles augmente. Pour les premiere et deuxième méthodes, nous remarquons une différence de puissance remarquable avec le nombre de mailles qui change. Ce n'est qu'après Ni=Nj=25 que la puissance commence à approcher la valeur asymptotique. Alors que pour la troisième méthode, les valeurs sont presque les mêmes pour toutes les valeurs Ni et Nj.

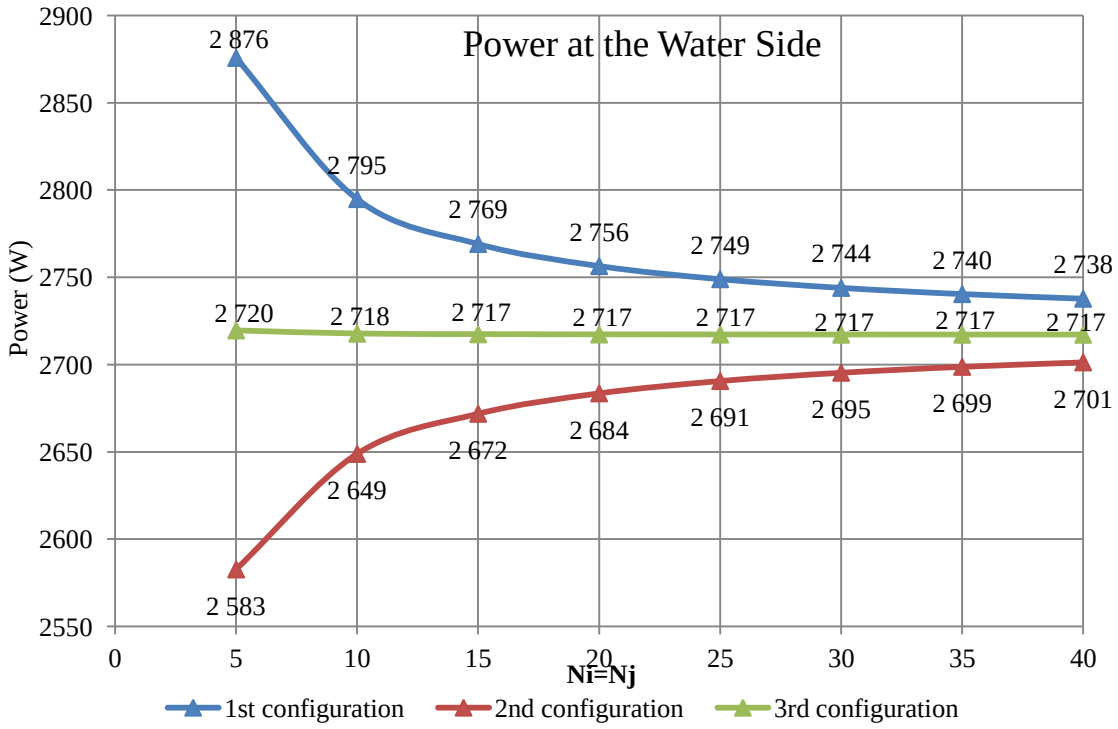

Figure 19: Variation de la puissance des 3 méthodes en fonction de la discrétisation du modèle

Les résultats de cette étude prouvent l'exactitude de la troisième méthode par rapport aux deux autres. On peut aussi remarquer clairement que la troisième méthode est la moins affectée par la modification du nombre de mailles dans le modèle. Cependant, cette méthode pourrait être la plus lente.

L'objectif de cette analyse de sensibilité est de sélectionner le nombre de mailles Ni et Nj de façon à obtenir une précision numérique acceptable avec une vitesse de simulation optimisée. Dans notre cas, il est très important de trouver un équilibre entre ces deux paramètres. La complexité du modèle consomme une grande partie de la capacité du processeur et provoque une simulation à faible vitesse. Les simulations réalisées précédemment sont exécutées pour différents Ni et Nj et le temps réel nécessaire à chaque simulation pour un nombre donné de mailles est calculé comme le montre la figure 3.13. D'après le graphique, le temps de simulation

varie légèrement entre les trois méthodes et le temps nécessaire pour effectuer une simulation varie de façon exponentielle avec l'augmentation du nombre de mailles. À Ni=10, les valeurs de la puissance varient entre 2 649 W et 2 795 W tandis que celles du temps varient entre 40 s et 55 s respectivement. Alors qu'à Ni=25, les valeurs de la puissance varient entre 2691 W et 2749 W tandis que celles du temps varient entre 645 s et 694 s respectivement. À mesure que Ni et Nj augmentent la différence en pourcentage de puissance diminue, mais le temps requis pour chaque simulation augmente en grande partie.

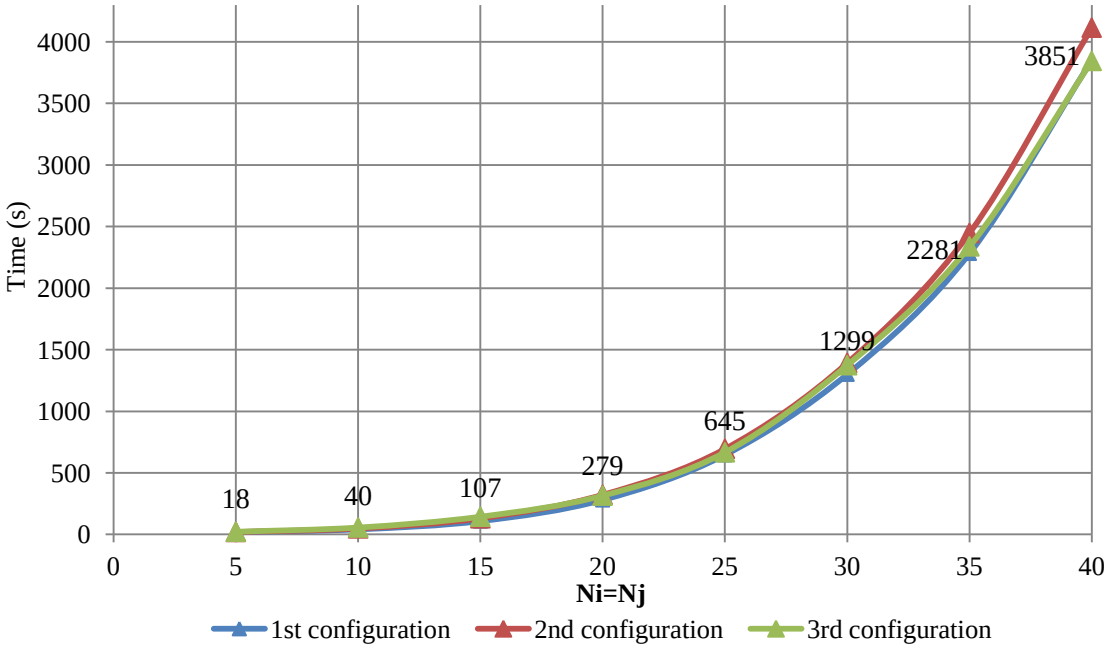

Figure 20 : Variation du temps nécessaire pour une simulation en fonction de la discrétisation du modèle dans les 3 méthodes

En analysant les graphiques précédents, nous concluons que la troisième méthode est la plus fiable; elle donne les résultats les plus précis, même avec une discrétisation grossière. Ainsi, la simulation d'un tel modèle prend le moins de temps, puisqu'on peut calculer des valeurs plus faibles de Ni et de Nj précises. Par conséquent, pour notre modèle, nous choisissons d'appliquer la troisième méthode et de le simuler avec Ni=Nj=10.

3.5 Vérification et validation du modèle

Toutes les variables ont été introduites dans le modèle, y compris les conditions d'air extérieur, les propriétés de l'eau, les débits massiques des fluides, l'épaisseur des canaux, les propriétés de la membrane, etc. Le logiciel utilise tous ces paramètres pour calculer les propriétés d'air et d'eau de sortie ainsi que la température à la surface de la membrane. Les propriétés de la membrane, comme son épaisseur et sa conductivité de masse, ont été tirées des valeurs calculées dans le chapitre précédent, tandis que sa conductivité thermique a été sélectionnée à partir de la littérature en considérant que la conductivité de notre membrane est similaire à celle d'une membrane ProporeMC (Afshin, 2010). Des simulations ont été effectuées et la validité du modèle a été vérifiée en comparant les résultats à ceux expérimentaux et à diverses observations.

L'expérience de validation implique la collecte de données à partir de différents capteurs ; la répétition de l'expérience est généralement nécessaire pour éviter les incertitudes dues aux erreurs du système. La validité du modèle suggéré a été analysée en comparant les résultats de la simulation aux données expérimentales obtenues suite aux 18 essais effectués.

Au début, on a effectué des expériences en considérant que l'air était uniformément réparti dans les 16 canaux et que le débit d'air par canal était donc constant. Pourtant, en analysant les résultats expérimentaux et en calculant la puissance du côté de l'eau et du côté de l'air, on s'est rendu compte qu'il y avait une différence entre ces valeurs. Par conséquent, pour des résultats plus précis, la vitesse de l'air a été mesurée à la sortie de chaque canal à l'aide d'un anémomètre à sonde à fil chaud. Il s'est avéré que le profil de vitesse de l'air n'était pas uniforme; sa distribution diffère d'un canal à l'autre. Les simulations ont été répétées en tenant compte de cette distribution non uniforme de l'air et les résultats ont montré que la différence en pourcentage entre la puissance prévue et la puissance réelle du côté de l'eau est de 14,46 % à 26,47 % pour les expériences effectuées à basse vitesse et de 2,29 % à 16,2 % pour celles effectuées à haute vitesse (tableau 2).

Tableau 3: Différence en pourcentage entre la puissance simulée et la puissance réelle

Power (W)	Experiment	Model	Percentage difference (%)
EXP 5	2431.95	2019.2	-16.97
EXP 6	2605.8	2228.9	-14.46
EXP 7	2499	1994.91	-20.17
EXP 8	2699.4	2105.08	-22.02
EXP 9	2322.75	1707.94	-26.47
EXP 14	2851.5	2786.2	-2.29
EXP 15	2626.35	2428.85	-7.52
EXP 16	2769.75	2489.64	-10.11
EXP 17	2804.46	2442.6	-12.9
EXP 18	2852.1	2390.15	-16.2

Le graphique suivant de la figure 10 montre la distribution de la puissance simulée par rapport à la puissance expérimentale de toutes les expériences conduites.

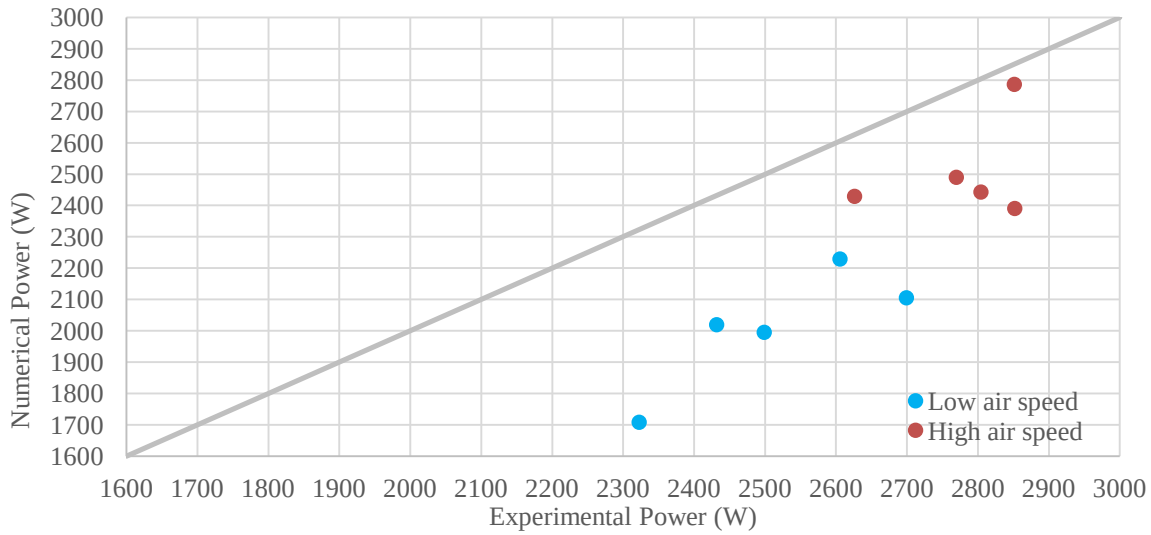

Figure 21: Distribution de puissance simulée par rapport à celle expérimentale pour toutes les expériences

3.6 Analyse d'incertitude

Une analyse d'incertitude a été effectuée sur les valeurs expérimentales en utilisant la méthode de Monte Carlo. Chaque valeur mesurée est bien identifiée et représentée par une fonction d'entrée et le PDF de chaque source d'entrée est exprimé par une distribution normale Gaussienne typique avec une valeur moyenne et un écart type. L'analyse d'incertitude expérimentale est évaluée pour certains canaux et les résultats de l'incertitude de la puissance du côté de l'eau se situent entre 12,7 % et 19,63 %. Ensuite, nous avons évalué l'impact des valeurs d'entrée sur le modèle avec leurs incertitudes sur les résultats numériques et les résultats montrent une incertitude relative à la puissance du côté de l'eau d'environ 7%.

3.7 Correction du coefficient de transfert de chaleur

Notre modèle sous-estime systématiquement la performance d'une valeur moyenne de 20%. Bien que l'incertitude due aux valeurs d'entrée soit de 7 %, ce qui signifie qu'il y a un écart. Compte tenu des résultats d'une étude de sensibilité effectuée sur l'ordre de grandeur des coefficients de transfert de chaleur, il a été démontré que le coefficient du côté liquide est négligeable par rapport à celui du côté air. Par conséquent, on applique une correction des corrélations de transfert de chaleur côté air qui ont été adoptées dans notre modèle pour voir si les résultats peuvent être améliorés.

Afin d'optimiser notre modèle et de réduire la différence de pourcentage entre le modèle et l'expérience, une fonction d'erreur est optimisée pour minimiser cette différence. L'erreur statistique utilisée est l'erreur absolue moyenne (MAE). Elle est calculée pour la puissance totale de l'échangeur de telle sorte que les valeurs prévues et mesurées correspondent à la puissance simulée par le modèle et à la puissance calculée expérimentalement à partir des données mesurées du côté de l'eau. Pour les expériences effectuées à basse vitesse, on a multiplié la corrélation de Nusselt suggérée par (Sieder et Tate, 1936) avec un facteur α. Alors que, pour les

expériences effectuées à haute vitesse, on a modifié la valeur de γ qui avait été proposée précédemment par (Dirker et al., 2017).

Dans Python, on a exécuté les simulations dans Dymola 1000 fois à chaque fois pour trouver une valeur de MAE par la méthode de Monte Carlo. Les résultats indiquent que, pour une valeur de $\alpha = 1{,}59$ et $\gamma = \frac{69\,500}{Re}$, une valeur minimale de MAE est atteinte et que la différence de pourcentage optimisée a été réduite à 7,33 % pour EXP9 et 6,3 % pour EXP18 au lieu de 26,47 % et 16,2 % respectivement. De plus, la différence entre les résultats numériques et expérimentaux concernant la température de l'air et l'humidité absolue était également acceptable.
Le tableau 3représente la puissance totale mesurée expérimentalement et simulée numériquement lorsque $\alpha = 1$ et $\alpha = 1{,}59$.

Tableau 4: Différence en pourcentage entre les résultats simulé et les résultats réels après optimisation pour les expériences effectuées à basse vitesse

Puissance (W)	Expérience	Modèle $\alpha = 1$	Modèle $\alpha = 1{,}59$	Différence de pourcentage optimisée (%)
EXP5	2431.95	2019.2	2515.3	3.43
EXP6	2605.8	2228.9	2775.68	6.52
EXP7	2499	1994.91	2494.5	-0.18
EXP8	2699.4	2105.08	2640.07	-2.20
EXP9	2322.75	1707.94	2152.42	-7.33

Le tableau suivant (tableau 4) résume la puissance expérimentale et la puissance simulée par le modèle pour $\gamma = \frac{34\,500}{Re}$ et $\gamma = \frac{69\,500}{Re}$.

Tableau 5: Différence en pourcentage entre les résultats simulé et les résultats réels après optimisation pour les expériences effectuées à haute vitesse

Puissance (W)	Expérience	Modèle $\gamma = \frac{34\,500}{Re}$	Modèle $\gamma = \frac{69\,500}{Re}$	Différence de pourcentage optimisée (%)
EXP14	2851.5	2786.2	3089.95	8.36
EXP15	2626.35	2428.85	2703.44	2.94
EXP16	2769.75	2489.64	2774.17	0.16
EXP17	2804.46	2442.6	2727.01	-2.76
EXP18	2852.1	2390.15	2672.15	-6.31

3.8 Résultats

Ainsi, le modèle proposé peut être considéré comme un outil crédible et prédictif qui peut être utilisé pour déterminer les performances d'un échangeur de chaleur et de masse à membrane similaire. La figure 11 représente la distribution de la puissance simulée par rapport à celle expérimentale de toutes les expériences effectuées après optimisation des corrélations des coefficients de transfert de chaleur.

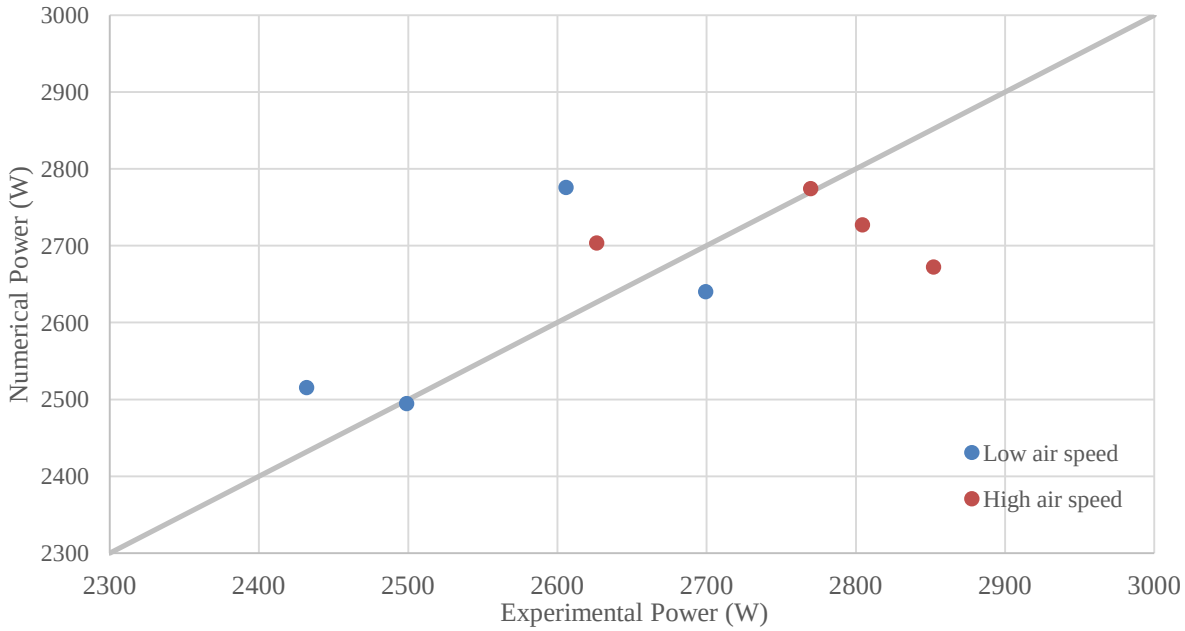

Figure 22: Distribution de puissance simulée par rapport à celle expérimentale pour toutes les expériences après optimisation

3.9 Conclusion

En conclusion, la différence entre la puissance prévue par le modèle et celle calculée expérimentalement atteint ses valeurs maximales de 26,5 % pour EXP9 et de 16,2 % pour EXP18. Incluses dans ces différences, les incertitudes intrinsèques représentent environ 6 à 7 % de l'incertitude totale. Afin de réduire cette différence, on a modifié les corrélations liées au coefficient de transfert de chaleur de l'air (étant le plus influent sur le coefficient global de transfert de chaleur) et on a cherché à trouver une valeur optimisée de MAE. Les résultats indiquent qu'après l'optimisation, la différence de pourcentage a été réduite à 7,33 % pour EXP9 et 6,3 % pour EXP18. De plus, la différence entre les résultats des simulations et ceux expérimentaux concernant la température et l'humidité absolue de l'air est également acceptable. Par conséquent, comme les résultats numériques et expérimentaux présentent des tendances de variation similaires, une conformité satisfaisante est déduites entre les deux, ce qui indique que le modèle développé évalue la performance d'un échangeur de masse et de chaleur à membrane à flux croisés de façon assez précise et réussit à simuler les caractéristiques opérationnelles de cet échangeur. Cependant, les expériences menées ne suffisent pas à généraliser cette conclusion pour tous les scénarios possibles et, par conséquent, il faudrait faire davantage d'expériences pour valider le modèle et prouver son exactitude dans plusieurs autres cas. Dans les étapes suivantes, certains paramètres pourraient être modifiés, comme par exemple élargir la plage du débit d'eau dont la limite supérieure est affectée par la puissance de la résistance (mentionnée précédemment) et la limite inférieure est influencée par la plage de pression de fonctionnement des buses. De plus, d'autres paramètres de conception peuvent être modifiés, comme le nombre de canaux ou la largeur d'un canal de l'échangeur. Pour des mesures plus précises, d'autres expériences peuvent être réalisées avec des capteurs plus précis ou en installant un conduit d'air

de sortie pour obtenir de meilleures lectures du côté de l'air. Dans ce chapitre, nous avons pu établir un modèle 2D pour évaluer la performance énergétique d’un échangeur de masse et de chaleur à membrane à flux croisés. Les résultats ont prouvé qu'il peut être considéré comme un outil crédible et prédictif qui pourrait s'appliquer à des échangeurs similaires. Par conséquent, le modèle proposé prédit l'efficacité du déshumidificateur et du régénérateur qui est un échangeur de membranes à flux croisé. Dans le chapitre suivant, ce modèle est utilisé dans l'évaluation de la performance d'un système hybride de compression de vapeur/ dessiccant liquide dans le cadre d’une climatisation saisonnière d'un bureau dans un immeuble du sud de la France.

Chapter 3 Modeling the Heat and Mass Exchanger and Experimental Validation

3.1 Introduction

Membrane based heat and mass exchangers have been studied extensively and proved to be effective tools for liquid desiccant air dehumidification applications. Previously accomplished numerical and experimental investigations revealed that the moisture removal rate and various performance of membrane based heat and mass exchangers depend significantly on its operating conditions and on the membrane's permeability. As demonstrated in the previous chapter, employing NWF-1 would be favorable because it has enduring structural properties, possesses one of the highest mass conductivities and has the lowest manufacturing cost. Thus in this chapter NWF-1 is used in a prototype with a novel concept of membrane based heat and mass exchanger as indicated in chapter 1. The proposed prototype is a liquid to air cross flow exchanger constructed and subjected to experimental testing on a dedicated test bench. NWF-1 is used to cover the channels, in which liquid is supposed to flow inside separating the air flow from the liquid flow (see figure 3.1). When the liquid passing inside the channels is a desiccant solution, it is essential that no direct contact is allowed with the air to avoid corrosion problems. In our test bench, for easier and riskless applications, instead of a desiccant solution, the liquid sprayed inside the channels is water. Several experiments are conducted to evaluate the performance of this exchanger considering different input conditions. In a way to predict its behavior, a detailed 2-D mathematical model is developed and written in Modelica language using Dymola software. Conjugate energy and mass transfer equations are derived and then discretized and solved using a finite volume approach at steady state. Simulations are performed accordingly and the validity of the model is checked by experimental verifications and observations. Later, an uncertainty analysis is performed on the experimental and numerical values through Monte Carlo method. An acceptable compatibility of the experimental and numerical outcomes would then prove that the model can be used for the prediction of the performance of such an exchanger.

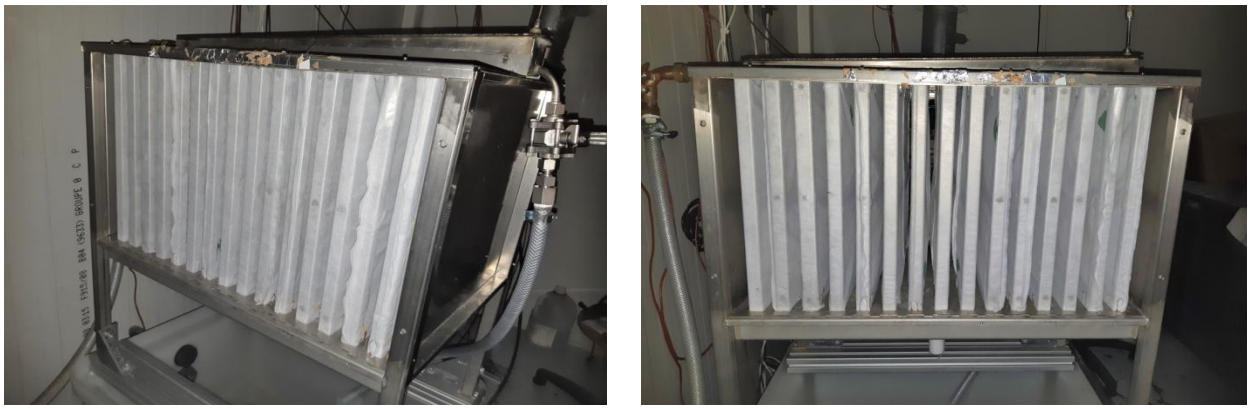

Figure 3.1: The prototype heat and mass exchanger

3.2 Test bench description

The apparatus is an air to liquid cross flow heat and mass exchanger, rectangular in shape made of stainless steel and composed of several channels. At its bottom, a tank initially filled with a liquid and having a volume around 0.1 m^3 is placed. The liquid, which is flowing vertically between the channels, leaves the exchanger through a funnel shaped duct and is then collected in the tank. Air leaves the exchanger directly to the room, ductless, due to space constraints. The solution is pumped from the tank and sprayed vertically through nozzles inside the channels. The surrounding air is driven by a ducted fan between the solution channels in a flow perpendicular to that of the liquid. An exchange of both heat and mass takes place between these two flowing streams. Figures 3.2 and 3.3 show a sketch of the test bench from a left and a front side view respectively.

The main components and the experimental procedure of the test bench are explained in the following paragraphs.

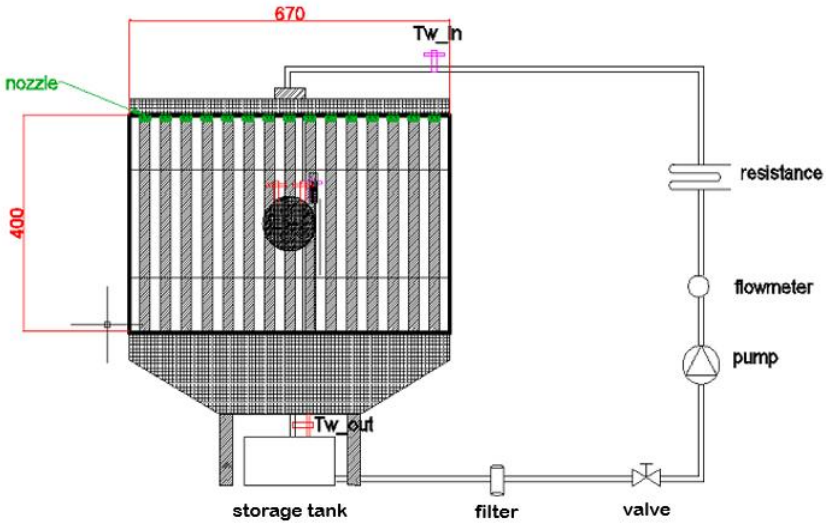

Figure 3.2: A drawing of the test bench from the front side view

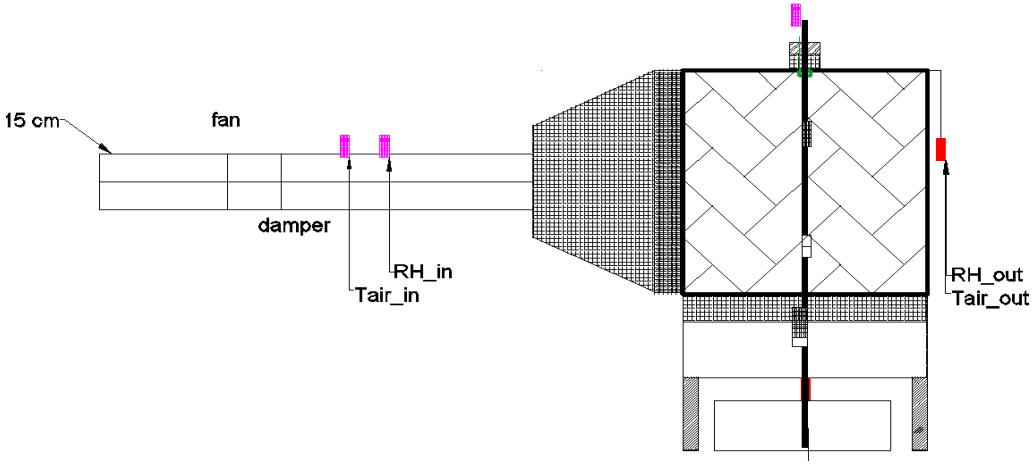

Figure 3.3: A drawing of the test bench from the left side view

3.2.1 Layout and components

Different components compose the test bench and they are listed below.

1. Heat and mass exchanger
2. Pump
3. Fan
4. Electrical resistor
5. Nozzles
6. Storage tank
7. Thermocouples
8. Hygrometers
9. Pressure sensors
10. Thermostat
11. Flow meter
12. Butterfly valves
13. Filter
14. Volume damper
15. Air vent
16. Data acquisition system

3.2.2 Description of the exchanger

The two main components that define the behavior of the exchanger are the channels and the nozzles. Each of these two elements with their characteristics and dimensions are thoroughly described in the coming part.

3.2.2.1 Channels

The exchanger is composed of a total of 15 channels with a frame made of stainless steel. Each channel has a width of 2 cm, a depth and a height of 40 cm each and is covered from both sides with the chosen membrane to prevent the direct contact between the solution and air as shown in figure 3.4a. The distance between two consecutive channels which corresponds to the width of the air passage is also 2 cm. So the total width of the exchanger along with a 5 cm steel frame (2.5 cm on each side) is 67 cm. The height and the depth of the exchanger (including the thickness of the steel frame) are 45 cm each.

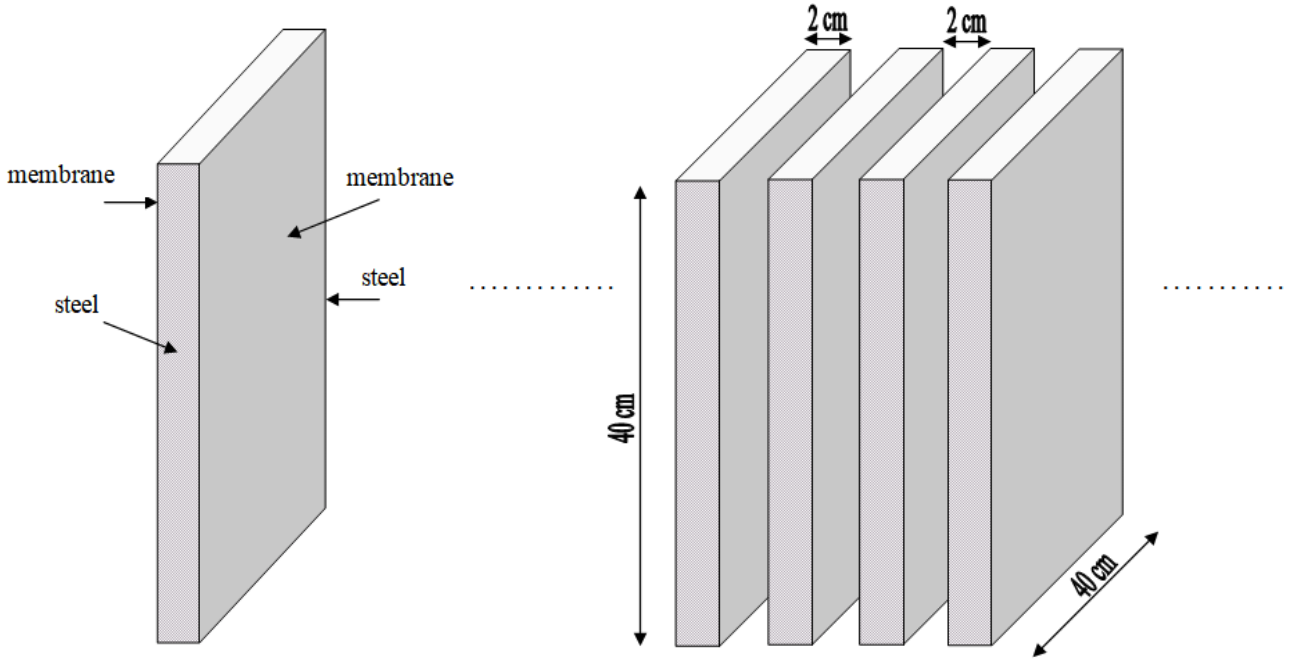

(a) (b)

Figure 3.4: a) One channel with the membrane placement, b) Four consecutive channels of the exchanger with dimensions

3.2.2.2 Nozzles

The nozzles are of compact type made of brass to avoid corrosion when the desiccant solution passes through them. They are chosen with the highest spray angle, 120°, to ensure maximum solution coverage where the repartition of the liquid is uniform and parabolic ("Flat fan nozzles," n.d.) (fig. 3.5 and 3.6). The chosen nozzle has a minimum passage diameter of 0.6 mm and with an allowable liquid volume flow rate varying from 0.71 to 2.24 l/min as the pressure difference across it changes from 1 to 10 bar. If the nozzles function at a different pressure range this would result in an undesired spray pattern. As mentioned in the data sheet, at a pressure of 2 bar and a vertical height of 250 mm, the width of the jet is 660 mm.

Figure 3.5: Flat jet nozzle

Angle de jet	Réf. buse Type	Mat.-no. 16 1.4305/303 SS	Mat.-no. 30 Laiton	A Ø [mm]	E Ø [mm]	V̇ [l/min] p [bar] 0,5	1,0	2,0	[US gal./min] à 40 psi	3,0	5,0	10,0	Largeur de jet B à p = 2 bar H = 250 mm	H = 500 mm
120°	610. 187	●	●	0,35	0,20	-	0,06	0,08	0,02	0,10	0,13	0,18	640	1220
	610. 217	●	●	0,40	0,20	-	0,08	0,11	0,03	0,14	0,18	0,25	650	1230
	610. 247	●	●	0,50	0,20	-	0,12	0,16	0,05	0,20	0,26	0,36	655	1245
	610. 277	○	○	0,60	0,30	-	0,16	0,22	0,07	0,27	0,35	0,49	655	1250
	610. 307	○	○	0,70	0,30	0,16*	0,23*	0,32	0,10	0,39	0,51	0,72	660	1260
	610. 337	○	○	0,90	0,40	0,22*	0,32*	0,45	0,14	0,55	0,71	1,01	660	1260
	610. 367	●	●	1,00	0,50	0,31*	0,44*	0,63	0,20	0,77	1,00	1,41	660	1265
	610. 407	●	●	1,20	0,60	0,50*	0,71	1,00	0,31	1,23	1,58	2,24	660	1270
	610. 447	●	●	1,35	0,60	0,62*	0,88	1,25	0,39	1,53	1,98	2,80	665	1270
	610. 487	○	○	1,50	0,60	0,80*	1,13	1,60	0,50	1,96	2,53	3,58	665	1270
	610. 517	○	○	1,65	0,90	0,95*	1,34	1,90	0,59	2,33	3,00	4,25	670	1275
	610. 567	○	○	2,00	0,90	1,25	1,77	2,50	0,78	3,06	3,95	5,59	670	1280
	610. 607	●	●	2,20	1,10	1,58	2,23	3,15	0,98	3,86	4,98	7,04	675	1285

A = Equivalent bore diameter · E = narrowest free cross section
* Differing spray pattern
Subject to technical modifications.

Figure 3.6: Dimensions and properties of the nozzle

3.2.3 Testing Procedure

In the exchanger there is the liquid circuit inside the channels that exchanges heat and mass with the surrounding air circuit.

3.2.3.1 Liquid circuit

First, we turn on the pump so that solution is transferred from the storage tank to the system. The liquid starts to circulate in the system to reach the nozzles. Second, we turn on the resistor and adjust its set point temperature to a fixed value T_{max}. The liquid circulating in the system heats up until it reaches the predefined set point temperature T_{max} where a thermostat manages the resistor's power to maintain liquid temperature around T_{max}.

A butterfly valve is placed before the pump to regulate the flow of the liquid passing from the tank to the nozzles. A flow meter is located after the pump in order to measure the flow of the solution circulating in the system. The hot solution is pumped to the exchanger and before being sprayed it passes through a horizontal header that supplies the nozzles. In this header an air vent and a pressure sensor are placed. The former is used to insure proper escape of air and the latter to measure the pressure of the liquid before the nozzles. The solution is sprayed vertically by the nozzles inside each channel and after a certain distance a thin film of the solution starts to appear falling on the membranes on both sides of the channel. The solution is then collected in the tank underneath the exchanger. A fine filter is placed in the liquid circuit prior to the header to remove any present impurities that might block the nozzles.

3.2.3.2 Air circuit

As for the air side, the fan is turned on and air at room temperature is being driven through a duct to pass from the outer sides of the channels perpendicular to the liquid flow. An anemometer is used to measure the velocity profile of air and then by multiplying the average velocity by the

considered area the air flow is deduced. At full speed, the fan gives an air flow of 690 m^3/h and a volume damper placed before the fan is used to reduce this flow sequentially.

3.2.3.3 Performance determination

In order to measure the performance of this exchanger in terms of heat transfer, the inlet and outlet temperatures of both air and the solution entering and leaving the exchanger are measured. In addition, to determine the amount of mass transfer, the change in the water vapor concentration in air is computed through measuring the difference in the relative humidity of air entering and air leaving. That is why a thermocouple and a hygrometer are placed in the air duct at about 20 cm before the exchanger to measure the temperature and the relative humidity of the inlet air. Due to the absence of an exit air duct, a thermocouple and a hygrometer are placed directly at the outlets of some air channels of the exchanger to measure the temperature and the relative humidity of the air leaving the exchanger. Two thermocouples are placed in the liquid pipe directly before entering the nozzles header and the temperature of the inlet solution is measured before being sprayed. Two thermocouples are also placed at the collection point of the liquid before falling into the tank to measure its outlet temperature. The average temperature at each side is considered to be the actual inlet and outlet solution temperature respectively.

The hygrometers and the thermocouples are connected to a data acquisition system by which their readings are plotted and saved continuously for further analysis. As the difference between the temperature of the solution and air gets bigger, the heat and mass transfer rises due to the increase in the difference between the vapor pressure of the two fluids. In case where the temperature of the solution is higher than that of air, as it is in the case of our experiments, the direction of flow of water vapor is from the solution to air. Hence the air should be leaving the exchanger loaded with water and thus with a higher absolute humidity.

3.3 Experiments

To test its performance a total of 18 experiments are done on the heat and mass exchanger. Instead of liquid desiccant solution, water is injected through the nozzles for easier and riskless applications. The apparatus is turned on and when the outlet air temperature and relative humidity become stable indicating that the steady state is reached (time to reach steady state is around 30 min); then, measurements are taken for an interval of 20 minutes. The measurement of the outlet air conditions is done using a hygrometer placed at the exit of three channels where the outlet air temperature and relative humidity are taken every minute. The inlet and outlet water temperature as well as the inlet and outlet air temperature and relative humidity are measured continuously and they will be shown for some experiments in later sections. The velocity of air passing in the exchanger is measured at the inlet duct before the fan using an anemometer with a telescopic vane probe at the inlet of the exchanger. Multiplying the mean speed by the cross section area of the duct gives the overall mass flow rate of air traversing the exchanger. The results of the inlet and outlet conditions are later used for the calculations of the performance of the exchanger.
Two sets of experiments are performed; one at low air speed and the other at full air speed. The first set of experiments is done with the volume damper partially opened so the fan was driving

air at a flow rate of around 330 m^3/h. In the second set of experiments the volume damper is fully opened and the full delivered air flow is around 690 m^3/h. In each set, 9 experiments are performed each time by changing the mass flow rate of water, the lowest flow rate was 4.5 lpm and the highest was 9.1 lpm. For values greater than 9.1 lpm the temperature difference between the inlet and outlet water would not be very significant and thus the measurement uncertainty would highly affect our results. The electrical resistor's maximum power is 3000 W and it is always working at full power having set T_{max} at very high limits. Thus the inlet water temperature changes from one experiment to another influenced by the variation of the flow rate. The parameters that are changed from one experiment to another are mainly the inlet air and water flow rates. The inlet air is the room air; its temperature and relative humidity are continuously measured. The inlet water temperature is set but it is affected by the resistor's fluctuations so it is continuously measured as well and stored by the data acquisition system.

3.4 Proposed heat and mass membrane exchanger model

A fundamental evaluation of the performance of heat and mass exchangers requires modeling tools. Several researchers have examined coupled heat and mass transfer in energy exchangers such as Moghaddam et al. (Ghadiri Moghaddam et al., 2013) who experimentally and numerically assessed the performance of a counter-flow liquid to air membrane energy exchanger (LAMEE). They investigated as well the effects of the air convective heat transfer coefficient and the resistance of the membrane on the performance of the LAMEE. Among the developed models, some were established as one dimensional used to predict analytical solutions of packed bed dehumidifiers and regenerators at steady state (Chengqin et al., 2005; Ren et al., 2007). Chengqin et al. used a solution with $CaCl_2$ as a desiccant and studied the effect of changing the inlet conditions such as the liquid concentration, temperature and flow rate as well as the air temperature, humidity and flow rate on the heat and mass transfer performance. Two-dimensional models were as well developed and examined in various studies (Khan, 1998; Vali et al., 2015). Vali et al. used a two dimensional numerical model to solve for a steady state flow in a counter cross flow parallel plate membrane exchanger and their model was validated later by experimental data. With a similar model Bergero et al. (Bergero et al., 2000) investigated a cross flow exchanger and justified his numerical results by performing experiments at different test conditions. Huang (Huang, 2015) also used a two dimensional steady state model to compare the performance of a quasi-counter flow parallel plate membrane contractor to a cross flow one. He concluded that compared to a cross flow contractor the sensible cooling and dehumidification effectiveness deteriorated by approximately 5-29% and 2-13% respectively under various air and solution flow rates and temperatures. A transient 2-D model was used by Namvar et al. (Namvar et al., 2013) to predict the performance of a counter cross liquid to air membrane based exchanger under summer and winter operating conditions and their model was then validated using experimental data.

The three main kinds of theoretical modeling approaches are the effectiveness-NTU (Stevens et al., 1989), the finite difference (Factor and Grossman, 1980), and the conjugate heat and mass transfer based on fitted algebraic equations (Y. Khan, 1994). The $\varepsilon - NTU$ method is less widely

spread in literature compared to the other two methods (Huang et al., 2018). Xie et al. (Xie et al., 2016) developed an $\varepsilon - NTU$ model for a counter-current dehumidifier and proved its reliability by experimental data. The $\varepsilon - NTU$ method is a simple method with a fast computation time yet its results are less accurate compared to the other methods especially when fluids properties may change through the exchanger. Finite difference methods are commonly applied for the modeling of membrane based liquid desiccant energy exchangers mainly for performance analysis and optimization. However, their application is limited when it comes to control design due to their complex model development and to the intensive iterations that are performed during the simulations to converge the results. Consequently, this method is much more time consuming relative to the others. Fumo and Goswami adopted a finite difference model in their work to evaluate the impact of varying operating conditions on air dehumidification and desiccant regeneration using LiCl desiccant solution. Their model showed satisfactory agreement with the experimental findings. In the finite difference method, the heat and mass transfer equations are derived from correlations of fundamental data such as Nusselt and Sherwood (Holman, 1989; Incropera and DeWitt, 1996). However, one main drawback of this method is that the obtained data is considered under uniform temperature (heat flux) or concentration (mass flux) boundary conditions the conception that does not precisely reflect the truly existing heat and mass properties at the boundary conditions of the membrane surface. The third method is used to avoid the drawback presented by the finite difference method. It determines the real boundary conditions at the surface of the membrane through separate mass and energy equations and thus provides better accuracy (Jafarian et al., 2019). Huang et al. (Huang et al., 2012) developed and validated a model using conjugate method for a cross flow parallel plate channels for liquid desiccant air dehumidification. The results of their numerical model was compared to experimental data and showed very good agreement with the findings.

Inspired by the literature results and since the proposed design in this work is novel and not studied before, the next sections present the developed numerical model.

3.4.1 Assumptions

In a way to predict the performance of the exchanger proposed in this thesis, a detailed 2-D numerical model is written in Modelica language using Dymola software for a liquid to air cross flow membrane heat and mass exchanger. Conjugate energy and mass transfer equations are derived and then discretized and solved by using a finite volume approach at steady state. Our model is generated considering the liquid as a desiccant solution of LiCl which is later tailored to water in order to reflect the real experimental case study of our test bench.

The liquid desiccant solution is sprayed in the nozzles and is supplied vertically inside the channels in the direction of z axis. While air is supplied outside the channels perpendicular to the liquid flow in direction of x axis with the two flows being completely separated by the chosen semi permeable membrane. All the parameters and boundary conditions are introduced into the model including the outdoor air conditions, the properties of the introduced desiccant solution, the mass flow rates, the thickness of the channels, the properties of the membrane, etc. The model uses all these parameters to calculate the output air and desiccant conditions and the temperature

at the surfaces of the membrane. The properties of the membrane including its thickness and mass conductivity are taken from the values determined in the previous chapter while its thermal conductivity was adopted from literature review by considering that the conductivity of our membrane is similar to that of Propore^{TM} membrane (Afshin, 2010). The properties of the humid air are taken from (McPherson, 1993) and the properties of LiCl solution in water are given by Conde (Conde, 2014, 2004).

In order to reduce the complexity of the model, several assumptions were made. These assumptions help in solving some physical problems without significantly affecting the results and accuracy of the calculations. The validity of the majority of these assumptions is discussed by Vali et al (Vali et al., 2009) and these assumptions can be stated as follows:

1. Both the air and the liquid desiccant flows are assumed to be at steady state.
2. All variables have 1-D variations in space, in the direction of flow.
3. The fluid flows are independent of the heat and mass transfer and the mass flow rates of dry air and dry desiccant are considered constant.
4. Only the transport of water vapor is permitted by the membrane while the transport of liquid water is not allowed and the membrane properties are independent of the temperature and humidity of the fluids.
5. The heat and mass transfer between the two adjacent fluids only occurs in the direction that is perpendicular to the membrane. The heat conduction and moisture diffusion in the direction of the fluid flows are neglected.
6. Water transfers from or to moist air as vapor. Latent heat of vaporization is always taken from the liquid solution or dissipated into it.
7. The exchanger's casing, the connecting pipes and other system components are considered to be adiabatic. Therefore, there is no heat transfer with the surrounding.
8. The salt solution is assumed to contain no other chemicals and impurities and it is considered to be well mixed before entering the exchanger.
9. The air and the desiccant solution are assumed to be in equilibrium at the solution-air interface which is located at the liquid-membrane interface.

Other assumptions and approximations will be stated later in the model development.

3.4.2 Definitions, properties and basic relations

In the following sections, the properties of the moist air and the desiccant solution are discussed with the ranges of variables.

3.4.2.1 Moist air

The mixture of air with water vapor may be characterized by the molar fraction of vapor, χ_v, that is the ratio of the number of water moles to the total number of moles. But the main variable used for the characterization of the moist air flow is the humidity ratio Y defined as the mass of vapor per kg of dry air. It is related to the molar fraction of vapor by:

$$Y = 0.622 \frac{\chi_v}{1 - \chi_v} \tag{3.1}$$

The constant 0.622 is in fact the ratio of the molar mass of water ($18.01528 g.mol^{-1}$) to that of dry air ($28.9635 g.mol^{-1}$). Inverting equation (3.1) gives χ_v:

$$\chi_v = \frac{Y}{Y + 0.622} \tag{3.2}$$

If the total pressure of a mixture is P_a (normally P_a = 101325 Pa), then that of water vapor is:

$$P_v = \chi_v P_a \tag{3.3}$$

Then we have the following relations:

$$Y = 0.622 \frac{P_v}{P_a - P_v} \tag{3.4}$$

$$P_v = \frac{Y}{Y + 0.622} P_a \tag{3.5}$$

If the air relative humidity and the temperature are known at some point of the system, then the partial pressure of vapor may be determined using:

$$P_v = RH \,.\, P_{v,sat} \tag{3.6}$$

For the calculation of the saturation pressure of water vapor, a formula adapted from (Bolton, 1980) is used. Compared to the tables found in (Ameen et al., 1993), it gives an error that is less than 1% in the range of temperature from $10°C$ to $80°C$.

$$P_{v,sat} = 611.2 \exp\left(\frac{17.63\, T_C}{T_C + 243.5}\right) \tag{3.7}$$

where T_C is the temperature in $°C$.

When the side of the membrane that is in contact with the air has a temperature that is less than the dew point temperature of the air, the absorbed water vapor condenses and thus the droplets of water might stick to the surface of the membrane. Therefore, it is important during the modeling phase to pay attention that the surface of the membrane that is in contact with the air must always have a temperature greater than the dew point temperature of the air at the specified conditions. Also note that the temperature of the membrane changes with time and with the direction of the flow, so at both the entrance and the exit of the membrane the difference in temperature between the surface of the membrane and the dew point of the air should always be positive.

Therefore, the calculation of the dew point temperature is very important, because it allows determining whether there is condensation or not on the membrane according to its surface temperature. The formula used is also adapted from (Bolton, 1980) and has a good accuracy compared to the tables given by Çengel and Boles (Çengel and Boles, 2015), with a maximum error that is less than $0.22°C$ for P_v ranging between $1kPa$ and $100kPa$. The dew point temperature in $°C$ is given by:

$$T_{dp,C} = \frac{243.5 \ln P_v - 1562}{24 - \ln P_v} \tag{3.8}$$

Dry air is considered as an ideal gas having a molar mass of $28.9635 g.mol^{-1}$. Its density at atmospheric pressure ($P_{atm} = 101325\ Pa$) is then:

$$\rho_{da} = \frac{353}{T} \tag{3.9}$$

As for the other properties of moist air, they are mainly taken from (Tsilingiris, 2008) and adapted with some simplifications. They are expressed in terms of the temperature, given in $°C$, and the molar fraction of vapor in air, χ_v.

The dynamic viscosity and the thermal conductivity of moist air are important for the calculation of the convective heat transfer coefficients. First, for the calculation of the dynamic viscosity:

$$\mu_a = \frac{\mu_{da} + \chi_v(0.7887\mu_v - \mu_{da})}{1 - 0.2113\chi_v} \tag{3.10}$$

with:

$$\mu_{da} = (4.7 + 0.046\ T_C) \times 10^{-6} \tag{3.11}$$

and

$$\mu_v = (80 + 0.4\ T_C) \times 10^{-6} \tag{3.12}$$

And for the thermal conductivity:

$$K_{T,a} = \frac{K_{T,da} + \chi_v\left(0.8536K_{T,v} - K_{T,da}\right)}{1 - 0.1464\chi_v} \tag{3.13}$$

ith:

$$K_{T,da} = 0.0241 + 7 \times 10^{-5} T_C \tag{3.14}$$

and

$$K_{T,v} = 0.0174 + 7 \times 10^{-5} T_C \tag{3.15}$$

Regarding the specific heat of air and vapor, taking the constant values below shows that the maximum error is around 0.4% for air and 1.7% for water vapor, for temperatures ranging from $10°C$ to $80°C$.

$$C_{p,da} = 1007\ J.kg^{-1}K^{-1} \tag{3.16}$$

and

$$C_{p,v} = 1814\ J.kg^{-1}K^{-1} \tag{3.17}$$

Last, the diffusion coefficient of water vapor in air at atmospheric pressure is important for the calculation of the convective mass exchange coefficient. According to (Mills, 1995), it is:

$$D_v = 1.97 \times 10^{-5} \left(\frac{T}{256}\right)^{1.685} \quad (3.18)$$

where T is the temperature in K.

3.4.2.1 Desiccant solution

The desiccant solution differs from the moist air by the fact that it is a solution of LiCl solid salt in liquid water and not a simple mixture of two ideal gases:

$$LiCl_{(solid)} + H_2O \rightarrow Li^+_{(aqueous)} + Cl^-_{(aqueous)} + H_2O \quad (3.19)$$

In these conditions, properties like density and specific heat may not be calculated using simple mixing formulas. On one hand, the volumes occupied by each substance cannot be estimated as in the case of gases; the calculation of the density is then impossible. On the other hand, the reaction described by eq. (3.19) is exothermal. Its enthalpy, the enthalpy of solution, Δh_S, is known only at $25°C$ and at low concentrations (Apelblat et al., 1984; Wolf et al., 1987) , which removes the possibility to deduce the specific heat of the solution using those of the substances in the mixing formula.

In these conditions, the properties of the desiccant solution as a whole have to be considered.

The desiccant solution may be characterized by the concentration of salt in the solution, that is:

$$\xi = \frac{m_d}{m_d + m_w} \quad (3.20)$$

But the main variable used for the characterization of the solution is the water ratio, X, defined as the ratio of the mass of water to that of dry desiccant, or the mass of water per kg of dry desiccant in the solution:

$$X = \frac{m_w}{m_d} \quad (3.21)$$

It can be easily shown that:

$$X = \frac{1}{\xi} - 1 \quad (3.22)$$

and:

$$\xi = \frac{1}{1 + X} \quad (3.23)$$

The properties of LiCl solution in water are given by Conde (Conde, 2014, 2004). First, the equivalent pressure of water vapor in the solution is given by:

$$\frac{P_{s,sat}(\xi, T)}{P_{v,sat}(T)} = [F_1(\xi) + F_2(\xi)\theta]F_3(\xi) \quad (3.24)$$

where:

$$\theta = \frac{T}{647.3} \tag{3.25}$$

$$F_1(\xi) = 2 - \left[1 + \left(\frac{\xi}{0.28}\right)^{4.3}\right]^{0.6} \tag{3.26}$$

$$F_2(\xi) = \left[1 + \left(\frac{\xi}{0.21}\right)^{5.1}\right]^{0.49} - 1 \tag{3.27}$$

$$F_3(\xi) = 1 - \left[1 + \left(\frac{\xi}{0.362}\right)^{-4.75}\right]^{-0.4} - 0.03 \exp\left[-\frac{(\xi - 0.1)^2}{0.005}\right] \tag{3.28}$$

Knowing $P_{s,sat}$, the equivalent humidity ratio in the solution may be determined by:

$$Y_s = 0.622 \frac{P_{s,sat}}{P_a - P_{s,sat}} \tag{3.29}$$

Determining Y_s is important for the modeling of the vapor mass transfer flow rate between the moist air and the desiccant solution, since the driving potential of that transfer is $(Y - Y_s)$.

The expression of the solution density is adapted from (Conde, 2004) in a simplified form and gives very accurate results, with a relative error of less than 0.1% for a big range of variation for X:

$$\frac{\rho_s(X,T)}{\rho_w(T)} = 1 + \frac{0.54}{X} - \frac{0.3}{X^2} + \frac{1}{X^3} \tag{3.30}$$

Considering the density of water as constant $\rho_w(T) = \rho_w = 1000 kg.m^{-3}$ gives a relative error of less than 1% for temperatures ranging between $5°C$ and $45°C$.

The dynamic viscosity of the solution is given by:

$$\frac{\mu_s(X,T)}{\mu_w(T)} = \exp\left(0.09\zeta^{3.6} + 1.39\zeta + 0.68\frac{\zeta}{\theta} - 0.58\zeta^2\right) \tag{3.31}$$

Where θ is the same as defined by eq. (3.25), and:

$$\zeta = \frac{\xi}{(1 - \xi)^{(1/0.6)}} \tag{3.32}$$

As for the viscosity of liquid water, it is adapted from (Furukawa, 1991) with a relative error less than 0.25%:

$$\mu_w(T) = 10^{-3} \exp\left(-5.83 + \frac{4.64}{\theta} - \frac{2.09}{\theta^2} + \frac{0.537}{\theta^3}\right) \tag{3.33}$$

The thermal conductivity of the solution is given by (Conde, 2004) as:

$$K_{T,s} = K_{T,w} - g_1 g_2 \tag{3.34}$$

where:

$$g_1 = \frac{\xi \rho_s}{42.39} \tag{3.35}$$

$$g_2 = (10.9 - 11.8\xi) \times 10^{-3} \tag{3.36}$$

While the thermal conductivity of water is expressed, after simplification with still a high accuracy, as:

$$K_{T,w} = 0.6065\ (0.21 + 1.75\theta) \tag{3.37}$$

The conductivity of water at $25°C$ ($0.6065 W.m^{-1}K^{-1}$) is taken from (Ramires et al., 1995).

The specific heat of the solution is taken from (Conde, 2004) with some simplifications:

$$\frac{C_{p,s}(\xi, T)}{C_{p,w}(T)} = 1 - f_1(\xi) f_2(T) \tag{3.38}$$

where:

$$f_1(\xi) = \begin{cases} 1.44\xi - 1.24\xi^2 - 0.12\xi^3 & if\ \xi \leq 0.31 \\ 0.13 + 0.63\xi & if\ \xi > 0.31 \end{cases} \tag{3.39}$$

$$f_2(T) = 58.5\tau^{0.02} - 105.63\tau^{0.04} + 47.8\tau^{0.06} \tag{3.40}$$

with:

$$\tau = \frac{T}{228} - 1 \tag{3.41}$$

The specific heat of water is considered constant, $C_{p,w}(T) = C_{p,w} = 4185\ J.kg^{-1}.K^{-1}$.

When water is added to the solution or rejected from it, due to the mass transfer of water vapor taking place across the membrane there is the enthalpy of water phase change h_{fg} (latent heat). It may be calculated by the formula given in (Furukawa, 1991):

$$h_{fg} = 2.9951 \times 10^6\ (1 - \theta)^{0.32966} \tag{3.42}$$

Last, the diffusion coefficient of water in the solution is found in (Conde, 2014):

$$\frac{D}{D_0} = 1 - \left[1 + \left(\frac{\sqrt{\xi}}{0.52}\right)^{-4.92}\right]^{-0.56} \tag{3.43}$$

Here, D_0 is the self diffusion coefficient of water. Its expression is found in (Holtz et al., 2000):

$$D_0 = 1.635 \times 10^{-8}\ \left(\frac{T}{215.05} - 1\right)^{2.063} \tag{3.44}$$

3.4.2.2 Ranges of variables

Considering rather extreme conditions, moist air enters the exchanger acting as a dehumidifier at a temperature of $35°C$ and a relative humidity around 65%. Using equations 3.5 and 3.6, it is shown that the molar fraction of water vapor is then around 0.036, and the humidity ratio is consequently around $0.0232kg$ per kg of dry air. As for the regenerator, the ambient air considered at $25°C$ is humidified to 100% relative humidity supposedly, it is found that the molar fraction of water vapor is around 0.03. As a consequence, it is considered that the maximum value of the molar fraction of water vapor in moist air is around 0.04, and that of the humidity ratio is around $0.026kg.kg^{-1}$.

As for the temperature of moist air, it is considered to range from $10°C$ to $80°C$. This range was used to justify the simplifications applied in the calculation of its properties in the previous paragraph.

In the desiccant solution, the range of the desiccant mass fraction should be determined carefully. In fact, the dehumidification and regeneration operations require that the relative vapor pressure of the aqueous solution be, respectively, lower and higher than the relative humidity of moist air. Then, it may be stated that the maximum value of the solution relative vapor pressure is around 0.6, and its minimum value around 0.3. Using eq. (3.24) or looking at the charts in (Conde, 2004), it may be deduced that the value of the desiccant mass fraction ξ should range from 0.25 to 0.35 approximately. This means that the water ratio in the solution, X, ranges from 1.85 to 3. Another limiting factor for ξ is the solubility boundary. It may be seen in (Conde, 2004) that, in the considered range of temperatures, that is from $10°C$ to $45°C$, the value of the desiccant mass fraction should not exceed 0.4 in order to avoid the crystallization of salt from the solution.

3.4.3 Mathematical and discretized model

The system consists of moist air flowing in the direction of an x axis, a solid semi permeable membrane parallel to the moist air flow and a liquid desiccant solution (LiCl-H_2O) flowing parallel to the membrane in the direction of z axis. The conservation equations of energy and mass are expressed for each sub-domain; moist air, desiccant solution and two half-membranes. Due to the difference in temperature between the surfaces of the membrane, the heat transfer across the membrane is studied and the resulting energy equations (Mohammad et al., 2013) are derived.

Considering a fixed control volume during time interval $[t, t+dt]$ the mass conservation equation may be written in a generic way as:

$$m(t+dt) = m(t) + m_{in} - m_{out} \tag{3.45}$$

but:

$$m(t+dt) = m(t) + \frac{\partial m}{\partial t} dt \tag{3.46}$$

then:

$$\frac{\partial m}{\partial t} dt = m_{in} - m_{out} \tag{3.47}$$

And the energy conservation reduces to the internal energy conservation, since the variations of kinetic and potential energy are negligible or zero:

$$U(t+dt) = U(t) + H_{in} - H_{out} + Q_{in} - Q_{out} \tag{3.48}$$

or:

$$\frac{\partial U}{\partial t} dt = H_{in} - H_{out} + Q_{in} - Q_{out} \tag{3.49}$$

a) Air side

➢ Mass conservation equation for water vapor

An elementary control volume is considered, between x and $x + dx$ as seen in the figure below (figure 3.7).

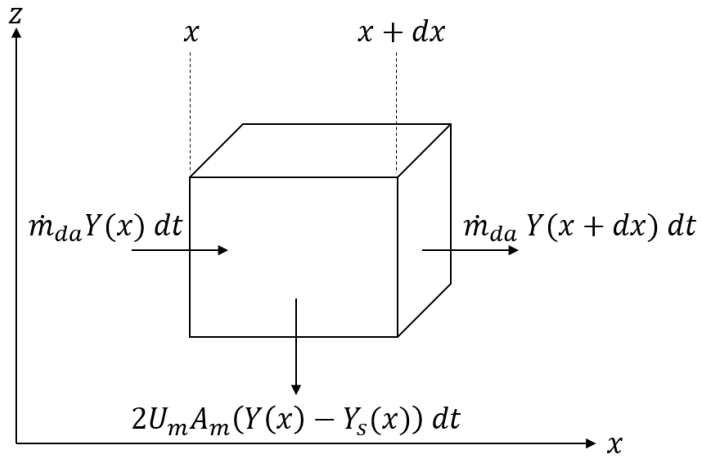

Figure 3.7: Mass conservation of the water vapor at the air side in an elementary control volume

The volume occupied by water vapor is $\chi_v A_a \, dx$ and that occupied by dry air is $(1 - \chi_v) A_a \, dx$. But since the maximum value of χ_v is around 0.04, as stated previously, it may be considered that the dry air occupies the entire volume. Then the mass of dry air is $\rho_{da} A_a \, dx$ and that of water vapor is consequently $\rho_{da} A_a \, dx \, Y$. dx does not depend on time because the control volume is fixed (Euler's approach). The mass of dry air entering or leaving the control volume with the flow during dt is $\dot{m}_{da} dt$, then that of water vapor is $\dot{m}_{da} dt \, Y$. Taking into account the mass transfer across the membrane, due to the difference of concentration of water between the moist air and the solution, the mass balance is written as:

$$A_a \frac{\partial (\rho_{da} Y)}{\partial t} dx dt = (\dot{m}_{da} dt \, Y)(x) - (\dot{m}_{da} dt \, Y)(x + dx) - 2U_M A_m (Y - Y_s) dt \tag{3.50}$$

Considering that:

$$Y(x + dx) = Y(x) + \frac{\partial Y}{\partial x} \, dx \tag{3.51}$$

Then dividing by dt, we get:

$$-\dot{m}_{da}\frac{\partial Y}{\partial x}dx - 2U_M A_m(Y - Y_s) = A_a\ \frac{\partial(\rho_{da}Y)}{\partial t}dx \tag{3.52}$$

But the density of dry air depends only on temperature, and the variations of the latter in time are rather slow. It is then assumed that ρ_{da} is independent of time:

$$-\dot{m}_{da}\frac{\partial Y}{\partial x}dx - 2U_M A_m(Y - Y_s) = \rho_{da}A_a\ \frac{\partial Y}{\partial t}dx \tag{3.53}$$

In all cases, in steady state:

$$-\dot{m}_{da}\frac{\partial Y}{\partial x}dx - 2U_M A_m(Y - Y_s) = 0 \tag{3.54}$$

➢ Energy conservation equation for moist air

The enthalpy entering or leaving the control volume with the flow during is $(\dot{m}_{da}h_{da} + \dot{m}_{da}\,Yh_v)$. As for the mass transfer across the membrane, it carries the enthalpy of vapor as stated in the assumptions. Last, a thermal convective exchange takes place between the membrane and the moist air stream. Considering the same assumption about neglecting the variations of ρ_{da} and a steady state, the enthalpy balance is then after simplification and replacement of dh with $C_p dT_a$:

$$-\dot{m}_{da}\left(C_{p,da} + YC_{p,v}\right)\frac{\partial T_a}{\partial x}dx - 2h_{Ta}A_a(T_a - T_{ma}) = 0 \tag{3.55}$$

a) <u>Solution side</u>

➢ Mass conservation equation for liquid water

An elemental control volume is considered, between z and $z + dz$. Here it is not at all possible to consider that the dry desiccant occupies the whole volume. In fact:

$$dm_s = \rho_s A_s dz = (1 + X)dm_d \tag{3.56}$$

then:

$$dm_d = \frac{\rho_s}{(1 + X)}A_s dz \tag{3.57}$$

Now, applying the same approach as for water vapor leads toat steady state:

$$-\dot{m}_d\frac{\partial X}{\partial z}dz + 2U_M A_m(Y - Y_s) = 0 \tag{3.58}$$

➢ Energy conservation equation for the desiccant solution

The enthalpy entering or leaving the control volume with the flow is $\dot{m}_d(1 + X)\,h_s$. As for the mass transfer across the membrane, it transports the enthalpy of vapor, as stated in the assumptions. Last, a thermal convective exchange takes place between the membrane and the desiccant solution flow.

In these conditions, the energy balance under steady state on an elemental control volume may be written as:

$$-\dot{m}_d(1+X)C_{p,s}\frac{\partial T_s}{\partial z}dz - 2h_{Ts}A_s(T_s - T_{ms}) + 2U_M A_m(Y - Y_s)(h_v - h_s) = 0 \quad (3.59)$$

Comparing $(h_v - h_s)$ with $(h_v - h_w)$, that is h_{fg}, for values of the temperature and the water ratio in the solution covering the entire ranges defined previously, it is observed that the maximum relative difference is around 2.25%. With h_{fg} being the enthalpy of vaporization defined as a function of temperature then finally:

$$-\dot{m}_d(1+X)C_{p,s}\frac{\partial T_s}{\partial z}dz - 2h_{Ts}A_s(T_s - T_{ms}) + 2U_M A_m(Y - Y_s)\left(h_{fg}\right) = 0 \quad (3.60)$$

b) Membrane

➢ Energy conservation equations in the membrane

The enthalpy balance in each half-membrane accounts for the conduction in the direction of the flow, the transversal conduction with the other half-membrane, considered instantaneous, with the temperatures $T_{m,a}$ and $T_{m,s}$ taken on the interfaces with the fluids, and the convective heat exchange with the neighboring fluid flow. As stated in the assumptions, the mass transfer across the membrane is considered instantaneous and does not affect its energy balance. In these conditions, under steady state, the energy conservation equations for the membrane are:

$$h_{Ta}A_a(T_{ma} - T_a) + \frac{K_{T,m}}{\delta}A_m(T_{ma} - T_{ms}) = 0 \quad (3.61)$$

$$h_{Ts}A_s(T_{ms} - T_s) + \frac{K_{T,m}}{\delta}A_m(T_{ms} - T_{ma}) = 0 \quad (3.62)$$

where: $K_{T,m}$ is in $\frac{W}{m.K}$, h_T in $\frac{W}{m^2.K}$, δ_m in m, C_p in $\frac{J}{kg.K}$, U_M in $\frac{kg}{m^2 s}$.

3.4.4 Numerical implementation of the model

The model is written using discretization method; each of the x axis and the z axis was discretized into segments of equal sizes. The number of discretization is noted by Ni and Nj in the horizontal and vertical directions respectively. The choice of the number of discretization is based on an analysis that is discussed in further steps. It studies the effect of the number of mesh on the precision of the numerical results maintaining a compromise between them and the computational time needed to finish a simulation. The discretized model represents one channel of the exchanger and thus modeling the whole exchanger is done by assembling several channels. Hence, the model of the prototype exchanger is composed of 16 sub models associated to the number of air channels. Figure 3.8 represents the exchanger with 15 liquid channels surrounded by 16 air channels. In the figure we can notice that from air channel number 2 till air channel number 15 there is an exchange between two half channels of liquid and two half channels of air. As for the first and last air channels (air channels 1 and 16) the exchange takes place between each of these air channels and the adjacent one half of the liquid channel. Therefore our 16 sub-models are divided accordingly; the first and last model represent an exchange between one air channel and half a liquid channel while all the others represent an exchange between an air channel and a liquid channel.

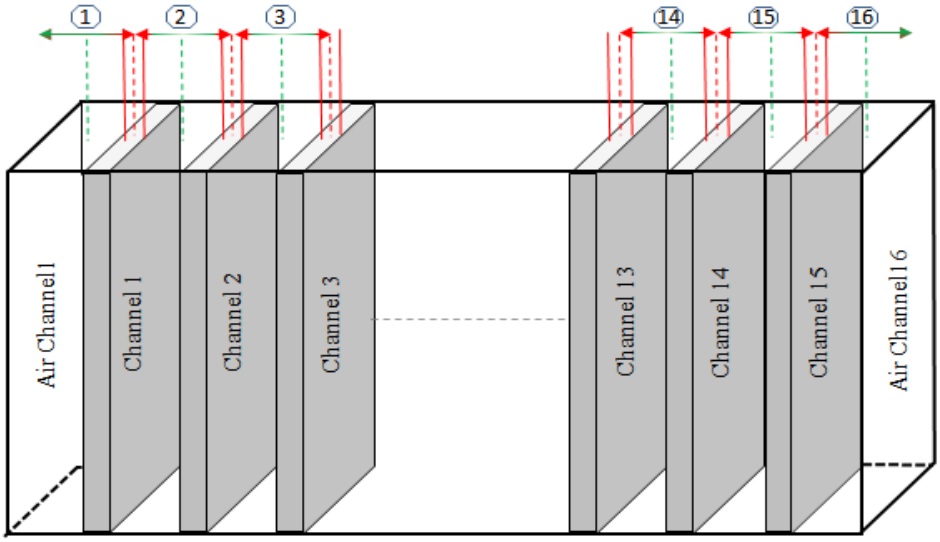

Figure 3.8: Section of the exchanger with 15 liquid channels

The mass and energy equations associated to the heat and mass exchange in the exchanger can be derived using the finite volume method (Monteiro et al., 2011).

3.4.4.1 Numerical scheme

As mentioned before, the surface of the membrane is represented by a series of grid points and its domain is discretized into N_i x N_j equal grid cells of size $dx.dz$ where $dx = \frac{L}{N_i}$ and $dz = \frac{Z}{N_j}$; L and Z representing the length and the height of a channel respectively. Our control volumes are chosen to be identical to the grid cells and nodal points are used within these control volumes for interpolating the field variables. In this case 4 nodes are specified for each control volume stored at the center of each edge as shown in figure 3.9. An (i, j) notation is used to designate the location of each cell where "i" and "j" are the indices along the x-axis and the z-axis corresponding to direction of air stream and desiccant solution stream respectively. The nodal quantities that apply to each node are related to the surface temperature, humidity, specific heat, heat transfer coefficient and concentration. There are three possible computations to approximate the values of these nodal quantities.

❖ **First computation**

The values of the nodal quantities related to the air parameters are computed considering the west surface interface of a general control volume (i,j) and those related to the solution are computed considering the north surface interface (fig.3.9). The mass and energy equations are derived accordingly at the air side, at the solution side and within the membrane at steady state.

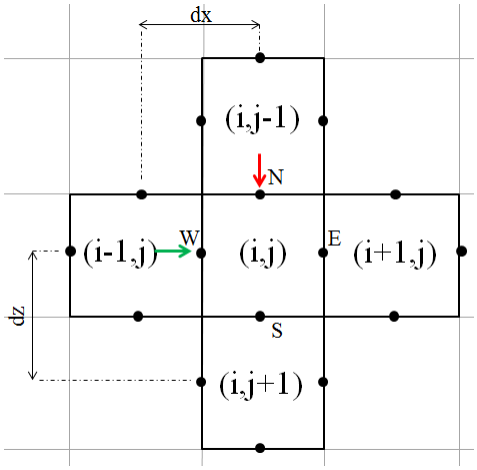

Figure 3.9: A representation of the grid nodal quantities of the 1st computation

a) Air side

➢ Mass conservation equation for water vapor

An elemental control volume of area dx x dz is considered. The mass flow of dry air entering or leaving the elemental control volume with the flow is $\frac{\dot{m}_{da}}{Z} dz$, then that of water vapor is $\frac{\dot{m}_{da}}{Z} Y dz$. Taking into account the mass transfer across the membrane, due to the difference of concentration of water between the moist air and the solution, the mass balance is written as:

$$\dot{m}_{da} \frac{dz}{Z} (Y[i+1,j] - Y[i,j]) + 2A_a U_M[i,j](Y[i,j] - Y_s[i,j]) = 0 \quad (3.63)$$

➢ Energy conservation equation for moist air

The enthalpy entering or leaving the elemental control volume with the flow is $\left(\frac{m_{da}}{Z} dz\ h_{da} + \frac{m_{da}}{Z} Y\ dz\ h_v\right)$. As for the mass transfer across the membrane, it carries the enthalpy of vapor as stated in the assumptions. Last, a thermal convective exchange takes place between the membrane and the moist air stream. The enthalpy balance at steady state is then:

$$\dot{m}_{da} \frac{dz}{Z} \left(C_{p,da}[i,j] + C_{p,v}[i,j] Y[i,j]\right)(T_a[i+1,j] - T_a[i,j]) + 2A_a\ h_{Ta}[i,j](T_a[i,j] - T_{ma}[i,j]) = 0 \quad (3.64)$$

b) Solution side

➢ Mass conservation equation for liquid water

The mass flow of dry desiccant entering or leaving the elemental control volume with the flow is $\frac{\dot{m}_d}{L} dx$ and that of liquid water is $\frac{\dot{m}_d}{L} X\ dx$. The mass balance on the solution side at steady state is then written as:

$$\dot{m}_d \frac{dx}{L} (X[i,j+1] - X[i,j]) - 2A_a U_M[i,j](Y[i,j] - Y_s[i,j]) = 0 \quad (3.65)$$

➢ Energy conservation equation for the desiccant solution

The total mass flow of the solution is $\dot{m}_s = \dot{m}_d + X\dot{m}_d = (1+X)\dot{m}_d$. The enthalpy entering or leaving the elemental control volume with the flow is $\frac{\dot{m}_d}{L}(1+X)dx\ \ h_s$. As for the mass transfer across the membrane, it transports the enthalpy of vapor, as stated in the assumptions. Last, a thermal convective exchange takes place between the membrane and the desiccant solution flow.

$$\begin{aligned}\dot{m}_d \frac{dx}{L}(1+X[i,j])C_{p,s}[i,j](T_s[i,j+1]-T_s[i,j]) \\ -2A_a\, U_M[i,j]h_{fg}[i,j](Y[i,j]-Y_s[i,j]) \\ +2A_s\, h_{Ts}[i,j](T_s[i,j]-T_{ms}[i,j])=0\end{aligned} \tag{3.66}$$

c) Membrane

➢ Energy conservation equations

$$A_a\, h_{Ta}[i,j](T_a[i,j]-T_{ma}[i,j]) - \frac{K_{T,m}}{\delta}\, A_m(T_{ma}[i,j]-T_{ms}[i,j])=0 \tag{3.67}$$

$$A_s\, h_{Ts}[i,j](T_s[i,j]-T_{ms}[i,j]) + \frac{K_{T,m}}{\delta}\, A_m(T_{ma}[i,j]-T_{ms}[i,j])=0 \tag{3.68}$$

❖ **Second computation**

Here, the values of the nodal quantities related to the air parameters are computed considering the east surface interface of a general control volume (i,j) and those related to the solution are computed considering the south surface interface (fig.3.10). Similarly, the mass and energy equations are derived accordingly at the air side, at the solution side and within the membrane.

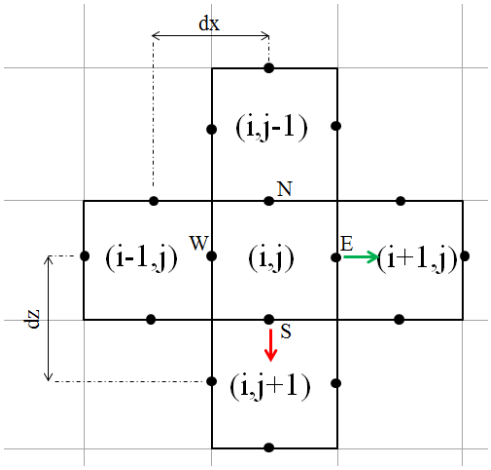

Figure 3.10: A representation of the grid nodal quantities of the 2nd computation

a) Air side

➢ Mass conservation equation for water vapor

$$\dot{m}_{da}\frac{dz}{Z}(Y[i+1,j]-Y[i,j]) + 2A_a U_M[i+1,j](Y[i+1,j]-Y_s[i,j+1])=0 \tag{3.69}$$

➢ Energy conservation equation for moist air

$$\dot{m}_{da}\frac{dz}{Z}\left(C_{p,da}[i+1,j]+C_{p,v}[i+1,j]Y[i+1,j]\right)(T_a[i+1,j]-T_a[i,j]) + 2A_a\, h_{Ta}[i+1,j](T_a[i+1,j]-T_{ma}[i+1,j])=0 \quad (3.70)$$

b) Solution side

➢ Mass conservation equation for liquid water

$$\dot{m}_d\frac{dx}{L}(X[i,j+1]-X[i,j])-2A_aU_M[i+1,j](Y[i+1,j]-Y_s[i,j+1])=0 \quad (3.71)$$

➢ Energy conservation equation for moist air

$$\dot{m}_d\frac{dx}{L}(1+X[i,j+1])C_{p,s}[i,j+1](T_s[i,j+1]-T_s[i,j]) - 2A_a\, U_M[i+1,j]h_{fg}[i,j+1](Y[i+1,j]-Y_s[i,j+1]) + 2A_s\, h_{Ts}[i,j+1](T_s[i,j+1]-T_{ms}[i,j+1])=0 \quad (3.72)$$

c) Membrane

➢ Energy conservation equations

$$A_a\, h_{Ta}[i+1,j](T_a[i+1,j]-T_{ma}[i+1,j]) - \frac{K_{T,m}}{\delta}\,A_m(T_{ma}[i+1,j]-T_{ms}[i,j+1])=0 \quad (3.73)$$

$$A_s\, h_{Ts}[i,j+1](T_s[i,j+1]-T_{ms}[i,j+1]) + \frac{K_{T,m}}{\delta}\,A_m(T_{ma}[i+1,j]-T_{ms}[i,j+1])=0 \quad (3.74)$$

❖ **Third computation**

As for the third, for more detailed modeling and more accurate understanding of the system's behavior, the values of the nodal quantities are taken as average values of the first two configurations. The nodal quantities related to the air parameters are computed considering the average at the west and east surfaces interface of a general control volume (i,j) and those related to the solution are computed considering the average at north and the south surfaces interface (fig. 3.11). Likewise, the mass and energy equations are derived accordingly at the air side, at the solution side and within the membrane.

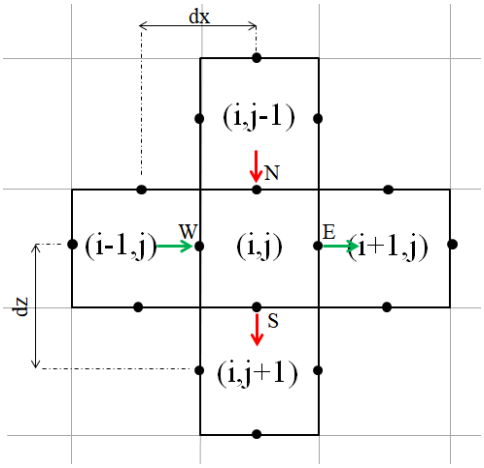

Figure 3.11: A representation of the grid nodal quantities of the 3rd computation

a) Air side

➢ Mass conservation equation for water vapor

$$\dot{m}_{da}\frac{dz}{Z}(Y[i+1,j]-Y[i,j]) + 2A_a\left(\frac{U_M[i,j]+U_M[i+1,j]}{2}\right)\left(\frac{Y[i,j]+Y[i+1,j]}{2} - \frac{Y_s[i,j]+Y_s[i,j+1]}{2}\right)=0 \quad (3.75)$$

➢ Energy conservation equation for moist air

$$\dot{m}_{da}\frac{dz}{Z}\left(\frac{C_{p,da}[i,j]+C_{p,da}[i+1,j]}{2} + \left(\frac{C_{p,v}[i,j]+C_{p,v}[i+1,j]}{2}\right)\left(\frac{Y[i,j]+Y[i+1,j]}{2}\right)\right)(T_a[i+1,j] - + 2A_a\left(\frac{h_{Ta}[i,j]+h_{Ta}[i+1,j]}{2}\right)\left(\frac{T_a[i,j]+T_a[i+1,j]}{2} - \frac{T_{ma}[i,j]+T_{ma}[i+1,j]}{2}\right)=0 \quad (3.76)$$

b) Solution side

- Mass conservation equation for liquid water

$$\dot{m}_d \frac{dx}{L}(X[i,j+1]-X[i,j]) - 2A_a\left(\frac{U_M[i,j]+U_M[i+1,j]}{2}\right)\left(\frac{Y[i,j]+Y[i+1,j]}{2} - \frac{Y_s[i,j]+Y_s[i,j+1]}{2}\right)=0 \quad (3.77)$$

- Energy conservation equation for moist air

$$\dot{m}_d \frac{dx}{L}(1+X[i,j+1])\left(\frac{C_{p,s}[i,j]+C_{p,s}[i,j+1]}{2}\right)(T_s[i,j+1]-T_s[i,j]) - 2A_a\left(\frac{U_M[i,j]+U_M[i+1,j]}{2}\right)\left(\frac{h_{fg}[i,j]+h_{fg}[i,j+1]}{2}\right)\left(\frac{Y[i,j]+Y[i+1,j]}{2} - \frac{Y_s[i,j]+Y_s[i,j+1]}{2}\right) + 2A_s\left(\frac{h_{Ts}[i,j]+h_{Ts}[i,j+1]}{2}\right)\left(\frac{T_s[i,j]+T_s[i,j+1]}{2} - \frac{T_{ms}[i,j]+T_{ms}[i,j+1]}{2}\right) = 0 \quad (3.78)$$

c) Membrane

- Energy conservation equations

$$A_a\left(\frac{h_{Ta}[i,j]+h_{Ta}[i+1,j]}{2}\right)\left(\frac{T_a[i,j]+T_a[i+1,j]}{2} - \frac{T_{ma}[i,j]+T_{ma}[i+1,j]}{2}\right) - \frac{K_{T,m}}{\delta}A_m\left(\frac{T_{ma}[i,j]+T_{ma}[i+1,j]}{2} - \frac{T_{ms}[i,j]+T_{ms}[i,j+1]}{2}\right) = 0 \quad (3.79)$$

$$A_s\left(\frac{h_{Ts}[i,j]+h_{Ts}[i,j+1]}{2}\right)\left(\frac{T_s[i,j]+T_s[i,j+1]}{2} - \frac{T_{ms}[i,j]+T_{ms}[i,j+1]}{2}\right) + \frac{K_{T,m}}{\delta}A_m\left(\frac{T_{ma}[i,j]+T_{ma}[i+1,j]}{2} - \frac{T_{ms}[i,j]+T_{ms}[i,j+1]}{2}\right) = 0 \quad (3.80)$$

For all the computations $dx = \frac{L}{Ni}$ and $dz = \frac{Z}{Nj}$ and the overall mass exchange coefficient is defined between the moist air stream and the membrane-solution interface by the following:

$$U_M = (\frac{1}{h_{Ma}} + \frac{\delta}{k_m} + \frac{1}{h_{Ms}})^{-1} \quad (3.81)$$

With h_{Ma} and h_{Ms} being the mass transfer coefficients of air and the solution respectively computed through mathematical correlations relating the Nusselt number and the heat transfer coefficients.

The three approximation methods can be used to derive the mass and energy equations that accompany the mass and heat transfer in indirect contact exchangers. In later steps, a sensitivity analysis is done on the model representing the test bench exchanger to compare these three approaches and to check their precision.

3.4.4.2 Convective heat and mass transfer coefficients

a) Air side

➢ Heat transfer coefficient

The heat exchange coefficient used in the modeling equations can be deduced from correlations relating Nusselt number Nu to Reynolds number Re and Prandtl number Pr.

$$Nu = f(Re, Pr) \quad (3.82)$$

These correlations are influenced by the thermal properties of the medium, the channel's geometry and the flow characteristics mainly temperature, viscosity and thermal conductivity. Their applicability is affected as well by the hydrodynamic and thermal boundary conditions. Different correlations exist for the various applications, inside or outside tubes, between two parallel plates, in falling films, etc. for laminar, turbulent and transitional flows (Incropera et al., 2007).

For laminar flow in circular tubes, the local Nusselt number is a constant throughout the fully developed region depending on the surface thermal conditions:

For a uniform surface heat flux:

$$Nu = 4.36 \quad (3.83)$$

For a uniform surface temperature:

$$Nu = 3.66 \quad (3.84)$$

For a smooth surface and fully developed turbulent conditions valid for $Re > 10{,}000$, Dittus-Boelter equation may be used:

$$Nu = 0.023\, Re^{\frac{4}{5}}\, Pr^{\frac{1}{3}} \quad (3.85)$$

For turbulent flow in tubes with $0.6 < Pr < 10^3$ and $2300 < Re < 10^6$ the correlation of Gnielinski defined for fully developed flows cited by (Incropera et al., 2007) may be used:

$$Nu = \frac{\left(\frac{ff}{8}\right)(Re - 1000)\,Pr}{1 + 12.7\left(\frac{ff}{8}\right)^{\frac{1}{2}}(Pr^{\frac{2}{3}} - 1)} \tag{3.86}$$

where for smooth tubes the friction factor ff is given by Darcy as in eq. (3.87).

$$ff = (0.79\,logRe - 1.64)^{-2} \tag{3.87}$$

Reynolds and Prandtl numbers are given by eq. (3.88) and eq. (3.89).

$$Re = \frac{\rho v D}{\mu} \tag{3.88}$$

$$Pr = \frac{\mu C_p}{K_T} \tag{3.89}$$

And the heat transfer coefficient h_T is related to Nusselt number by eq. (3.90)

$$Nu = \frac{h_T D}{K_T} \tag{3.90}$$

Then to calculate the heat transfer coefficient use eq. (3.91)

$$h_T = \frac{K_T Nu}{D} \tag{3.91}$$

Where μ is the dynamic viscosity of air at the given inlet conditions in $Pa.s$ or equivalently $\frac{k}{m.s}$, K_T is the thermal conductivity in $\frac{W}{m.K}$, v is the velocity air in $\frac{m}{s}$, D is the hydraulic diameter of a channel in m given by:

$$D = \frac{2\,L\,W}{(L + W)} \tag{3.92}$$

with L and W being the length and the width of a channel respectively.

Reynolds number is mainly used to determine the type of the flow. For a fluid moving between two plane parallel surfaces, a flow is considered to be laminar if its Reynolds number is less than 2000. Yet, the Nusselt number Nu differs along the flow, for instance in the entrance region of a pipe or a duct Nu is usually greater than that in the fully developed region. Thus to find out the characteristics of the flow; whether it is fully developed or still in the entrance region of the developing phase, an assessment of the boundary conditions should be performed. Therefore, to choose which correlation to adopt for each flow one essential element to be inspected is the growth of the boundary layer thickness.

➢ Boundary layer thickness

For flow over any surface, there always exists a velocity boundary layer and hence surface friction. The boundary layer thickness is the distance across a boundary layer from the walls to a point where the flow velocity has essentially reached the 'free stream' velocity (“Boundary layer

thickness," 2019). Boundary layers may be either laminar or turbulent depending on Reynolds number associated to the fluid. In practice, the critical values of this number, which characterizes the transition from laminar flow to turbulence, are given for each geometric configuration. For low values of Reynolds the boundary layer has laminar characteristics where the fluid's velocity changes uniformly as we move away from the wall (Hall, 2015). For higher values of Reynolds number this layer becomes turbulent where the velocity is disordered and the flow becomes unsteady with time. For laminar and turbulent flows the boundary layer thickness over a flat plate is given by (Schlichting, 1960) respectively in eq. (3.93) and eq. (3.94):

$$\delta_b \approx \frac{4.91x}{\sqrt{Re_x}} \tag{3.93}$$

$$\delta_b \approx \frac{0.37x}{Re_x^{\frac{1}{5}}} \tag{3.94}$$

with δ_b being the overall thickness of the boundary layer, x being the distance at a point of the wall where we need to find δ_b, and Re_x being the Reynolds number at x.

If the flow is still in a transitional regime other heat transfer correlations exist. For a developing laminar flow at a length l, correlations reported by (Sieder and Tate, 1936) are used to calculate the Nusselt number:

$$Nu_l = 1.86\,\tau^{-\frac{1}{3}}\left(\frac{\mu}{\mu_p}\right)^{0.14} \tag{3.95}$$

where $\tau = \frac{l}{D.Re_D.Pr}$ and $\frac{\mu}{\mu_p}$ is the ratio of the bulk viscosity over the viscosity near the wall. This correlation is valid for $0.48 < Pr < 16.7$.

For turbulent flows, to account for the coefficients in a non-fully developed transitional flow regimes Hausen proposed the addition of a correction factor to the correlation given by Gnielinski in eq. (3.101). He suggested to multiply the equation by $(1 + \left(\frac{D}{L}\right)^{\frac{2}{3}})$ taking into account the entrance region as cited by (Dirker et al., 2017) . According to previous work performed by (Dirker et al., 2017) this factor was then modified to better predict their experimental results to become $(1 + \left(\gamma\frac{D}{L}\right)^{\frac{2}{3}})$ where $\gamma = \frac{34{,}500}{Re}$. Then the modified Nusselt number is given by eq. (3.96):

$$Nu = \frac{\left(\frac{ff}{8}\right)(Re - 1000)\,Pr}{1 + 12.7\left(\frac{ff}{8}\right)^{\frac{1}{2}}(Pr^{\frac{2}{3}} - 1)}(1 + \left(\gamma\frac{D}{L}\right)^{\frac{2}{3}}) \tag{3.96}$$

where D and L are respectively the hydraulic diameter and the length of a channel in m.

➢ Mass transfer coefficient

The convective mass transfer coefficient may be determined using specific correlations relating Sherwood number Sh to Reynolds number Re and Schmidt number Sc (Incropera et al., 2007) as in the following:

$$Sh = f(Re, Sc) \tag{3.97}$$

$$Sh = \frac{h_M L}{\rho D} \tag{3.98}$$

$$Sc = \frac{\mu}{\rho D} \tag{3.99}$$

Then:

$$h_M = \frac{\rho D\ Sh}{L} \tag{3.100}$$

The Chilton-Colburn analogy (Incropera et al., 2007) may also be used to deduce these coefficients from the heat convection ones by:

$$h_M = \frac{h_T}{C_p\ Le^{2/3}} \tag{3.101}$$

Where Le is the Lewis number defined as:

$$Le = \frac{K_T}{\rho\ C_p\ D_v} \tag{3.102}$$

Where ρ is the density of air and D_v is the diffusivity of vapor in air.

b) Water side

➢ Heat transfer coefficient

- Correlations related to jet

On the other side of the membrane, water is sprayed through nozzles with a flat jet angle in a direction parallel to the membranes. Different researchers have investigated the heat transfer mechanism occurring in spraying process in several domains. In most of these processes it was ensured that the nozzle axis was always normal to the target surface and sometimes the impingement was over an inclined surface. In spray and jet cooling techniques coolants are sprayed through nozzles over a hot surface provoking phase change when the sprayed liquid heats up (Wang et al., 2011; Wu et al., 2019; Xia et al., 2006). The heat transfer rate showed a great dependence on different parameters including the nozzle's geometry and the flow pattern after jet impingement. It is also influenced by the behavior of the jet depending on its angle, on the nozzle orifice dimensions and other parameters (Royne and Dey, 2006; Vinze et al., 2016). Several correlations were developed relating the Nusselt number to the spray Reynolds number and in the following some of them are stated and discussed.

An experimentally derived correlation deduced by Specht (Specht, 2014) provided the following average function for a single circular nozzle being determined for air application (as the flow moves from laminar to turbulent the exponent of Re increases)

$$Nu = 0.12\, Re^{0.67} Pr^{0.4} \tag{3.103}$$

where $Re = \frac{v\, d}{\vartheta}$, d being the diameter of the nozzle in m, v the speed at which the flow exits the nozzle in $\frac{m}{s}$ and ϑ the kinematic viscosity of the fluid in $\frac{m^2}{s}$.

Other experimental studies were performed by Scholtz and Trass for parabolic velocity profile circular jets normally impinging a surface with a laminar boundary layer condition. They proposed the following Nusselt correlation valid for $1 < Pr < 10$ and $Re < 4000$ and cited by (Lienhard, 2005):

$$Nu_x = 1.648\, {Re_x}^{\frac{1}{2}} Pr^{0.361} \tag{3.104}$$

where $Re = \frac{v\, D}{\vartheta}$, D being the diameter of the jet in m, v the speed of the coming jet in $\frac{m}{s}$.

The heat transfer coefficient is then deduced from the Nusselt correlation by eq. (3.91).

- Correlations related to falling films

The above mentioned correlations consider that the jet is impinged normal to a horizontal surface and as a matter of fact none of these correlations reflects the real case. In our case water is sprayed through flat jet nozzles in a direction parallel to the surface of the membranes. Thus our search is extended to examine the correlations of falling films.

In falling films, heat transfer takes place between a thin liquid film and a surface that absorbs or emits heat and the film falls over this surface because of the gravitational force. Coefficients of heat and mass transfer for falling films have been widely studied and Nusselt correlations were determined theoretically and experimentally in different applications. For shell and tube heat exchangers Kern's correlation is used to estimate the shell side Nusselt equation (Zhu, 2013):

$$Nu = 0.36\, Re^{0.55}\, Pr^{\frac{1}{3}} \tag{3.105}$$

where $Re = \frac{\rho v D_e}{\mu}$ and D_e being the equivalent shell side diameter m.

Another equation for heat transfer in falling films is discussed by Schnabel and Schlünder where three correlations are given for laminar, transition and turbulent flows as cited in (Åkesjö et al., 2018).

$$Nu = \begin{cases} 1.43\, Re^{-\frac{1}{3}} & (\text{Laminar } Re < 2300\ ) \\ 0.042\, Re^{0.2}\, Pr^{0.344} & (\text{Transition } 2300 < Re < 4000\ ) \\ 0.014\, Re^{0.4}\, Pr^{0.344} & (\text{Turbulent } Re > 4000) \end{cases} \tag{3.106}$$

where $Re = \frac{\Gamma}{\mu}$ and $\Gamma = \frac{\dot{m}}{\alpha}$ is the mass flow rate of the fluid per unit width in $\frac{kg}{m.s}$.

In this correlation the heat transfer coefficient is related to the Nussselt number by the following equation eq. (3.107)

$$h_T = \frac{K_T\, Nu}{\delta_f} \tag{3.107}$$

where δ_f is the film thickness in m (Yoshioka and Hasegawa, 2012).

➢ Mass transfer coefficient

The mass transfer coefficient at the water side is calculated by the Chilton-Colburn analogy mentioned in eq. (3.100).

However, in reality even a falling film does not totally represent the flow pattern of our exchanger. This is because whenever the spray is not fully distributed with an angle of 120°, the flow isn't considered as a film since it would be still diverging and the channel would not be completely within the spray coverage. Therefore, a comparison of the order of magnitude between the correlations related to jets and those related to falling films is performed in order to check the differences and to decide which of them to select and to employ in our model. For this reason a typical example is considered for our case study taking typical input air and water conditions and analyzing the output results based on the different discussed correlations.

3.5 Application done on the prototype

In our test bench the liquid sprayed inside the channels is water and thus the properties of water instead of desiccant are used in our model. Therefore the mass conservation equation at the liquid side is not applicable anymore and the mass flow rate of the desiccant solution $\dot{m}_d\ (1 + X[i,j])$ is replaced by that of water $\dot{m}_w$.

Table 3.1: A summary of the design parameters and the inlet conditions of a typical example

Exchanger	Length (m)	0.4
	Height (m)	0.4
	Number of water channels	15
	W_a (m)	0.02
	W_s (m)	0.02
	Ni	20
	Nj	20
Membrane	δ (m)	1.57×10^{-4}
	k_m (m^2/s)	4.3×10^{-6}
	K_T (W/m.K)	0.334
Air conditions	T (°C)	20
	RH (%)	70
	Velocity per channel (m/s)	1.2
	Flow per channel (m^3/h)	34.56
Water conditions	T (°C)	35
	Total flow (lpm)	8
	Flow per channel (kg/s)	8.89×10^{-3}

To be able to compare liquid side correlations and the three computations of the model, a typical example of our test bench inlet values is considered and the inlet air and solution conditions are summarized in table 3.1 along with the main design parameters of the exchanger.

3.5.1 Selection of water side heat transfer coefficient correlation

Water is moving with a very low Reynolds number due to its low speed and thus the flow is laminar. In order to be able to choose which heat transfer coefficient to assume at the water side a sensitivity analysis is performed on the previously suggested correlations for laminar flows accorded to both jets and falling films. A comparison is done on the output power given by the simulations by fixing the air side heat transfer coefficient to the modified correlation of Gnielinski presented previously. Simulations were performed following the model of the third computation and the results were compared to those of the other two correlations related to falling films. A summary of the different Nusselt equations giving the heat and mass transfer at the water side are shown in table 3.2 along with the predicted total power.

Table 3.2: Comparison of the different heat transfer correlations

Circular nozzle (Specht, 2014) $Nu = 0.12\ Re^{0.67} Pr^{0.4}$	$h_T = \frac{K_T Nu}{L}\ (W/m.K)$	185
	$h_M = \frac{h_T}{C_p\ Le^{2/3}}\ (kg/m^2.s)$	13.4
	Total power (W)	2746
Parabolic velocity profile circular jets (Lienhard, 2005) $Nu_x = 1.648\ Re_x^{\frac{1}{2}}\ Pr^{0.361}$	$h_T = \frac{K_T Nu}{L}\ (W/m.K)$	420
	$h_M = \frac{h_T}{C_p\ Le^{2/3}}\ (kg/m^2.s)$	30.9
	Total power (W)	2764
Shell side film (Zhu, 2013) $Nu = 0.36\ Re^{0.55}\ Pr^{\frac{1}{3}}$	$h_T = \frac{K_T Nu}{L}\ (W/m.K)$	90
	$h_M = \frac{h_T}{C_p\ Le^{2/3}}\ (kg/m^2.s)$	6.7
	Total power (W)	2717
Falling films (Åkesjö et al., 2018) $Nu = 1.43\ Re^{-\frac{1}{3}}$	$h_T = \frac{K_T Nu}{L}\ (W/m.K)$	36
	$h_M = \frac{h_T}{C_p\ Le^{2/3}}\ (kg/m^2.s)$	2.7
	Total power (W)	2645

From the above comparison we can notice that the difference between these correlations affects the value of the exchanger's total power by about 4.5%. It is important to mention that these results are just for one example with a given exchanger design and inlet conditions but similar results are computed for other values.

Knowing that all the above correlations in fact do not reflect the conditions of our case, we are going to choose the correlation given by (Zhu, 2013) that provides an average value among the tested correlations. In this case the effect of choosing such a heat transfer coefficient would be ±2.2% on the total power of the exchanger.

For the coming steps of the model validation the modified Nusselt correlation provided by Gnielinski (eq. (3.96)) and that provided by Kern (eq. (3.105)) are adopted for the air side and water side respectively.

3.5.2 Comparison of the three computations schemes

As discussed before, the third computation is the average of the other two and it should provide more accurate results. In the coming step these three computations are compared by their accuracy, the time needed to finish a simulation and how they are affected by some modeling parameters. For this comparison, the output power is calculated for each computation by varying the model discretization.

The creation and selection of discretization size in the model is an important step since during simulations meshing is considered to be the most memory intensive measure. Thus choosing a convenient number of mesh can help reduce memory requirements decreasing the computational time needed for a simulation. On the other hand, lowering the number of mesh can affect the accuracy of the numerical results of our model. A convenient mesh size guarantees a more accurate numerical outcome while a poor mesh size affects the convergence of the solution. In order to find an acceptable number of mesh by which there is a compromise between the accuracy of the model and the restrictions of memory and time, a sensitivity analysis is performed. This is done by simulating the models of the three computations' schemes several times modifying only the number of mesh Ni and Nj in each. The study concentrates on the total power of the exchanger and examines its variation with the increase of Ni and Nj from 5 to 40 by a step of 5 every time. This study gives an idea about the effect of changing the mesh size on the numerical results regarding the total water power of the exchanger as shown in figure 3.12. From the graph it can be observed that as the number of mesh increases the 3 curves representing the power of the exchanger start to get flatter approaching an asymptote. As for very small values of Ni and Nj these values are far from this asymptotic value. It can be noticed as well that the difference of the total power calculated by the 3 computations decreases as the number of mesh increases. For the first and second computations we notice that there is a remarkable difference in the power as the number of mesh changes. It is not until Ni=Nj=25 that the power starts approaching the asymptotic value. While for the third configuration, the power values are almost the same for whatever values of Ni and Nj.

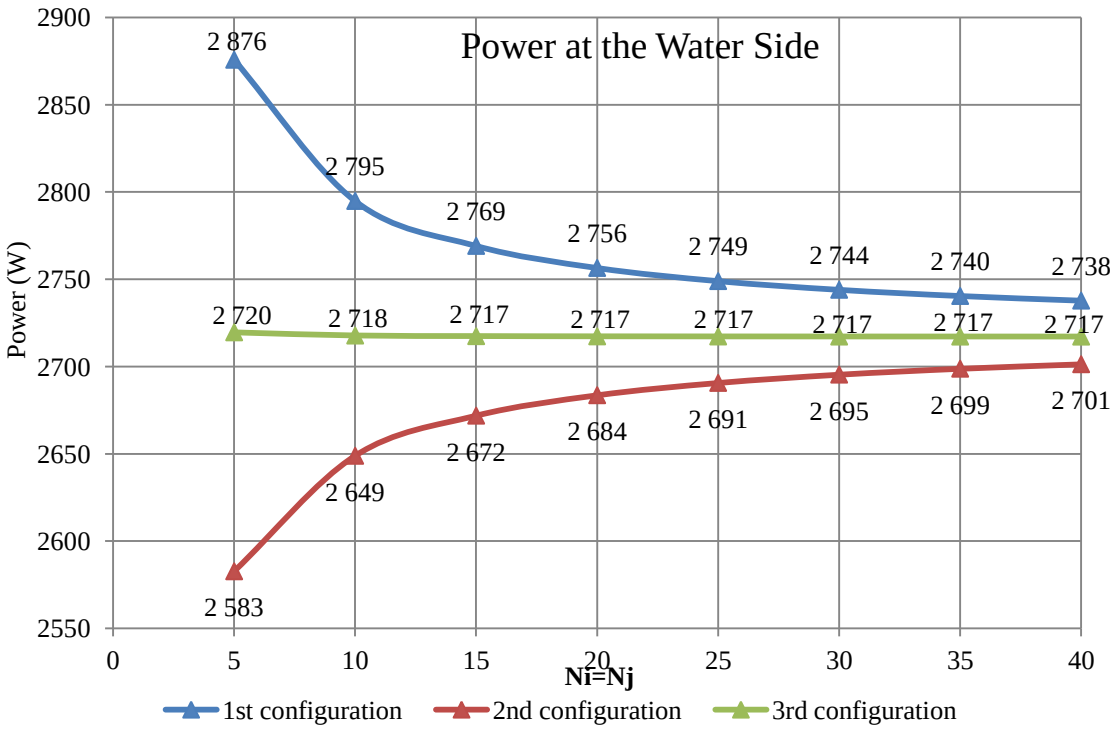

Figure 3.12: Variation of the power of the 3 computations as a function of the model discretization

The results of this study prove the accuracy of the third computation over the other two. It can be clearly noticed as well that the third computation is the least affected by changing the number of mesh in the model. However, this computation might be the slowest.

The purpose of this sensitivity analysis is to select the number of mesh Ni and Nj in a way to get an acceptable numerical precision with an optimized simulation speed. In our case it is very important to find a balance between these two parameters. The complexity of the model consumes a great fraction of the processor's memory and provokes a low speed simulation. The previously realized simulations are executed by varying Ni and Nj and the real time needed for every simulation for a given number of mesh is computed as shown in figure 3.13. From the graph it is observed that the simulation time slightly varies between the three configurations and the time needed to compute one simulation varies exponentially with the increase in the number of mesh. At Ni=10 the values of the power vary between 2649 W and 2795 W while those of time vary between 40 s and 55 s respectively. While at Ni=25 the values of the power vary between 2691 W and 2749 W while those of time vary between 645 s and 694 s respectively. As Ni and Nj further increase the percentage difference in power decreases but the time required for each simulation largely rises.

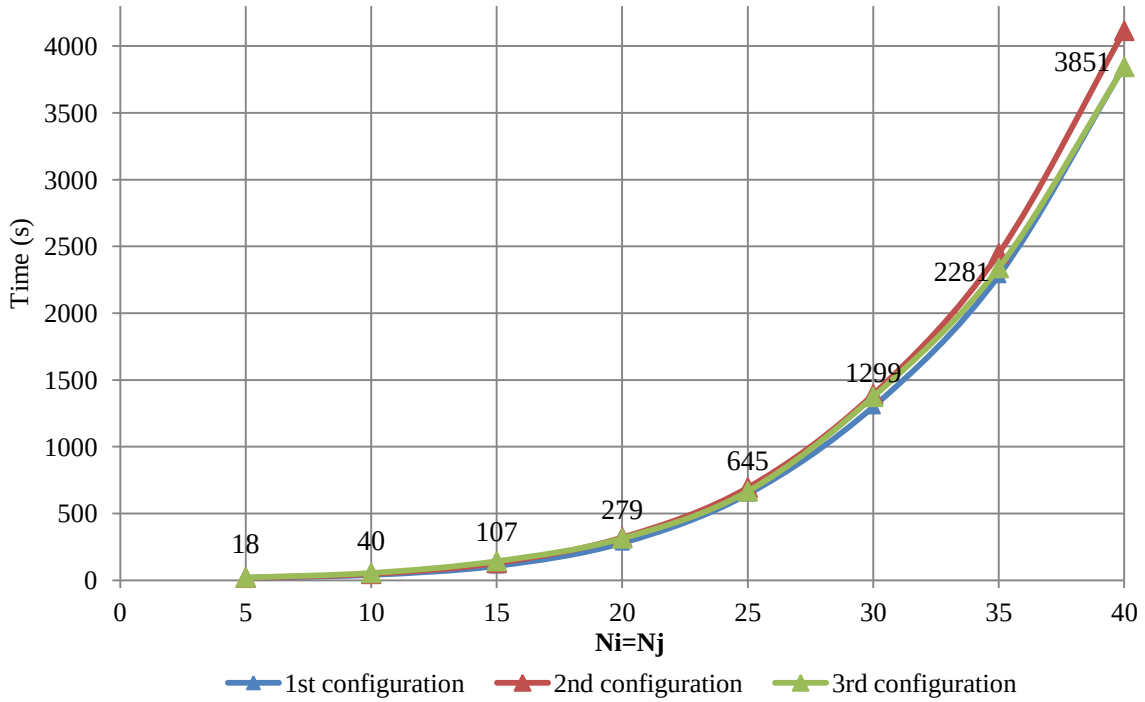

Figure 3.13: Variation of the time needed for one simulation as a function of the model discretization in the 3 computations

By analyzing the preceding graphs, we conclude that the third computation is the most reliable; it is stable and it gives the most precise results even with small discretization numbers. Thus simulating such a model consumes the least time since at smaller values of Ni and Nj accurate results may be computed. Therefore, for our model, we choose to apply the third configuration and simulate it with Ni=Nj=10.

3.5.3 Model verification and validation

The validity of this model or any other model should be properly checked by experimental verifications and observations. It is concerned with quantifying the accuracy of the model by comparing the simulation numerical results with the experimental data. The validation experiment involves the collection of data from different sensors and the repetition of the experiment is generally necessary to avoid uncertainties due to systematic error and uncontrollable variability. In general, physical experiments provide data needed for the model validation and thus all the assumptions must be understood, well defined and controlled in the experiment. If proved to agree with the experiment, the model reduces both cost and time and provides reliable predictive results on the performance of such a membrane based heat and mass exchanger. Therefore, this would be considered as an important achievement from the scientific point of view and a powerful tool from the industrial one. If the model simulation outcome was not in agreement with the experimental results, both the model and the experiment should be revised. Model revision includes changing the basic assumptions, correlations, initial conditions, or boundary values. While experimental revision involves checking the inaccuracy related to the

position of the sensors, improving measurement technique, or changing the experimental procedure.

In the light of the series of the 18 experimental tests performed on the exchanger, the validity of the above suggested model is analyzed by comparing the simulation results to the experimental data in the following sections.

3.5.3.1 Experimental data

As discussed before two sets of experiments were done; one set at a low air speed and another set at a full air speed. Each set is made of 9 experiments where every experiment is performed at a different total water flow rate varying from 4.5 lpm to 9.1 lpm. The respective high and low air speed per channel are around $1.5\,m/s$ and $0.72\,m/s$ corresponding to a channel flow rate of $43.2\,m^3/h$ and $20.7\,m^3/h$. The experiments with their conditions are summarized in table 3.3:

Table 3.3: Initial inlet conditions of each experiment

Experiment	$\dot{m}_a$ (m^3/h)	$\dot{m}_w$ (L/min)	T_a $(°C)$	RH_a $(\%)$	T_w $(°C)$	Pressure at nozzle (bars)
Exp 1	20.7	4.5	24.3	85.6	38.7	0.79
Exp 2	20.7	5.3	26.8	71.7	44.0	0.86
Exp 3	20.7	6	25.5	78.9	39.3	0.95
Exp 4	20.7	6.6	27.0	76.2	42.3	1
Exp 5	20.7	7.3	26.0	78.1	38.7	1.11
Exp 6	20.7	7.7	26.6	77.3	40.1	1.18
Exp 7	20.7	8.2	27.1	78.7	38.9	1.25
Exp 8	20.7	8.7	26.4	77.3	39.0	1.33
Exp 9	20.7	9.1	26.4	81.7	36.9	1.4
Exp 10	43.2	4.5	29.2	70.6	45.1	0.79
Exp 11	43.2	5.3	29.2	72.0	43.0	0.86
Exp 12	43.2	6	29.2	72.0	41.4	0.95
Exp 13	43.2	6.6	29.2	72.3	40.0	1
Exp 14	43.2	7.3	28.9	77.9	40.2	1.11
Exp 15	43.2	7.7	28.0	82.1	38.3	1.18
Exp 16	43.2	8.2	29.0	76.6	38.5	1.25
Exp 17	43.2	8.7	28.9	74.9	37.9	1.33
Exp 18	43.2	9.1	28.8	72.8	37.3	1.4

In experiments 1 to 4 and 10 to 13 the pressure at one nozzle is less than 1 bar and thus as discussed earlier the flow pattern of the jet is non-uniformly distributed across the channel and the channels are not at full water coverage.

3.5.3.2 Model validation

➢ First case: Uniform air velocity

The simulations were first performed considering that the air is uniformly distributed in all the 16 channels and thus the air flow per channel was taken constant.

The same parameters that are used in the experiment are introduced to the model. A constant air speed throughout the channels of the exchanger, thus a constant flow rate that differs from one

experiment to another, is considered. For comparison reasons the air outlet results of the numerical model are analyzed at the same channels at which the experimental values were measured. The dimensions of the exchanger and the properties of the membrane are set the same as in the previous discussion of the typical example (table 3.1). The simulations of the model are done by considering the same inlet conditions as those measured in the experiment. Insert the inlet air flow rate and its average temperature and relative humidity as measured by the thermocouple and hygrometer. Also insert the inlet water flow rate and average temperature. In a way to determine the most convenient air heat transfer correlation used for our calculations in the model validation, the boundary layer thickness is calculated at the air side. This value is crucial to understand the behavior of the flow in the air channels.

Boundary layer thickness calculation

In all the experiments air is entering at a temperature between 15°C and 30°C, at a relative humidity between 60% and 95% and with a speed that ranges from 0.5m/s to 1.7m/s per channel of 40cm height and 2 cm thickness. Consequently, the Reynolds number of air moving at low speed is around 1500 while at high speed it is around 2500 indicating a laminar flow in the former and a turbulent flow in the latter. By calculating δ_b for both laminar and turbulent flows it can be noticed that both flows are developing and haven't reached the fully developed state.
For experiments done at low air speed (laminar flow) δ_b is given by eq. (3.93).

The thickness of a channel is 2 cm, the flow is considered as fully developed at δ_b=1 cm. Substituting δ_b by 0.01 in eq. (3.93) yields to a value of $x = 0.43$ (x being the distance at a point flow). This means that the flow in the channel is still in the hydrodynamic entrance region where the velocity profile keeps changing. Therefore in our model the correlation suggested by (Sieder and Tate, 1936) and mentioned earlier in eq. (3.95) is used to calculate the air heat transfer coefficient for the first set of experiments done at low air speed.

For experiments done at high air speed (turbulent flow) δ_b is given by eq. (3.94). Similarly, substituting δ_b by 0.01 in eq. (3.94) yields to a value of $x = 0.2$. This means that in the first 20 cm of the channel, i.e., in half of the channel the flow is still in the hydrodynamic entrance. After the 20 cm the velocity profile would not change anymore and the flow becomes a fully developed turbulent flow. Therefore, in our model the modified correlation of Gnielinski in eq (3.96) is used to calculate the air heat transfer coefficient for the second set of experiments done at high air speed.

Results

When simulating the model with the inlet conditions for every experiment, experiments 1 to 4 and 10 to 13 appeared to have different trends from the others; the model seemed to overestimate the actual power in most of the experiments unlike the others that were underestimated by the model. Therefore, for more reliable results these experiments are not going to be included in our analysis and model validation. Only experiments with a proper flow pattern are studied and thoroughly discussed. The values of the inlet water and air conditions in EXP5, EXP8, EXP14,

and EXP17 are summarized in the following the tables (tables 3.4 to 3.7). The results of the model are shown in the tables as well.

Table 3.4: Experimental and numerical results of EXP5 with uniform air speed

		Experiment			Model
		Channel 4	Channel 9	Channel 12	One channel
Inlet air	T_a (°C)	26.0	26.0	26.0	26.0
	RH (%)	78.1	78.1	78.1	78.1
	Y (g/kg)	16.5	16.5	16.5	16.5
	$\dot{m}_a$ (m^3/h)	20.7	20.7	20.7	20.7
Inlet water	$\dot{m}_w$ (g /s)	8.1	8.1	8.1	8.1
	T_w (°C)	38.7	38.7	38.7	38.7
Outlet air	T_a (°C)	29.7	31.1	30.9	29.3
	RH (%)	83.1	94.6	92.6	90.6
	Y (g/kg)	22.0	27.3	26.3	23.5
	Q_L (W)	91.5	180.4	164.7	113.6
	Q_S (W)	26.0	35.7	34.2	23.3
	Q_{Ta} (W)	117.5	216.1	198.9	136.9
Outlet water	T_w (°C)	33.9			34.7
	Q_{Tw} (W)	2433.7			2024.6

Table 3.5: Experimental and numerical results of EXP8 with uniform air speed

		Experiment			Model
		Channel 4	Channel 9	Channel 12	One channel
Inlet air	T_a (°C)	26.4	26.4	26.4	26.4
	RH (%)	77.3	77.3	77.3	77.3
	Y (g/kg)	16.7	16.7	16.7	16.7
	$\dot{m}_a$ (m^3/h)	20.7	20.7	20.7	20.7
Inlet water	$\dot{m}_w$ (g /s)	9.7	9.7	9.7	9.7
	T_w (°C)	39.0	39.0	39.0	39.0
Outlet air	T_a (°C)	30.4	31.7	32.0	29.8
	RH (%)	84.6	94.5	96.7	90.2
	Y (g/kg)	23.4	28.2	29.4	24.0
	Q_L (W)	111.6	193.3	212.8	118.8
	Q_S (W)	28.5	37.3	39.2	23.9
	Q_{Ta} (W)	140.1	230.6	252.0	142.7
Outlet water	T_w (°C)	34.5			35.5
	Q_{Tw} (W)	2696.6			2110.6

Table 3.6: Experimental and numerical results of EXP14 with uniform air speed

		Experiment			Model
		Channel 4	Channel 9	Channel 12	One channel
Inlet air	T_a (°C)	28.9	28.9	28.9	28.9
	RH (%)	77.9	77.9	77.9	77.9
	Y (g/kg)	19.6	19.6	19.6	19.6
	$\dot{m}_a$ (m^3/h)	43.2	43.2	43.2	43.2
Inlet water	$\dot{m}_w$ (g /s)	8.1	8.1	8.1	8.1
	T_w (°C)	40.2	40.2	40.2	40.2
Outlet air	T_a (°C)	31.3	31.0	30.8	31.0
	RH (%)	82.2	85.6	84.8	85.4
	Y (g/kg)	23.9	24.5	23.9	24.4
	Q_L (W)	149.7	170.4	151.2	162.0
	Q_S (W)	35.2	30.8	27.8	30.8
	Q_{Ta} (W)	185.0	201.2	179.0	192.8
Outlet water	T_w (°C)	34.6			34.6
	Q_{Tw} (W)	2852			2836.4

Table 3.7: Experimental and numerical results of EXP17 with uniform air speed

		Experiment			Model
		Channel 4	Channel 9	Channel 12	One channel
Inlet air	T_a (°C)	28.9	28.9	28.9	28.9
	RH (%)	74.9	74.9	74.9	74.9
	Y (g/kg)	18.8	18.8	18.8	18.8
	$\dot{m}_a$ (m^3/h)	43.2	43.2	43.2	43.2
Inlet water	$\dot{m}_w$ (g /s)	9.7	9.7	9.7	9.7
	T_w (°C)	37.9	37.9	37.9	37.9
Outlet air	T_a (°C)	30.8	31.1	30.7	30.7
	RH (%)	80.5	85.7	84.1	82.5
	Y (g/kg)	22.7	24.6	23.6	23.0
	Q_L (W)	137.1	203.6	166.8	143.0
	Q_S (W)	28.7	32.5	26.6	25.7
	Q_{Ta} (W)	165.8	236.0	193.4	168.7
Outlet water	T_w (°C)	33.2			33.8
	Q_{Tw} (W)	2805.5			2486.6

➢ Second case: Non-uniform air velocity

The experiments discussed previously were performed by considering a uniform distribution of air speed in the exchanger. Thus, the preceding numerical results were derived with identical inlet air flow rate in all channels and the comparison between them and the experimental results was done accordingly. Yet by analyzing the experimental results and calculating the power at the water side and at the air side, we realize that there is a discrepancy between these values. One of the reasons might be that the measurement of the inlet air velocity is not so accurate and its distribution might not be uniform throughout the exchanger. In reality, the velocity profile is not

uniform; the distribution of air differs from one channel to another. Therefore, for more accurate results the speed of air is measured at the outlet of each channel using a hot wire probe anemometer. The channel is 40 cm high, the speed of air is measured in 5 different locations across the channel and the average speed is calculated. Then by multiplying this average speed by the cross section of the channel we get the air flow rate in a channel.

The measurement of the outlet air conditions is done using a hygrometer placed at the exit of air channels number 4, 9 and 12 where the outlet air temperature and relative humidity are measured every minute. As for the water side, the temperature sensor is placed at the bottom of the exchanger where the exiting water is collected measuring by that the overall outlet water temperature of all channels together. In the model, we set the values of the inlet air mass flow rates channel by channel as calculated from the measured air speed. For comparison reasons the air outlet results of the numerical model are analyzed at air channels number 4, 9 and 12.

Results

Tables 3.8 to 3.12 sum up the characteristics of air and water entering the exchanger as well as the experimental and numerical outlet results for EXP5, EXP8, EXP14 and EXP17.

Table 3.8: Experimental and numerical results of EXP5 with non-uniform air speed

		Experiment			Model		
		Channel 4	Channel 9	Channel 12	Channel 4	Channel 9	Channel 12
Inlet air	T_a (°C)	26.0	26.0	26.0	26.0	26.0	26.0
	RH (%)	78.1	78.1	78.1	78.1	78.1	78.1
	Y (g/kg)	16.5	16.5	16.5	16.5	16.5	16.5
	$\dot{m}_a$ (m^3/h)	25.3	15.1	18.4	25.3	15.1	18.4
Inlet water	$\dot{m}_w$ (g /s)	8.1	8.1	8.1	8.1	8.1	8.1
	T_w (°C)	38.7	38.7	38.7	38.7	38.7	38.7
Outlet air	T_a (°C)	29.7	31.1	30.9	28.9	30.0	29.6
	RH (%)	83.1	94.6	92.6	89.3	92.9	91.5
	Y (g/kg)	22.0	27.3	26.3	22.6	25.1	24.1
	Q_L (W)	111.8	132.0	146.7	120.4	102.8	109.6
	Q_S (W)	31.8	26.1	30.4	25.0	20.8	22.4
	Q_{Ta} (W)	143.6	158.1	177.1	145.3	123.6	131.9
Outlet water	T_w (°C)	33.9			34.5	35.1	34.9
	Q_{Tw} (W)	2433.7			2019.2		

Table 3.9: Experimental and numerical results of EXP8 with non-uniform air speed

		Experiment			Model		
		Channel 4	Channel 9	Channel 12	Channel 4	Channel 9	Channel 12
Inlet air	T_a (°C)	26.4	26.4	26.4	26.4	26.4	26.4
	RH (%)	77.3	77.3	77.3	77.3	77.3	77.3
	Y (g/kg)	16.7	16.7	16.7	16.7	16.7	16.7
	$\dot{m}_a$ (m^3/h)	25.3	15.1	18.4	25.3	15.1	18.4
Inlet water	$\dot{m}_w$ (g /s)	9.7	9.7	9.7	9.7	9.7	9.7
	T_w (°C)	39.0	39.0	39.0	39.0	39.0	39.0
Outlet air	T_a (°C)	30.4	31.7	32.0	29.4	30.5	30.0
	RH (%)	84.6	94.5	96.7	88.8	92.5	91.0
	Y (g/kg)	23.4	28.2	29.4	23.0	25.7	24.6
	Q_L (W)	136.4	141.4	189.5	126.1	107.2	114.5
	Q_S (W)	34.9	27.3	34.9	25.6	21.3	22.9
	Q_{Ta} (W)	171.2	168.7	224.4	151.8	128.4	137.4
Outlet water	T_w (°C)	34.5			35.3	35.8	35.6
	Q_{Tw} (W)	2696.6			2105.1		

Table 3.10: Experimental and numerical results of EXP14 with non-uniform air speed

		Experiment			Model		
		Channel 4	Channel 9	Channel 12	Channel 4	Channel 9	Channel 12
Inlet air	T_a (°C)	28.9	28.9	28.9	28.9	28.9	28.9
	RH (%)	77.9	77.9	77.9	77.9	77.9	77.9
	Y (g/kg)	19.6	19.6	19.6	19.6	19.6	19.6
	$\dot{m}_a$ (m^3/h)	53.6	37.5	49.6	53.6	37.5	49.6
Inlet water	$\dot{m}_w$ (g /s)	8.1	8.1	8.1	8.1	8.1	8.1
	T_w (°C)	40.2	40.2	40.2	40.2	40.2	40.2
Outlet air	T_a (°C)	31.3	31.1	30.8	30.8	31.2	30.9
	RH (%)	82.2	85.7	84.8	84.3	86.1	84.7
	Y (g/kg)	23.9	24.6	23.9	23.8	24.8	24.0
	Q_L (W)	186.7	148.4	174.3	174.8	152.6	170.3
	Q_S (W)	43.7	26.7	31.9	34.1	28.4	32.9
	Q_{Ta} (W)	230.4	175.1	206.1	208.9	181.0	203.2
Outlet water	T_w (°C)	34.6			34.1	35.0	34.3
	Q_{Tw} (W)	2852			2786.2		

Table 3.11: Experimental and numerical results of EXP17 with non-uniform air speed

		Experiment			Model		
		Channel 4	Channel 9	Channel 12	Channel 4	Channel 9	Channel 12
Inlet air	T_a (°C)	28.9	28.9	28.9	28.9	28.9	28.9
	RH (%)	74.9	74.9	74.9	74.9	74.9	74.9
	Y (g/kg)	18.8	18.8	18.8	18.8	18.8	18.8
	$\dot{m}_a$ (m^3/h)	53.6	37.5	49.6	53.6	37.5	49.6
Inlet water	$\dot{m}_w$ (g /s)	9.7	9.7	9.7	9.7	9.7	9.7
	T_w (°C)	37.9	37.9	37.9	37.9	37.9	37.9
Outlet air	T_a (°C)	30.8	31.1	30.7	30.5	30.8	30.6
	RH (%)	80.5	85.7	84.1	81.4	83.1	81.8
	Y (g/kg)	22.7	24.6	23.6	22.5	23.4	22.7
	Q_L (W)	171	177.3	192.2	155.2	134.1	150.9
	Q_S (W)	35.6	28.14	30.5	28.7	23.7	27.6
	Q_{Ta} (W)	206.5	205.5	222.7	183.8	157.8	178.5
Outlet water	T_w (°C)	33.2			33.4	34.1	33.6
	Q_{Tw} (W)	2805.5			2442.6		

For the rest of the experiments a summary of the power predicted numerically and calculated experimentally is shown in the following table along with the percentage difference between them.

Table 3.12: percentage difference between the predicted power and the actual power

Power (W)	Experiment	Model	Percentage difference (%)
EXP 5	2431.95	2019.2	-16.97
EXP 6	2605.8	2228.9	-14.46
EXP 7	2499	1994.91	-20.17
EXP 8	2699.4	2105.08	-22.02
EXP 9	2322.75	1707.94	-26.47
EXP 14	2851.5	2786.2	-2.29
EXP 15	2626.35	2428.85	-7.52
EXP 16	2769.75	2489.64	-10.11
EXP 17	2804.46	2442.6	-12.9
EXP 18	2852.1	2390.15	-16.2

The following graph in fig. 3.14 shows the distribution of the predicted power versus the experimental power of all the conducted experiments.

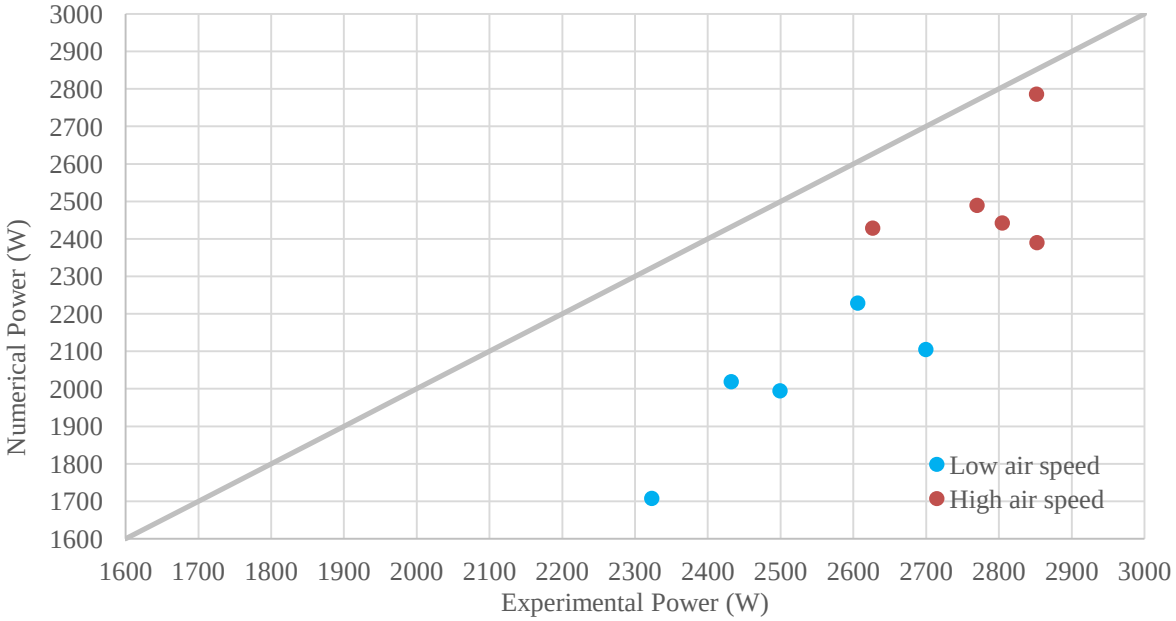

Figure 3.14: Predicted versus experimental power distribution for all experiments

3.5.3.3 Mean Absolute Error (MAE)

To validate the performance and the accuracy of a model qualitatively, some standard methods that use statistical error tests are generally applied mainly the Mean Absolute Error (MAE) and the Root Mean Square Error (RMSE). During the evaluation of the model, a lower value of MAE or RMSE indicates a better performance and improved predicted values. MAE method is adopted in our study to compare the value predicted by the model to that calculated experimentally. It is the average of the total sum of the absolute prediction errors between the model and experiment and is calculated by the following formula (Lee and Jeong, 2019).

$$MAE = \frac{1}{n}\sum_{i=1}^{n}\left|\frac{x_{exp} - x_{model}}{x_{exp}}\right| .100 \qquad (3.108)$$

where x_{exp} is the actual value from the experiment, x_{model} is the predicted value by the model, and n is the number of experimental data.

MAE is calculated for the total power of the exchanger such that the predicted and measured values are the total power simulated by the model and the power calculated experimentally from the measured data at the water side. Two separate MAE were determined; one for all experiments done at high air speed and another for those performed at low air speed and the calculated MAE was 0.098 and 0.199 respectively.

3.5.4 Uncertainty analysis

The uncertainty of the readings taken in our experiments for the measured values of some input parameters affect the output results. The overall power of the exchanger is determined at the

water side by multiplying the water mass flow rate by its specific heat and the difference in temperature of the inlet and outlet water. At the air side, the power is determined by multiplying the air mass flow rate by the difference in its enthalpy at the inlet and the outlet. All these parameters are inferred from our measured values and thus evaluating the accuracy of our measurements and the quality of our readings is essential to better determine the performance of our exchanger. Consequently, an uncertainty analysis is performed similar to the one explained previously in chapter 2. Every measured value is well identified and represented by an input function and the PDF of every input source is expressed by a typical normal Gaussian distribution with a mean value and a standard deviation. Later, an uncertainty analysis is done on the model taking into account the uncertainties on the numerical input sources.

3.5.4.1 Experimental uncertainties

The experimental uncertainties are those related to the input parameters mainly to the measurements taken at the air and water side.

❖ **Measured values**

➢ Air speed (m/s)

One measurement uncertainty that affects the results of our simulations is the one related to the speed of air which directly impacts the air flow rate. The speed of air inside each channel is measured for 5 times. Thus the PDF of type A uncertainty is represented by the mean of these 5 measurements $\overline{V}$ and the standard deviation due to the repeatability noted by std_A.

A hot wire anemometer is used with a certified uncertainty of ±3% of 0.05m/s for ranges of speed between 0.15 and 3m/s. Therefore the mean of type B uncertainty is zero and its standard deviation is 0.03*0.05= 0.015 m/s noted by std_B.

As for the combined uncertainty, the mean is the average value for each channel $\overline{V}$ and the standard deviation $std_V = \sqrt{({std_A}^2 + {std_B}^2)}$.

The air speed uncertainties are represented for each channel in table 3.13:

Table 3.13: Uncertainty at low and high air speed channel by channel

Channel	High air speed (m/s)	std_V	Uncertainty (%)	Low air speed (m/s)	std_V	Uncertainty (%)
1	1.542	3.60E-02	2.34	0.598	4.06E-02	6.79
2	1.191	2.22E-02	1.87	0.595	2.14E-02	3.60
3	1.857	5.67E-02	3.05	0.770	3.31E-02	4.31
4	1.861	3.83E-02	2.06	0.878	2.72E-02	3.10
5	2.100	5.32E-02	2.53	1.064	2.50E-02	2.35
6	1.242	4.11E-02	3.31	0.867	2.24E-02	2.58
7	1.587	2.84E-02	1.79	0.870	2.44E-02	2.80
8	0.879	2.80E-02	3.18	0.582	2.35E-02	4.04
9	1.301	3.72E-02	2.86	0.526	2.44E-02	4.63
10	1.650	7.35E-02	4.46	0.749	3.18E-02	4.24
11	1.680	7.31E-02	4.35	0.831	3.85E-02	4.64
12	1.720	2.63E-02	1.53	0.640	2.79E-02	4.37
13	2.186	8.46E-02	3.87	0.858	3.37E-02	3.93
14	1.111	3.42E-02	3.08	0.495	2.03E-02	4.11
15	1.143	2.41E-02	2.11	0.678	3.84E-02	5.66
16	0.947	3.04E-02	3.20	0.500	2.03E-02	4.05

➢ Air flow rate (kg/s or m^3/h)

The air flow rate is related to the air speed through the following formula:

$$\dot{m}_a(kg/s) = 1.2 * V * W * H = 1.2 * B \quad (3.109)$$

Where W and H are the thickness and the height of a channel respectively in m, and $B = V * W * H$ ($\bar{B} = \bar{V} * \bar{W} * \bar{H}$). w and h are measured by a steel tape of a total length 3m with an accuracy class II. Thus according to EU standards, the tolerance of such a tape is ±0.9 mm. Thus the type B PDFs of the thickness and the height have a mean $\bar{W} = 0.02\,m$ and $\bar{H} = 0.4\,m$ respectively and their standard deviations are 0.0009 m.

Therefore, the PDF of the air flow rate has a mean value $\overline{\dot{m}_a} = 1.2 * \bar{B}$ and a standard deviation equal to $std_{\dot{m}_a} = 1.2 * std_B$.

$$\left(\frac{std_B}{\bar{B}}\right)^2 = \left(\frac{std_V}{\bar{V}}\right)^2 + \left(\frac{std_W}{\bar{W}}\right)^2 + \left(\frac{std_H}{\bar{H}}\right)^2$$
$$\left(\frac{std_B}{\bar{B}}\right)^2 = \left(\frac{std_V}{\bar{V}}\right)^2 + \left(\frac{0.0009}{0.02}\right)^2 + \left(\frac{0.0009}{0.4}\right)^2 \quad (3.110)$$

For example for channel number 12, the mean velocity at high speed is 1.72 m/s then the mean mass flow rate is $0.0165\,kg/s$ and the standard deviation is $7.86 * 10^{-4} kg/s$ (or $\overline{\dot{m}_a} = 49.55\,m^3/h$ and $std_{\dot{m}_a} = 2.358\,m^3/h$). The air flow rate uncertainties are represented for each channel in table 3.14:

Table 3.14: Uncertainty on the air flow rate at low and high air speed channel by channel

Channel	Air flow rate at low speed (m^3/h)	$std_{\dot{m}_a}$	Uncertainty (%)	Air flow rate at high speed (m^3/h)	$std_{\dot{m}_a}$	Uncertainty (%)
1	17.21	1.40	8.15	44.41	2.25	5.07
2	17.14	0.99	5.77	34.31	1.67	4.88
3	22.16	1.38	6.23	53.47	2.91	5.44
4	25.29	1.38	5.47	53.60	2.66	4.95
5	30.63	1.56	5.08	60.47	3.13	5.17
6	24.96	1.30	5.19	35.76	2.00	5.59
7	25.04	1.33	5.31	45.69	2.21	4.85
8	16.77	1.02	6.05	25.33	1.40	5.52
9	15.14	0.98	6.46	37.46	2.00	5.34
10	21.57	1.33	6.19	47.52	3.01	6.34
11	23.92	1.55	6.47	48.40	3.03	6.26
12	18.43	1.16	6.27	49.55	2.36	4.76
13	24.70	1.48	5.98	62.95	3.74	5.94
14	14.24	0.87	6.10	31.99	1.75	5.46
15	19.53	1.41	7.24	32.92	1.64	4.97
16	14.39	0.87	6.06	27.28	1.51	5.53

Other input variables also possess some uncertainties that affect the overall power including the inlet air temperature and relative humidity as well as the inlet water temperature and mass flow rate.

- Air temperature (°C) and relative humidity (%)

The inlet air temperature and relative humidity are measured by a ducted type hygrometer with a certified uncertainty of ±0.3°C for a range of temperature between 0°C and 50°C and ±3% for a relative humidity between 10% and 90%. For every value of the temperature and relative humidity, a PDF is used where the mean is taken as the value of the measured temperature or relative humidity and the standard deviation is 0.3°C or 3% respectively.

- Water temperature (°C)

The inlet water temperature is measured by a thermocouple with a certificate stating an uncertainty of ±0.5°C. So the mean of the PDF is the value of the measured water temperature and the standard deviation is 0.5.

- Water flow rate (kg/s)

The mass flow rate of water is measured by a flow meter with a standard accuracy of ±0.3% of the measured value. Therefore the mean of the PDF is the measured mass flow rate $\dot{m}_w$ and its standard deviation is $\pm 0.003\dot{m}_w$.

- Data Acquisition System (DAS)

There is also the uncertainty related to the DAS where the sensors measuring the inlet water temperature as well as the inlet air temperature and relative humidity are connected to. The DAS itself has a defined uncertainty in indicating the value of the measured signal. This uncertainty is studied separately and it is noticed that it is very small in comparison with that given by the

sensors themselves hence the uncertainty related to the DAS is going to be neglected. In addition to the above mentioned uncertainties there are the uncertainties related to the output measurements.

- Outlet air temperature (°C) and relative humidity (%)

The outlet air temperature and relative humidity are measured by a different hygrometer data logger and its calibration certificate states an uncertainty of ±0.3°C at temperature 25°C and ±2% for a relative humidity measured at 25°C. So similar to the inlet PDFs, the PDFs of the outlet air temperature and relative humidity are taken as the value of the measured temperature or relative humidity and the standard deviation is 0.3°C or 2% respectively.

- Outlet water temperature (°C)

The outlet water temperature is measured by the same thermocouple as the inlet water temperature with a certificate stating an uncertainty of ±0.5°C. So the mean of the PDF is the value of the measured water temperature and the standard deviation is 0.5.

Table 3.15 shows the different uncertainties presented on the inlet and output parameters on one experiment to express explicit values.

Table 3.15: A summary of the Gaussian PDF for all input uncertainties of EXP18

Input source	Type	PDF	PDF parameters		
			Mean	std	Uncertainty (%)
Air mass flow rate channel 4 (kg/s)	A&B	Gaussian	0.01786	$8.851x10^{-4}$	4.95
Air mass flow rate channel 9 (kg/s)	A&B	Gaussian	0.01248	$6.664x10^{-4}$	5.34
Air mass flow rate channel 12 (kg/s)	A&B	Gaussian	0.01651	$7.859x10^{-4}$	4.76
Inlet Air Temperature (°C)	B	Gaussian	28.8	0.3	-
Inlet Relative Humidity (%)	B	Gaussian	72.8	3	-
Inlet Water Temperature (°C)	B	Gaussian	37.3	0.5	-
Water Mass Flow Rate (kg/s)	B	Gaussian	0.01011	$3.03x10^{-5}$	-
Outlet Air Temperature channel 4 (°C)	B	Gaussian	30.5	0.3	-
Outlet Relative Humidity channel 4 (%)	B	Gaussian	79	2	-
Outlet Air Temperature channel 9 (°C)	B	Gaussian	30.9	0.3	-
Outlet Relative Humidity channel 9 (%)	B	Gaussian	85	2	-
Outlet Air Temperature channel 12 (°C)	B	Gaussian	30.6	0.3	-
Outlet Relative Humidity channel 12 (%)	B	Gaussian	83.8	2	-
Outlet Water Temperature (°C)	B	Gaussian	32.8	0.5	-

❖ The effect of input uncertainty on the experimental results

The effect of the uncertainty of the combined input and output parameters on the experimental results is studied for every experiment. The total power of the exchanger at the air side is calculated from the sensible and latent heat transfer with $Q_L = \dot{m}_a h_{fg}\, \Delta Y$ and $Q_S = \dot{m}_a C_{p,a} \Delta T_a$. While that at the water side it is calculated form the difference in water temperature entering and leaving the exchanger $Q_w = \dot{m}_w C_{p,w} \Delta T_w$. By adopting a Monte Carlo approach, the new results of the power at the water and the air side (latent and sensible) are calculated for 10,000 times and then the mean and the standard deviation of both powers are deduced. Since the output

measurements are taken at just three channels then the experimental uncertainty analysis is evaluated for these channels only. The following table (table 3.16) shows the different experimental uncertainties on the power at the water and the air side for channels 4, 9 and 12.

Table 3.16: Uncertainties on the experimental results at the water side and the air side

Uncertainty (%)	Q_w	$Q_{L,4}$	$Q_{S,4}$	$Q_{L,9}$	$Q_{S,9}$	$Q_{L,12}$	$Q_{S,12}$
EXP5	14.88	18.72	12.7	11.66	10.55	12.26	10.69
EXP6	14.75	16.73	11.5	11.29	10.22	11.27	10.49
EXP7	15.95	19.32	13.78	11.91	10.92	13.58	11.92
EXP8	15.86	16.26	11.88	11.44	10.2	10.63	9.82
EXP9	19.63	20.13	13.76	12.51	11.27	13.41	11.41
EXP14	12.7	27.12	18.47	23.74	20.89	26.19	22.97
EXP15	14.62	33.55	18.81	26.21	20.3	29.32	21.5
EXP16	14.69	29.63	21.48	21.57	21.83	25.64	24.58
EXP17	15.29	28.43	22.19	23.74	20.89	23.74	23.86
EXP18	15.63	29.69	25.44	19.35	20.85	21.9	24.54

3.5.4.2 Model uncertainties

The percentage difference between the predicted and the actual values concerning the total power ranges between -2.2% and -16.2% for full air speed and between -14.46% to -26.47% for low air speed as the water mass flow rate increases from 7.3 lpm to 9.1 lpm. To understand the origin of this difference, a local assessment is done on the parameters that have an influence on the model's output.

❖ **Parametric assessment**

At first, there is the uncertainty due to the measured values similar to those of the experimental uncertainty. The uncertainties related to the inlet air temperature and relative humidity and to the inlet water temperature and flow rate influence the results of the model and their impact is studied and analyzed in tables 3.17 and 3.18.

Second, there is the uncertainty due to the input conditions mainly the uncertainty related to the air speed or the air flow rate. This uncertainty is also studied separately to check its influence on our numerical results.

Last, reconsider chapter 2 where the mass conductivity of the membrane k_m was tested experimentally. It was recognized that k_m is an important factor in the formula of the mass transfer coefficient U_M and thus its value has an influence on the total power of the exchanger. An uncertainty analysis assessment was carried out on k_m and the previous calculations gave an uncertainty of 18.23% which seems to be a large value. Therefore, an evaluation of the influence of this uncertainty on the results of the power of the exchanger should be done. For the installed membrane the mean mass conductivity $k_{m,mean}$is 4.3×10^{-6} kg/m.s with a standard deviation 7.84×10^{-7} kg/m.s. In order to determine the impact of this uncertainty on the numerical results, simulations are performed by changing k_m in the model through a Gaussian distribution and then adopting a Monte Carlo approach to evaluate the total power change (at the water side and the air side). The evaluation of the uncertainty on the model is performed only on two experiments to

have an idea about the order of magnitude of the effect of the different uncertainties on the numerical forecasted results. These two experiments are EXP9 and EXP18 having a water mass flow rate of 9.1 lpm at low and high air speed respectively. They were chosen to be thoroughly studied because as seen previously these two experiments possess the highest percentage difference between the model predictions and the experimental results when comparing the total power given by the exchanger.

All the input parameters of EXP9 and EXP18 are represented by their Gaussian PDF's in the following tables. The uncertainty on the air mass flow rate for every channel was mentioned earlier in table 3.14 for the experiments performed at low and high air speed and thus in the following tables (tables 3.17 and 3.18) it is only indicated for one channel.

Table 3.17: A summary of the Gaussian PDF for all input uncertainties of EXP9

Input source	Type	PDF	PDF parameters		
			Mean	std	Uncertainty (%)
Membrane Mass conductivity (kg/m.s)	A	Gaussian	4.3×10^{-6}	7.84×10^{-7}	18.23
Air mass flow rate channel 1 (m^3/h)	A&B	Gaussian	17.21	1.40	8.15
Air Inlet Temperature (°C)	B	Gaussian	26.37	0.3	
Inlet Relative Humidity (%)	B	Gaussian	81.73	3	
Water Temperature (°C)	B	Gaussian	36.85	0.5	
Water Mass Flow Rate (kg/s)	B	Gaussian	0.01011	$3.03x10^{-5}$	0.3

Table 3.18: A summary of the Gaussian PDF for all input uncertainties of EXP18

Input source	Type	PDF	PDF parameters		
			Mean	std	Uncertainty (%)
Membrane Mass conductivity (kg/m.s)	A	Gaussian	4.3×10^{-6}	7.84×10^{-7}	18.23
Air mass flow rate channel 1 (m^3/h)	A&B	Gaussian	44.41	2.25	5.07
Air Inlet Temperature (°C)	B	Gaussian	28.79	0.3	
Inlet Relative Humidity (%)	B	Gaussian	72.76	3	
Water Temperature (°C)	B	Gaussian	37.26	0.5	
Water Mass Flow Rate (kg/s)	B	Gaussian	0.01011	$3.03x10^{-5}$	0.3

❖ **Effect of input uncertainty on the numerical results**

The effects of the uncertainty of the measured values, of the input conditions and of k_m on the total power of the exchanger as predicted by the model are analyzed separately in tables 3.19 and 3.20.

At first, we introduce the PDF's of the measured values in the model through Python and run the simulations in Dymola for 10,000 times. Each simulation computes a value of the total load at the water side as well as the latent and sensible loads for channels 4, 9 and 12.

Then, we keep the measured values constant and change the air mass flow rate according to its deduced PDF and repeat the same procedure. Finally, we set the measured values and the input

conditions as constants and change k_m according to the Gaussian distribution and find the predicted power at the air and water sides.

These tables represent the effects of the uncertainties of the measured values, the input parameters and of the membrane mass conductivity separately on the power of the exchanger at the water side and the air side. Then these uncertainties are all combined together to examine their overall influence on the power and in each table a resulting average value, a standard deviation and an uncertainty is provided.

Table 3.19: The effect of different input uncertainties on the numerical results at water and air side for EXP9

	Total power	$Q_{L,4}$	$Q_{S,4}$	$Q_{L,9}$	$Q_{S,9}$	$Q_{L,12}$	$Q_{S,12}$
Uncertainty on measured values							
Average (W)	1708.81	101.70	21.68	86.15	17.91	92.12	19.32
Std (W)	95.30	5.81	1.25	4.95	1.03	5.28	1.11
Uncertainty (%)	5.58	5.71	5.75	5.75	5.74	5.74	5.74
Uncertainty on $\dot{m}_a$							
Average (W)	1706.68	101.60	21.68	86.01	17.89	92.00	19.31
Std (W)	8.47	1.64	0.41	2.00	0.47	1.92	0.46
Uncertainty (%)	0.50	1.62	1.91	2.32	2.61	2.08	2.39
Uncertainty on k_m							
Average (W)	1700.33	101.05	21.70	85.66	17.92	91.57	19.34
Std (W)	53.78	4.21	0.12	3.01	0.06	3.45	0.08
Uncertainty (%)	3.16	4.17	0.55	3.52	0.36	3.77	0.43
Uncertainty on all							
Average (W)	1700.59	101.09	21.69	85.68	17.91	91.62	19.33
Std (W)	109.33	7.35	1.31	6.14	1.13	6.59	1.20
Uncertainty (%)	6.43	7.27	6.04	7.17	6.29	7.19	6.23

Table 3.20: The effect of different input uncertainties on the numerical results at water and air side for EXP18

	Total power	$Q_{L,4}$	$Q_{S,4}$	$Q_{L,9}$	$Q_{S,9}$	$Q_{L,12}$	$Q_{S,12}$
Uncertainty on measured values							
Average (W)	2455.51	148.92	35.88	128.85	29.37	144.81	34.47
Std (W)	136.07	8.46	2.12	7.39	1.72	8.24	2.03
Uncertainty (%)	5.54	5.68	5.91	5.74	5.85	5.69	5.89
Uncertainty on $\dot{m}_a$							
Average (W)	2387.73	152.64	27.23	131.52	22.47	148.27	26.20
Std (W)	15.46	2.68	0.64	3.39	0.73	2.68	0.62
Uncertainty (%)	0.65	1.76	2.33	2.58	3.23	1.81	2.37
Uncertainty on k_m							
Average (W)	2377.38	151.60	27.29	130.84	22.54	147.35	26.27
Std (W)	106.31	9.14	0.50	6.79	0.29	8.63	0.45
Uncertainty (%)	4.47	6.03	1.85	5.19	1.28	5.85	1.72
Uncertainty on all							
Average (W)	2371.08	151.29	27.26	130.46	22.48	146.98	26.22
Std (W)	174.75	12.95	2.26	10.70	1.85	12.46	2.15
Uncertainty (%)	7.37	8.56	8.27	8.21	8.25	8.47	8.21

3.5.4.3 Domain of uncertainty numerically versus experimentally

The domain of uncertainty is assessed on the exchanger's total power at the water side and the air side.

➢ Total power at the water side

The domain of uncertainty on the total power at the water side; experimentally and numerically is shown in the graph of figure 3.15 for both experiments.

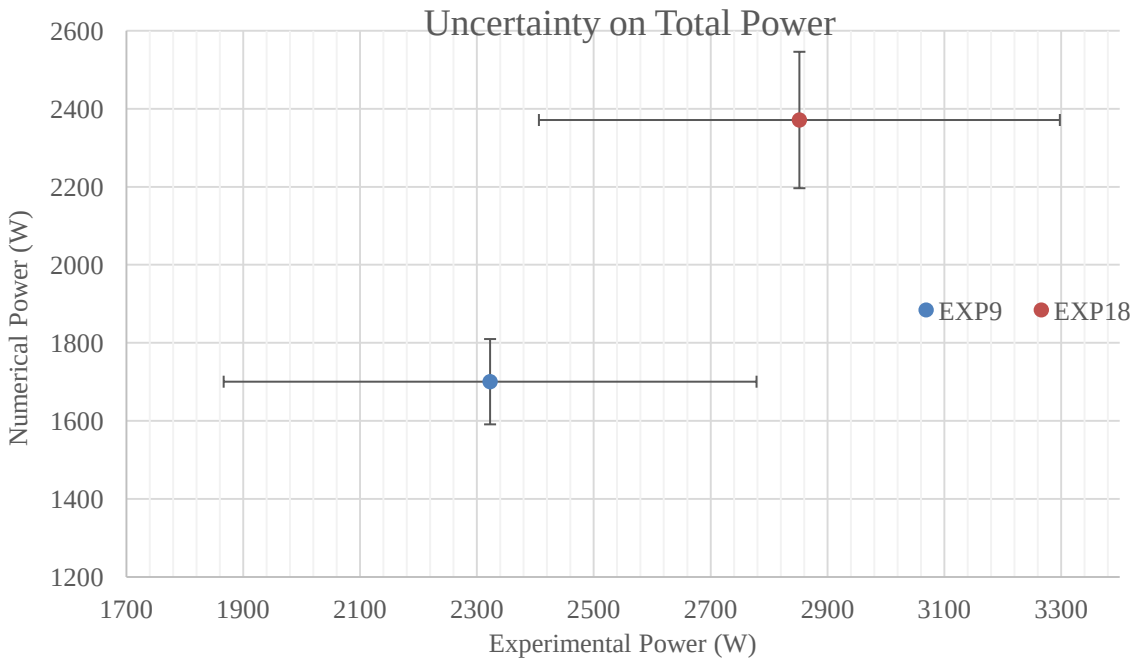

Figure 3.15: Uncertainty on the total power numerically and experimentally (water side)

➢ Power at the air side

The following graphs (fig. 3.16) represent the uncertainty on the power at the air side (sensible and latent) for the three studied channels.

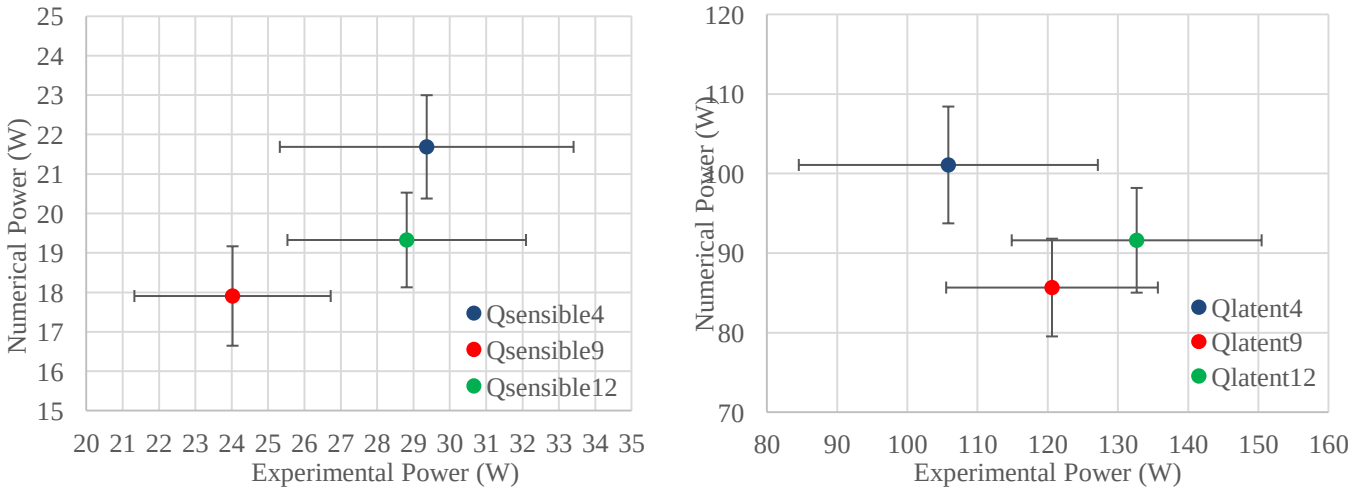

(a)

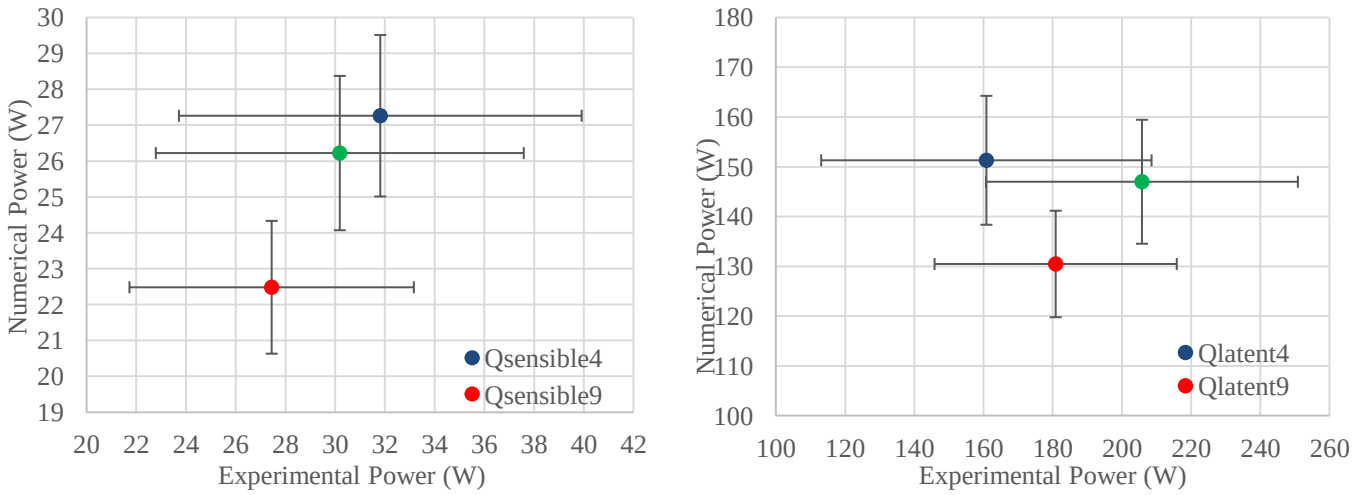

(b)

Figure 3.16: Uncertainty on the sensible and latent loads of a) EXP9 and b) EXP18

Analysis

As a conclusion, the total uncertainty on the output power due to the uncertainty of the measured values, on the input conditions and on the mass conductivity of the membrane is 6.43% for EXP9 7.37% for EXP18. In fact, the real error is greater than this value as it can be noticed from the comparison between the total predicted power and the measured power. It is around 26.47% and 16.2% for EXP9 and EXP18 respectively.

This means that the residual error may be due to the suggested correlations of the heat transfer. From the calculations, it can be noticed that the heat transfer coefficient of water is highly greater than that of air especially in the experiments done at low air speed then the resistance at the water side is small in comparison with that at the air side. Therefore, in a way to optimize our model and reduce the percentage difference and between the model and the experiment, we try to modify the heat transfer correlation at the air side and examine its influence on the numerical results.

3.5.5 Air side heat transfer coefficient correction

When creating a predictive model an error function is optimized to minimize the difference between the predicted and actual value. The value of the error represents the precision of the forecasted value and in a way to improve the accuracy of our model and to better predict the experimental results optimizing MAE is essential. In the field of forecasting, minimizing MAE is a highly used method. To minimize MAE, we apply an improvement on the air side heat transfer correlations that were adopted in our model. For the experiments performed at low air speed, we multiply the Nusselt correlation of eq. (3.95) with a factor α. While for the experiments done at high air speed, we modify the value of γ that was previously indicated in eq. (3.96).

3.5.5.1 Optimization of MAE for the first set of experiments carried out at low air speed

Let α be the coefficient by which the air heat transfer coefficient is multiplied. Now try to find a value of α that corresponds to the lowest value of MAE. Through Python, we run the simulations

in Dymola for 1,000 times each time finding a value of MAE through the Monte Carlo approach. The results indicate that for a value of $\alpha = 1.59$, MAE would have a minimum value corresponding to 0.038. Table 3.21 represents the total power as measured experimentally and predicted numerically when $\alpha = 1$ and $\alpha = 1.59$.

Table 3.21: The percentage difference between the predicted and the actual results after optimization for experiments done at low air speed

Power (W)	Experiment	Model $\alpha = 1$	Model $\alpha = 1.59$	Optimized percentage difference (%)
EXP5	2431.95	2019.2	2515.3	3.43
EXP6	2605.8	2228.9	2775.68	6.52
EXP7	2499	1994.91	2494.5	-0.18
EXP8	2699.4	2105.08	2640.07	-2.20
EXP9	2322.75	1707.94	2152.42	-7.33

3.5.5.2 Optimization of MAE for the second set of experiments carried out at high air speed

For the tests carried out at high air speed, the entrance coefficient $(1 + \left(\gamma \frac{D}{L}\right)^{\frac{2}{3}})$ of eq. (3.96) where $\gamma = \frac{34{,}500}{Re}$ suggested is modified. A new value of γ is determined by means of optimization and minimizing the value of MAE. The same is done through Python and simulations are repeated 1,000 times each time changing γ and searching for the lowest value of MAE. The optimal result converges towards a value of MAE=0.0397 when $\gamma = \frac{69{,}500}{Re}$. The following table (table 3.22) summarizes the experimental power and that predicted by the model for $\gamma = \frac{34{,}500}{Re}$ and $\gamma = \frac{69{,}500}{Re}$.

Table 3.22: The percentage difference between the predicted and the actual results after optimization for experiments done at low high speed

Power (W)	Experiment	Model $\gamma = \frac{34{,}500}{Re}$	Model $\gamma = \frac{69{,}500}{Re}$	Optimized percentage difference (%)
EXP14	2851.5	2786.2	3089.95	8.36
EXP15	2626.35	2428.85	2703.44	2.94
EXP16	2769.75	2489.64	2774.17	0.16
EXP17	2804.46	2442.6	2727.01	-2.76
EXP18	2852.1	2390.15	2672.15	-6.31

Results

Figure 3.17 represents the distribution of the predicted power versus the experimental power of all the conducted experiments after optimizing the correlations of the heat transfer coefficients.

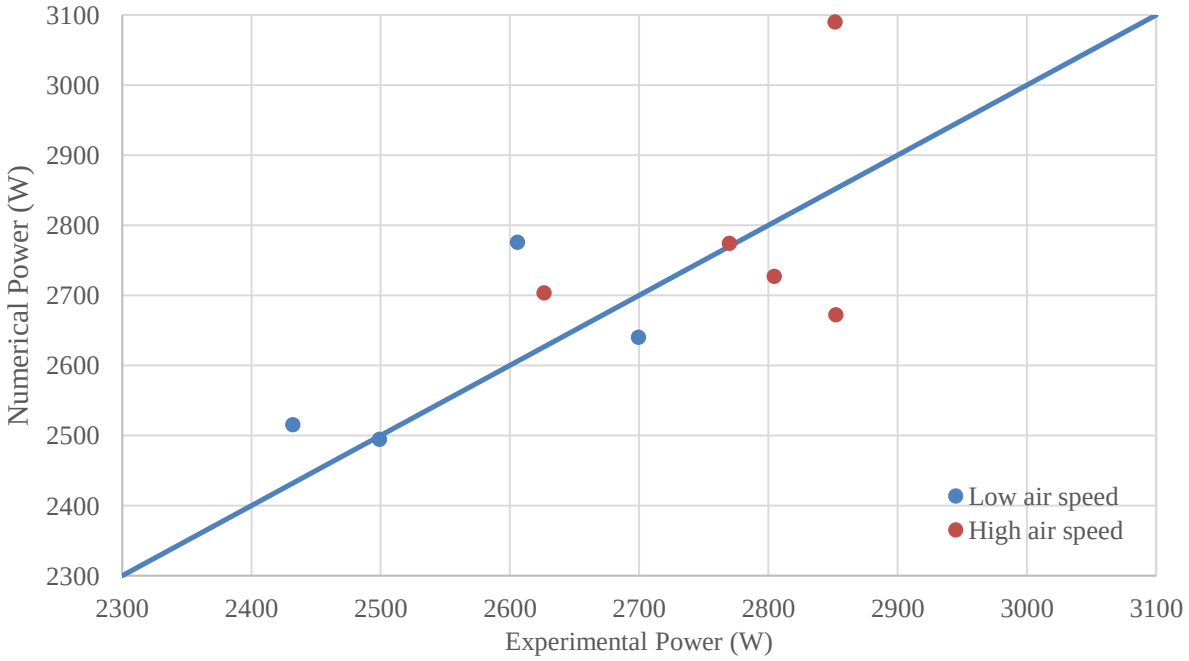

Figure 3.17: Predicted versus experimental power distribution for all experiments after optimization

For a detailed comparison at the air side as well, EXP9 and EXP18 are studied. Table 3.23 summarizes the outlet air and water conditions as measured experimentally and numerically for $\alpha = 1$ and $\alpha = 1.59$ in EXP9 while table 3.24 summarizes them for $\gamma = \frac{34{,}500}{Re}$ and $\gamma = \frac{69{,}500}{Re}$ in EXP18.

Table 3.23: Detailed comparison of the numerical results before and after optimization for EXP9

		Experiment			Model $\alpha = 1$			Model $\alpha = 1.59$		
		Ch 4	Ch 9	Ch 12	Ch 4	Ch 9	Ch 12	Ch 4	Ch 9	Ch 12
Inlet air	T_a (°C)	26.4	26.4	26.4	26.4	26.4	26.4	26.4	26.4	26.4
	RH (%)	81.7	81.7	81.7	81.7	81.7	81.7	81.7	81.7	81.7
	Y (g/kg)	17.6	17.6	17.6	17.6	17.6	17.6	17.6	17.6	17.6
	$\dot{m}_a$ (g/s)	8.4	5.1	6.0	8.4	5.1	6.0	8.4	5.1	6.0
Inlet water	$\dot{m}_w$ (g /s)	10.1	10.1	10.1	10.1	10.1	10.1	10.1	10.1	10.1
	T_w (°C)	36.9	36.9	36.9	36.9	36.9	36.9	36.9	36.9	36.9
Outlet air	T_a (°C)	29.7	30.9	30.9	28.9	29.9	29.5	29.7	30.9	30.5
	RH (%)	86.4	96.5	93.6	90.4	93.3	92.1	90.5	93.4	92.3
	Y (g/kg)	22.9	27.6	26.6	22.9	25.0	24.1	24.0	26.7	25.6
	Q_L (W)	105.8	120.6	132.7	103.2	87.6	93.6	126.4	107.1	114.6
	Q_S (W)	29.4	24.0	28.8	22.0	18.2	19.6	28.9	23.6	25.6
	Q_{Ta} (W)	135.2	144.6	161.5	125.2	105.8	113.2	155.3	130.7	140.2
Outlet water	T_w (°C)	33.2			34.0	34.4	34.2	33.3	33.8	33.6
	Q_{Tw} (W)	2322.8			1734.6			2152.4		

Table 3.24: Detailed comparison of the numerical results before and after optimization for EXP18

		Experiment			Model $\alpha = 1$			Model $\alpha = 1.59$		
		Ch 4	Ch 9	Ch 12	Ch 4	Ch 9	Ch 12	Ch 4	Ch 9	Ch 12
Inlet air	T_a (°C)	28.8	28.8	28.8	28.8	28.8	28.8	28.8	28.8	28.8
	RH (%)	72.8	72.8	72.8	72.8	72.8	72.8	72.8	72.8	72.8
	Y (g/kg)	18.1	18.1	18.1	18.1	18.1	18.1	18.1	18.1	18.1
	$\dot{m}_a$ (g/s)	17.9	12.5	16.5	17.9	12.5	16.5	17.9	12.5	16.5
Inlet water	$\dot{m}_w$ (g /s)	10.1	10.1	10.1	10.1	10.1	10.1	10.1	10.1	10.1
	T_w (°C)	36.9	36.9	36.9	36.9	36.9	36.9	36.9	36.9	36.9
Outlet air	T_a (°C)	30.5	30.9	30.6	30.3	30.6	30.4	30.5	30.9	30.6
	RH (%)	79 .04	85.0	83.8	79.7	81.4	80.1	80.0	81.9	80.4
	Y (g/kg)	21.9	24.1	23.3	21.8	22.6	22.0	22.1	23.2	22.4
	Q_L (W)	160.8	180.8	205.8	152.7	131.7	148.4	167.2	147.6	163.3
	Q_S (W)	31.8	27.4	30.2	27.2	22.5	26.2	31.0	26.2	30.0
	Q_{Ta} (W)	192.6	208.3	235.9	179.9	154.2	174.6	198.2	173.9	193.3
Outlet water	T_w (°C)	32.8			33.1	33.7	33.2	32.7	33.2	32.8
	Q_{Tw} (W)	2852.1			2390.2			2672.2		

3.6 Conclusion

In this chapter, a numerical model of the novel exchanger is developed and a prototype is built and tested. The tests performed with water demonstrated the feasibility of the new design and allowed to determine its performance. Measured data were also used to validate and tune the numerical model.

As a conclusion, the percentage difference between the power predicted by the model and that calculated experimentally, is at its maximum values of 26.47% for EXP9 and 16.2% for EXP18. Among this difference, the intrinsic uncertainties constitute around 6 to 7% of the total uncertainty. In a way to reduce this difference, we proposed a modification of the correlations related to the heat transfer coefficient at the air side (being the most influencing on the overall heat transfer coefficient) and we solved for an optimized value of MAE. The results indicate that after the optimization the percentage difference was reduced to 7.33% for EXP9 and 6.3% for EXP18. Moreover, the difference between the numerical and experimental outcomes concerning the air temperature and absolute humidity are also acceptable. Thus the suggested model can be considered as a credible and predictive tool that might be applicable to determine the performance of a similar membrane based heat and mass exchanger. Yet, the performed experiments are insufficient to generalize this conclusion for all possible scenarios and hence more experiments should be carried out to validate the model and prove its accuracy for several other cases. In further steps, some parameters might be changed such as expanding the range of the water flow rate where the upper limit is affected by the power of the resistor as mentioned before and the lower limit is influenced by the range of the working pressure of the nozzles. Moreover, other design parameters can be changed such as the number of channels or the width of a channel of the exchanger. For more accurate measurements, other experiments can be done

with more precise sensors or with the presence of an outlet air duct to obtain better readings on the air side. Finally, the prototype should be operated with a desiccant solution instead of water to check its operation with the salt.

In the following chapter, the validated model is used to build a hybrid system model and study its performance in an air conditioning application.

Chapitre 4 Étude de Cas : Une Conception Flexible d'un Système de Climatisation Hybride dans un Bureau (résumé)

4.1 Introduction

Dans les bâtiments, la climatisation est principalement assurée par des systèmes de compression de vapeur avec un nombre croissant d'unités de climatisation installées, comme indiqué au chapitre 1. Pourtant, ces systèmes sont inefficaces pour contrôler l'humidité à l'intérieur des bâtiments. D'autres systèmes, tels que les systèmes hybrides, ont été étudiés dans le but d'améliorer la performance énergétique en intégrant les échangeurs membranaires de chaleur et de masse dans les systèmes traditionnels de climatisation. Ces systèmes hybrides ont gagné un intérêt croissant en raison de leur refroidissement efficace en contrôlant séparément les charges latentes et sensibles, et donc de leur consommation réduite d'électricité. Toutefois, la performance de ces systèmes dépend radicalement des conditions opératoires dans lesquelles le rapport entre la charge latente et la charge sensible à l'intérieur du bâtiment change en conséquence, comme indiqué au chapitre 1. Ainsi, dans les applications où un rapport de charge latente-sensible non constant est requis, ces systèmes font preuve d'un manque de flexibilité. Dans ce cas, il pourrait être possible d'utiliser la configuration du système hybride citée dans les recherches de Bergero et Chiari (Bergero et Chiari, 2011) qui offre une performance très efficace sur une gamme des conditions opératoires en fonction du rapport entre la charge latente et la charge sensible mais cette gamme reste insuffisante.

Dans ce chapitre, un système hybride est utilisé pour effectuer la climatisation saisonnière d'un bureau dans un immeuble du sud de la France. Ce système est composé d'un cycle de desiccant liquide et d'un cycle de compression de vapeur. Le modèle précédemment suggéré et validé dans le chapitre 4 est utilisé pour évaluer la performance des échangeurs de chaleur et de masse du cycle du desiccant. Le présent chapitre a pour but d'analyser le comportement des différentes architectures en régime permanent et de comparer leur performance par une simulation saisonnière d'un bureau situé à Nice (43,3°N, 5,4°E). Plusieurs architectures sont proposées et les résultats sont comparés à ceux d'un cycle de compression de vapeur classique. Ce chapitre décrit chaque composant du cycle de compression de vapeur ainsi que ses équations de modélisation. Ensuite, un modèle complet est utilisé pour évaluer la performance de chaque architecture du système hybride dans les différents mois de l'année où le refroidissement est nécessaire. Les conclusions de ce chapitre donneraient un aperçu de la contribution des systèmes hybrides à la réduction du coût de l'énergie lorsqu'ils sont convenablement appliqués dans les bâtiments.

4.2 Description du bâtiment

Le bureau est situé au troisième étage dans un immeuble de 5 étages à Nice d'un climat méditerranéen : les températures étant élevées en été et modérées au printemps et en automne.

Chaque étage a une hauteur de 3 m et une superficie de 100 m^2. L'enveloppe de l'immeuble représente réellement celles des bâtiments à Nice. Les horaires d'occupation, d'activité, d'éclairage, d'équipement de bureau et de système de HVAC sont proposés pour chaque pièce selon l'occupation des bureaux (entre 9 et 18 h). Chaque mois, les conditions ambiantes et l'humidité relative de l'air à l'intérieur du bureau changent. La figure 1 montre la température mensuelle et l'humidité relative de l'air ambiant ainsi que l'humidité relative mensuelle de l'air intérieur. La température du point de refroidissement intérieur est fixée à 24 °C et le bâtiment est simulé à l'aide de Designbuilder qui utilise EnergyPlus comme outil d'interface.

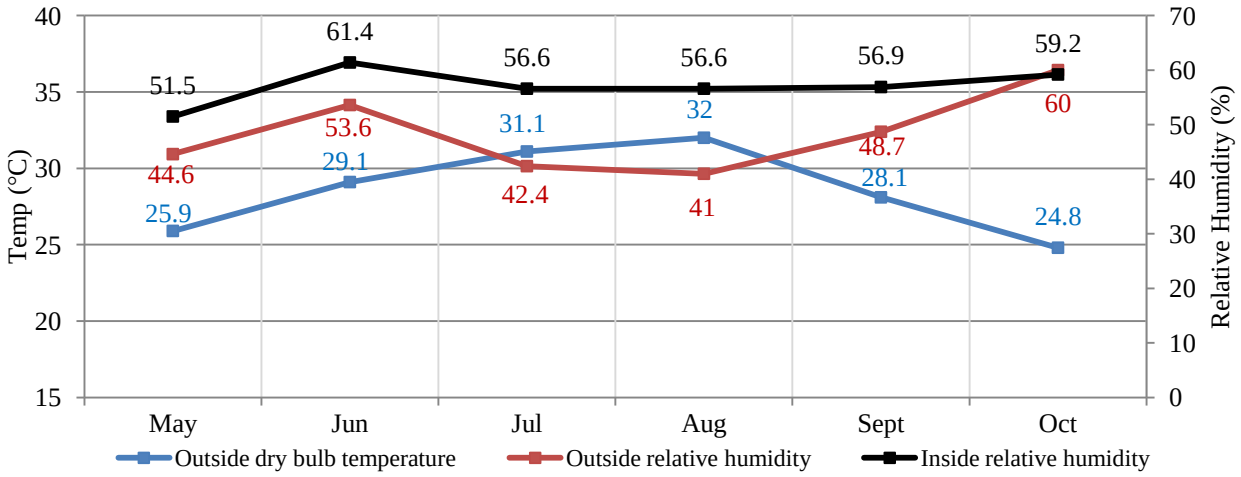

Figure 18: Température et humidité relative de chaque mois

La charge de climatisation est calculée pour 6 mois de l'année où le refroidissement est nécessaire de mai à octobre. La charge de climatisation totale à l'intérieur du bureau varie d'un mois à l'autre, comme le montre la figure 2, et elle est divisée en charges latente et sensible. Le rapport de la charge latente sur la charge sensible (R') varie comme présenté dans la figure 2.

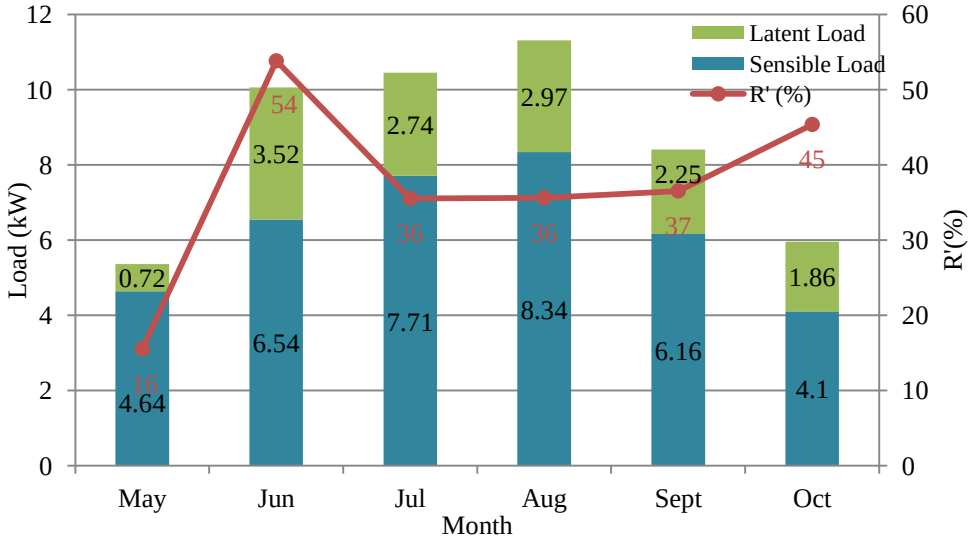

Figure 19: Distribution mensuelle de la charge de refroidissement

4.3 Refroidissement et déshumidification dans la configuration du cas de base

Le contrôle du refroidissement et de l'humidité de ce bureau est en fait effectué en utilisant le cycle conventionnel de compression de vapeur.

Comme le montre la figure 3, ils sont constitués d'un compresseur, d'un condenseur, d'un détendeur et d'un évaporateur où le réfrigérant R-134a est le fluide de travail dans notre cas. Comme nous l'avons déjà mentionné, la réduction de la température de l'air en dessous de son point de rosée diminue l'efficacité du cycle et, dans certains cas, lorsque des niveaux d'humidité très faibles sont requis l'utilisation d'un tel système traditionnel ne serait plus possible.

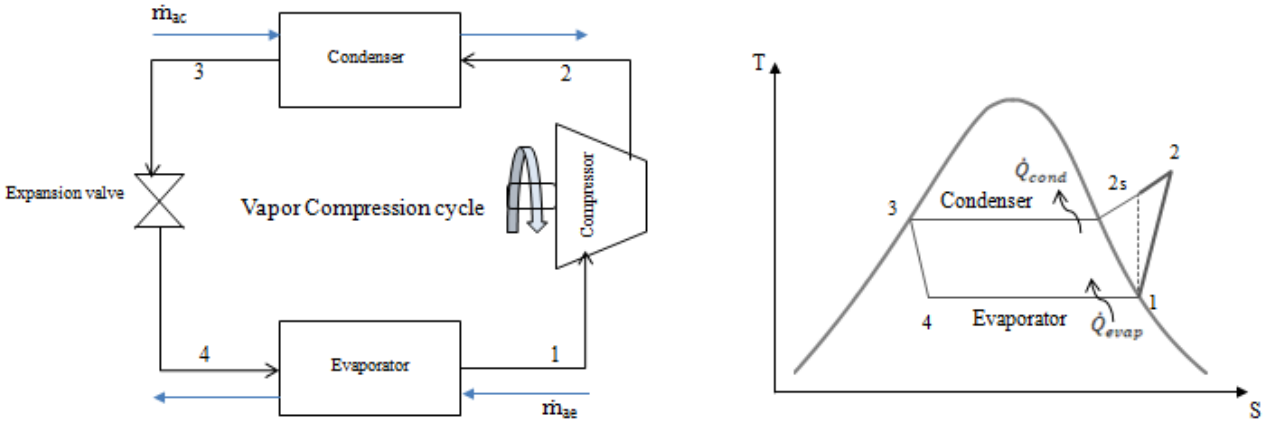

Figure 320: Cycle de compression de vapeur avec un diagramme T-S

Les débits mensuels de masse d'air, les charges latente et sensible, la consommation d'énergie et la COP d'un tel système sont présentés dans le tableau 1.

Table 25: Charges enlevées par le cycle de compression de vapeur

Mois	$\dot{m}_{a1}$ (m^3/h)	$Q_{L,\ required}$ (W)	Q_L (W)	Q_S (W)	Consommation totale (kW)	$COP_{overall}$
Configuration du cas de base						
Mai	650	720	640	4640	1.48	3.58
Juin	910	3520	3379	6540	3.05	3.26
Juillet	1080	2740	2590	7710	3.34	3.08
Aout	1160	2970	2808	8340	3.73	2.99
Septembre	860	2250	2129	6160	2.47	3.35
Octobre	575	1860	1775	4100	1.58	3.72

Les résultats obtenus pour un tel système ont montré que, pour une température et une humidité relative intérieures fixes, il est impossible d'évacuer la charge latente exigée, sauf à des températures d'évaporation extrêmement basses. Ce qui réduirait considérablement le coefficient de performance (COP) du système. Dans notre cas, nous avons choisi de limiter la température d'évaporation à 0°C permettant de cette façon d'assurer la charge latente d'environ 88% à 96% avec un COP entre 3 et 3,6 pendant les 6 mois.

Cela a mis en évidence la limite des systèmes traditionnels à atteindre les conditions d'entrée désirées et l'intérêt de la recherche de systèmes alternatifs capables de résoudre ce problème. Par

conséquent, on a proposé un système hybride flexible de compression de vapeur à base de desiccant liquide. Ce système participe à l'élimination de la charge latente par déshumidification et de la charge sensible par refroidissement grâce à la compression de vapeur. Les systèmes hybrides communément utilisés ont d'abord été exposés et les échangeurs de chaleur ont ensuite été intégrés aux systèmes pour améliorer leur performance et leur flexibilité.

4.4 Systèmes hybrides communs

Ils sont composés d'un cycle de compression de vapeur et d'un cycle de dessiccant liquide ayant pour rôle l'élimination de toute la charge latente et d'une partie de la charge sensible (fig.4).

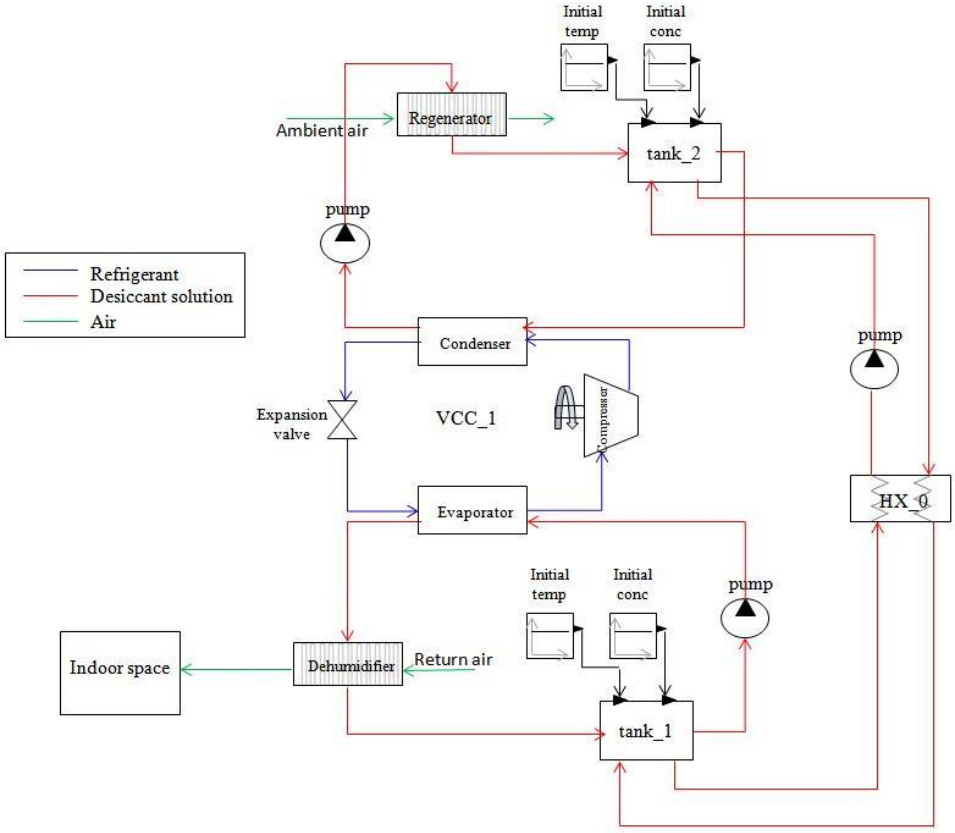

Figure 21: Schéma d'un système hybride avec réservoirs de stockage

Le système de dessiccation liquide est principalement constitué d'un cycle de déshumidification et d'un cycle de régénération. Le premier consiste en un déshumidificateur, un réservoir de stockage et une pompe. Le déshumidificateur est un échangeur membranaire de masse et de chaleur à flux croisé. La solution de dessiccation (LiCl) absorbe l'humidité de l'air à cause de la différence de pression de vapeur entre la surface du desiccant et l'air. La réactivation du dessiccant est obtenue par un processus de régénération qui maintient la concentration de la solution. Dans le régénérateur, l'eau absorbée pendant le processus de déshumidification est retirée de la solution. Le cycle de régénération est constitué d'un régénérateur (qui est aussi un échangeur membranaire de masse et de chaleur à flux croisé), d'une pompe et d'un réservoir de stockage. Ce cycle utilise la chaleur excessive fournie par le condenseur du cycle de compression de vapeur pour chauffer la solution avant qu'elle n'entre dans le régénérateur. L'évaporateur du

cycle de compression de vapeur sert à refroidir la solution dessiccante qui, à son tour, refroidit et déshumidifie l'air simultanément. Le réservoir du cycle de déshumidification (tank_1) est utilisé pour stocker la solution diluée sortant du déshumidificateur et elle est continuellement pompée au régénérateur pour être réactivée. Le réservoir du cycle de régénération (tank_2) sert à stocker la solution concentrée qui est de nouveau pompée au cycle de déshumidification pour absorber la vapeur d'eau de l'air. La concentration de la solution diluée trouvée dans tank_1 est toujours ajustée en ajoutant une solution plus concentrée dans tank_2.

Afin d'augmenter la flexibilité du système hybride communément utilisé décrit précédemment, on a proposé une conception plus avancée qui pourrait optimiser le traitement des charges latentes et sensibles.

4.5 Systèmes hybrides flexibles proposés

Dans notre nouveau système, des échangeurs de chaleur ont été ajoutés contribuant à l'échange de la chaleur sensible avec l'air traité ou avec l'air ambiant. L'emplacement de ces échangeurs de chaleur a une conséquence sur les performances énergétiques, par conséquent, différentes configurations ont été étudiées. La première (fig.5) consiste à ajouter des échangeurs de chaleur avant le déshumidificateur et le régénérateur alors que la seconde consiste à les insérer après (fig.6).

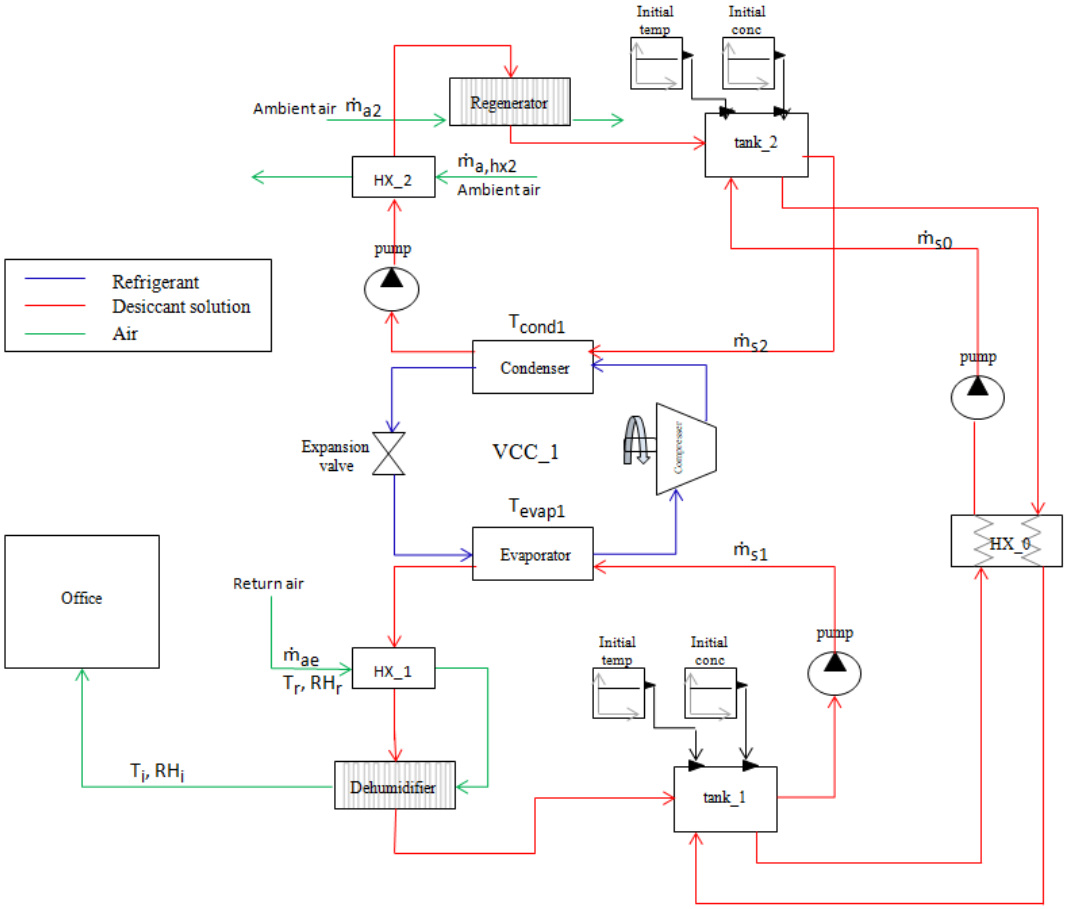

Figure 22: Schéma de la première configuration

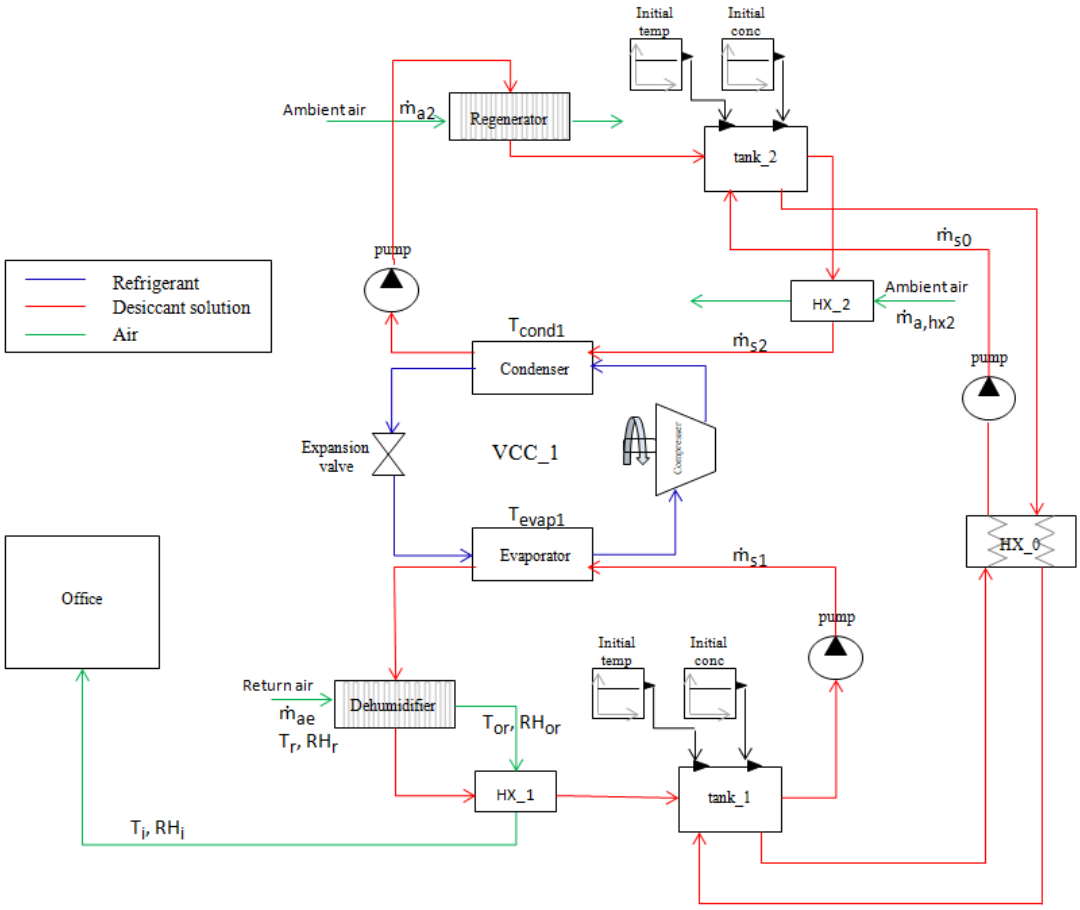

Figure 3.23: Schéma de la deuxième configuration

Une troisième configuration (fig.7) est suggérée où, au lieu d'ajouter des échangeurs, un deuxième cycle de compression de vapeur est inséré après le cycle de déshumidification. Dans ce troisième cas, l'évaporateur du cycle de compression ajouté joue le rôle de l'échangeur de chaleur de la deuxième configuration.

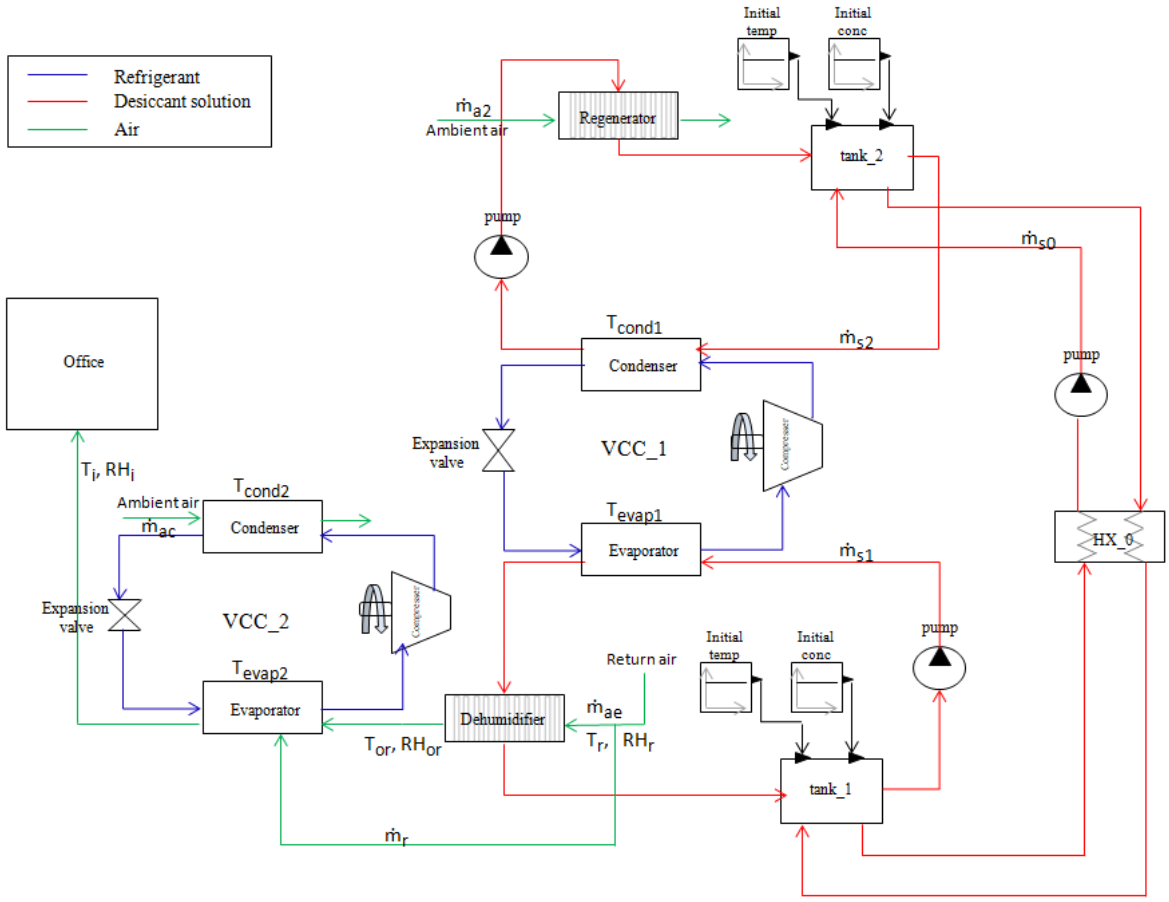

Figure 24: Schéma de la troisième configuration

Dans toutes les configurations, le déshumidificateur supprime la totalité de la charge latente et une partie de la charge sensible. La charge sensible restante est évacuée par les échangeurs de chaleur dans les deux premières configurations et par le cycle de compression de vapeur dans la troisième configuration. Afin d'évaluer la performance d'un tel système et d'estimer sa capacité à évacuer toute la charge latente et sensible, le modèle du système est réalisé intégrant le modèle de l'échangeur de chaleur et de masse validé dans le chapitre précédent. Les modèles des autres composants de ce système (le cycle de compression de vapeur, les échangeurs de chaleur, les pompes et les réservoirs) sont aussi brièvement décrits dans ce chapitre

4.5.1 Modélisation du système hybride

Les différentes conceptions des trois configurations conduisent à 18 simulations de sorte que pour chaque configuration, 6 simulations ont été faites, chacune correspond à un mois comme expliqué précédemment. La température de l'air ambiant et l'humidité relative ont été précisées fixées ainsi que les conditions de l'air intérieur et les simulations ont été effectuées en régime permanent. Il y a plusieurs paramètres qui influencent la charge évacuée et sa distribution, notamment la conception du déshumidificateur et du régénérateur ainsi que les débits massiques du réfrigérant, de la solution et de l'air qui circulent dans le système. Les dimensions du déshumidificateur et du régénérateur ont été choisies de manière adaptée aux 18 simulations.

Nous avons fait le choix d’utiliser la même géométrie pour l’ensemble des configurations, vu que l'objectif de cette étude est de montrer la flexibilité relative de chaque conception et le domaine dans lequel son application est la plus efficace. Ces dimensions sont présentées dans le tableau 1.

Tableau 6: Dimensions du déshumidificateur et des régénérateurs dans toutes les configurations

	Nombre de canaux	L	Z
Régénérateur	20	0.4	0.4
déshumidificateur	48	0.5	0.5

4.6 Résultats

Étant donné que le système est complexe avec plusieurs éléments reliés entre eux, des simulations ont été effectuées par le biais d'un logiciel externe, Python. Les simulations ont été réalisées pour chacun des 6 mois des trois configurations et 10 000 itérations ont été opérées. À chaque itération, les paramètres d'entrée qui influent directement ou indirectement les grandeurs d’interêt ont été modifiées jusqu'à ce que les charges mensuelles latentes et sensibles soient totalement retirées du bureau. Parmi les 10 000 résultats obtenus, de nombreuses valeurs ne répondaient pas aux charges sensibles et latentes requises, alors que le reste présente une solution pour notre système proposé. Pour chaque solution acceptable, le COP du système a été calculé, les résultats ont été ordonnés et la combinaison des sources d’entrée correspondant au COP le plus élevé a été choisi.

Le tableau 2 récapitule pour les trois configurations, les valeurs optimales des paramètres d'entrée qui donnent le COP le plus élevé. Il donne également les résultats de sortie, y compris les charges, la consommation d'énergie et le COP. Les conditions de l’air d’alimentation sont également indiquées.

Tableau 7: Résumé des paramètres d'entrée, de sortie et des conditions de l'air d'alimentation dans les trois configurations

	Paramètres d'entrée							Quantités observées						Air d'alimentation	
Mois	$\dot{m}_{s1}$ (kg/s)	$\dot{m}_{s2}$ (kg/s)	$\dot{m}_{s0}$ (kg/s)	$\dot{m}_{ae}$ (m^3/h)	$\dot{m}_{ac}$ (m^3/h)	$\dot{m}_{a,hx2}$ (m^3/h)	T_{evap1} (˚C)	Q_L (W)	Q_S (W)	Q_{S1} (W)	Q_{S2} (W)	Power (kW)	$COP_{overall}$ (-)	T_i (˚C)	RH_i (%)
$1^{ère}$ configuration															
Mai	1	0.5	0.11	2300	175	1600	12.6	722	4630	399	4231	1.27	5.08	18.1	71.1
Juin	2	1.4	0.08	5100	3900	350	14.7	3529	6643	804	5839	3.44	3.19	20.2	71.3
Juillet	1.8	1.7	0.12	4500	2900	2200	13.45	2742	7754	614	7140	3.30	3.55	19.0	71.7
Aout	1.5	1.4	0.09	3200	2000	2200	10.6	2973	8364	283	8081	3.89	3.17	16.3	81.2
Sept	1.7	0.8	0.13	4700	1800	1450	14.7	2247	6149	776	5373	2.43	3.97	20.2	68.0
Oct	1.1	1.2	0.12	2950	2750	420	14.5	1865	4105	528	3577	1.63	4.36	19.9	70.6
$2^{ème}$ configuration															
Mai	1.1	1.1	0.11	4400	115	3500	14.3	721	4647	2766	1881	1.33	4.82	20.9	61.1
Juin	1.8	1.2	0.14	5020	2000	1400	12.5	3520	6545	3784	2761	3.39	3.39	20.1	72.0
Juillet	1.6	0.6	0.13	5100	1400	2200	13.7	2736	7704	3285	4419	2.97	3.94	19.5	69.9
Aout	0.9	0.7	0.04	5900	2000	2800	11.6	2967	8368	4309	4059	3.12	3.75	19.8	69.0
Sept	1.1	1.1	0.07	3400	1600	3150	12.9	2251	6195	2727	3468	2.19	4.16	18.6	73.3
Oct	0.7	0.4	0.13	4550	1000	1500	12.7	1863	4095	3266	829	1.50	4.79	21.3	66.5
$3^{ème}$ configuration															
Month	$\dot{m}_{s1}$ (kg/s)	$\dot{m}_{s2}$ (kg/s)	$\dot{m}_{s0}$ (kg/s)	$\dot{m}_{ae}$ (m^3/h)	$\dot{m}_{ac}$ (m^3/h)	T_{evap1} (˚C)	T_{evap2} (˚C)	Q_L (W)	Q_S (W)	Q_{S1} (W)	Q_{S2} (W)	Power (kW)	$COP_{overall}$ (-)	T_i (˚C)	RH_i (%)
Mai	0.3	0.2	0.14	2700	2100	17.8	17.9	719	4640	719	3921	1.17	5.65	20.9	60.1
Juin	1.2	0.52	0.11	5000	710	16.4	17.8	3524	6540	2069	4471	2.88	3.84	20.8	70.1
Juillet	0.6	0.4	0.11	5000	1100	15.9	16.9	2739	7710	1608	6102	2.71	4.28	19.9	68.7
Aout	0.7	0.5	0.11	5000	2420	14.3	17.3	2969	8340	2863	5477	3.05	4.05	20.3	67.4
Sept	0.5	0.8	0.08	3800	1650	14	16.9	2250	6160	2192	3968	2.04	4.48	19.9	68.0
Oct	0.5	0.5	0.1	5000	860	16.2	18.6	1852	4100	1740	2360	1.37	5.02	21.6	65.8

4.7 Analyses

Les températures d'évaporation et de condensation déterminent le COP du système et dépendent fortement de la concentration de la solution ainsi que des débits massiques de l'air dans le régénérateur, les échangeurs de chaleur et le déshumidificateur. La concentration de solution dans le système varie donc d'un mois à l'autre et ses valeurs dans le cycle de régénération sont indiquées dans le tableau suivant (tableau 3) ainsi que les températures de condensation et d'évaporation.

Tableau 8: Températures de condensation et d'évaporation avec pourcentage de concentration de solution

Mois	T_{cond1} (°C)	T_{evap1} (°C)	T_{cond2} (°C)	T_{evap2} (°C)	Concentration dans le régénérateur (%)
$1^{ère}$ configuration					
Mai	35.01	12.6	--	--	21.61
Juin	50.69	14.65	--	--	30.83
Juillet	45.63	13.35			28.83
Aout	48.48	10.6			29.80
Septembre	43.74	14.65	--	--	27.37
Octobre	39.13	14.45	--	--	26.00
$2^{ème}$ configuration					
Mai	33.83	14.3	--	--	21.47
Juin	47.1	12.5			27.61
Juillet	44.44	13.65			27.62
Aout	44.12	11.55	--	--	27.22
Septembre	40.39	12.9	--	--	26.12
Octobre	36.87	12.65	--	--	21.60
$3^{ème}$ configuration					
Mai	33.06	17.8	36.55	17.88	27.32
Juin	54.64	16.45	39.68	17.1	31.8
Juillet	49.49	15.9	41.83	16.4	30.86
Aout	48.55	14.25	42.51	16.02	30.28
Septembre	42.43	14	38.69	16.91	27.84
Octobre	40.75	16.15	35.48	18.56	26.28

Une comparaison du COP du système entre le cycle conventionnel et les trois systèmes hybrides flexibles étudiés indique que le système conventionnel possède le COP le plus bas parmi toutes les autres configurations (fig 8). La comparaison des résultats des trois configurations entre eux, permet de constater que dans la troisième configuration les chiffres des COP de tous les mois sont supérieurs à ceux des autres configurations. L'analyse des COP des première et deuxième configurations montre que la première configuration est plus performante que la deuxième seulement pour le mois de mai. Pendant les autres mois (juin à octobre), la deuxième configuration s'est avérée plus efficace.

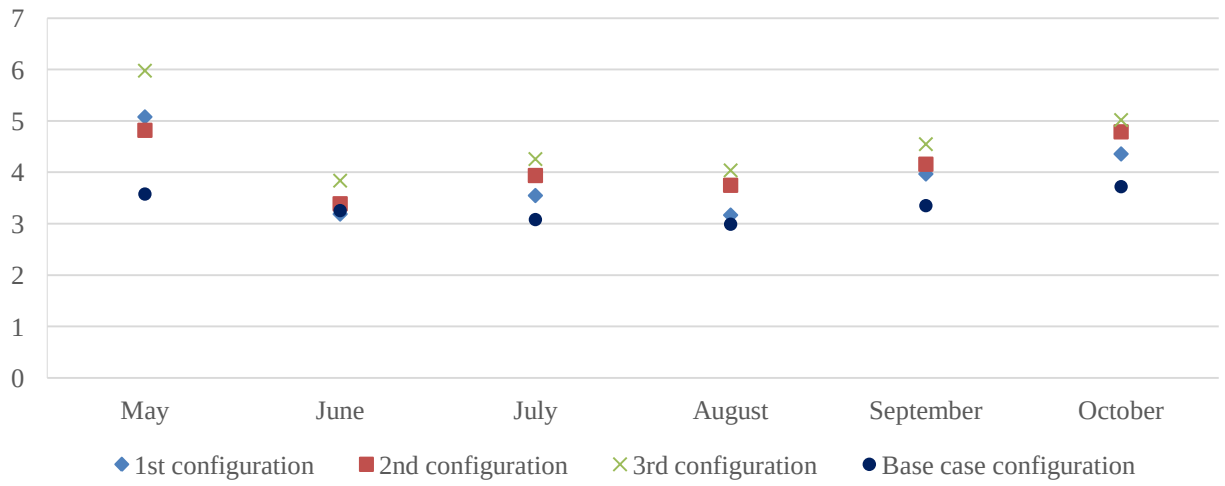

Figure 25: Comparaison du COP du système de cas de base et des trois configurations étudiées

4.8 Conclusion

Cette comparaison nous permet de tirer les conclusions suivantes : Pour un rapport R' élevé, et pour un faible taux d'humidité dans l'air extérieur, il est plus efficace d'utiliser la première configuration. Il s'agit de retirer d'abord une partie de la charge sensible d'air et ensuite de le sécher par le déshumidificateur. En contrepartie, pour un rapport R' faible et pour taux d'humidité dans l'air extérieur élevé, il est plus intéressant de déshumidifier l'air d'abord et de le renvoyer ensuite pour un refroidissement supplémentaire, suivant ainsi la deuxième configuration.

Les résultats ont montré que les trois configurations proposées sont flexibles et peuvent fonctionner quel que soit le rapport de la charge latente sur la charge sensible. Cette caractéristique dépasse les systèmes proposés dans la littérature où la performance est étudiée et discutée pour un point nominal critique ou pour une gamme restreinte de conditions d'exploitation. Les systèmes étudiés offrent des solutions alternatives prometteuses par rapport aux systèmes traditionnels, améliorant de façon significative les performances et réduisant la consommation électrique des bâtiments. La troisième configuration dans laquelle deux cycles de compression de vapeur ont été utilisés a révélé son efficacité pour chacun des six mois étudiés. Cependant, cette configuration est la plus coûteuse parmi les autres, et il reste à prouver si le faible coût de fonctionnement serait capable de compenser le coût initial élevé. Il faut ainsi trouver un compromis entre l'efficacité du système et son prix. En outre, les résultats numériques ont montré que les débits du réfrigérant, de la solution de dessication et de l'air varient en fonction des mois afin d'éliminer les charges latente et sensible.

La concentration de la solution de dessiccation diffère également et, pour atteindre la concentration optimale, le système passe par un régime transitoire qui doit être plus étudié. Une modification de ces paramètres selon les différentes conditions d'entrée exige un système de contrôle pour réguler les débits et les concentrations dans le système sans intervention manuelle. Dans les étapes prochaines, notre système flexible proposé devrait être méticuleusement étudié avec un modèle dynamique et un système de contrôle approprié afin de pouvoir répondre aux demandes en constante évolution.

Chapter 4 Case Study: Flexible Design of a Hybrid Air Conditioning System in an Office

4.1 Introduction

Air conditioning in buildings is mostly performed using vapor compression systems with an increasing amount of installed AC units as mentioned in chapter 1. Yet these systems waste energy when it comes to humidity control inside buildings. Alternative systems, such as hybrid systems, have been studied with the aim of improving the energy performance consisting of the integration of membrane based heat and mass exchangers within the traditional air conditioning systems. These hybrid systems have gained an increasing interest due to their efficient cooling through controlling latent and sensible loads separately and thus their reduced electricity consumption. In addition, they have shown a great competence in maintaining thermal comfort with proper indoor air quality. However, the performance of these systems radically depends on the outside operating conditions where the ratio of latent to sensible load inside the building changes accordingly as presented in the state of the art in chapter 1. Thus in applications where a non-constant latent to sensible load ratio is required these systems show a lack of flexibility. In this case it might be feasible to use the configuration of the hybrid system cited earlier in the research of Bergero and Chiari (Bergero and Chiari, 2011) that offers a highly efficient performance over a range of operating conditions depending on the ratio of the latent to sensible load.

In this chapter a hybrid system, including the novel design of membrane exchanger studied in chapter 3, is assessed. This system is considered to perform the seasonal air conditioning of an office in a mid-rise building in Nice in the south of France. The main objective of this case study is to understand the flexibility issues in these hybrid systems. Accordingly, several architectures of such a hybrid system are proposed and the results are compared to that of a conventional vapor compression cycle. This chapter describes each component of the vapor compression cycle along with its modeling equations. The model validated in chapter 3 is used to assess the performance of the heat and mass exchangers of the liquid desiccant system. Then a complete model is used to assess the performance of each architecture of the hybrid system in the different months of the year where cooling is required. The findings of this chapter would provide insight about the contribution of hybrid systems in reducing the energy cost when cleverly implemented in buildings.

4.2 Case study

4.2.1 Building description

A baseline office in Nice (43.3˚N, 5.4˚E), a city in the south of France, is simulated in this study. Nice has a Mediterranean climate with warm spring and autumn and with a hot summer. The office is located on the third floor within a mid-rise building of 5 floors. Each floor is 3 m high and has an area of 100 m^2; it consists of 2 workplaces, an open space, a meeting room, an entrance, a lunchroom and a toilet. The design of the building's envelope is considered as the real case construction. The coefficients of heat transmission U-value of the exterior walls, the interior walls, the roof and the floor are taken from ("EURIMA - U-values in Europe," n.d.). The window to wall ratio is about 20% and side fins of 30 cm depth are installed on the windows. The U-value of the glazing is 2 $W/m^2.K$ made of 2 double clear panes of 6 mm each, separated by a 6 mm layer of argon, with a solar heat gain coefficient SHGC of 0.57. The infiltration rate is considered to be as 0.5 ACH. Schedules of occupancy are specified for every room where generally people are present in the building from 9 to 18 h. The schedules of activity, lighting, office equipment and HVAC system are proposed accordingly. The inside cooling set point temperature is 24˚C and the building is simulated using Designbuilder that uses EnergyPlus as an interface tool.

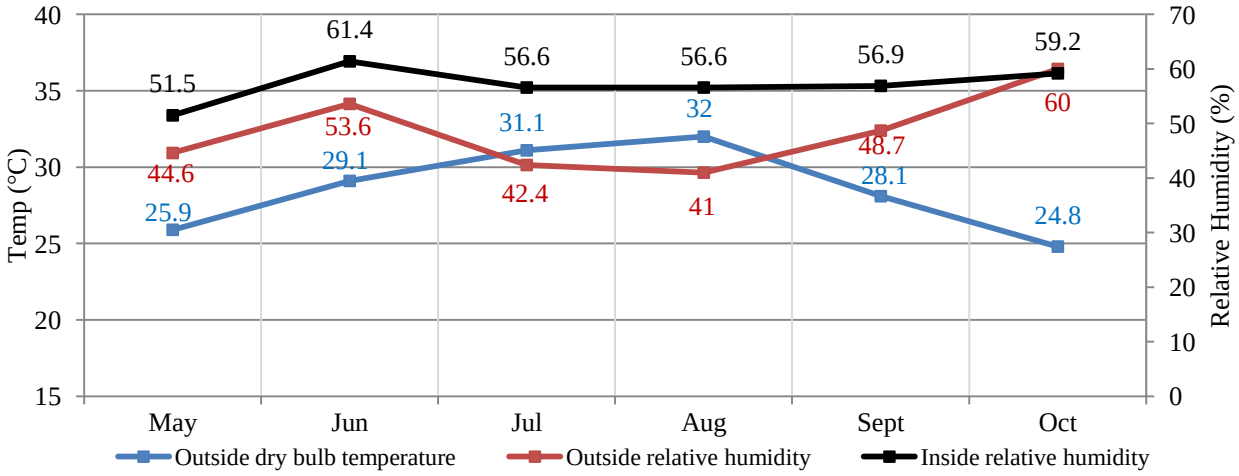

Figure 4.1: Temperature and relative humidity in each month.

In each month the ambient conditions change and so does the relative humidity of the air inside the office. Fig. 4.1 shows the monthly temperature and relative humidity of the ambient air as well as the monthly indoor air relative humidity.

Cooling is needed from May to October and these six months of the year are studied thoroughly in this chapter. The cooling load is calculated for these months and it can be noticed that the total cooling load inside the office differs from one month to another as shown in fig. 4.3. It is divided into latent load and sensible load. The ratio of the latent to sensible load (R') varies from one month to another and its different values are noted also in fig. 4.2.

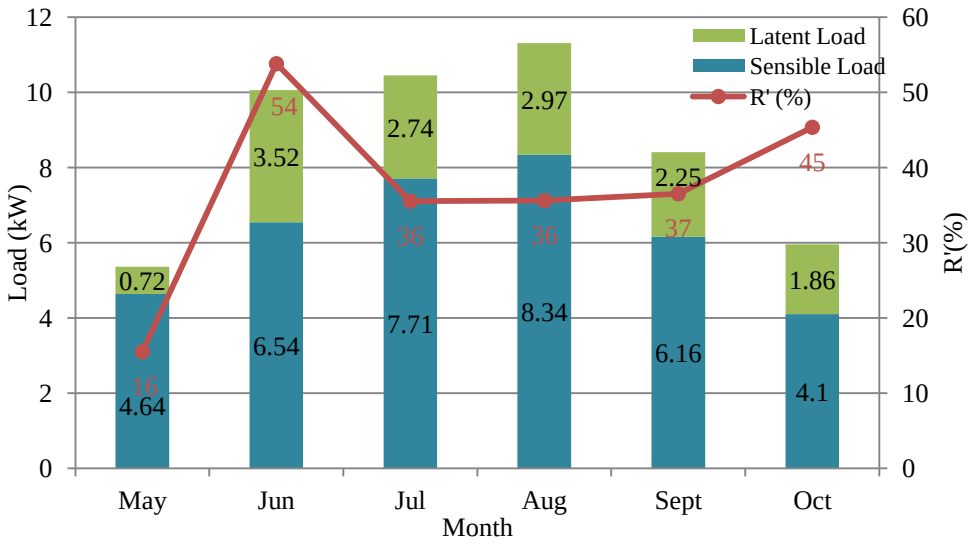

Figure 4.2: Monthly cooling load distribution.

4.2.2 Cooling and dehumidification in the base case configuration

Conventional vapor compression cycles are the most commonly used to perform the cooling of such an office. As shown in figure 4.3, they consist of a compressor, a condenser, an expansion valve and an evaporator where refrigerant R-134a is considered to be the working fluid in our case. As mentioned before, reducing the air temperature below its dew point decreases the efficiency of the cycle and in some cases where very low humidity levels are required using such a traditional system would be no more feasible.

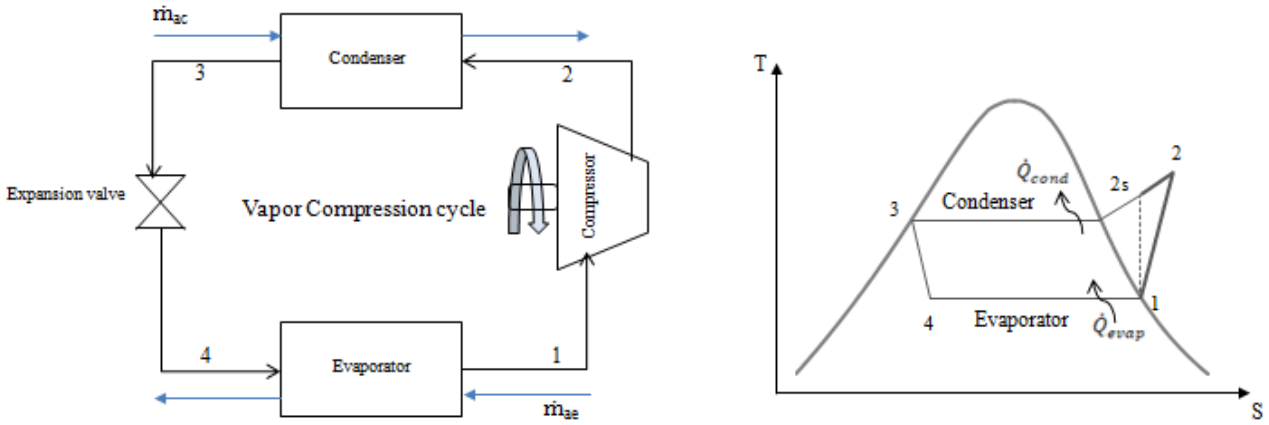

Figure 4.3: Vapor compression cycle with T-S diagram

4.2.2.1 Simplified model of the vapor compression system

To examine the performance of a vapor compression system the heat transfer and energy conservation equations are briefly described for every component.

➢ Compressor (process 1-2): Compression

A simplified model for a volumetric compressor is developed. The geometrical parameters are taken constant with a swept volume of $4.69x10^{-5}$ m^3. The model calculates the power of the compressor by the following equation (4.1):

$$W_{comp} = \dot{m}_{ref}.(h_2 - h_1) \quad (4.1)$$

Where h_2 is calculated considering a constant isentropic efficiency as 60% through (4.2):

$$\eta_{is} = \frac{h_{2s} - h_1}{h_2 - h_1} * 100 \quad (4.2)$$

The mass flow rate of the refrigerant is calculated by the following formula of equation (4.3):

$$\dot{m}_{ref} = \frac{Q_{total}}{h_1 - h_4} = \frac{Q_{evap}}{h_1 - h_4} \quad (4.3)$$

Where Q_{total} is the total cooling load removed by the evaporator.

➢ Condenser (process 2-3): Constant pressure heat rejection

The heat transfer rate from the refrigerant to the air is obtained by applying energy balance for each stream at the refrigerant side and the air side where $\dot{Q}_{cond} = \dot{Q}_{a2}$ and are calculated as the following eq. (4.4) and (4.5).

Refrigerant side:

$$\dot{Q}_{cond} = \dot{m}_{ref}(h_3 - h_2) \quad (4.4)$$

Air side:

The total load removed at the air side (at the condenser no humidity change) is calculated by (4.5)

$$\dot{Q}_{ac} = \dot{m}_{ac}.\Delta h_{ac} = \dot{m}_{ac}\left(h_{a,2} - h_{a,3}\right) = \dot{m}_{ac}.C_{p,ac}.\Delta T_{ac} = \dot{m}_{ac}.C_{p,ac}.(T_{a,2} - T_{a,3}) \quad (4.5)$$

The mass flow rate of air entering the condenser is considered to be controlled by a variable speed fan. It is calculated assuming a fixed temperature difference between the inlet and the outlet air across the condenser ($\Delta T_{a,2} = 8$). A minimum temperature difference between the two streams (air and refrigerant) in the condenser is considered to be 3 K.

➢ Expansion valve (process 3-4): Throttling

It is assumed that the expansion valve is perfectly insulated and the following equality is valid (4.6).

$$h_3 = h_4 \quad (4.6)$$

➢ Evaporator (process 4-1): Constant pressure heat addition

The heat transfer rate from the air to the refrigerant is equal to the total heat transfer rate of the evaporator (latent and sensible). It is divided into latent and sensible load removal. The energy balance for each stream at the refrigerant side and the air side is applied where $\dot{Q}_{evap} = \dot{Q}_{ae}$.

Refrigerant side:

The heat transfer rate is given by the following equation (4.7):

$$\dot{Q}_{evap} = \dot{m}_{ref}(h_1 - h_4) \quad (4.7)$$

Air side:

The total, sensible and latent heat transfer rates are given by eq. (4.8).

$$\dot{Q}_{ae} = \dot{m}_{ae}.\Delta h_{ae} = \dot{m}_{ae}\,(h_{a,4} - h_{a,1})$$
$$\dot{Q}_{S,ae} = \dot{m}_{ae}.C_{p,ae}.\Delta T_{ae} = \dot{m}_{ae}.C_{p,ae}.(T_{a,4} - T_{a,1}) \quad (4.8)$$
$$\dot{Q}_{L,ae} = \dot{m}_{ae}.h_{fg,ae}.\Delta Y_{ae} = \dot{m}_{ae}h_{fg,ae}.(Y_{a,4} - Y_{a,1})$$

Similar to the condenser, the pinch defining the minimum temperature difference between the two streams in the evaporator is set to 3. The total load and the sensible load are given and fixed for each month and the latent load is calculated by the modeling equations.

The inlet air flow rate to the evaporator ($\dot{m}_{ae}$) is assumed to be controlled in a way to meet both the required latent and sensible load. If the evaporation temperature reaches 0°C and the removed latent load does not meet the needed load, this latter is considered as unmet.

In practice, this control strategy is more sophisticated than the standard equipment (split systems) where the evaporation temperature is low by design and kept constant by the compressor control. The sensible load only is controlled by the fan speed while the humidity removal is a consequence (the humidity is not controlled). However, this strategy is chosen to have a fair comparison.

4.2.2.2 Results and analysis

➢ Power consumption

The power consumed by the compression cycle is that consumed by the compressor and by the fans that deliver air to the system.

- Compressors

Knowing the mass flow rate of the refrigerant and its enthalpy in each step of the cycle the power of the compressor can be calculated by the above given formula.

- Fans

There are two fans in the system, one delivering air to the condenser and another to the evaporator. The power of the fans is calculated by eq. (4.9) by roughly assuming a static pressure of 100 Pa.

$$W_f(W) = \dot{m}_a H_f \quad (4.9)$$

Where $\dot{m}_a$ is the mass flow rate of air in m^3/s and H_f is the static pressure of the fan in Pa.

➢ COP

The COP of the system is then calculated by the following formula (4.10):

$$COP_{overall} = \frac{Q_{evap}}{\mathrm{W}_{comp} + \sum W_f} \quad (4.10)$$

The results of the monthly air mass flow rates as well as the latent and sensible loads, the power consumption and the COP are shown in table 4.1 for the base case configuration.

Table 4.1: Loads removed by the vapor compression cycle

Month	$\dot{m}_{a1}$ (m^3/h)	$Q_{L,\ required}$ (W)	Q_L (W)	Q_S (W)	Total power consumption (kW)	$COP_{overall}$
Base case configuration						
May	650	720	640	4640	1.48	3.58
June	910	3520	3379	6540	3.05	3.26
July	1080	2740	2590	7710	3.34	3.08
August	1160	2970	2808	8340	3.73	2.99
September	860	2250	2129	6160	2.47	3.35
October	575	1860	1775	4100	1.58	3.72

In order to increase the latent load removed by the evaporator, the mass flow rate of the air entering the evaporator $\dot{m}_{ae}$ should be decreased. This causes the decrease in the evaporator's temperature thus reducing the COP of the system. In our case, we chose to limit the evaporation temperature to 0°C and thus the values of $\dot{m}_{ae}$ are determined accordingly. At this temperature the evaporator is unable to remove the entire latent load for all the studied months. In this case our control strategy leads exactly to what is done in practice in the actual split systems. Thus as a conclusion, for a fixed indoor air temperature and relative humidity, a conventional vapor compression cycle is unable to remove the required latent load except at extremely low evaporation temperatures. This shows the deficiency of traditional systems to reach desired inlet conditions and triggers the search for alternative systems that are capable to handle this issue. Therefore, a hybrid liquid desiccant based vapor compression system is investigated in a way to reach the required latent and sensible load inside the baseline office.

4.3 Hybrid system description

The hybrid system suggested in this study is similar to the hybrid systems mentioned before composed of two main subsystems: a traditional vapor compression cycle and a membrane based liquid desiccant system. The liquid desiccant system is mainly made of a dehumidification cycle and a regeneration cycle as shown in fig. 4.4. The first cycle is made up of a dehumidifier, a storage tank and a pump. The dehumidifier is a cross flow heat and mass membrane based exchanger, it dehumidifies the air. The desiccant solution (LiCl) absorbs moisture from the air through the difference in the vapor pressure between the surface of the desiccant material and the air. After absorbing water vapor from the process air, the solution must be reactivated in order to be able to absorb the same amount of water vapor again. Thus its concentration and temperature should be continuously maintained constant at the entry of the dehumidifier. To restore its temperature, the evaporator of the vapor compression cycle cools the desiccant solution before entering the dehumidifier. As for the desiccant reactivation, regeneration process takes place to retain the solution's concentration. In the regenerator, the water that is absorbed during the dehumidification process is removed from the desiccant solution. This occurs by increasing the surface vapor pressure of the desiccant through heating the solution. The regeneration cycle is

made of a regenerator (which is also a cross flow membrane heat and mass exchanger), a pump and a storage tank and it uses the excess heat given by the condenser of the vapor compression cycle to heat the solution before entering the regenerator. It should be noted that at steady state the mass flow rate of the water vapor removed by the dehumidifier is transferred to the regenerator where it is released to the driven ambient air.

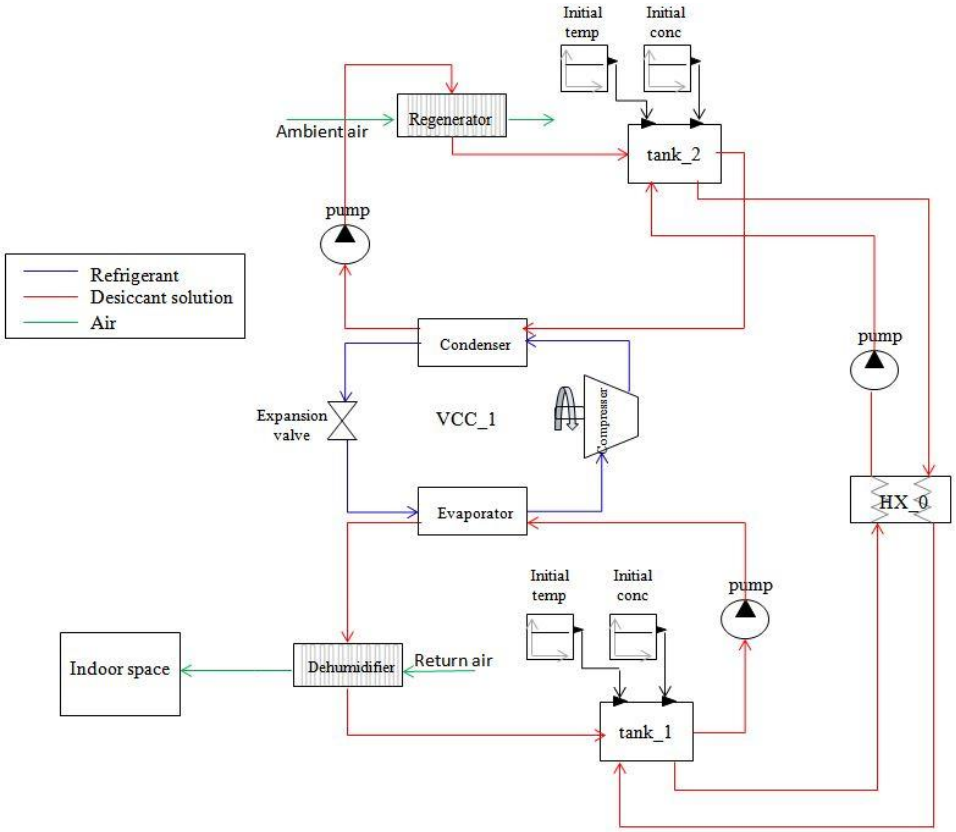

Figure 4.4: Schematic of a hybrid system with storage tanks

The storage tank in the dehumidification cycle (tank_1) is used to store the diluted solution leaving the dehumidifier which is continuously pumped to the regenerator for reactivation. The tank in the regeneration cycle (tank_2) is for storing the concentrated solution which is again pumped to the first cycle to absorb the water vapor from the return air and so on. Before reaching a steady state the concentration of the solution inside the tank of the first cycle decreases with time while that of the second cycle increases. The concentration of the diluted solution found in tank_1 is always adjusted by adding more concentrated solution from tank_2. The starting temperature and concentration of the solution are specified as initial conditions inside the tanks which are not necessarily equal in both tanks.

The action of preheating the solution before entering the condenser and pre-cooling it before entering the evaporator is very important. It intends to save some of the energy required in the process of regeneration and dehumidification respectively. Thus also a new cycle exists which consists of the two storage tanks: tank_1 and tank_2, a heat exchanger hx_0 and a pump. As the desiccant solution flows from one tank to the other, it passes through a heat exchanger where heat is transferred to or from the solution. The heat exchanger is used to increase the solution's

temperature before entering the regeneration cycle and to reduce its temperature before entering the dehumidification cycle. This circuit adds flexibility to the system by allowing us to assign different solution concentrations and flow rates in the two cycles. The pumps are used to define the mass flow rates of the solution in each cycle.

The desiccant cycle is able to play the role of both dehumidifying and cooling the air at the same time. The evaporator of VCC_1 is used to cool the desiccant solution which in turn cools and dehumidifies the air simultaneously. A previous study was done by (Mustapha et al., 2017) where different architectures were analyzed to find the most efficient one among them. The configurations were proposed according to whether the solution removes the latent and sensible loads entirely, or the whole latent load and part of the sensible load or only the latent load without interfering with the sensible load. In the case where part of the sensible load is removed by the solution, air would pass by another vapor compression cycle in order to reach the desired temperature before entering the indoor conditioned space. The results showed that optimizing the amount of the sensible load removed by the liquid desiccant solution led to an increase in the COP of the system and a decrease in the overall power consumption by around 30%.

4.3.1 Configurations

The above described system represents a good alternative for conventional cycles, yet, such a system might also lack some flexibility when the latent to sensible ratio varies in an important range. Aiming to properly handle the latent and sensible loads of the previously described baseline office a more developed system is proposed. It consists of the addition of heat exchangers that transfer sensible heat from the air in the dehumidification cycle and to the ambient air in the regenerator cycle increasing the flexibility of the system. The placement of the heat exchangers is a critical issue and thus different configurations are studied. The first one consists of adding heat exchangers before the dehumidifier and the regenerator and the second involves inserting them after the dehumidifier and the regenerator. A third configuration is suggested where instead of adding heat exchangers, a second vapor compression cycle is inserted after the dehumidification cycle. In this case the evaporator of this added compression cycle plays the role of a heat exchanger of the second configuration. In all configurations the dehumidifier of the desiccant system removes the entire latent load and part of the sensible load. The remaining sensible load is removed by the heat exchangers in the first two configurations and by the vapor compression cycle in the third configuration. Another configuration exists where both, latent and sensible loads, are entirely removed by the desiccant system without the help of additional equipment. This configuration has a poor flexibility outside the months with high latent to sensible load ratio and failed to prove any seasonal effectiveness because the desiccant system shows high performance in removing latent loads rather than sensible loads. Thus when the dimensions of the dehumidifier are chosen to be able to remove the entire latent load, the sensible load removal would be small. Consequently, the mass flow rate of the air in the dehumidifier should be greatly increased in order to increase the sensible load removal. This leads to the increase of the solution’s concentration leading to an increase in the condensation temperature and hence the COP of the system decreases. So due to its very low COP, this configuration is eliminated from our study. A

comparison is performed to compare the seasonal performance and the energy consumption of each of the 3 configurations.

4.3.1.1 Description

❖ 1st configuration

The first configuration is presented by fig. 4.5. A heat exchanger hx_1 is placed before the dehumidifier and it is used to cool the air before being dehumidified and supplied to the room. hx_2 is placed before the regenerator and its role is to cool the desiccant solution before being regenerated.

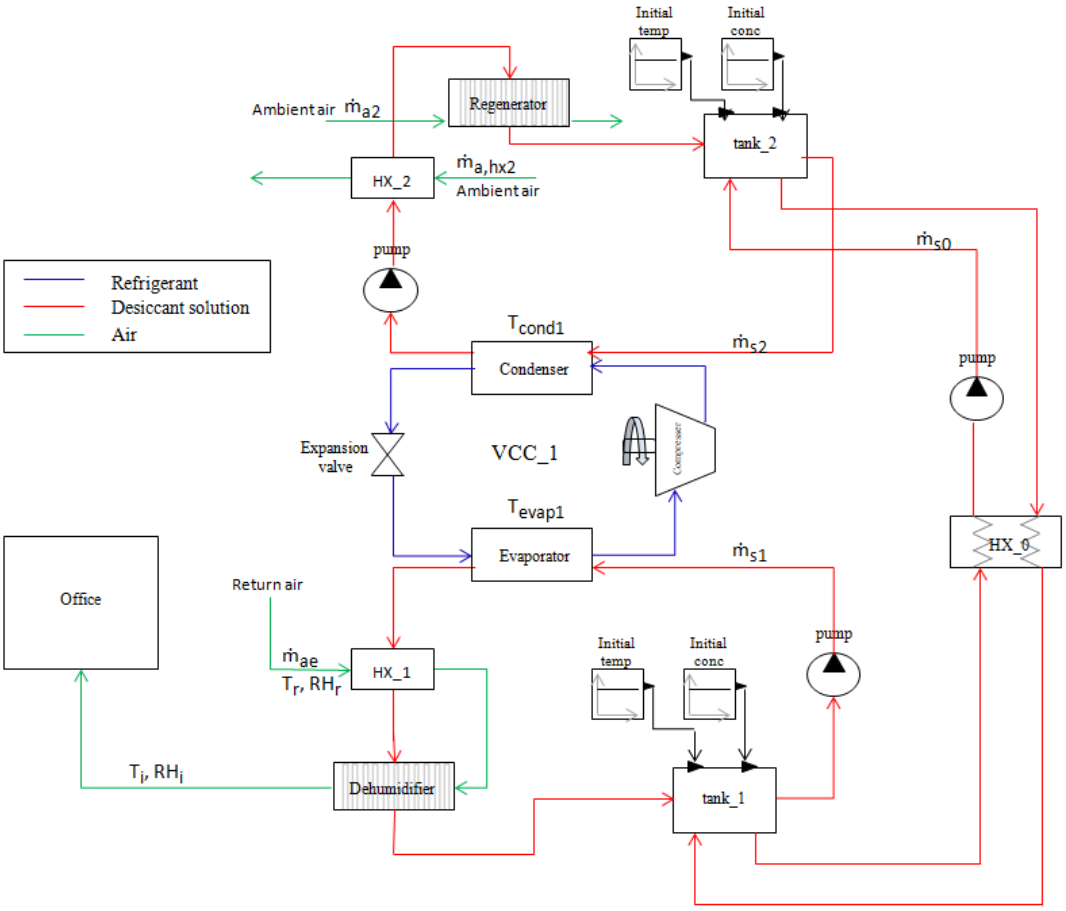

Figure 4.5: Schematic of the first configuration

Air that has been recycled from the office enters hx_1 at the indoor temperature and relative humidity of the office (T_r, RH_r) and with a given mass flow rate ($\dot{m}_{a1}$). This air is then transferred to the dehumidifier which not only removes the humidity, but it further cools the air in order to meet the supply conditions. On the solution side, the sensible load added to the solution in hx_1 along with the load added in the dehumidifier should be equal to the load removed by the evaporator of the vapor compression cycle. But this is not exactly the case because of the presence of the storage tank tank_1. The solution entering tank_1 is at a temperature slightly less than that when leaving it and this leads to an additional sensible heat on the solution side (due to the heat that is not totally recovered in the hx_0). Therefore, the load added to the solution in the

dehumidifier, along with that added in hx_1 and in tank_1 are equal to the load removed from the solution by the evaporator of the vapor compression cycle.

In the regeneration cycle, unlike the case of hx_1 where the air flow is in series with the dehumidifier, the flow rate of the air entering hx_2 is independent of that in the regenerator. The ambient air passing in hx_2 is used to slightly decrease the temperature of the solution. The ambient air passing through the regenerator is used to cool the solution and simultaneously remove some of the water in order to return the solution to its initial concentration. Similar to the dehumidification cycle, in the regeneration cycle the sensible load removed from the solution in hx_2, with the sensible load removed in tank_2 and the total load removed in the regenerator must be equal to the load added to the solution by the condenser of the vapor compression cycle.

After leaving the regenerator, the solution is sent back to the storage tank (tank_2). It is then pumped to tank_1 after being further cooled in hx_0 by the cold solution as explained before.

Taking as example the month of August, the return air coming from the office is at 24°C and 56.6% relative humidity which corresponds to an absolute humidity of 10.5 g/kg (d.a). When the office is at these return conditions, the supply air of a proposed mass flow rate 3200 m^3/h should be at 16.34 °C and 81.2% relative humidity in order to meet the latent load which is 2.97 kW and the sensible load which is 8.34 kW. In hx_1 air is partially cooled by the cold desiccant solution that leaves the evaporator. After leaving hx_1, the same cooled air now enters the dehumidifier in order to be dried. The air at the entrance of the dehumidifier is at 16.6 °C and 89.35% relative humidity which correspond to an absolute humidity of 10.5 g/kg (d.a). The dry air leaving the dehumidifier has an absolute humidity of 9.37 g/kg.d.a. The latent load removed by the dehumidifier should be equal to the latent load in the office. Now the air that leaves the dehumidifier has the proper supply conditions and is ready to be delivered to the room with a temperature, a relative humidity and an absolute humidity of 16.34°C, 81.2% and 9.37 g/kg (d.a) respectively. The results of the calculation are shown in details in later steps.

❖ 2nd configuration

In the second configuration, as per fig. 4.6, the placement of the heat exchangers is changed. Here, hx_1 is placed after the dehumidifier and hx_2 after the regenerator. Again the mass flow rate of the ambient air entering the regenerator and that entering hx_2 are not necessarily equal. On the contrary, the same flow rate of the air that enters the dehumidifier is transferred to hx_1. The concept of this configuration is the same as the previous one but here the cooling of the supply air is done after its dehumidification and the cooling of the desiccant solution is done after its regeneration. hx_1 uses the cold desiccant solution to lower the temperature of air and hx_2 uses the cool ambient air to lower the temperature of the desiccant solution.

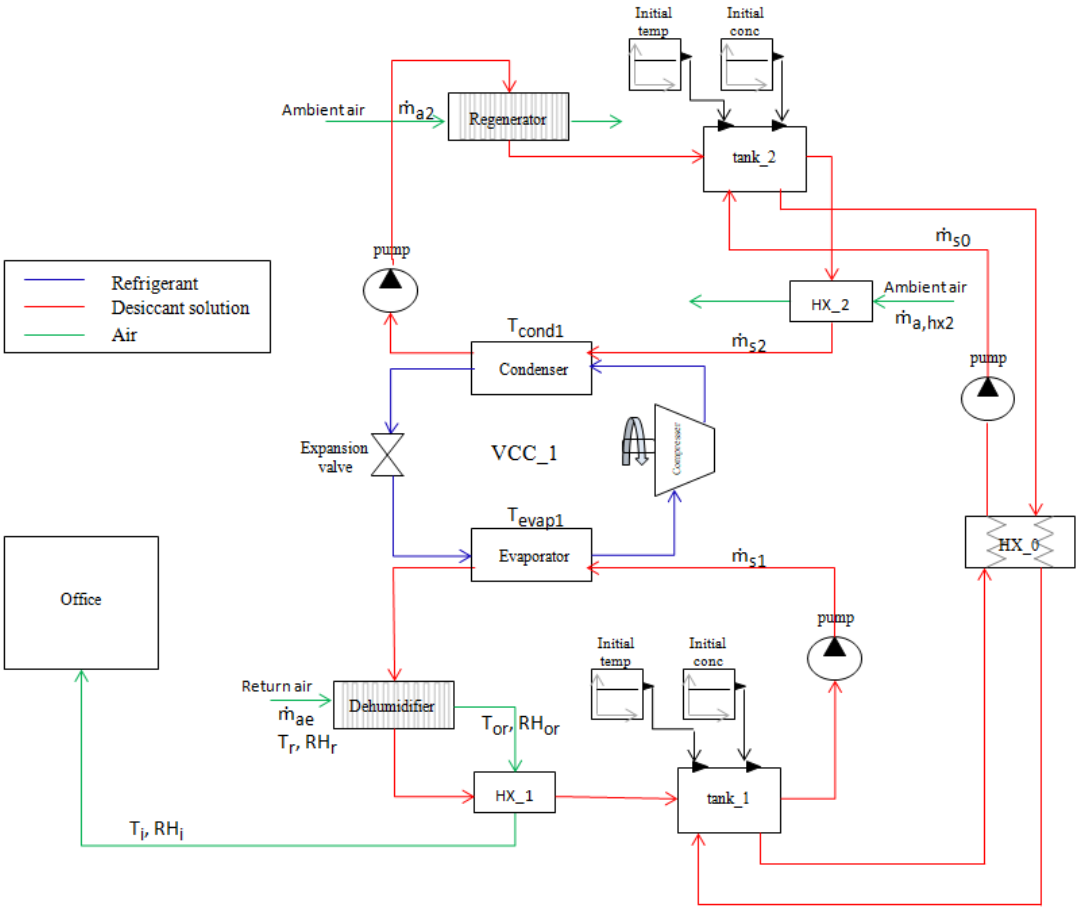

Figure 4.6: Schematic of the second configuration

❖ 3rd configuration

In the third configuration, the heat exchangers were removed and hx_1 was replaced by a second vapor compression cycle VCC_2 as shown in fig. 4.7. The evaporator of VCC_2 plays the same role as the heat exchanger hx_1 which is to further decrease the temperature of the air before being supplied to the office. At the entrance of the second evaporator the dry air leaving the dehumidifier is mixed with a part of the return air recycled from the room ($\dot{m}_r$). Mixing the air not only increases the evaporation temperature of VCC_2 and thus the COP of the second vapor compression cycle, but also increases the temperature of the supply air at the inlet of the office as it will be seen later. So in this configuration two degrees of freedom are added to the system. The first is ($\dot{m}_r$) which is chosen such that the total air mass flow rate that enters the second evaporator is 5000 m^3/h. In case ($\dot{m}_{ae}$) was already 5000 m^3/h then no mixing takes place. The other degree of freedom is the mass flow rate of the ambient air that is entering the second condenser ($\dot{m}_{ac}$). The value of $\dot{m}_{ac}$ is selected such that the difference in the inlet and outlet air temperature along the condenser is 8˚C.

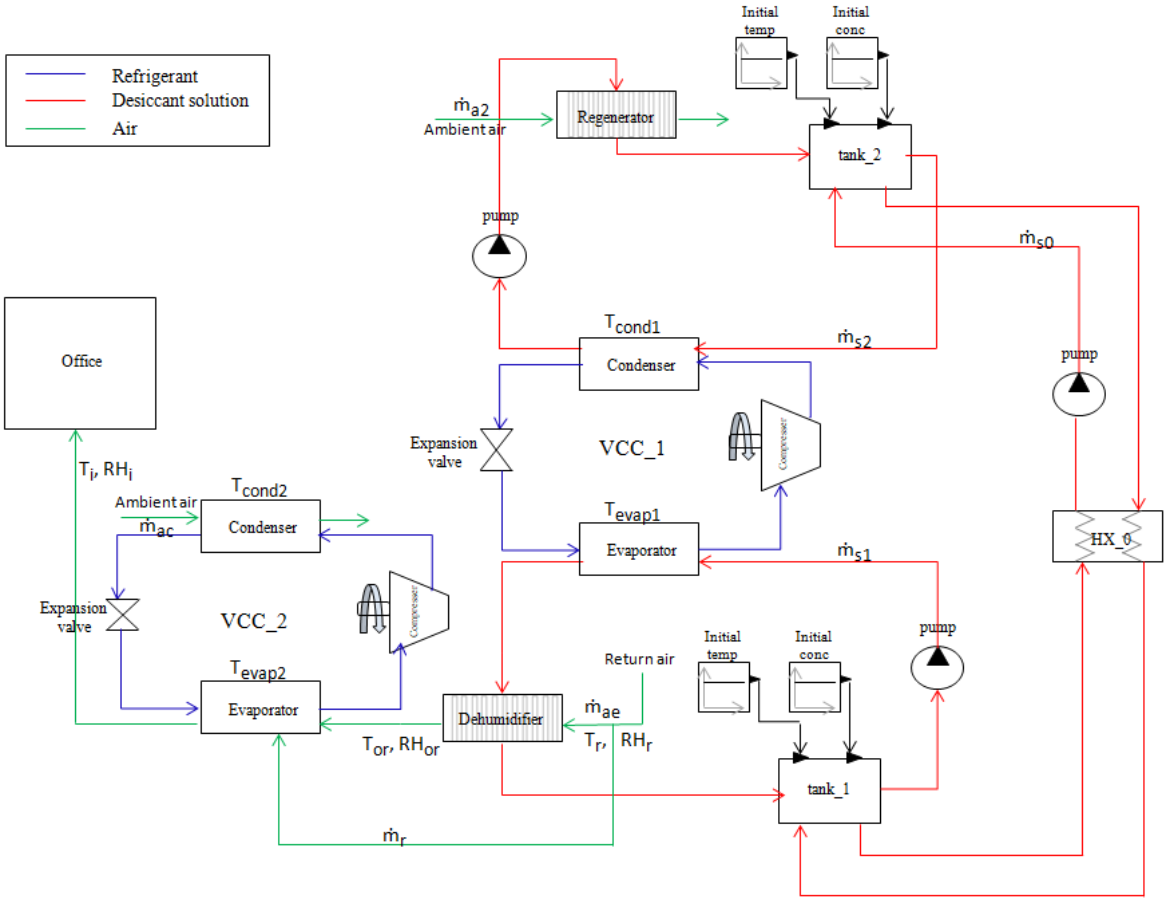

Figure 4.7: Schematic of the third configuration

4.3.2 Modeling the hybrid system

For the modeling of such a system, a mathematical model for each component is written in Modelica language using Dymola software and is described in the following steps.

4.3.2.1 Vapor compression cycles

For VCC_1 and VCC_2 the modeling is the same as described for the base case but the only difference is that in VCC_1 the exchange is between the refrigerant and the desiccant solution instead of air. Same assumptions are taken regarding the compressor's design and efficiency, the temperature difference across the condenser, the perfectly insulated expansion valve and the fixed pinch in the condenser and evaporator.

4.3.2.2 Desiccant cycle

➢ Heat exchangers

Heat transfer takes place between the desiccant solution on one side and air on the other side. It is worth noting that the total heat transfer rate leaving the hot fluid must be equal to the total heat transfer rate absorbed by the cold fluid. Hence $Q_{hf} = Q_{cf}$ according to eq. (4.11).

$$Q_{hf} = \dot{m}_{hf} C_{p,hf} (T_{hf,i} - T_{hf,o})$$
$$Q_{cf} = \dot{m}_{cf} C_{p,cf} (T_{cf,i} - T_{cf,o}) \quad (4.11)$$

In hx_0, the solution coming from the regenerator is the hot fluid and that coming from the dehumidifier is the cold one. In hx_2 the solution is the hot fluid and the air is the cold one; for the heat exchanger of the dehumidification cycle (hx_1) the cold stream is represented by the desiccant solution and the hot one is represented by the air that needs to be processed.
The pinch defining the minimum temperature difference between the two streams in the heat exchangers is set to 3.

➢ Storage tanks

The solution entering the storage tank has a temperature and concentration different from that leaving it due to the connection between tank_1 and tank_2. These values change with time and thus the new outlet solution conditions are calculated by equations (4.12) and (4.13)

$$\frac{dT_o}{dt} = \frac{\dot{m}_{s,1} C_{p,avg1}\left(T_{i,1} - T_o\right) + \dot{m}_{s,2} C_{p,avg2}\left(T_{i,2} - T_o\right)}{\rho A H C_{p,o}} \tag{4.12}$$

$$\frac{dC_o}{dt} = \frac{\dot{m}_{s,1} C_1 + \dot{m}_{s,2} C_2 - C_o(\dot{m}_{s,1} + \dot{m}_{s,2})}{\rho A H} \tag{4.13}$$

Where H is the height of the tank and A is its area, $C_{p,avg1}$ and $C_{p,avg2}$ are the average specific heat of the solution that is coming from the dehumidifier (or regenerator) and hx_0 respectively and they are calculated by eq. (4.14). $C_{p,o}$ is the outlet specific heat of the solution at temperature T_o and concentration C_o.

$$C_{p,avg1} = \frac{C_{p,1} + C_{p,o}}{2}$$
$$C_{p,avg2} = \frac{C_{p,2} + C_{p,o}}{2} \tag{4.14}$$

$C_{p,1}$ and $C_{p,2}$ being the specific heat of the solution that is coming from the dehumidifier (or regenerator) and hx_0 respectively.

➢ Pumps

The role of the pumps in the system is to move a certain mass flow rate of the desiccant solution within a cycle or from one cycle to another. The pumps are used to control the mass flow rates of the solution in each cycle. The power needed to drive a pump is calculated by the following equation (4.15):

$$W_p(W) = \dot{m}_s H_p \tag{4.15}$$

Where $\dot{m}_s$ is the mass flow rate of the solution in $\frac{m^3}{s}$ and H_p is the head of the pump in Pa.

➢ Fans

The fans are used to deliver air to the components where an exchange is needed between air and the desiccant solution or between air and the refrigerant. The power produced by a fan is calculated by (4.9) as stated previously.

➢ Dehumidifier and regenerator

The modeling of the dehumidifier and the regenerator is based on the previously validated model of the cross flow membrane exchangers. These exchangers are made of several channels where a desiccant solution of lithium chloride (LiCl) is supplied vertically inside the channels (direction of z axis). On the outer side of the channels air is supplied in a perpendicular direction (direction of x axis) in a way where no direct contact is allowed between the air and the solution as shown in fig. 4.8. The model is done using discretization method; each of the x axis and the z axis were discretized into 10 segments of equal sizes (Ni=Nj=10) after proving that this number is sufficient to get reliable predictions. The width of each channel is 1 cm (corresponds to the height where the solution flows) and the distance between two consecutive channels is also equal to 1 cm (corresponds to the height where the air flows). The membranes separating the two fluids is the same membrane tested and chosen before (NWF-1) with its given properties. The width (L) and the height (Z) of each of the dehumidifier and the regenerator are proposed and the modeling is done accordingly.

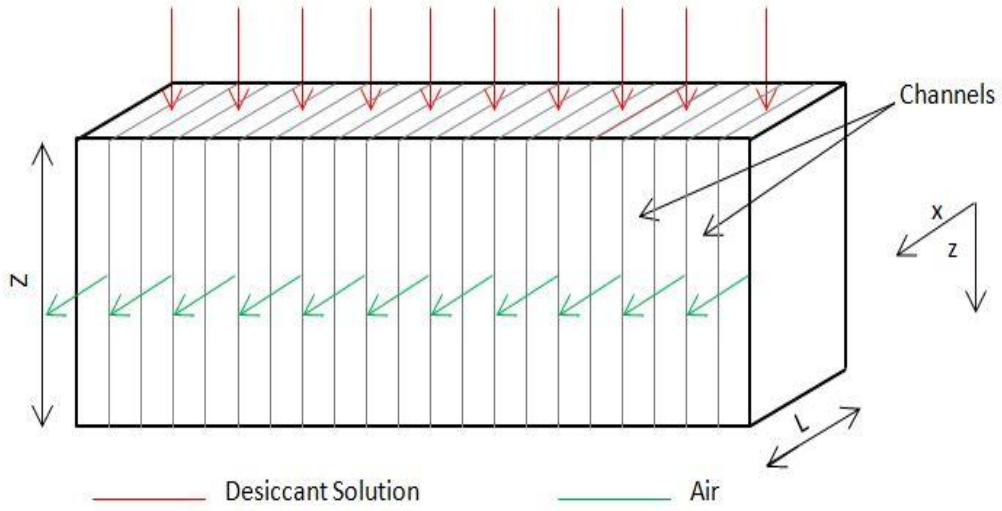

Figure 4.8: A drawing of a cross flow heat and mass exchanger.

The results of the previously performed experimental validation of the membrane exchanger model showed an acceptable compatibility predicting the heat and mass transfer within 20% of the measurements. This proved that the model can be applied in the prediction of the performance of such exchangers. Thus the energy and mass equations for the dehumidifier and regenerator are derived following that model using the third computation presented in the previous chapter that proved its robustness and reliability even for small discretization values. The equations are defined by the following at the steady state:

a) Air side

➢ Mass conservation equation for water vapor

$$\dot{m}_{da}\frac{dz}{Z}(Y[i+1,j]-Y[i,j]) + 2A_a\left(\frac{U_M[i,j]+U_M[i+1,j]}{2}\right)\left(\frac{Y[i,j]+Y[i+1,j]}{2} - \frac{Y_s[i,j]+Y_s[i,j+1]}{2}\right)=0 \quad (4.16)$$

➢ Energy conservation equation for moist air

$$\dot{m}_{da}\frac{dz}{Z}\left(\frac{C_{p,da}[i,j]+C_{p,da}[i+1,j]}{2} + \left(\frac{C_{p,v}[i,j]+C_{p,v}[i+1,j]}{2}\right)\left(\frac{Y[i,j]+Y[i+1,j]}{2}\right)\right)(T_a[i+1,j]-T_a[i,j]) + 2A_a\left(\frac{h_{Ta}[i,j]+h_{Ta}[i+1,j]}{2}\right)\left(\frac{T_a[i,j]+T_a[i+1,j]}{2} - \frac{T_{ma}[i,j]+T_{ma}[i+1,j]}{2}\right)=0 \quad (4.17)$$

b) Solution side

➢ Mass conservation equation for liquid water

$$\dot{m}_d\frac{dx}{L}(X[i,j+1]-X[i,j]) - 2A_a\left(\frac{U_M[i,j]+U_M[i+1,j]}{2}\right)\left(\frac{Y[i,j]+Y[i+1,j]}{2} - \frac{Y_s[i,j]+Y_s[i,j+1]}{2}\right)=0 \quad (4.18)$$

➢ Energy conservation equation for moist air

$$\dot{m}_d\frac{dx}{L}(1+X[i,j+1])\left(\frac{C_{p,s}[i,j]+C_{p,s}[i,j+1]}{2}\right)(T_s[i,j+1]-T_s[i,j]) - 2A_a\left(\frac{U_M[i,j]+U_M[i+1,j]}{2}\right)\left(\frac{h_{fg}[i,j]+h_{fg}[i,j+1]}{2}\right)\left(\frac{Y[i,j]+Y[i+1,j]}{2} - \frac{Y_s[i,j]+Y_s[i,j+1]}{2}\right) + 2A_s\left(\frac{h_{Ts}[i,j]+h_{Ts}[i,j+1]}{2}\right)\left(\frac{T_s[i,j]+T_s[i,j+1]}{2} - \frac{T_{ms}[i,j]+T_{ms}[i,j+1]}{2}\right) = 0 \quad (4.19)$$

c) Membrane

➢ Energy conservation equations

$$A_a\left(\frac{h_{Ta}[i,j]+\ h_{Ta}[i+1,j]}{2}\right)\left(\frac{T_a[i,j]+T_a[i+1,j]}{2}-\frac{T_{ma}[i,j]+T_{ma}[i+1,j]}{2}\right)-\frac{K_T}{\delta}\ A_m\left(\frac{T_{ma}[i,j]+T_{ma}[i+1,j]}{2}-\frac{T_{ms}[i,j]+T_{ms}[i,j+1]}{2}\right)=0 \quad (4.20)$$

$$A_s\left(\frac{h_{Ts}[i,j]+\ h_{Ts}[i,j+1]}{2}\right)\left(\frac{T_s[i,j]+T_s[i,j+1]}{2}-\frac{T_{ms}[i,j]+T_{ms}[i,j+1]}{2}\right)+\frac{K_T}{\delta}\ A_m\left(\frac{T_{ma}[i,j]+T_{ma}[i+1,j]}{2}-\frac{T_{ms}[i,j]+T_{ms}[i,j+1]}{2}\right)=0 \quad (4.21)$$

Where

$$U_M=\left(\frac{1}{h_{Ma}}+\frac{\delta}{k_m}\ +\frac{1}{h_{Ms}}\right)^{-1}$$

$$dx=\frac{L}{Ni} \quad (4.22)$$

$$dz=\frac{Z}{Nj}$$

4.3.3 Discussion of the simulation protocol

The different designs of the three configurations allow simulating 18 models such that for every configuration 6 simulations are done corresponding to each month as explained before. The ambient air temperature and relative humidity are given to the system as well as the indoor air conditions and the simulations are performed at steady state.

4.3.3.1 Design strategy

Our system has several related elements that affect the quantity and distribution of load removal. They include the design of the dehumidifier and regenerator as well as the mass flow rates of the solution and air circulating in the system. When the system is complex with several interacting elements and related parameters, the simulations can be done through an external software that determines the values of the design and control variables while maximizing the system COP. This separate control avoids redundancy and provides less time consuming operations through bypassing mesh construction and configuration reading at each solver call in Dymola. For this purpose, Python is used to perform the simulations where for each month of the three configurations optimization iterations are conducted. In each iteration the input sources that directly or indirectly influence the determination of the measured quantities are changed until the required monthly latent and sensible loads are removed from the office. Such input sources are

considered to give a feasible case. Among the feasible cases, the one with the highest system COP is chosen.

4.3.3.2 Design of dehumidifier and regenerator

The dimensions of the dehumidifier and the regenerator are changed in a way to be able to remove the entire latent load. Modifying the dimensions of the dehumidifier would cause more critical changes than modifying the dimensions of the regenerator. By adjusting the number of channels, the width (in the direction of the air flow) and the height (in the direction of the solution flow) of these two heat and mass exchangers, we consequently change the amount of latent and sensible loads removed by the system. These dimensions could be different from one configuration to another in order to optimize the system and to find the highest possible COP. However, for a comparative approach, they are taken the same in all configurations because the aim of this study is to show the relative flexibility of each design and where its application is the most effective. These dimensions are chosen in a way to be relevant in all the 18 simulations and they are presented in table 4.2.

Table 4.2: Dimensions of the dehumidifiers and regenerators in all configurations

	Number of Channels	L	Z
Regenerator	20	0.4	0.4
Dehumidifier	48	0.5	0.5

4.3.3.3 Control parameters

The control parameters are identified by being the parameters that have an impact on the results of the latent and sensible loads as well as the system's COP. The first parameter is the mass flow rate of the solution, but the solution circulates in three cycles each with a different flow rate value. Thus the input source related to the solution consists of its mass flow rate in the dehumidifier, in the regenerator, and in the heat exchanger hx_0. Second is the mass flow rate of air which also consists of that in the dehumidifier, in the regenerator, and in the heat exchanger hx_2 (in the third configuration hx_2 is removed). The last input source is the evaporation temperature of the first compression cycle that in turn determines the temperature of the solution entering the dehumidifier. In total there are 7 input sources for the first two configurations and 6 input sources for the third configuration. The probability density function of each input source is represented by a typical normal Gaussian distribution where the set of values are more likely to fall near the mean rather than further away. i.e. 68% of the data falls within one standard deviation of the mean, 95% of the data falls within two standard deviations of the mean and 99.7% of the data falls within three standard deviations of the mean.

Out of the 10,000 iteration results that we get, there are many values that do not meet the required sensible and latent loads while there are a few that do and these are the values that represent a solution for our proposed system. For every true solution the system's COP is calculated. We arranged the results and chose the combination of the input sources that corresponds to the highest COP.

4.3.3.4 Observed quantities

The measured quantities in our case are the latent and sensible loads removed by the system, as well as the total power consumed and the overall system COP.

➢ Latent load

The latent load is totally removed by the dehumidifier and is calculated by eq. (4.23).

$$Q_L = \dot{m}_{ae}\, h_{fg}\, (Y_{or} - Y_r) \tag{4.23}$$

where Y_{or}=Y_i for the first two configurations.

➢ Sensible load

The sensible load that needs to be removed from the system is given for every month. A part of this load is removed by the dehumidifier (Q_{S1}) and the remaining share (Q_{S2}) is extracted by the heat exchangers hx_1 in the first two configurations and by the evaporator of the second vapor compression cycle in the third configuration.

$$Q_S = Q_{S1} + Q_{S2} \tag{4.24}$$

For the first configuration:

$$\begin{aligned} Q_{S1} &= \dot{m}_{ae} C_p (T_i - T_{or}) \\ Q_{S2} &= \dot{m}_{ae} C_p (T_{or} - T_r) \\ Q_S &= \dot{m}_{ae} C_p (T_i - T_r) \end{aligned} \tag{4.25}$$

For the second configuration:

$$\begin{aligned} Q_{S1} &= \dot{m}_{ae} C_p (T_{or} - T_r) \\ Q_{S2} &= \dot{m}_{ae} C_p (T_i - T_{or}) \\ Q_S &= \dot{m}_{ae} C_p (T_i - T_r) \end{aligned} \tag{4.26}$$

And for the third configuration the power of the second evaporator is calculated by fixing the total sensible load and then subtracting the sensible load removed by the dehumidifier.

$$\begin{aligned} Q_{S1} &= \dot{m}_{ae} C_p (T_{or} - T_r) \\ Q_{S2} &= \dot{m}_{ae} C_p (T_i - T_{or}) + \dot{m}_r C_{p,r} (T_i - T_r) \\ Q_S &= \dot{m}_{ae} C_p (T_i - T_r) + \dot{m}_r C_{p,r} (T_i - T_r) \end{aligned} \tag{4.27}$$

➢ Power consumption

The total power consumption is the summation of that consumed by the compressors, the fans and the pumps.

- Compressors

In the first and second configuration, the power consumption of the vapor compression cycle is that used by the compressor. As for the third configuration it is the summation of that used by the two compressors.

- Fans

For the first two configurations there are three fans in the system, one delivering air to the dehumidifier, another to the regenerator and the third to hx_2. The power of the fans is calculated by roughly assuming a static pressure of 100 Pa. As for the third configuration, in addition to the fans delivering air to the dehumidifier and the regenerator, there exist two more fans one supplying air to the condenser ($\dot{m}_{ac}$) and the other to the evaporator ($\dot{m}_{r}$) of the second vapor compression cycle. The static pressure of the fans supplying air to the regenerator and the condenser is also roughly assumed 100 Pa. As for the fan supplying air to the dehumidifier, the mass flow rate ($\dot{m}_r$) is added to ($\dot{m}_{ae}$) considering a higher static pressure for the two air sources to be of 150 Pa.

- Pumps

Three pumps exist in the system, one in the dehumidification cycle, another in the regeneration cycle and the third in the intermediate cycle. For the power calculation of the pumps the head is roughly assumed 1.5 bars.

➢ COP

The overall COP of the system is calculated by eq. (4.28) for the first and second configurations:

$$COP_{overall} = \frac{Q_{evap1}}{\mathrm{W}_{comp1} + \sum W_f + \sum W_p} \quad (4.28)$$

For the third configuration where two vapor compression cycles are present, the overall COP is calculated by (4.29):

$$COP_{overall} = \frac{Q_{evap1} + Q_{evap2}}{\sum W_{comp} + \sum W_f + \sum W_p} \quad (4.29)$$

4.3.3.5 Results

The simulations are done by changing the previously mentioned input parameters and the results showing the best combination giving the highest COP are presented in table 4.3.

➢ Input parameters

The mass flow rates of the air and the solution play an important role in changing the load removal capacity. The values of the best combinations of the input sources of all the configurations are shown in table 4.3.

Table 4.3: Input parameters to the system for the three configurations

Month	$\dot{m}_{s1}$ (kg/s)	$\dot{m}_{s2}$ (kg/s)	$\dot{m}_{s0}$ (kg/s)	$\dot{m}_{ae}$ (m^3/h)	$\dot{m}_{ac}$ (m^3/h)	$\dot{m}_{a,hx2}$ (m^3/h)	T_{evap1} (K)
1^{st} configuration							
May	1	0.5	0.11	2300	175	1600	285.75
June	2	1.4	0.08	5100	3900	350	287.8
July	1.8	1.7	0.12	4500	2900	2200	286.5
August	1.5	1.4	0.09	3200	2000	2200	283.75
September	1.7	0.8	0.13	4700	1800	1450	287.8
October	1.1	1.2	0.12	2950	2750	420	287.6
2^{nd} configuration							
May	1.1	1.1	0.11	4400	115	3500	287.45
June	1.8	1.2	0.14	5020	2000	1400	285.65
July	1.6	0.6	0.13	5100	1400	2200	286.8
August	0.9	0.7	0.04	5900	2000	2800	284.7
September	1.1	1.1	0.07	3400	1600	3150	286.05
October	0.7	0.4	0.13	4550	1000	1500	285.8
Month	$\dot{m}_{s1}$ (kg/s)	$\dot{m}_{s2}$ (kg/s)	$\dot{m}_{s0}$ (kg/s)	$\dot{m}_{ae}$ (m^3/h)	$\dot{m}_{ac}$ (m^3/h)	T_{evap1} (K)	T_{evap2} (K)
3^{rd} configuration							
May	0.3	0.2	0.14	2700	2100	290.95	290.44
June	1.2	0.52	0.11	5000	710	289.6	290.25
July	0.6	0.4	0.11	5000	1100	289.05	289.55
August	0.7	0.5	0.11	5000	2420	287.4	289.17
September	0.5	0.8	0.08	3800	1650	287.15	289.47
October	0.5	0.5	0.1	5000	860	289.3	291.35

- Observed quantities

The results of the simulations are shown in tables 4.4 and 4.5 indicating the latent and sensible load removal as well as the power consumption and the overall COP of the system.

Table 4.4: Loads removed by the system and the COP of the 1st and 2nd configurations

Month	Q_L (W)	Q_{S1} (W)	Q_{S2} (W)	Q_S (W)	Power (kW)	$COP_{overall}$
1st configuration						
May	722	399	4231	4630	1.27	5.08
June	3529	804	5839	6643	3.44	3.19
July	2742	614	7140	7754	3.30	3.55
August	2973	283	8081	8364	3.89	3.17
September	2247	776	5373	6149	2.43	3.97
October	1865	528	3577	4105	1.63	4.36
2nd configuration						
May	721	2766	1881	4647	1.33	4.82
June	3520	3784	2761	6545	3.39	3.39
July	2736	3285	4419	7704	2.97	3.94
August	2967	4309	4059	8368	3.12	3.75
September	2251	2727	3468	6195	2.19	4.16
October	1863	3266	829	4095	1.50	4.79

Table 4.5: Loads removed by the system and the COP of the 3rd configuration

Month	Q_L (W)	Q_{S1} (W)	Q_{S2} (W)	Q_S (W)	Power (kW)	COP_1	COP_2	$COP_{overall}$
3rd configuration								
May	719	719	3921	4640	1.17	5.19	6.91	5.65
June	3524	2069	4471	6540	2.88	3.45	6.62	3.84
July	2739	1608	6102	7710	2.71	3.58	5.76	4.28
August	2969	2863	5477	8340	3.05	3.58	5.7	4.05
September	2250	2192	3968	6160	2.04	4.21	6.3	4.48
October	1852	1740	2360	4100	1.37	4.75	8.61	5.02

➢ Load removal distribution by equipment

Figures 4.9(a) and 4.9(b) show the distribution of the sensible load removal by the dehumidifier and by the heat exchanger in the first and second configurations respectively as well as the latent load removed by the dehumidifier and the COP of the system. Figure 4.9(c) presents the load removed by the dehumidifier (latent and sensible) and by the evaporator (sensible) of the second vapor compression cycle as well as the overall COP in the third configuration.

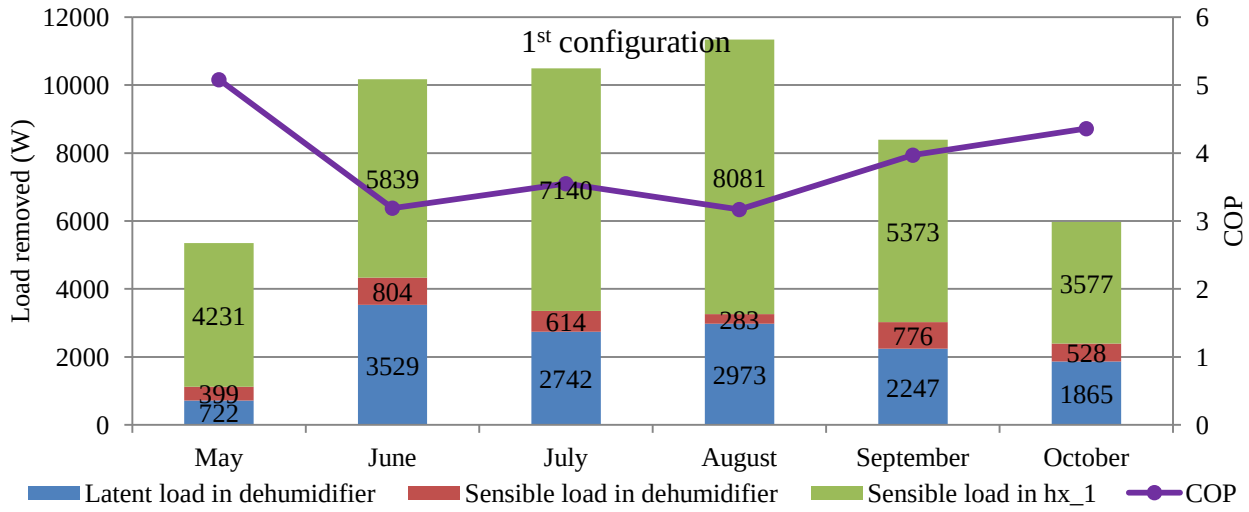

(a)

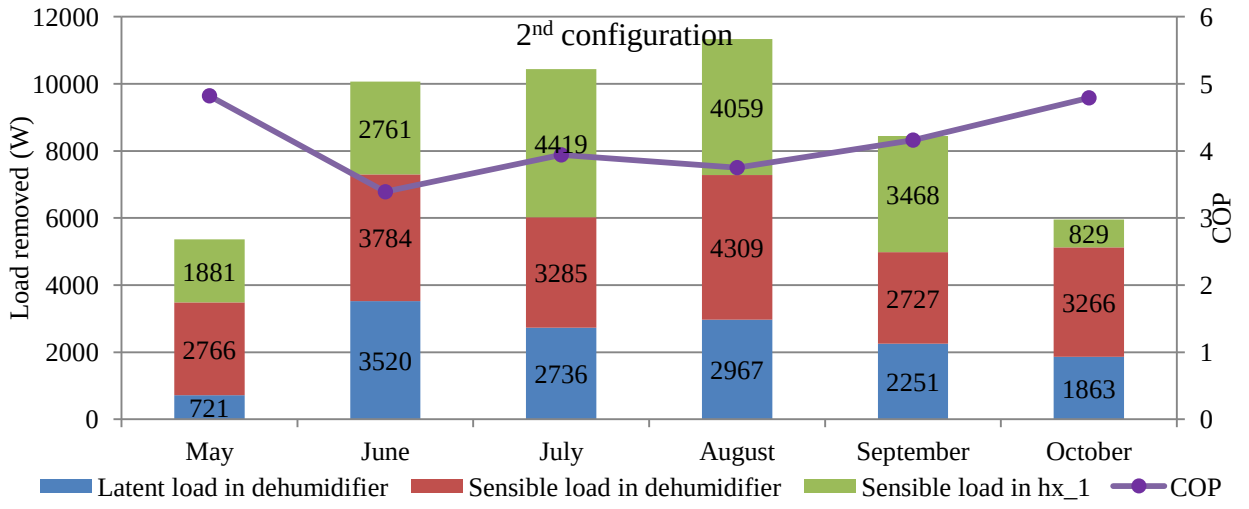

(b)

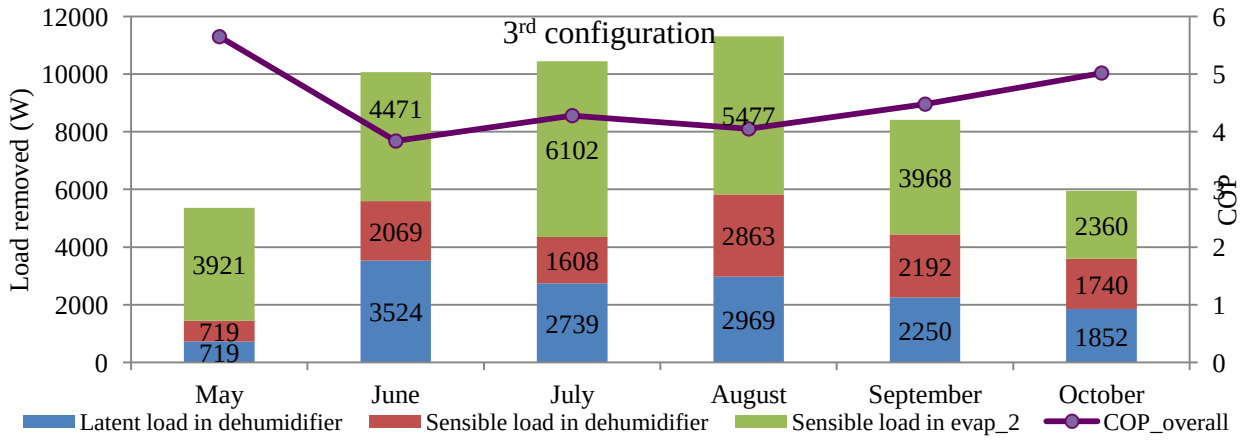

(c)

Figure 4.9: Calculated COP and distribution of cooling load removal (a) 1st configuration, (b) 2nd configuration, (c) 3rd configuration

➢ Supply indoor air conditions

Unlike traditional systems, the air supplied to the office in these hybrid systems could have higher temperatures. Generally, in vapor compression cycles, the larger the air mass flow rate that enters the evaporator, the lower is the difference in temperature between the inlet and the outlet air across the evaporator. This is considered a limitation for the conventional systems because if large air mass flow rate is supplied, the temperature would not be sufficiently decreased to reach values below the dew point and thus the humidity that would be removed from the air would not be enough. This problem is avoided by using the desiccant system that allows the proper control of humidity even at higher air mass flow rates and temperatures. The values of the temperature and relative humidity of the supply air (T_i, RH_i) for the 3 configurations are shown in table 4.6.

Table 4.6: Calculated temperature and relative humidity of the supply air

	1st configuration			2nd configuration			3rd configuration		
Month	T_i (˚C)	RH_i (%)	Y_i (g/kg)	T_i (˚C)	RH_i (%)	Y_i (g/kg)	T_i (˚C)	RH_i (%)	Y_i (g/kg)
May	18.1	71.1	9.16	20.9	61.1	9.34	20.9	60.1	9.21
June	20.2	71.3	10.49	20.1	72.0	10.54	20.8	70.1	10.68
July	19.0	71.7	9.76	19.5	69.9	9.84	19.9	68.7	9.89
August	16.3	81.2	9.37	19.8	69.0	9.88	20.3	67.4	9.95
September	20.2	68.0	9.98	18.6	73.3	9.74	19.9	68.0	9.82
October	19.9	70.6	10.22	21.3	66.5	10.49	21.56	65.81	10.53

4.3.3.6 Summary

The following table 4.7 summarizes for the three configurations the optimal values of the input parameters that gave the highest COP. It also gives the results of the outputs including the loads, the power consumption and the COP. The supply indoor air conditions are as well indicated.

Table 4.7: A summary of the input values, the outputs and supply air conditions in the three configurations

	Input parameters							Observed quantities						Supply indoor air	
Month	$\dot{m}_{s1}$ (kg/s)	$\dot{m}_{s2}$ (kg/s)	$\dot{m}_{s0}$ (kg/s)	$\dot{m}_{ae}$ (m^3/h)	$\dot{m}_{ac}$ (m^3/h)	$\dot{m}_{a,hx2}$ (m^3/h)	T_{evap1} (˚C)	Q_L (W)	Q_S (W)	Q_{S1} (W)	Q_{S2} (W)	Power (kW)	$COP_{overall}$ (-)	T_i (˚C)	RH_i (%)
1st configuration															
May	1	0.5	0.11	2300	175	1600	12.6	722	4630	399	4231	1.27	5.08	18.1	71.1
Jun	2	1.4	0.08	5100	3900	350	14.7	3529	6643	804	5839	3.44	3.19	20.2	71.3
Jul	1.8	1.7	0.12	4500	2900	2200	13.45	2742	7754	614	7140	3.30	3.55	19.0	71.7
Aug	1.5	1.4	0.09	3200	2000	2200	10.6	2973	8364	283	8081	3.89	3.17	16.3	81.2
Sept	1.7	0.8	0.13	4700	1800	1450	14.7	2247	6149	776	5373	2.43	3.97	20.2	68.0
Oct	1.1	1.2	0.12	2950	2750	420	14.5	1865	4105	528	3577	1.63	4.36	19.9	70.6
2nd configuration															
May	1.1	1.1	0.11	4400	115	3500	14.3	721	4647	2766	1881	1.33	4.82	20.9	61.1
Jun	1.8	1.2	0.14	5020	2000	1400	12.5	3520	6545	3784	2761	3.39	3.39	20.1	72.0
Jul	1.6	0.6	0.13	5100	1400	2200	13.7	2736	7704	3285	4419	2.97	3.94	19.5	69.9
Aug	0.9	0.7	0.04	5900	2000	2800	11.6	2967	8368	4309	4059	3.12	3.75	19.8	69.0
Sept	1.1	1.1	0.07	3400	1600	3150	12.9	2251	6195	2727	3468	2.19	4.16	18.6	73.3
Oct	0.7	0.4	0.13	4550	1000	1500	12.7	1863	4095	3266	829	1.50	4.79	21.3	66.5
3rd configuration															
Month	$\dot{m}_{s1}$ (kg/s)	$\dot{m}_{s2}$ (kg/s)	$\dot{m}_{s0}$ (kg/s)	$\dot{m}_{ae}$ (m^3/h)	$\dot{m}_{ac}$ (m^3/h)	T_{evap1} (˚C)	T_{evap2} (˚C)	Q_L (W)	Q_S (W)	Q_{S1} (W)	Q_{S2} (W)	Power (kW)	$COP_{overall}$ (-)	T_i (˚C)	RH_i (%)
May	0.3	0.2	0.14	2700	2100	17.8	17.9	719	4640	719	3921	1.17	5.65	20.9	60.1
Jun	1.2	0.52	0.11	5000	710	16.4	17.8	3524	6540	2069	4471	2.88	3.84	20.8	70.1
Jul	0.6	0.4	0.11	5000	1100	15.9	16.9	2739	7710	1608	6102	2.71	4.28	19.9	68.7
Aug	0.7	0.5	0.11	5000	2420	14.3	17.3	2969	8340	2863	5477	3.05	4.05	20.3	67.4
Sept	0.5	0.8	0.08	3800	1650	14	16.9	2250	6160	2192	3968	2.04	4.48	19.9	68.0
Oct	0.5	0.5	0.1	5000	860	16.2	18.6	1852	4100	1740	2360	1.37	5.02	21.6	65.8

4.3.4 Analysis

Figure 11 shows a comparison of the system's COP between the base case and the three studied flexible hybrid systems.

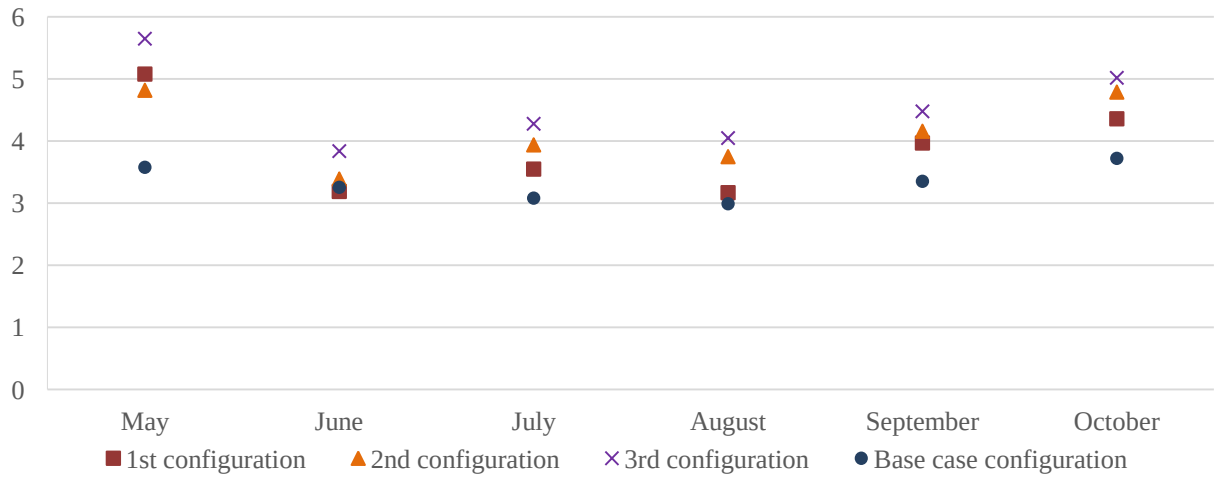

Figure 4.10: comparison of the COP of the base case system and the three studied configurations

It is observed that the base case system consisting of a conventional vapor compression cycle possesses the lowest COP among all the other configurations. It can be clearly observed by comparing the results of the three configurations that in the third configuration the figures of the COPs of all the months are higher than the other configurations. Analyzing the COPs of the 6 months simulated by the first and second configurations shows that the first configuration is more performing than the second only for the month of May. While for the other months from June to October, the second configuration has proved to be more efficient.

We may say that whenever the ratio of latent to sensible load is low, it is more favorable to reduce the temperature of air prior to dehumidifying it. Comparing the results of the second configuration in the months where it is more favorable shows a contradiction with the fact that as the ambient air temperature decreases as the COP of the system increases. We can recognize that even though the ambient temperature in August is higher than that in June, still the COP of the system in August is greater than that of June. The same can be noticed if we compare June with July. This is because whenever the latent load is, higher which is the case of June, in order to increase the latent load removal in the dehumidifier, the evaporation temperature decreases causing the COP to decrease.

The evaporation and the condensation temperatures determine the COP of the system and they are highly dependent on the concentration of the solution as well as on the mass flow rates of air in the regenerator, in the heat exchangers, and in the dehumidifier. The solution concentration in the regenerator as well as the condensation and evaporation temperatures of the vapor compression cycles are shown in table 4.8.

Table 4.8: Condensation and evaporation temperatures with percentage concentration of solution.

Month	T_{cond1} (°C)	T_{evap1} (°C)	T_{cond2} (°C)	T_{evap2} (°C)	$C_{s,reg}$ (kg/kg)
1st configuration					
May	35.01	12.6	--	--	0.216
June	50.69	14.65	--	--	0.308
July	45.63	13.35			0.288
August	48.48	10.6			0.298
September	43.74	14.65	--	--	0.274
October	39.13	14.45	--	--	0.260
2nd configuration					
May	33.83	14.3	--	--	0.215
June	47.1	12.5			0.276
July	44.44	13.65			0.276
August	44.12	11.55	--	--	0.272
September	40.39	12.9	--	--	0.261
October	36.87	12.65	--	--	0.216
3rd configuration					
May	33.06	17.8	36.55	17.88	0.273
June	52.5	16.35	39.7	17.75	0.310
July	50	15.85	41.84	16.85	0.311
August	47.3	14.25	42.54	17.25	0.297
September	42.43	14	38.69	16.91	0.278
October	40.75	16.15	35.48	18.56	0.263

When comparing the behavior of the first two configurations in October, we observe that by passing from the first configuration to the second, the amount of latent and sensible loads removed increases if no changes are proposed to the input parameters. The mass flow rate of the regeneration air if decreased, the latent load removal decreases while the sensible load removal is not affected. In order to decrease the sensible load control, the mass flow rate of the air in the dehumidifier should be increased which in turn greatly decreases the latent load control. These changes cause the concentration of the solution to increase, thus increasing the condensation temperature and reducing the COP of the system. But again to slightly increase the latent load removal, the air mass flow rate in hx_2 should be increased and the solution mass flow rate in the dehumidifier should be decreased which in turn lowers the concentration of the solution reducing the condensation temperature and increasing the COP. Thus the COP in the second configuration is higher than that in the first due to the difference in the condensation temperature (affected by the higher regeneration air mass flow rate).

As mentioned before, the third configuration shows the highest values of COP in each of the six studied months. Yet, the chosen input values could be optimized by changing the mass flow rates of the air entering the condenser on one side and of the recycled air entering the evaporator on another side.

More globally, the three proposed configurations are flexible and can operate in a wide range of latent to sensible load ratio. This feature surpasses the proposed systems in literature where

the performance is studied and discussed for a critical nominal point or for a tight range of operating conditions.

4.4 Conclusions and outlook

Three different configurations of a flexible hybrid liquid desiccant membrane based system have been proposed and studied in six months of a year where cooling is needed in an office located in a Mediterranean climate. Energy and mass equations were used to do the modeling and the results showed that the ratio of latent to sensible load plays an important role in determining the most relevant application of a certain configuration. The following conclusions can be drawn:

(1) Compared to a vapor compression system, hybrid systems allow using a higher air mass flow rate to achieve higher supply air temperatures and thus higher evaporation temperatures.
(2) The installation of storage tanks in the system increases its flexibility where the concentration of the desiccant solution could be varied between the dehumidification cycle and the regeneration cycle.
(3) Whenever the ratio of latent to sensible load inside the room is of a low value, it is more efficient to remove part of its sensible load first and then to dry it by the dehumidifier.
(4) When the ratio of latent to sensible load inside the room is high, it is favorable to dehumidify the air first and then send it for further cooling.
(5) Using two vapor compression cycles showed to be the highest performing system for the studied months where cooling is needed.

The results show that the studied systems present promising alternatives for traditional systems where they can significantly improve the performance and decrease the consumption of electricity in buildings. The third configuration where two vapor compression cycles were used revealed its effectiveness in each of the six studied months. However, this configuration is the most costly among the others, and still it should be proved whether the low running cost would be able to compensate for the high initial cost. Thus a compromise should be reached between the effectiveness of the system and its price. Moreover, the numerical results showed that in every month the flow rates of the refrigerant, the desiccant solution and the air are changed for proper latent and sensible load removal. The concentration of the desiccant solution also differs and in order to reach the optimal concentration, the system passes through a transient regime changing from one month to another that needs to be further examined. Such a change in these parameters between different inlet conditions recommends a control system to regulate the flows and the concentrations in the system without any manual intervention. In further steps our proposed flexible system should be thoroughly studied with a dynamic model and a proper control system to be able to respond to the continuously changing demands.

Conclusion and General Outlook

The primary objective of this work was to deeply understand the hybrid refrigeration system technology for highly efficient coupled heat and mass transfers to be able to integrate such a system in different applications.

The first section of the thesis described the global energy situation with its serious environmental concerns causing significant climate change with long term effects on people's health and well-being. Statistical analysis showed a rise in energy demand and thus in electricity consumption as a result of climate change, global temperature increment, population growth and a greater thermal comfort desire. The building sector appeared to be the highest electricity consumer contributing to around 50%; with space cooling occupying the lion's share. Conventional vapor compression cycles are the commonly used systems for air conditioning despite their drawbacks. They consume excessive energy trying to lower the moisture content in air, they deliver low indoor air quality and they bring damage to the environment through the used refrigerants. For these reasons providing healthy indoor environment with low energy demand is a considerable engineering challenge and the search for innovative technologies that could respond to it has risen. Thus, a literature review was then done on hybrid liquid desiccant systems that are environmentally friendly, feasible and cost effective alternatives. They help reach the required levels of humidity more effectively and without compromising indoor air quality and comfort conditions especially in hot and humid weather. In these systems, humidity control was separated from temperature control systems improving their overall energy efficiency and reducing their resultant energy costs. The dehumidifier and the regenerator of such hybrid systems were considered the main challenging components since their design could greatly affect the control of both temperature and humidity. Therefore, heat and mass exchangers were thoroughly investigated mainly the indirect type using membranes as separators between the desiccant solution and air preventing corrosion problems. However, after describing the existing designs of these exchangers it could be noticed that they still have certain drawbacks regarding the system flexibility and the membrane properties and price. These drawbacks were deeply examined and overcome by a novel proposed design defined by spraying the desiccant vertically inside the channels of the exchanger. Another improvement was by suggesting the use of non-woven fabrics to act as membranes in heat and mass exchangers due to their significant advantages mainly regarding their vapor permeability, their moisture resistance and their low cost. The proper understanding and modeling of coupled heat and mass transfers within the porous membranes are considered key factors to efficiently integrate them into processes and to benefit from the advantages of these systems compared to existing conventional technologies.

In a later chapter, the non-woven fabrics along with other materials were tested experimentally using a modified cup method in order to find out their water vapor permeability also known as mass conductivity. The modified method, unlike the upright cup method described in ASTM E96 standard, was able to predict the water vapor transmission rate in highly permeable porous materials using a detailed inverse methodology. The experiments were capable of determining the mass conductivities of the tested membranes and the results were later subjected to an uncertainty analysis to assess the accuracy of this

technique using Monte Carlo method. According to the results, the non-woven fabric NWF-1 possessed the best compromise between the mass conductivity ($km = 4.3x10^{-6}\ kg/m.s$), the required enduring properties and a low price. This fabric is then employed as a membrane in a prototype of a liquid to air cross flow heat and mass exchanger. It was used to cover the channels, in which liquid flows inside, separating the two fluids. Experiments were conducted to evaluate the performance of the exchanger considering different input conditions. They involved the collection of data from different sensors inserted in the test bench and experiments were repeated to avoid uncertainties due to systematic error and uncontrollable variability. Then, in a way to predict the behavior of this exchanger, a detailed 2-D mathematical model was developed and written in Modelica language using Dymola software. Conjugate energy and mass transfer equations were derived and then discretized and solved using a finite volume approach at steady state. Simulations were performed and the validity of the model was checked by experimental verifications and observations. An acceptable compatibility of the experimental and numerical outcomes proved that the model could be used for the prediction of the performance of such an exchanger. Later, an uncertainty analysis was performed on the results by Monte Carlo method. Then in a way to optimize our model, an error function was optimized to minimize the difference between the power predicted numerically and calculated experimentally.

In the last chapter a hybrid system was used to perform the seasonal air conditioning of an office in Nice having a Mediterranean climate where the indoor ratio of the latent to sensible load was always changing. The previously validated model was used to assess the performance of the heat and mass exchangers of the liquid desiccant system. Each component of the vapor compression cycle was described along with its modeling equations. Then a complete model was used to assess the performance of the hybrid system in the different months of the year where cooling is required. To increase the flexibility of the system heat exchangers were added. The placement of the heat exchangers is a critical issue and thus different configurations were studied. The first one consisted of adding heat exchangers before the dehumidifier and the regenerator while the second involved inserting them right after. A third configuration was suggested where instead of adding heat exchangers, a second vapor compression cycle was inserted after the dehumidification cycle. The simulation results of each configuration were compared to those of a conventional vapor compression cycle and they provided insight about the contribution of hybrid systems in reducing the energy cost when cleverly implemented in buildings. The findings claimed that whenever the ratio of latent to sensible load inside the room (R') is of a high value it was more efficient to remove part of its sensible load first and then to dry it by the dehumidifier. For low values of (R'), it was favorable to dehumidify the air first and then cool it.

The investigations within this study not only revealed the optimization potential of membrane heat and mass exchangers but also provoked future work. From this study it was shown that the properties of the membrane are key factors that affect the performance of the exchangers. The proposed non-woven fabric membrane tested in chapter 2 was chosen for its high mass conductivity and low manufacturing cost. Yet, the performance and functionality of the tested membranes might be adversely affected over time. Thus it would be interesting to check the durability and the lifetime of these kinds of membranes and try to find practical guidelines to

optimize them if needed. It is also beneficial to examine the pollution transfer across the membranes to decide if they are suitable to be used in residential buildings or in food storage rooms. In addition, the exchanger should also be functioned with a liquid desiccant instead of water to check for compatibility of the non-woven fabrics with chemicals and to insure long term performance.

The findings of the last chapter gave an idea about the best operating parameters that would remove the load for every typical outdoor condition. The numerical results indicated that for each month the flow rates of the refrigerant, of the desiccant solution and of the air were changed for proper latent and sensible load removal. The concentration of the desiccant solution varied as well and in order to reach the optimal concentration, the system passed through a transient regime. In later research the transient behavior of the system should be examined to check the time needed to reach equilibrium while moving from one condition to another through a dynamic model. The model should be helpful in studying the effect of the changing mass flow rates, temperatures and concentrations on the transient performance. Moreover, such a change in these target parameters at different inlet conditions recommends a control system to regulate the flows and the concentrations in the system without any manual intervention. These findings open up some perspectives focusing on investigating a control strategy for the system performance improvement upon varying operation conditions. The strategy aims to control the target parameters to successfully converge them to the desired values towards a steady state in reduced transient time.

Another recommendation for a future work would include the reconstruction of the exchanger prototype with an increased number of channels and larger dimensions to be tested with increased air and water temperatures and mass flow rates. Furthermore, it could be beneficial to build the entire hybrid liquid desiccant air conditioning system described in the last chapter. The system would be fully assessed in the prospect of manufacturing and testing within timeframe, cost and potential technical constraints. Additionally, experimental tests could be performed directly on the full system discovering and technically understanding unexpected phenomena, and improving the accuracy in interpreting the system functionality. Then the results estimated numerically would be compared to the experimental data aiming to closely examine the precision and the robustness of the suggested model that can be used later to predict large scale operations.

References

A. P. S. Sawhney, Kimmel, L.B., Ruppenicker, G.F., Thibodeaux, D.P., 1993. A Unique Polyester Staple-Core / Cotton-Wrap Yarn Made on a Tandem Spinning System.

Abdel-Salam, A.H., Ge, G., Simonson, C.J., 2013. Performance analysis of a membrane liquid desiccant air-conditioning system. Energy and Buildings 62, 559–569. https://doi.org/10.1016/j.enbuild.2013.03.028

Abdel-Salam, A.H., Simonson, C.J., 2016. State-of-the-art in liquid desiccant air conditioning equipment and systems. Renewable and Sustainable Energy Reviews 58, 1152–1183. https://doi.org/10.1016/j.rser.2015.12.042

Afshin, M., 2010. Selection of the liquid desiccant in a run-around membrane energy exchanger.

Åkesjö, A., Vamling, L., Sasic, S., Olausson, L., Innings, F., Gourdon, M., 2018. On the measuring of film thickness profiles and local heat transfer coefficients in falling films. Experimental Thermal and Fluid Science 99, 287–296. https://doi.org/10.1016/j.expthermflusci.2018.07.028

Al-Waked, R., Nasif, M.S., Mostafa, D.B., 2018. Enhancing the performance of energy recovery ventilators. Energy Conversion and Management 171, 196–210. https://doi.org/10.1016/j.enconman.2018.05.105

Ameen, F.R., Coney, J.E.R., Sheppard, C.G.W., 1993. Experimental study of warm-air defrosting of heat-pump evaporators. International Journal of Refrigeration 16, 13–18. https://doi.org/10.1016/0140-7007(93)90015-Z

Apelblat, A., Weintraub, R., Tamir, A., 1984. Enthalpy of solution of lithium chloride and of lithium chloride monohydrate in water. The Journal of Chemical Thermodynamics 16, 935–941. https://doi.org/10.1016/0021-9614(84)90161-7

ASTM E 96 Standard Test Methods for Water Vapor Transmission of Materials., 2013. . ASTM International, West Conshohocken, PA.

Bai, H., Zhu, J., Chen, Z., Chu, J., Liu, Y., 2018. Performance evaluation of a membrane-based flat-plate heat and mass exchanger used for liquid desiccant regeneration. Applied Thermal Engineering 139, 569–584. https://doi.org/10.1016/j.applthermaleng.2018.05.011

Bansal, P., Fothergill, D., Fernandes, R., 2010. Thermal analysis of the defrost cycle in a domestic freezer. International Journal of Refrigeration 33, 589–599. https://doi.org/10.1016/j.ijrefrig.2009.11.012

Baqir, A.Sh., Mahood, H.B., Hameed, M.S., Campbell, A.N., 2016. Heat transfer measurement in a three-phase spray column direct contact heat exchanger for utilisation in energy recovery from low-grade sources. Energy Conversion and Management 126, 342–351. https://doi.org/10.1016/j.enconman.2016.08.013

Bell, S., 1999. Measurement Good Practice Guide No. 11 (Issue 2) 41.

Bergero, S., Chiari, A., 2011. On the performances of a hybrid air-conditioning system in different climatic conditions. Energy, PRES 2010 36, 5261–5273. https://doi.org/10.1016/j.energy.2011.06.030

Bergero, S., Chiari, A., 2010. Performance analysis of a liquid desiccant and membrane contactor hybrid air-conditioning system. Energy and Buildings 42, 1976–1986. https://doi.org/10.1016/j.enbuild.2010.06.003

Bergero, S., Chiari, A., Isetti, C., 2000. On the performance of a plane plate membrane contactor for air dehumidification.

Birol, D.F., 2018. The Future of Cooling.

Boles, M.A., Cengel, Y.A., 1998. Chapter 10: Refrigeration Cycles, in: Thermodynamics: An Engineering Approach. p. 15.

Bolton, D., 1980. The Computation of Equivalent Potential Temperature. Mon. Wea. Rev. 108, 1046–1053. https://doi.org/10.1175/1520-0493(1980)108<1046:TCOEPT>2.0.CO;2

Bose, B.K., 2010. Global Warming: Energy, Environmental Pollution, and the Impact of Power Electronics. IEEE Industrial Electronics Magazine 4, 6–17. https://doi.org/10.1109/MIE.2010.935860

Boundary layer thickness, 2019. . Wikipedia.

Bouzenada, S., Kaabi, A.N., Frainkin, L., Salmon, T., Léonard, A., 2016. Experimental Comparative Study on Lithium Chloride and Calcium Chloride Desiccants. Procedia Computer Science, The 7th International Conference on Ambient Systems, Networks and Technologies (ANT 2016) / The 6th International Conference on Sustainable Energy Information Technology (SEIT-2016) / Affiliated Workshops 83, 718–725. https://doi.org/10.1016/j.procs.2016.04.159

Bruining, W.J., 1989. A general description of flows and pressures in hollow fiber membrane modules. Chemical Engineering Science 44, 1441–1447. https://doi.org/10.1016/0009-2509(89)85016-X

Byrne, P., Miriel, J., Lénat, Y., 2011. Experimental study of an air-source heat pump for simultaneous heating and cooling - Part 2: Dynamic behaviour and two-phase thermosiphon defrosting technique. Applied Energy 88, 3072–3078. https://doi.org/10.1016/j.apenergy.2011.03.002

Byun, J.-S., Lee, J., Jeon, C.-D., 2008. Frost retardation of an air-source heat pump by the hot gas bypass method. International Journal of Refrigeration 31, 328–334. https://doi.org/10.1016/j.ijrefrig.2007.05.006

Canada, Office of Energy Efficiency, 2004. Heating and cooling with a heat pump. Office of Energy Efficiency, Ottawa.

Capozzoli, A., Mazzei, P., Minichiello, F., Palma, D., 2006. Hybrid HVAC systems with chemical dehumidification for supermarket applications. Applied Thermal Engineering 26, 795–805. https://doi.org/10.1016/j.applthermaleng.2005.10.014

Çengel, Y.A., Boles, M.A., 2015. Thermodynamics an engineering approach ED8 - StuDocu [WWW Document]. URL https://www.studocu.com/en/document/cavite-state-university/bachelor-of-science-in-industrial-engineering/book-solutions/thermodynamics-an-engineering-approach-ed8/2684204/view (accessed 5.16.19).

Chen, Y., Deng, N., Xin, B.-J., Xing, W.-Y., Zhang, Z.-Y., 2019. Structural characterization and measurement of nonwoven fabrics based on multi-focus image fusion. Measurement 141, 356–363. https://doi.org/10.1016/j.measurement.2019.04.034

Cheng, Q., Zhang, X., 2013. Review of solar regeneration methods for liquid desiccant air-conditioning system. Energy and Buildings 67, 426–433. https://doi.org/10.1016/j.enbuild.2013.08.053

Chengqin, R., Yi, J., Guangfa, T., Yianpin, Z., 2005. A characteristic study of liquid desiccant dehumidification/regeneration processes. Solar Energy 79, 483–494. https://doi.org/10.1016/j.solener.2004.12.010

Cho, H.-J., Cheon, S.-Y., Jeong, J.-W., 2019. Experimental analysis of dehumidification performance of counter and cross-flow liquid desiccant dehumidifiers. Applied Thermal Engineering 150, 210–223. https://doi.org/10.1016/j.applthermaleng.2019.01.006

Climate Change 2014 Summary for Policymakers (Synthesis Report), 2014.

Concentrations de CO2 dans l'Atmosphere. Elements de Prospective, 2015.

Conde, M.R., 2014. Aqueous solutions of lithium and calcium chlorides: property formulations for use in air conditioning equipment design.

Conde, M.R., 2004. Properties of aqueous solutions of lithium and calcium chlorides: formulations for use in air conditioning equipment design. International Journal of Thermal Sciences 43, 367–382. https://doi.org/10.1016/j.ijthermalsci.2003.09.003

Dai, Y.J., Wang, R.Z., Zhang, H.F., Yu, J.D., 2001. Use of liquid desiccant cooling to improve the performance of vapor compression air conditioning. Applied Thermal Engineering 21, 1185–1202. https://doi.org/10.1016/S1359-4311(01)00002-3

Daou, K., Wang, R.Z., Xia, Z.Z., 2006. Desiccant cooling air conditioning: a review. Renewable and Sustainable Energy Reviews 10, 55–77. https://doi.org/10.1016/j.rser.2004.09.010

Das, R.S., Jain, S., 2017. Experimental investigations on a solar assisted liquid desiccant cooling system with indirect contact dehumidifier. Solar Energy 153, 289–300. https://doi.org/10.1016/j.solener.2017.05.071

Ding, Y., Ma, G., Chai, Q., Jiang, Y., 2004. Experiment investigation of reverse cycle defrosting methods on air source heat pump with TXV as the throttle regulator. International Journal of Refrigeration 27, 671–678. https://doi.org/10.1016/j.ijrefrig.2004.01.008

Dirker, J., Meyer, J.P., Kohlmeyer, B.W., 2017. Local heat transfer coefficients at the inlet of an annular flow passage. International Journal of Heat and Mass Transfer 113, 268–280. https://doi.org/10.1016/j.ijheatmasstransfer.2017.05.044

ESA, 2018. Spotlight on sea-level rise [WWW Document]. European Space Agency. URL https://www.esa.int/Our_Activities/Observing_the_Earth/Spotlight_on_sea-level_rise (accessed 9.28.19).

EURIMA - U-values in Europe [WWW Document], n.d. URL https://www.eurima.org/u-values-in-europe/ (accessed 5.14.18).

Evans, P., 2016. How Cooling Towers work. The Engineering Mindset. URL http://theengineeringmindset.com/how-cooling-towers-work/ (accessed 6.15.18).

Factor, H.M., Grossman, G., 1980. A packed bed dehumidifier/regenerator for solar air conditioning with liquid desiccants. Solar Energy 24, 541–550. https://doi.org/10.1016/0038-092X(80)90353-9

Farrance, I., 2014. Uncertainty in Measurement: A Review of Monte Carlo Simulation Using Microsoft Excel for the Calculation of Uncertainties Through Functional Relationships, Including Uncertainties in Empirically Derived Constants. The Clinical biochemist. Reviews / Australian Association of Clinical Biochemists 35, 37.

Feron, P.H.M., Jansen, A.E., 2002. CO2 separation with polyolefin membrane contactors and dedicated absorption liquids: performances and prospects. Separation and Purification Technology 27, 231–242. https://doi.org/10.1016/S1383-5866(01)00207-6

Flat fan nozzles, n.d.

Fong, K.F., Lee, C.K., Chow, T.T., Fong, A.M.L., 2011. Investigation on solar hybrid desiccant cooling system for commercial premises with high latent cooling load in subtropical Hong Kong. Applied Thermal Engineering 31, 3393–3401. https://doi.org/10.1016/j.applthermaleng.2011.06.024

Fu, H.-X., Liu, X.-H., 2017. Review of the impact of liquid desiccant dehumidification on indoor air quality. Building and Environment 116, 158–172. https://doi.org/10.1016/j.buildenv.2017.02.014

Furukawa, M., 1991. Practical expressions for thermodynamic and transport properties of commonly used fluids | Journal of Thermophysics and Heat Transfer [WWW Document]. URL https://arc.aiaa.org/doi/10.2514/3.296 (accessed 5.17.19).

Gabelman, A., Hwang, S.-T., 1999. Hollow fiber membrane contactors. Journal of Membrane Science 159, 61–106. https://doi.org/10.1016/S0376-7388(99)00040-X

Ge, F., Guo, X., Hu, Z., Chu, Y., 2011. Energy savings potential of a desiccant assisted hybrid air source heat pump system for residential building in hot summer and cold winter zone in China. Energy and Buildings 43, 3521–3527. https://doi.org/10.1016/j.enbuild.2011.09.021

Ge, G., Ghadiri Moghaddam, D., Abdel-Salam, A.H., Besant, R.W., Simonson, C.J., 2014. Comparison of experimental data and a model for heat and mass transfer performance of a liquid-to-air membrane energy exchanger (LAMEE) when used for air dehumidification and salt solution regeneration. International Journal of Heat and Mass Transfer 68, 119–131. https://doi.org/10.1016/j.ijheatmasstransfer.2013.09.016

Ghadiri Moghaddam, D., Oghabi, A., Ge, G., Besant, R.W., Simonson, C.J., 2013. Numerical model of a small-scale liquid-to-air membrane energy exchanger: Parametric study of membrane resistance and air side convective heat transfer coefficient. Applied Thermal Engineering 61, 245–258. https://doi.org/10.1016/j.applthermaleng.2013.07.017

Gluesenkamp, K., Radermacher, R., 2011. 11 - Heat-activated cooling technologies for small and micro combined heat and power (CHP) applications, in: Beith, R. (Ed.), Small and Micro Combined Heat and Power (CHP) Systems, Woodhead Publishing Series in Energy. Woodhead Publishing, pp. 262–306. https://doi.org/10.1533/9780857092755.2.262

Griffin, D.P., 2017. CDP Carbon Majors Report 2017 16.

Guimaraes Couto, P.R., Carreteiro, J., de Oliveir, S.P., 2013. Monte Carlo Simulations Applied to Uncertainty in Measurement, in: Chan, W.K.V. (Ed.), Theory and Applications of Monte Carlo Simulations. InTech. https://doi.org/10.5772/53014

Gurubalan, A., Maiya, M.P., Tiwari, S., 2017. Performance characterization of membrane dehumidifier with desiccants in flat-plate arrangement. Energy and Buildings 156, 151–162. https://doi.org/10.1016/j.enbuild.2017.09.040

Hall, N., 2015. Boundary Layer [WWW Document]. URL https://www.grc.nasa.gov/WWW/k-12/airplane/boundlay.html (accessed 5.27.19).

Hoffenbecker, N., Klein, S.A., Reindl, D.T., 2005. Hot gas defrost model development and validation. International Journal of Refrigeration 28, 605–615. https://doi.org/10.1016/j.ijrefrig.2004.08.016

Holman, J.P., 1989. Heat transfer. McGraw-Hill.

Holtz, M., Heil, S.R., Sacco, A., 2000. Temperature-dependent self-diffusion coefficients of water and six selected molecular liquids for calibration in accurate 1H NMR PFG measurements - Physical Chemistry Chemical Physics (RSC Publishing) [WWW Document]. URL https://pubs.rsc.org/en/content/articlelanding/2000/cp/b005319h#!divAbstract (accessed 5.17.19).

Huang, S.-M., 2015. Heat and mass transfer in a quasi-counter flow parallel-plate membrane-based absorption heat pump (QPMAHP). Journal of Membrane Science 496, 39–47. https://doi.org/10.1016/j.memsci.2015.08.027

Huang, S.-M., Yang, M., Hong, Y., Ye, W.-B., 2018. Performance correlations of an adjacently internally-cooled membrane contactor applied for liquid desiccant air dehumidification. Applied Thermal Engineering 129, 1660–1669. https://doi.org/10.1016/j.applthermaleng.2017.10.154

Huang, S.-M., Yang, M., Yang, X., 2014. Performance analysis of a quasi-counter flow parallel-plate membrane contactor used for liquid desiccant air dehumidification. Applied Thermal Engineering 63, 323–332. https://doi.org/10.1016/j.applthermaleng.2013.11.027

Huang, S.-M., Zhang, L.-Z., 2013. Researches and trends in membrane-based liquid desiccant air dehumidification. Renewable and Sustainable Energy Reviews 28, 425–440. https://doi.org/10.1016/j.rser.2013.08.005

Huang, S.-M., Zhang, L.-Z., Tang, K., Pei, L.-X., 2012. Fluid flow and heat mass transfer in membrane parallel-plates channels used for liquid desiccant air dehumidification. International Journal of Heat and Mass Transfer 55, 2571–2580. https://doi.org/10.1016/j.ijheatmasstransfer.2012.01.003

Huang, S.-M., Zhang, L.-Z., Yang, M., 2013. Conjugate heat and mass transfer in membrane parallel-plates ducts for liquid desiccant air dehumidification: Effects of the developing entrances. Journal of Membrane Science 437, 82–89. https://doi.org/10.1016/j.memsci.2013.02.048

Huang, S.-M., Zhong, Z., Yang, M., 2016. Conjugate heat and mass transfer in an internally-cooled membrane-based liquid desiccant dehumidifier (IMLDD). Journal of Membrane Science 508, 73–83. https://doi.org/10.1016/j.memsci.2016.02.026

Hyun, Y.J., Hyun, J.H., Chun, W.G., Kang, Y.H., 2005. An experimental investigation into the operation of a direct contact heat exchanger for solar exploitation. International Communications in Heat and Mass Transfer 32, 425–434. https://doi.org/10.1016/j.icheatmasstransfer.2004.06.003

IEA, 2018. Global Energy and CO2 Status Report 2018. Energy Demand.

Incropera, F.P., 2007. Natural Convection, in: Fundementals of Heat and Mass Transfer. John Wiley, Hoboken, NJ.

Incropera, F.P., DeWitt, D.P., 1996. Introduction to Heat Transfer, third ed. ed. John Wiley & Sons, New York.

Incropera, F.P., DeWitt, D.P., Bergman, T.L., Lavine, A.S., 2007. Fundamentals of Heat and Mass Transfer - 6th Edition.

International Energy Agency and the United Nations Environment Program, 2018. 2018 Global Status Report - Towards a zero-emission, efficient and resilient buildings and construction sector.

ISO 2528 Sheet materials – Determination of water vapour transmission rate – Gravimetric (dish) method., 1995. . International Organization for Standardization, Geneva.

Jafarian, H., Sayyaadi, H., Torabi, F., 2019. Numerical modeling and comparative study of different membrane-based liquid desiccant dehumidifiers. Energy Conversion and Management 184, 735–747. https://doi.org/10.1016/j.enconman.2019.01.099

Jani, D.B., Mishra, M., Sahoo, P.K., 2016. Solid desiccant air conditioning – A state of the art review. Renewable and Sustainable Energy Reviews 60. https://doi.org/10.1016/j.rser.2016.03.031

Johnson, D.W., Yavuzturk, C., Pruis, J., 2003. Analysis of heat and mass transfer phenomena in hollow fiber membranes used for evaporative cooling. Journal of Membrane Science 227, 159–171. https://doi.org/10.1016/j.memsci.2003.08.023

Joseph W. Lstiburek, 2017. It’s All Relative. Magic and Mystery of the Water Molecule. ASHRAE Journal.

Khalil, A., 2012. An experimental study on multi-purpose desiccant integrated vapor-compression air-conditioning system. https://doi.org/10.1002/er.1767

Khan, A.Y., 1998. Cooling and dehumidification performance analysis of internally-cooled liquid desiccant absorbers. Applied Thermal Engineering 18, 265–281. https://doi.org/10.1016/S1359-4311(97)00074-4

Khan, A.Y., Sulsona, F.J., 1998. Modelling and parametric analysis of heat and mass transfer performance of refrigerant cooled liquid desiccant absorbers. International Journal of Energy Research 22, 813–832. https://doi.org/10.1002/(SICI)1099-114X(199807)22:9<813::AID-ER403>3.0.CO;2-M

Kistler, K.R., Cussler, E.L., 2002. Membrane Modules for Building Ventilation. Chemical Engineering Research and Design, Process and Product Development 80, 53–64. https://doi.org/10.1205/026387602753393367

Kovats, R., Butler, C., 2012. Global health and environmental change: linking research and policy. Current Opinion in Environmental Sustainability 7.

Larson, M., Simonson, C., Besant, R., Gibson, P., 2007. The elastic and moisture transfer properties of polyethylene and polypropylene membranes for use in liquid-to-air energy exchangers. Journal of Membrane Science 302, 136–149. https://doi.org/10.1016/j.memsci.2007.06.050

Lee, W.-J., Jeong, J.H., 2019. Development of a numerical analysis model for a multi-port mini-channel heat exchanger considering a two-phase flow distribution in the header. Part I: Numerical modeling. International Journal of Heat and Mass Transfer 138, 1264–1280. https://doi.org/10.1016/j.ijheatmasstransfer.2019.04.100

Li, W., Yao, Y., 2018. Study on the method for testing the water vapor diffusion resistance of membranes. Polymer Testing 69, 80–90. https://doi.org/10.1016/j.polymertesting.2018.04.030

Liang, C.H., 2014. Experiments Investigation of the Parallel-plates Enthalpy Exchangers. Energy Procedia, International Conference on Applied Energy, ICAE2014 61, 2699–2703. https://doi.org/10.1016/j.egypro.2014.12.281

Lienhard, J.H., 2005. Heat Transfer by Impingement of Circular Free-Surface Liquid Jets.

Lin, J., Huang, S.-M., Wang, R., Chua, K.J., 2018. Thermodynamic analysis of a hybrid membrane liquid desiccant dehumidification and dew point evaporative cooling system. Energy Conversion and Management 156, 440–458. https://doi.org/10.1016/j.enconman.2017.11.057

Liu, X., Gabour, L.A., Lienhard, V., J.H., 1993. Stagnation-Point Heat Transfer During Impingement of Laminar Liquid Jets: Analysis Including Surface Tension. J. Heat Transfer 115, 99–105. https://doi.org/10.1115/1.2910677

Mahood, H.B., 2008. Direct-contact heat transfer of a single volatile liquid drop evaporation in an immiscible liquid. Desalination, European Desalination Society and Center for Research and Technology Hellas (CERTH), Sani Resort 22 –25 April 2007, Halkidiki, Greece 222, 656–665. https://doi.org/10.1016/j.desal.2007.01.188

Mahood, H.B., Campbell, A.N., Thorpe, R.B., Sharif, A.O., 2015. Heat transfer efficiency and capital cost evaluation of a three-phase direct contact heat exchanger for the utilisation of low-grade energy sources. Energy Conversion and Management 106, 101–109. https://doi.org/10.1016/j.enconman.2015.09.023

McPherson, M.J., 1993. Subsurface Ventilation and Environmental Engineering, in: Subsurface Ventilation Engineering. p. 834.

Mills, A.F., 1995. Heat and Mass Transfer. Chicago, Ill: Irwin.

Min, Y., Chen, Y., Yang, H., 2019. Numerical study on indirect evaporative coolers considering condensation: A thorough comparison between cross flow and counter flow. International Journal of Heat and Mass Transfer 131, 472–486. https://doi.org/10.1016/j.ijheatmasstransfer.2018.11.082

Misha, S., Mat, S., Ruslan, M.H., Sopian, K., 2012. Review of solid/liquid desiccant in the drying applications and its regeneration methods. Renewable and Sustainable Energy Reviews 16, 4686–4707. https://doi.org/10.1016/j.rser.2012.04.041

Mohammad, A.Th., Mat, S.B., Sopian, K., Al-abidi, A.A., 2016. Review: Survey of the control strategy of liquid desiccant systems. Renewable and Sustainable Energy Reviews 58, 250–258. https://doi.org/10.1016/j.rser.2015.12.333

Mohammad, A.Th., Mat, S.B., Sulaiman, M.Y., Sopian, K., Al-abidi, A.A., 2013. Survey of liquid desiccant dehumidification system based on integrated vapor compression

technology for building applications. Energy and Buildings 62, 1–14. https://doi.org/10.1016/j.enbuild.2013.03.001
Monteiro, E., Almeida, R., Rouboa, A., 2011. Finite Volume Method Analysis of Heat Transfer in Multiblock Grid during Solidification. Heat Transfer - Mathematical Modelling, Numerical Methods and Information Technology. https://doi.org/10.5772/14443
Mukhopadhyaya, P., Kumaran, M.K., Lackey, J., 2005. Use of the modified cup method to determine temperature dependency of water vapor transmission properties of building materials. Journal of Testing and Evaluation 33, 316–322.
Murphy, B., 2010. Terms of Confusion Part 2 Permeability Test Methods. Sherwin-Williams Waterblog. URL https://sherwinblogs.com/2010/02/01/terms-of-confusion-part-2-permeability-test-methods/ (accessed 11.2.18).
Mustapha, R., Khoury, K.E., Zoughaib, A., 2017. A Hybrid no Frost Refrigeration System Using a Membrane Based Desiccant System. Presented at the 30th International Conference on Efficiency, Cost, Optimisation, Simulation and Environmental Impact of Energy Systems (ECOS 2017).
Namvar, R., Ge, G., Simonson, C.J., Besant, R.W., 2013. Transient heat and moisture transfer characteristics of a liquid-to-air membrane energy exchanger (LAMEE) model verification and extrapolation. International Journal of Heat and Mass Transfer 66, 757–771. https://doi.org/10.1016/j.ijheatmasstransfer.2013.07.068
Nie, J., Li, Z., Hu, W., Fang, L., Zhang, Q., 2017. Theoretical modelling and experimental study of air thermal conditioning process of a heat pump assisted solid desiccant cooling system. Energy and Buildings 153, 31–40. https://doi.org/10.1016/j.enbuild.2017.07.075
Nielsen, K.K., Engelbrecht, K., Bahl, C.R.H., 2013. The influence of flow maldistribution on the performance of inhomogeneous parallel plate heat exchangers. International Journal of Heat and Mass Transfer 60, 432–439. https://doi.org/10.1016/j.ijheatmasstransfer.2013.01.018
Niu, X., Xiao, F., Ge, G., 2010. Performance analysis of liquid desiccant based air-conditioning system under variable fresh air ratios. Energy and Buildings 42, 2457–2464. https://doi.org/10.1016/j.enbuild.2010.08.027
NOAA, U.D. of C., 2019. ESRL Global Monitoring Division - Global Greenhouse Gas Reference Network [WWW Document]. URL https://www.esrl.noaa.gov/gmd/ccgg/trends/gl_full.html (accessed 3.25.19).
Nomura, T., Tsubota, M., Sagara, A., Okinaka, N., Akiyama, T., 2013. Performance analysis of heat storage of direct-contact heat exchanger with phase-change material. Applied Thermal Engineering 58, 108–113. https://doi.org/10.1016/j.applthermaleng.2013.03.041
Onsekizoglu, P., 2012. Membrane Distillation: Principle, Advances, Limitations and Future Prospects in Food Industry. https://doi.org/10.5772/37625
Pabby, A.K., Sastre, A.M., 2013. State-of-the-art review on hollow fibre contactor technology and membrane-based extraction processes. Journal of Membrane Science 430, 263–303. https://doi.org/10.1016/j.memsci.2012.11.060
Qi, R., Lu, L., 2014. Energy consumption and optimization of internally cooled/heated liquid desiccant air-conditioning system: A case study in Hong Kong. Energy 73, 801–808. https://doi.org/10.1016/j.energy.2014.06.086
Qin, C.K., Schmitz, G., 2006. Engine-driven desiccant-assisted hybrid air-conditioning system.

Rafique, M.M., Gandhidasan, P., Bahaidarah, H.M.S., 2016. Liquid desiccant materials and dehumidifiers – A review. Renewable and Sustainable Energy Reviews 56, 179–195. https://doi.org/10.1016/j.rser.2015.11.061

Rambhad, K.S., Walke, P.V., Tidke, D.J., 2016. Solid desiccant dehumidification and regeneration methods—A review. Renewable and Sustainable Energy Reviews 59, 73–83. https://doi.org/10.1016/j.rser.2015.12.264

Ramires, M.L.V., Nieto de Castro, C.A., Nagasaka, Y., Nagashima, A., Assael, M.J., Wakeham, W.A., 1995. Standard Reference Data for the Thermal Conductivity of Water [WWW Document]. URL https://keio.pure.elsevier.com/en/publications/standard-reference-data-for-the-thermal-conductivity-of-water (accessed 5.17.19).

Ren, C.Q., Tu, M., Wang, H.H., 2007. An analytical model for heat and mass transfer processes in internally cooled or heated liquid desiccant–air contact units. International Journal of Heat and Mass Transfer 50, 3545–3555. https://doi.org/10.1016/j.ijheatmasstransfer.2006.12.034

Richter, J., Staněk, K., 2016. Measurements of Water Vapour Permeability – Tightness of Fibreglass Cups and Different Sealants and Comparison of μ-value of Gypsum Plaster Boards. Procedia Engineering 151, 277–283. https://doi.org/10.1016/j.proeng.2016.07.377

Ritchie, H., Roser, M., 2017. CO_2 and other Greenhouse Gas Emissions. Our World in Data.

Royne, A., Dey, C.J., 2006. Effect of nozzle geometry on pressure drop and heat transfer in submerged jet arrays. International Journal of Heat and Mass Transfer 49, 800–804.

Ruiz, J., Cutillas, C.G., Kaiser, A.S., Ballesta, M., Zamora, B., Lucas, M., 2016. Experimental study of drift deposition from mechanical draft cooling towers in urban environments. Energy and Buildings 125, 181–195. https://doi.org/10.1016/j.enbuild.2016.04.076

Sabek, S., Tiss, F., Chouikh, R., Guizani, A., 2016. Experimental investigation and numerical validation of total heat exchanger and membrane phenomena. Energy and Buildings 133, 131–140. https://doi.org/10.1016/j.enbuild.2016.09.045

Schlichting, H., 1960. Boundary Layer Theory BY: DR.Hermann Schlichting. McGraw-Hill.

Seenivasan, D., Selladurai, V., Senthil, P., 2014. Optimization of Liquid Desiccant Dehumidifier Performance Using Taguchi Method. Advances in Mechanical Engineering 6, 506487. https://doi.org/10.1155/2014/506487

Seng, B., Magniont, C., Lorente, S., 2018. Characterization of a precast hemp concrete block. Part II: Hygric properties. Journal of Building Engineering. https://doi.org/10.1016/j.jobe.2018.09.007

Shen, J., Qian, Z., Xing, Z., Yu, Y., Ge, M., 2019. A review of the defrosting methods of air source heat pumps using heat exchanger with phase change material. Energy Procedia, 2nd International Conference on Energy and Power, ICEP2018, 13–15 December 2018, Sydney, Australia 160, 491–498. https://doi.org/10.1016/j.egypro.2019.02.197

Sieder, E.N., Tate, G.E., 1936. Heat Transfer and Pressure Drop of Liquids in Tubes. Ind. Eng. Chem. 28, 1429–1435. https://doi.org/10.1021/ie50324a027

Sloane Taliaferro, 2015. Documentation and testing of nineteenth-century lime wash recipes in the united states.

Specht, E., 2014. Impinging Jet Drying, in: Modern Drying Technology. pp. 1–26. https://doi.org/10.1002/9783527631704.ch01

Staffell, I., Brett, D., Brandon, N., Hawkes, A., 2012. A review of domestic heat pumps. Energy & Environmental Science.

Stevens, D.I., Braun, J.E., Klein, S.A., 1989. An effectiveness model of liquid-desiccant system heat/mass exchangers. Solar Energy 42, 449–455. https://doi.org/10.1016/0038-092X(89)90045-5

Sustainable Development Scenario [WWW Document], 2018. URL https://www.iea.org/weo/weomodel/sds/ (accessed 3.30.19).
Tsilingiris, P.T., 2008. Thermophysical and transport properties of humid air at temperature range between 0 and 100 °C - ScienceDirect [WWW Document]. URL https://www.sciencedirect.com/science/article/pii/S0196890407003329 (accessed 5.16.19).
Vali, A., Ge, G., Besant, R.W., Simonson, C.J., 2015. Numerical modeling of fluid flow and coupled heat and mass transfer in a counter-cross-flow parallel-plate liquid-to-air membrane energy exchanger. International Journal of Heat and Mass Transfer 89, 1258–1276. https://doi.org/10.1016/j.ijheatmasstransfer.2015.06.043
Vali, A., Simonson, C.J., Besant, R.W., Mahmood, G., 2009. Numerical model and effectiveness correlations for a run-around heat recovery system with combined counter and cross flow exchangers. International Journal of Heat and Mass Transfer 52, 5827–5840. https://doi.org/10.1016/j.ijheatmasstransfer.2009.07.020
Vinze, R., Chandel, S., Limaye, M.D., Prabhu, S.V., 2016. Influence of jet temperature and nozzle shape on the heat transfer distribution between a smooth plate and impinging air jets. International Journal of Thermal Sciences 99, 136–151. https://doi.org/10.1016/j.ijthermalsci.2015.08.009
Wang, Y., Liu, M., Liu, D., Xu, K., 2011. Heat Flux Correlation for Spray Cooling in the Nonboiling Regime. Heat Transfer Engineering 32, 1075–1081. https://doi.org/10.1080/01457632.2011.556505
Wang, Z., Zhang, X., Li, Z., 2017. Investigation on the coupled heat and mass transfer process between extremely high humidity air and liquid desiccant in the counter-flow adiabatic packed tower - ScienceDirect [WWW Document]. URL https://www.sciencedirect.com/science/article/pii/S001793101632419X (accessed 5.2.19).
Wenju, H., Yiqiang, J., Minglu, Q., Long, N., Yang, Y., Shiming, D., 2011. An experimental study on the operating performance of a novel reverse-cycle hot gas defrosting method for air source heat pumps. Applied Thermal Engineering 31, 363–369. https://doi.org/10.1016/j.applthermaleng.2010.09.024
Wilkinson, D.P., Smith, P.K., Joffe, M., Haines, P.A., 2007. A global perspective on energy: health effects and injustices. THE LANCET 370, 965–978.
Wolf, G., Jahn, H., Pekarek, V., Vacek, V., 1987. Enthalpy of dissolution of lici and LiCl·H2O in water at 25° C at low concentrations [WWW Document]. URL https://www.sciencedirect.com/science/article/pii/004060318788190X (accessed 5.17.19).
Woods, J., Pellegrino, J., Kozubal, E., Slayzak, S., Burch, J., 2009. Modeling of a membrane-based absorption heat pump. Journal of Membrane Science 337, 113–124. https://doi.org/10.1016/j.memsci.2009.03.039
World Employment and Social Outlook 2018 – Greening with jobs, 2018. . World Employment and Social Outlook 28.
World Energy Outlook [WWW Document], 2018. URL https://www.iea.org/weo/ (accessed 3.26.19).
Wu, R., Hong, T., Cheng, Q., Zou, H., Fan, Y., Luo, X., 2019. Thermal modeling and comparative analysis of jet impingement liquid cooling for high power electronics. International Journal of Heat and Mass Transfer 137, 42–51. https://doi.org/10.1016/j.ijheatmasstransfer.2019.03.112
Wu, X.N., Ge, T.S., Dai, Y.J., Wang, R.Z., 2018. Review on substrate of solid desiccant dehumidification system. Renewable and Sustainable Energy Reviews 82, 3236–3249. https://doi.org/10.1016/j.rser.2017.10.021

Xia, J.L., Järvi, J., Nurminen, E., Peuraniemi, E., Gasik, M., 2006. COOLING OF GAS BY A WATER SPRAY IN A STRAIGHT DUCT – CROSS FLOW 9.

Xie, Y., Xu, Z., Mei, N., 2016. Evaluation of the effectiveness-NTU method for countercurrent humidifier. Applied Thermal Engineering 99, 1270–1276. https://doi.org/10.1016/j.applthermaleng.2016.01.112

Y. Khan, A., 1994. Sensitivity analysis and component modelling of a packed-type liquid desiccant system at partial load operating conditions. https://doi.org/10.1002/er.4440180703

Yang, L., Yan, Y., Ma, J., Liu, B., 2013. Effects of inter-fiber spacing and thermal residual stress on transverse failure of fiber-reinforced polymer–matrix composites. Computational Materials Science 68, 255–262. https://doi.org/10.1016/j.commatsci.2012.09.027

Yin, H.-J., Yang, Z., Chen, A.-Q., Zhang, N., 2012. Experimental research on a novel cold storage defrost method based on air bypass circulation and electric heater. Energy, 7th Biennial International Workshop "Advances in Energy Studies" 37, 623–631. https://doi.org/10.1016/j.energy.2011.10.040

Yoshioka, K., Hasegawa, S., 2012. Heat Transfer to Falling Water Film on a Vertical Surface. Journal of Nuclear Science and Technology 12, 618–625. https://doi.org/10.1080/18811248.1975.9733162

Yu, B.F., Hu, Z.B., Liu, M., Yang, H.L., Kong, Q.X., Liu, Y.H., 2009. Review of research on air-conditioning systems and indoor air quality control for human health. International Journal of Refrigeration 32, 3–20. https://doi.org/10.1016/j.ijrefrig.2008.05.004

Zhang, L., Hihara, E., Saikawa, M., 2012. Combination of air-source heat pumps with liquid desiccant dehumidification of air. Energy Conversion and Management 57, 107–116. https://doi.org/10.1016/j.enconman.2011.12.023

Zhang, L.-Z., 2006. Investigation of moisture transfer effectiveness through a hydrophilic polymer membrane with a field and laboratory emission cell. International Journal of Heat and Mass Transfer 49, 1176–1184. https://doi.org/10.1016/j.ijheatmasstransfer.2005.08.029

Zhang, L.-Z., Huang, S.-M., 2011. Coupled heat and mass transfer in a counter flow hollow fiber membrane module for air humidification. International Journal of Heat and Mass Transfer 54, 1055–1063. https://doi.org/10.1016/j.ijheatmasstransfer.2010.11.025

Zhang, L.-Z., Huang, S.-M., Chi, J.-H., Pei, L.-X., 2012. Conjugate heat and mass transfer in a hollow fiber membrane module for liquid desiccant air dehumidification: A free surface model approach. International Journal of Heat and Mass Transfer 55, 3789–3799. https://doi.org/10.1016/j.ijheatmasstransfer.2012.03.034

Zhang, L.-Z., Liang, C.-H., Pei, L.-X., 2010. Conjugate heat and mass transfer in membrane-formed channels in all entry regions. International Journal of Heat and Mass Transfer 53, 815–824. https://doi.org/10.1016/j.ijheatmasstransfer.2009.11.043

Zhang, L.Z., Niu, J.L., 2002. Effectiveness Correlations for Heat and Moisture Transfer Processes in an Enthalpy Exchanger With Membrane Cores. Journal of Heat Transfer 124, 922. https://doi.org/10.1115/1.1469524

Zhang, L.-Z., Wang, Y.-Y., Wang, C.-L., Xiang, H., 2008. Synthesis and characterization of a PVA/LiCl blend membrane for air dehumidification. Journal of Membrane Science 308, 198–206. https://doi.org/10.1016/j.memsci.2007.09.056

Zhang, L.-Z., Zhang, N., 2014. A heat pump driven and hollow fiber membrane-based liquid desiccant air dehumidification system: Modeling and experimental validation. Energy 65, 441–451. https://doi.org/10.1016/j.energy.2013.10.014

Zhang, T., Liu, X., Jiang, Y., 2012. Performance optimization of heat pump driven liquid desiccant dehumidification systems. Energy and Buildings 52, 132–144. https://doi.org/10.1016/j.enbuild.2012.06.002

Zhao, B., Peng, N., Liang, C., Yong, W.F., Chung, T.-S., 2015. Hollow Fiber Membrane Dehumidification Device for Air Conditioning System. Membranes 5, 722–738. https://doi.org/10.3390/membranes5040722

Zhao, X., Li, J.M., Riffat, S.B., 2008. Numerical study of a novel counter-flow heat and mass exchanger for dew point evaporative cooling. Applied Thermal Engineering 28, 1942–1951. https://doi.org/10.1016/j.applthermaleng.2007.12.006

Zhao, X, Liu, S., Riffat, S.B., 2008. Comparative study of heat and mass exchanging materials for indirect evaporative cooling systems. Building and Environment 43, 1902–1911. https://doi.org/10.1016/j.buildenv.2007.11.009

Zhu, F. (Xin X.), 2013. Energy and Process Optimization for the Process Industries. John Wiley & Sons.

Zohuri, B., 2017. Heat Exchanger Types and Classifications, in: Compact Heat Exchangers. Springer International Publishing, Cham, pp. 19–56. https://doi.org/10.1007/978-3-319-29835-1_2

RÉSUMÉ

L'objectif principal de cette thèse est de proposer une méthodologie et un outil de modélisation pour concevoir des systèmes hybrides de réfrigération et de climatisation à haute performance, abordables et flexibles. Il se concentre sur des systèmes hybrides basés sur le couplage d'un cycle de dessiccation et un cycle de compression de vapeur permettant un contrôle efficace de l'humidité dans les applications de climatisation et un fonctionnement sans givre dans les applications de réfrigération. Le travail a été développé pour étudier une nouvelle conception d'un échangeur membranaire de chaleur et de masse à l'aide de membranes originales et d'une nouvelle conception liée à la distribution de liquide. La conception tire parti des matériaux à faible coût qui sont testés expérimentalement à l'aide d'une nouvelle méthodologie pour déduire leur perméabilité de la vapeur d'eau qui affecte significativement le transfert de masse. Un prototype de l'échangeur membranaire proposé est alors construit et une approche de modélisation des phénomènes de transfert de chaleur et de masse est développée et appuyée par des caractérisations expérimentales. Ce modèle est ensuite utilisé pour étudier l'intérêt énergétique de l'intégration de ces échangeurs dans les applications de climatisation et pour concevoir une architecture flexible capable de faire face à la variation saisonnière du rapport de charge latente à sensible. Les résultats montrent que le système hybride étudié présente des solutions alternatives prometteuses comparé aux cycles conventionnels, où ils peuvent améliorer de façon significative les performances et réduire la consommation d'électricité.

MOTS CLÉS

Systèmes hybrides, échangeurs de chaleur et de masse, membranes, desiccant liquide, performances saisonnières, efficacité de l’énergie.

ABSTRACT

The major objective of this thesis is to propose a methodology and a modeling tool to design high performance, affordable and flexible hybrid refrigeration and air conditioning systems. It focuses on hybrid systems based on coupling a desiccant cycle with a vapor compression cycle allowing an efficient humidity control in air conditioning applications and a frost free operation in refrigeration applications. The work was developed to investigate a novel design of a membrane based heat and mass exchanger using original membrane materials and new design related to liquid distribution. The design takes advantage of materials with low cost that are experimentally tested using a new methodology to infer their water vapor permeability that greatly affects the mass transfer. A prototype of the designed membrane exchanger is then built and a modeling approach of the heat and mass transfer phenomena is developed and is supported by experimental characterization. This model is then used to study the energy interest of the integration of these exchangers in air conditioning applications and to design a flexible architecture able to cope with the seasonal variation of the latent to sensible load ratio. The results show that the studied hybrid systems present promising alternatives for conventional cycles where they can significantly improve the performance and decrease the consumption of electricity.

KEYWORDS

Hybrid systems, heat and mass exchangers, membranes, liquid desiccant, seasonal performance, energy efficiency.